# Lattice-supersolids in bosonic quantum gases with Rydberg excitations

DISSERTATION

zur Erlangung des Doktorgrades
der Naturwissenschaften

vorgelegt beim Fachbereich Physik
der JOHANN WOLFGANG GOETHE - UNIVERSITÄT
in FRANKFURT AM MAIN

von

Andreas GEISSLER
aus Miltenberg am Main

Frankfurt am Main, Februar 2018
(D 30)

vom Fachbereich Physik der

Johann Wolfgang Goethe - Universität

als Dissertation angenommen

| | |
|---|---|
| *Dekan:* | Prof. Dr. Owe Philipsen |
| *Gutachter:* | Prof. Dr. Walter Hofstetter |
| | Priv.-Doz. Dr. Axel Pelster |

Datum der Disputation: 15. Oktober 2018

*"The imagination of nature is far, far greater than the imagination of man."*

Richard P. Feynman – [FL88]

# *Zusammenfassung*

Diese Arbeit ist der Bestimmung des reichhaltigen Phasendiagramms im Vielteilchen-Grundzustand und der zugehörigen spektralen Eigenschaften eines ultrakalten Quantengases bosonischer Atome in einem zweidimensionalen optischen Gitter unter dem Einfluss kohärent angeregter Rydbergzustände gewidmet. Da diese atomaren Anregungen starke langreichweitige Van-der-Waals-Wechselwirkungen zwischen den sogenannten Rydbergatomen hervorrufen, können diese eine Symmetriebrechung der diskreten Translationssymmetrie des optischen Gitters verursachen. In isolierenden Phasen kommt es dabei zu einer Treppe von Dichtewelle-Strukturen, welcher mitunter das Attribut „teuflisch“ zugeschrieben wird, wenn es möglich ist, zwischen zwei Stufen gegebener Dichte von Rydberganregungen, bei hinreichend feiner Einstellung der Systemparameter, stets noch weitere Stufen zu finden. Demgegenüber stehen Phasen bei denen ein makroskopischer Anteil der Teilchen als Gitter-Superfluid vorliegt. In diesen Phasen ist es ebenfalls möglich, dass die Van-der-Waals-Wechselwirkung der Rydberanregungen eine Dichtewelle bewirkt, sodass es in der Kombination zur Gitter-Supersolidität kommt. Gekennzeichnet ist diese durch eine langreichweitige Ordnung, welche sich sowohl über die Nebendiagonalelemente der Dichtematrix (Kennzeichen der Superfluidität) als auch über die Diagonale der Dichtematrix erstreckt und dabei die diskrete Translationssymmetrie des Gitters bricht (Kennzeichen der Dichtewelle).

In scheinbar paradoxer Weise vereint ein Supersolid somit zwei Eigenschaften, die im klassischen Verständnis unvereinbar miteinander scheinen. Zum einen besitzt Materie in dieser Phase einen flüssigen Anteil mit verschwindender Viskosität, hat jedoch gleichzeitig auch Eigenschaften eines Kristalls, welche sich insbesondere durch ihre steife Struktur auszeichnen. Die erste Vorhersage einer solchen Phase geht zurück auf Andreev und Lifshitz, die 1969 die Möglichkeit der reibungsfreien Bewegung bosonischer Kristalldefekte durch ein Kristallgitter vorhersagten. Ihr Vorschlag beruhte auf der Beobachtung, dass das Spektrum der Quasiteilchen, also von quantisierten Gitterfluktuationen, wie zum Beispiel Störstellen, in einem Kristall bosonischer Teilchen bei steigender Wecheslwirkungsstärke ein lokales Minimum für einen Impuls ungleich Null ausbildet, das sogenannte "Roton-Minimum".

Zur Zeit der Vorhersage einer solchen Phase galt Helium-4 in seiner kristallinen Phase noch als aussichtsreichster Kandidat des experimentellen Nachweises. Da man den Anteil des Heliums, der sich in einem superfluiden Zustand befindet, aufgrund der fehlenden Viskosität als entkoppelt vom verbleibenden Kristall ansehen kann, schlug Legget 1970 vor, dass man den Nachweis mit Hilfe eines Torsionspendels führen kann. Sollte diese Phase tatsächlich in Helium auftreten, dann sollte sie sich in einer Abweichung der Rotationsträgheit des Pendels bemerkbar machen. Obschon zahlreiche Experimente im Jahr 2004, angefangen mit jenen von Kim und Chan, sowie in den folgenden Jahren vielversprechende Resultate zu geben schienen, haben sich die vielfach beobachteten Signale als Folge eines anderen, bisher unbekannten Effekts erwiesen. Diese sogenannte Quantenplastizität verursacht eine Versteifung des festen Heliums, was sich in einer dem Supersolid ähnlichen Weise auf die Rotationsträgheit auswirkt. Daher erweist sich das Supersolid aktuell als schwer realisierbar in festem Helium.

Im Jahr 2017 jedoch haben zwei Gruppen von einander unabhängig über die

Beobachtung supersolider Eigenschaften in zwei grundsätzlich verschiedenen Quantengas-Experimenten berichtet. Bemerkenswert dabei ist auch, dass sich beide Systeme in einem Regime befinden, das scheinbar im Widerspruch zur Supersolidität in festem Helium steht. Ultrakalte Quantengase zeichnen sich insbesondere durch ihre sehr geringe Dichte von $10^{-15}\mathrm{cm}^3$ und weniger aus, die sechs Größenordnungen unter der Dichte eines Gases bei Raumtemperatur und Normaldruck liegt. Demgegenüber sind zur Erzeugung von festem Helium sehr hohe Drücke und damit auch hohe Dichten notwendig. Die stark verdünnten atomaren Dämpfe der Quantengase hingegen werden mit Hilfe optischer Fallen in einer Vakuumkammer in der Schwebe gehalten.

Bevor wir uns mit den Details der genannten Experimente beschäftigen, ist an dieser Stelle zu betonen, dass es sich in beiden Fällen um Beispiele für die Realisierung eines – in beiden Fällen – analogen Quantensimulators handelt. Dieses Konzept geht zurück auf Feynman, der 1982 vorschlug ein sehr fein einstellbares Quantensystem zu verwenden um damit ein anderes Quantensystem nachzuahmen, das sich aus grundverschiedenen Bestandteilen zusammensetzt, oder um ein System zu erzeugen für das keine natürlich vorkommende Entsprechung existiert. Experimente dieser Art wurden erstmals 1995 von Ketterle und Wieman in ultrakalten Quantengasen realisiert, womit sie ein vollkommen neues Feld der Physik eröffneten.

In den experimentellen Beobachtungen des Supersolids von Lénoard et al. wird die Brechung einer kontinuierlichen Translationssymmetrie eines atomaren Bose-Einstein-Kondensates beobachtet, das sich in zwei gekreuzten optischen Kavitäten befindet. Bedingt durch die Kopplung der Atome an die Photonen, welche in den Kavitäten gefangen sind, erfahren die Atome eine starke, effektiv unendlichreichweitige Wechselwirkung, die letztlich ursächlich für den Übergang in den supersoliden Zustand ist.

Demgegenüber handelt es sich bei dem Experiment von Li et al. um ein schwach wechselwirkendes atomares Bose-Einstein-Kondensat, bei dem Raman-induziertes Tunneln zwischen zwei Gitterplätzen eines Übergitters eine effektive Spin-Bahn-Kopplung in der zum Übergitter orthogonalen Richtung hervorruft. Dadurch ist es möglich, die beiden effektiven Spin-Komponenten, die durch die beiden Gitterplätze des Untergitters repräsentiert sind, mit entgegengesetztem Impuls von identischem Betrag in Interferenz zu bringen. Da diese eine stehende und räumlich oszillierende Dichteschwankung des Kondensats bewirkt, deren räumliche Phase sich spontan beim Einschalten des Raman-tunnelns einstellt, kann man auch hier ein Supersolid beobachten.

Im Zuge dieser Arbeit beschäftigen wir uns mit einem System, in dem der Phasenübergang zu einem Gitter-Supersolid, das die diskrete Translationssymmetrie eines zugrundeliegenden Gitters bricht, in Analogie zu erstem Experiment, durch eine stark langreichweitige Wechselwirkung hervorgerufen wird. Diese wird realisiert über die starken Van-der-Waals-Kräfte zwischen neutralen Rydbergatomen, die aufgrund der hohen Polarisierbarkeit der Elektronenoribtale von Rydbergzuständen auftreten. Dadurch kommt es zu langreichweitigen Wechselwirkungen, welche sich in einem optischen Gitter, mit der experimentell typischen Gitterkonstante von 532 nm, über mehrere Gitterplätze erstrecken. Die Ausprägung dieser Wechselwirkung wird dabei sehr stark von den Parametern des anregenden Lasers bestimmt. Zu erwähnen sind hierbei insbesondere die Rabifrequenz, die sich aus den

Laserintensitäten ergibt sowie die Verstimmung der Laserfrequenz von den Frequenzen der angeregten Übergänge zum gewünschten Rydbergzustand. Des weiteren ist zu betonen, dass sich selbst atomare optische Gittersystem bereits durch einen hohen Grad der Steuerbarkeit grundlegender Parameter auszeichnen. Dies gilt insbesondere für die lokale Hubbard-Wechselwirkung und die Tunnelrate zwischen einzelnen Gitterplätzen, die sich durch die Tiefe des optischen Gitters und dabei, dank des Einflusses von Feshbach-Resonanzen auf die lokale Wechselwirkung, unabhängig voneinander einstellen lassen.

Betrachten wir den Fall einer abstoßende Van-der-Waals-Wechselwirkung, ist es denkbar, dass es in diesen Systemen zu einer spontanen Symmetriebrechung der diskreten Translationssymmetrie des zugrunde liegenden optischen Gitters kommt. Im wesentlichen beobachtet man hierbei zwei Szenarien: Für isolierende Phasen ergibt sich eine Dichtewelle-Struktur der in Rydbergzustände angeregten Atome. Ist die optimale Dichte der Rydberganregungen unvereinbar mit der Struktur des optischen Gitter, bewirkt dies die zuvor genannte teuflische Treppe von Dichtewellen, die insbesondere als Funktion der Frequenzverstimmung sichtbar wird. Ebenso bestimmt die Verstimmung auch jene Dichtewelle-Strukturen, welche man in den supersoliden Phasen beobachten kann. Aufgrund der dem Superfluid inhärenten Fluktuationen können beliebig feine Stufen dann jedoch nicht mehr stabilisiert werden, wodurch sich die Stufenstruktur im superfluiden Regime vereinfacht.

Im Verlauf dieser Arbeit besprechen wir insbesondere das Gitter-Supersolid, das sich in optischen Gitterfallen realisieren lässt. Die starke Van-der-Waals-Wechselwirkung zwischen hoch angeregten atomaren Rydbergzuständen ermöglicht die Selbstordnung eines homogenen Gitter-Supersolids durch Formierung einer Dichtewelle-Struktur. Der erste Teil dieser Arbeit, bestehend aus den ersten drei Kapiteln, ist einem Überblick zu den Grundlagen solcher System gewidmet.

Im ersten Kapitel besprechen wir sowohl einige grundlegende Methoden als auch (Mess-)Techniken der umfangreichen „toolbox“, welche in üblichen Quantengasexperimenten zur Verfügung stehen, beziehungsweise solche, die die notwendigen Temperaturen auf einer Mikrokelvin-Skala und darunter erst ermöglichen. Zudem geben wir eine Zusammenfassung der grundlegenden theoretischen Konzepte zum Verständnis von Superfluidität und Supersolidität, insbesondere in zweidimensionalen Systemen.

Hierauf folgt das zweite Kapitel, in welchem wir die wesentlichen Grundlagen der Rydberg-Physik in Quantenvielteilchensystemen diskutieren. Dabei legen wir das Hauptaugenmerk auf die Ermöglichung langreichweitiger Wechselwirkungen zur Erzeugung eines Modells mit ausgeprägten nichtlokalen Korrelationen. Zudem besprechen wir den Einfluss der endlichen Lebensdauer der Rydberganregungen auf mögliche Vielteilchenzustände, wobei die entsprechende Zeitskala in einer Umgebung bei Raumtemperatur insbesondere durch lawinenartige Dephasierungsprozesse bestimmt ist. Das Kapitel schließt mit einer kurzen Analyse über die Anwendbarkeit der Hartree-Näherung für Vielteilchensysteme, bei denen die Atome nahe der Resonanz eines einzelnen Atoms in den Rydbergzustand angeregt werden. Die Wechselwirkung sorgt hierbei für eine Molekularfeldverstimmung der Energien weiterer Anregungen in der Umgebung bereits angeregter Rydbergzustände, was weitere Übergänge blockiert. Somit erhält man einen Rydberganteil, der unter dem eines freien Atoms in einem identischen Lichtfeld liegt. Bei diesem Effekt spricht man von der „Rydberg-Blockade“.

Die einleitenden Kapitel schließen im dritten Kapitel mit einer kurzen Einführung über die Realisierung des Bose-Hubbard Modells in optischen Gittersystemen,

einschließlich der Erweiterung bedingt durch die kohärente Anregung von Rydbergzuständen. Dabei werden die Fälle der Rydberganregung nahe und fern der Einteilchenanregung als zwei fundamental verschiedene Szenarien diskutiert.

Auf diesen Teil folgen drei Kapitel, in welchen wir theoretischen Methoden einführen und wesentliche Erweiterungen diskutieren um das betrachtete Modell angemessen beschreiben zu können. Zunächst geben wir dazu im vierten Kapitel einen Überblick über die bosonische „Dynamische Molekularfeld-Theorie“ (B-DMFT), die ursprünglich von Vollhardt für die Analyse fermionischer Vielteilchensysteme vorgeschlagen wurde. Deren Grundidee ist die Verallgemeinerung des Molekularfeldes von einer typischerweise statischen Größe auf eine dynamische, welche man als Weiss'sche Green's Funktion bezeichnet. Ausgehend von dem Modell einer Anderson-Störstelle beschreibt diese Methode einen gegebenen Gitterplatz als Realisierung eines ebensolchen Modells, wobei das Verhalten des restlichen Gitters selbst-konsistent über genannte Green's Funktion beschrieben wird. Der Vorteil dieser Methode liegt darin, dass sie nicht-perturbativ ist und jegliche lokalen Fluktuationen exakt berücksichtigt. Dabei werden Korrelationen nächster Nachbarplätze im Gitter auf der Ebene der nicht-lokalen Einteilchenfluktuationen in Form der Weiss'schen Green's Funktion ebenfalls mit einkalkuliert. Da die bosonische Variante dieser Methode Anwendung findet, ist zudem stets noch ein statisches Molekularfeld zu berücksichtigen, das wegen der möglichen Bose-Einstein-Kondensation in Form des Kondensat-Ordnungsparameters vorliegt. Motiviert durch die langreichweitige Wechselwirkung der Rydberganregungen führen wir zudem die Erweiterung von B-DMFT auf eine ortsraumaufgelöste Methode (RB-DMFT) ein und ergänzen diese um den Hartree-Ansatz, der auf die Wechselwirkungsterme angewandt wird. Dadurch ergänzen wir den Satz selbst-konsistenter Parameter noch um die ortsaufgelöste Dichte der Rydberganregungen. Abschließend zeigen wir, wie man mittels der RB-DMFT auch Aussagen über das dynamische Verhalten eines gegebenen Systems in Form der Spektralfunktion erhält.

Mit dem fünften Kapitel führen wir ergänzend eine effiziente Methode zur Trunkierung der lokalen Fock-Basis bosonischer Systeme ein. Da Bosonen aufgrund ihrer Kommutationsrelationen keine natürlich beschränkte Fock-Basis besitzen, bedingt jede numerische Methode, die auf diese Basis zurückgreift, eine Beschränkung (Trunkierung) auf eine begrenzte Zahl von Fock-Zuständen, um Simulationen in endlicher Zeit überhaupt zu ermöglichen. Dies kann in der Anwesenheit eines Kondensats und bei hoher Teilchendichte von mehr als einem Teilchen je Gitterplatz rasch zur Notwendigkeit sehr hoher Trunkierung und damit numerisch aufwendigen Rechnungen führen. Da jene Vielteilchensysteme, die wir in dieser Arbeit betrachten, bereits ausgedehnte Einheitszellen erforderlich machen, führen wir in diesem Kapitel einen lokalen Zustand mit kohärentem Schweif ein, den „coherent-tail state“ (CTS), der durch einen Parameter beschrieben werden kann. Diesem Zustand liegt die Beobachtung zugrunde, dass sich der Grundzustand eines idealen Bosegases quasi exakt durch einen kohärenten Zustand beschreiben lässt. In diesem Kapitel zeigen wir, dass sich der freie Parameter bei der Bestimmung des Vielteilchenzustandes ergibt durch die Minimierung der entsprechenden Energie. Dies zeigen wir sowohl anhand der Gutzwiller-Wellenfunktion als auch für die B-DMFT. Eine Optimierung der Resultate der jeweiligen Methode ist in beiden Fällen zu beobachten, wobei diese „weiche“ Trunkierung insbesondere im Falle der B-DMFT die Simulationszeit, bei gleichbleibender Genauigkeit um mehr als eine Größenordnung zu reduzieren vermag.

Ausgehend von dem Gutzwiller-Ansatz für den Grundzustand eines bosonischen Systems, zeigen wir im sechsten Kapitel, dass man Fluktuationen, die von der

Gutzwiller-Wellenfunktion vernachlässigt werden, exakt in der Eigenbasis des effektiven Gutzwiller-Hamiltonians darstellen kann. Wie bereits in der Doktorarbeit von Bissbort geschildert, erlaubt dies die exakte Darstellung der vernachlässigten Terme des effektiven Modells in quasi-bosonischen Erzeugungs- und Vernichtungsoperatoren lokaler Gutzwiller-Anregungen. In Analogie zur linearisierten Gutzwiller-Bewegungsgleichung kann man sich dann auf den führenden Term von quadratischer Ordnung in diesen Operatoren beschränken, wodurch man ein System nichtwechselwirkender Quasiteilchen erhält, denen die Gutzwiller-Wellenfunktion als Quasi-Vakuum dient. Ein wesentlicher Schwerpunkt dieses Kapitels stellt die Erweiterung der ursprünglichen Beschreibung auf ein mehrkomponentiges System dar, dessen Gutzwiller-Grundzustand, bedingt durch die langreichweitigen Wechselwirkung, durch einen Ansatz mit einer Übergitterstruktur beschrieben wird. Dadurch wird die Berücksichtigung einer reduzierten Brillouin-Zone notwendig, die mit der Rückfaltung von Quasiteilchen-Moden und dem Auftreten vermiedener Bandkreuzungen einhergeht. Dieses Kapitel endet mit einer Schilderung zur expliziten Bestimmung zahlreicher, für Experimente relevanter Spektralfunktionen, welche man Dank der Quasiteilchenbeschreibung für den Grundzustand des Quasiteilchen-Hamiltonians extrahieren kann. Mit einer Herleitung von Korrekturen der Gutzwiller-Lösung für den Kondensat-Ordnungsparameter, der lokalen Dichte, sowie der Dichtematrix schließen wir die Diskussion der verwendeten theoretischen Methoden.

Mit Hilfe der beschriebenen Methoden analysieren wir in den verbleibenden beiden Kapiteln die Phasen und spektralen Eigenschaften frei beweglicher Atome in einem optischen Quadratgitter unter dem Einfluss von Rydberganregungen. Dazu unterscheiden wir zum einen den Fall der Rydberganregung fern von der Einteilchenresonanz, also das sogenannte „(weak) dressing“, und zum anderen den Fall der Rydberganregung nahe der Einteilchenresonanz, was wir in dieser Arbeit als „strong dressing“ bezeichnen wollen. Beide Fälle werden hierbei im großkanonischen Ensemble betrachtet.

Der erstgenannte Fall wird im siebten Kapitel betrachtet. Dabei wird ein System bestehend aus einem Quantengas von Rubidium-87 ($^{87}$Rb) angenommen, wobei zwei atomare Hyperfein-Grundzustände vorliegen sollen. Der erste dieser Grundzustände wird stark rot-verstimmt in einen Rydbergzustand angeregt, wobei der zweite nicht davon betroffen ist. Beide Teilchenkomponenten können dabei jedoch lokal miteinander wechselwirken. Da die Rydberganregung in der ersten Komponente ein langreichweitiges Wechselwirkungspotential hervorruft, das für kurze Distanzen gegen eine Konstante strebt und für große Distanzen wie die Van-der-Waals-Wechselwirkung gegen Null geht, beobachten wir in dieser Komponente eine Tendenz zur Formierung einer Dichtewelle. Da die andere Komponente lediglich lokale mit der ersten in Wechselwirkung tritt, überträgt sich die Dichtewelle auf die zweite Komponente selbst dann, wenn die erste in einem isolierenden Zustand ist und in der zweiten noch ein Superfluid vorliegt. Dadurch ergibt sich ein großer Parameterbereich, in dem das Gitter-Supersolid möglich ist. Im weiteren analysieren wir zudem die spektralen Eigenschaften für repräsentative Phasen. Da dieses Modell einem weiteren ähnelt, welches ein System polarer Moleküle beschreibt, geben wir auch eine kurze Analyse der Phasen jenes Modells an.

Im achten und letzten Kapitel besprechen wir ein Quantengas, bei dem die Rydberganregung bei nur geringer Verstimmung des Anregungslasers erfolgt. Auch hier betrachten wir ein zweikomponentiges System, wobei die eine Komponente durch die Grundzustandsatome gegeben ist, während die andere durch die Rydbergatome gegeben ist. Aufgrund der skalenfreien Van-der-Waals-Wechselwirkung

können wir für den gefrorenen Fall des Modells, also bei verschwindend geringer Tunnelrate, eine (durch Annahmen bedingt) unvollständige „teuflische“ Treppe von Dichtewellen finden, die beginnen sich aufzulösen, sobald ein superfluider Anteil vorliegt. Somit schließen sich bei hinreichend großer Tunnelrate supersolide Phasen an die Dichtewellen an. Bei einer Reduzierung der Verstimmung ergibt sich ein Übergang zur supersoliden Phase mit minimaler Einheitszelle (Schachbrett-Supersolid), die abschließend in ein homogenes Superfluid übergeht. Während sich der blau-verstimmte Bereich des Phasendiagramms durch einen hohen lokalen Rydberganteil auszeichnet, liegt dieser Wert im Schachbrett-Supersolid bei nur einigen Prozent. Daher ist letztere Phase für die experimentelle Realisierung zu favorisieren, da die Lebensdauer der Rydberganregungen einen begrenzenden Faktor darstellt. Zudem ist auch zu erwarten, dass das Schachbrett-Supersolid bereits bei kleinen Systemgrößen zu beobachten ist. Da diese Phase stark durch Vielteilcheneffekte bedingt ist, welche am Rand des Systems nur reduziert auftreten, besprechen wir ergänzend eine Methode um diesem Randeffekt entgegenzuwirken. Für ein solches Beispielsystem zeigen wir, wie sich die lokale Zustandsdichte im System mit Wechselwirkung von der ohne Wechselwirkung unterscheidet. Für die experimentell relevanten Phasen analysieren wir abschließend verschiedene spektrale Eigenschaften, wie die Zusammensetzung der Quasiteilchenbänder sowie die entsprechenden Spektralfunktionen.

# *Abstract*

In the course of this thesis we will discuss a certain kind of supersolid, the lattice-supersolid, which can be realized using quantum gases in an optical lattice trap. The lattice-supersolid, which simultaneously possesses off-diagonal and diagonal long-range order in its density matrix and also breaks the discrete translational symmetry of an underlying lattice, is induced by self-ordering of the gas due to strong long-range van der Waals interactions. In the considered scenario, the interactions are facilitated by the excitation of atomic Rydberg states, which exhibit enhanced van der Waals forces.

In the first part of this thesis, we will review relevant basics of quantum gases, Rydberg physics and introduce the extended Bose-Hubbard model. We will start with the relevant methods and devices of the vast toolbox available in common quantum gas experiments, as well as consider the main concepts behind superfluidity and supersolidity. This is followed by an introduction of some basic concepts of Rydberg atoms in quantum many-body systems, with a focus on the facilitation of long-range interactions and the implementation in a theoretical model. Thereafter a brief introduction will be given, on the realization of the Bose-Hubbard model in optical lattice systems and its extension to include Rydberg states, which concludes the introductory part of this thesis.

In the following part, we will introduce the theoretical tools used to derive the results presented in the final part. First, an introduction to a real-space extension of bosonic dynamical mean-field theory (RB-DMFT) for bosonic systems with long-range interactions in the Hartree approximation will be given. This method is based on the non-perturbative self-consistent evaluation of the lattice Green's function, which also incorporates the effect of nearest neighbor correlations due to the non-condensed particles. Then we will focus on a quasiparticle expansion of the Bose-Hubbard model, which has its foundation in linearized fluctuations of a static mean-field ground-state, allowing for the prediction of a vast range of experimentally relevant observables. Lastly we will introduce an efficient truncation scheme for the local bosonic Fock-basis, which allows for the simulation of phases with high condensate density at a vastly reduced computational effort.

In the final part, we will apply both methods to itinerant bosonic gases in two-dimensional optical lattices, in order to predict the equilibrium ground-state phases, as well as the signatures of supersolidity and its formation in spectral functions and the dynamic and static structure factor. Thereby we will consider two limiting cases. Firstly, we will consider a two-component gas, as realized by two hyperfine ground states, for example, of rubidium-87 ($^{87}$Rb), where one component is off-resonantly excited to a Rydberg state, which generates a soft-core shaped interaction potential. Secondly, we will discuss the opposing limit, using near-resonant excitations of Rydberg states, where the interacting component now directly corresponds to the Rydberg state, which interacts via a van der Waals potential. In both cases we will discuss the rich variety of supersolid phases, which are found for a wide range of parameters. We will also discuss how some of these phases can be realized in experiment.

In the subsequent appendices we will discuss some methodological details. Most notably, we will consider the possible Fock-extension of the Hartree approximation, introduced in the RB-DMFT treatment of the extended Bose-Hubbard model.

# *Publications*

This work is based upon the research presented in the following publications:

PUBLISHED

Yongqiang Li, **Andreas Geißler**, Walter Hofstetter and Weibin Li,
*Supersolidity of lattice Bosons immeres in strongly correlated Rydberg dressed atoms*,
Physical Review A **97**, 023619 (2018)

**Andreas Geißler** and Walter Hofstetter,
*Infinite occupation number basis of bosons: Solving a numerical challenge*,
Physical Review B **95**, 224516 (2017)

**Andreas Geißler**, Ivana Vasić and Walter Hofstetter,
*Condensation versus long-range interaction: Competing quantum phases in bosonic optical lattice systems at near-resonant Rydberg dressing*,
Physical Review A **95**, 063608 (2017)

IN PREPARATION

**Andreas Geißler**, Ulf Bissbort and Walter Hofstetter,
*Quasiparticle spectra of bosonic lattice gases at near-resonant Rydberg-dressing*

Mathieu Barbier, **Andreas Geißler** and Walter Hofstetter,
*Dissipation-induced steady states in bosonic Rydberg-dressed quantum gases in an optical lattice*

# Contents

*Gewidmet meiner Frau Anna-Maria*
*und meiner Tochter Emilia Marie*

# Introduction

Isaac Newton famously wrote

> *If I have seen further it is by standing on [the] sho[u]lders of giants.*
>
> — Isaac Newton [NT59]

giving an inspiring metaphor for the progress of all of scientific research. To illustrate his point, let us consider the many layers of discoveries and technical advances that lay the foundation to the work presented in this thesis; first with a focus on the theoretical framework, then with a focus on the physical phenomenon known as supersolidity, but with no claim for completeness along each way. As we will see, it is giants all the way down.

As the physics we will discuss in this thesis relies on some core concepts of **quantum mechanics**, let us start at the dawn of this theory, when it was common scientific consensus that the framework of physics, nowadays known as classical physics, was mostly complete, with only minor details that still had to be sorted out. One of these concerned the radiation emitted from any piece of matter as it is heated up. In this process it starts to emit an incandescent glow, first red in color, until a bright white glow can be observed as the temperature is further increased. The perception of the white color stems from the emission of electromagnetic radiation over the whole visible spectrum (with a wavelength ranging from 380 nm to 750 nm). In case of a blackbody, which is best modeled by an evacuated box with a tiny hole drilled into its side, the spectral radiance describing the emitted light intensity at a given wavelength solely depends on the temperature of the object. Due to its simplicity a blackbody should thus make for an optimal object of physical analysis. But as Rayleigh and Jeans [Ray00; Jea05] worked out the corresponding relation based on the then known rules of (classical) electrodynamics and statistical thermodynamics, their theoretical relation only fit well with the experimental observations for long wavelengths, while it actually even predicted an unphysical divergent spectral radiance at small wavelengths (independently also found by Einstein [Ein05]). Their observation was later called **ultraviolet catastrophe**, a phrase coined by Ehrenfest in 1911 [Ehr11].

This paradoxical situation led Planck to begin his research studying the problem. As he got the opportunity to work with the experimental data of Kurlbaum and Rubens in the summer of 1900 [Hei11], his suggested interpolation between the Rayleigh-Jeans law and the empirical Wien's law (which is correct for short wavelengths) [Wie96] proved to give a complete agreement with their experimental observations. This discovery initiated Plancks actual theoretical venture. The hovering question was: What is the correct interpretation of the novel formula? Based on his previous research he concluded that the formula could be interpreted as an assertion about the properties of the elementary oscillators (i.e. the atoms constituting the radiating matter), predicting that they cannot change their energy continuously, but only in discrete steps, which are now known as **quantum jumps**. The publication of this **quantum hypothesis** in the December of 1900 [Pla01] heralded the start of quantum physics.

The hypothesis was at odds with contemporary physics and Planck's attempt at reconciling both led to failure in fundamental points. It took another five years until Einstein added another important piece, suggesting that also the energy of light is quantized [Ein05], work yielding him the Nobel prize in physics of 1921 (awarded in 1922). This insight allowed for an explanation of the photoelectric effect, as first observed by Lenard in 1900 [Len00]. His experiment showed that the kinetic energy of electrons emitted from a metal surface, induced by the irradiation with ultraviolet light, does not at all depend on the intensity of the light, but only on its wavelength. This did not only lead Einstein to the conclusion that the energy of light, and therefore light itself, is quantized, but also the realization of an apparent contradiction, the **wave-particle duality**. Light previously was considered a wave phenomenon, which is in stark contradiction to the new perspective of light as a particle, which could not explain the observed diffraction of light. He realized that neither perspective by itself fully explains the nature of light, but depending on the specific situation either or sometimes both do.

In 1911 Rutherford introduced his model of an atom [Rut11]. From the scattering of $\alpha$-particles in a thin gold foil, he concluded that the, at that time known, constituents of an atom, negatively charged electrons and equal positive charges, are distributed with most of the mass and all positive charge in the atom nucleus, while the electrons orbit the nucleus similar to the planets orbiting the sun. Based on this experimental account, Bohr published a series of works in 1913 [Boh13a; Boh13c; Boh13b], in which he detailed the idea of quantized energy levels in the context of discrete classical electron orbits, explaining the spectral lines of hydrogen via quantum jumps between individual orbits, and thus on a more fundamental level then previously described by the Rydberg formula [Boh54]. As a semi-classical description it also gives an asymptotically exact description for sufficiently high excitations of a single electron, known as **Rydberg states**, in any other atomic element. His basic assumptions were confirmed in the Franck-Hertz experiment one year later [FH14], as well as was the extension via the Sommerfeld-Wilson quantization condition for the direction of the angular momentum [Wil15; Som16] in the Stern-Gerlach experiment [GS22]. But as the whole quantum theory at that time was based on a heuristic of selection rules for classical orbits, it inevitably failed in many regards, an obvious being its limitation to closed (stationary) orbits.

It was de Broglie who suggested that the wave-particle duality should be extended to matter itself [De 25], especially for the electrons in an atom. Considering the electron as a wave surrounding the atom nucleus, it can only be a stationary one, due to the geometry of the system. His proposed correspondence between the wavelength and the momentum of the particle then serves as a bridge between the quantization condition and the ominous duality. Considering everything in terms of waves naturally led to the idea of replacing the equations for the position and velocity of an electron by equations for the frequency and amplitude of the corresponding matter wave. This switch in perspective led Heisenberg [Hei25; AMS04] and subsequently also Born and Jordan [BJ25; BHJ26] to the development of a self-consistent theory of quantum mechanics formulated as matrix mechanics in 1925, which in term of Diracs operator calculus [Dir81] serves as the framework of the theoretical considerations presented in this thesis. Schrödinger published his alternative formulation, which is directly based on de Broglie's idea of the matter wave, just months later in 1926 [Sch26a; Sch26b; Sch26c; Sch26d], also proving the equivalence of both formulations [Sch26e].

With the methodological groundwork in place let us now take a step back to introduce the physical phenomena, which are of primary interest in this thesis. To

do so we have to go back to the year 1925, in which Einstein predicted the collective condensation of an ideal (i.e. non-interacting) homogeneous Bose gas into the lowest energy state at sufficiently low temperatures [Ein25], thus implying the existence of quantum phenomena on a macroscopic scale of a large number of particles (**many-body systems**) well beyond the original objects of quantum mechanics. This conjecture was based on his generalization of preceding work by Bose about the quantum statistics of photons [Bos24] to massive particles [Ein24]. The theoretical framework of this **Bose-Einstein condensation** (BEC) was later used to interpret the disappearance of viscosity, called **superfluidity**, in liquid helium-4, when cooled to very low temperatures, as first observed by Kapitza [Kap38], and Allen and Misner [AM38] in 1938. But this did not quite work as the simple BEC theory predicted a complete condensation, while an empirical two fluid model introduced by Tisza [TIS38] and London [Lon38] was more consistent with observed phenomena such as the coexistence of two values for the speed of sound in superfluid helium. As shown by Penrose and Onsager in 1956 [PO56], this is due to the presence of strong interactions between Helium atoms, which limits the fraction of particles participating in the condensed state to $8\%$, even in the limit of zero temperature.

Along the way it was also discovered that the homogeneous many-body ground-state of an interacting BEC, such as superfluid helium, can be perturbed by the generation (excitation) of quantized fluctuations also named quasiparticles. These quasiparticles have an associated energy, which is positive in relation to the ground-state, thus raising the total energy when excited. But for sufficiently strong interactions a local minimum appears in the energy of quantized fluctuations of a certain wavelength. In 1969 this observation led Andreev and Lifshitz [AL69] to the prediction of a seemingly paradoxical state of matter. They proposed the possibility of a **supersolid** phase, meaning a many-body state with crystalline properties which allows for a dissipationless flow of crystal defects through the crystal lattice. For hole type defects this implies an effective flow of atoms passing through one another in the opposite direction with no friction whatsoever.

It was thus suggested by Leggett in 1970 [Leg70] that it should be possible to observe a change in the behavior of a rotational oscillator consisting of a solid piece of $^4$He, as a fraction of its atoms effectively decouple from the rest in a supersolid state. While an anomaly of this type was later observed in a 2004 experiment by Kim and Chan [KC04a; KC04b], which even was replicated by other groups, their results were met with strong skepticism by only a few but vocal critics [Rei10]. As Reppy took the opportunity to cooperate with Rittner, a graduate student trying to also replicate the findings, he stepped back from going into retirement. While at first they also observed the increased oscillation, as did Chan and Kim, they then decided to let the helium heat up just above $1$ K, cool it down again and repeat the experiment. In this second run the change in oscillation frequency was significantly reduced. This implies that the observed effect was not (primarily) due to the intrinsic quantum behavior of a pure crystal, but preexisting defects had to be involved. After they published their results in 2006 [RR06], further observations were made also by other groups, which contradicted the presence of a supersolid state. For example no sign of a persistent superfluid flow was to be found and experiments by Day and Beamish [DB07] instead suggested that the increase in oscillation frequency could also be explained by the elasticity of solid helium, which decreases as the helium is cooled down. This stiffening effect, which is related to the shear modulus of the solid, is regarded to as **quantum plasticity**. As Kim and Chan repeated their experiment in a setup that is free of this effect they no longer found any sign of supersolidity [KC12]. Therefore supersolidity remains elusive in solid $^4$He.

However in 2017 two groups reported the observation of supersolid signatures in two distinct setups of **ultracold quantum gas** experiments [Léo+17b; Li+17]. These experiments were conducted in a regime completely at odds with solid $^4$He, as they involve highly dilute atomic vapors, which are kept in a vacuum chamber and held in place by **optical traps**. We will discuss the specific details in Sec. 1.1.2, but for now they serve as strong examples for the possibilities of quantum gas experiments as **quantum simulators**: It was suggested by Feynman in 1982 [Fey82] to use a finely tunable quantum system to emulate the quantum physics of another system, which at its core is of entirely different nature, or even without semblance in naturally occurring systems. Actual experiments of that kind were first realized by Cornell and Wieman (JILA) [And+95], and Ketterle (MIT) [Dav+95], starting a whole new field of physics. It is this field in which the topic of the present work is placed.

In the course of this thesis we will discuss another kind of supersolid, the **lattice-supersolid**, which can be realized using quantum gases in an **optical lattice** trap. The supersolid then is induced by self-ordering of the gas due to strong long-range **van der Waals interactions**, as facilitated by the excitation of atomic Rydberg states. In Chap. 1 we will review the relevant methods and devices of the vast toolbox available in common quantum gas experiments, as well as consider the main concepts behind superfluidity and supersolidity. This is followed up by Chap. 2, which introduces some basic concepts of Rydberg atoms in quantum many-body systems, with a focus on the facilitation of long-range interactions and the implementation in a theoretical model. Thereafter a brief introduction on the realization of the Bose-Hubbard model in optical lattice systems and an extension to include Rydberg states is given in Chap. 3, which concludes the introductory part of this thesis. In the following part, consisting of Chaps. 4 through 5, we will introduce the theoretical tools used to derive the results presented in the final Chaps. 7 and 8. An introduction to a real-space extension of bosonic dynamical mean-field theory (RB-DMFT) for bosonic systems with long-range interactions in the Hartree approximation is given in Chap. 4, which rests on the non-perturbative self-consistent evaluation of the lattice Green's function. The focus of Chap. 6 lies on a quasiparticle expansion, which is based on linearized fluctuations of a static mean-field ground-state, allowing for the prediction of a vast range of experimentally relevant observables. Lastly we will introduce an efficient truncation scheme for the local bosonic Fock-basis in Chap. 5, which allows for the simulation of phases with high condensate density at a vastly reduced computational effort. In the final two chapters we will apply both methods to itinerant bosonic gases in two-dimensional optical lattices in order to predict the equilibrium ground-state phases, as well as the signatures of supersolidity and its formation in spectral functions and the dynamic and static structure factor. In the first of the two (Chap. 7) we will consider a two-component gas, as realized by two hyperfine ground states, for example, of rubidium-87 ($^{87}$Rb), where one component is off-resonantly excited to a Rydberg state, which generates a soft-core shaped interaction potential. In the latter (Chap. 8) we will discuss the opposing case using near-resonant excitations of Rydberg states, where the interacting component now directly corresponds to the Rydberg state, which interacts via a van der Waals potential. In the subsequent appendices we discuss some methodological details. In App. A we will consider the possible extension of the Hartree approximation, introduced in Chap. 4, to a Hartee-Fock type description. To motivate the use of the Hartree approximation we will give some brief remarks about the scaling of the effective number of nearest neighbors for a strong long-range interaction in App. B. Finally in App. D we will discuss the validity of approximations made in Chap. 8.

# Chapter 1

# Ultracold atoms in optical lattices

In this chapter we will briefly discuss the basic properties of dilute atomic gases in optical lattices (OL) as well as methods to manipulate and cool them. For further details the reader is recommended to consult the references given in each section. A good introduction is given in [PS08] and [BZ08], while also [PS03] is recommended. This chapter roughly follows [PS08], but with a focus on trapping, cooling and manipulation of the atomic cloud, as well as optical lattices and superfluidity. We also discuss supersolidity and experimental methods for the observation of these systems, which are relevant within this thesis.

## 1.1 Bose-Einstein-condensation

In everyday life one usually encounters only three states of matter: gaseous, liquid and solid in order of decreasing internal energy. All these can be understood at least semi-classically for simple materials. But as early as 1925 Einstein predicted another phase, in which a macroscopic majority of the particles of a non-interacting many-body system resides in the lowest energy quantum state [Ein24; Ein25]. In the zero temperature limit actually all particles are predicted to condense in the ground-state. His work was a generalization of preceding work by Bose about the quantum statistics of photons [Bos24] to massive particles, for which the statistics of Bose applies. These particles are therefore called **bosons** nowadays. The statistics of bosons follows from the fact that quantum particles are indistinguishable, which is a fundamental difference to classical particles. When counting the microstates of a classical system, we expect to obtain different states when exchanging any pair of particles for a given many particle state. But this is different in the real world, where there are only quantum particles. For those particles, only two possibilities are known when exchanging an arbitrary (indistinguishable) pair of particles in a many particle state. Either the quantum state remains the same, then we speak of bosons and the number classical microstates simply has to be divided by $N!$ in the partition function, as this is the number of permutations for $N$ bosons in the corresponding quantum state. Or the quantum state changes sign under each exchange of an arbitrary pair of indistinguishable particles, which applies to **fermions**.

This property immediately implies the Pauli exclusion principle of fermions. If we assume that any single particle state were occupied twice by indistinguishable fermions, then an exchange of the two would change the sign of the state while the state would also have to remain the same. This is a contradiction which can only by resolved by forbidding such states, as we assume all physical states to be normalizable.

Bosons on the other hand do not have such a restriction. In fact, a higher occupation of any single particle state is even enhanced compared to classical particles and

can be arbitrarily high. This brings us back to the condensation introduced at the beginning now known as Bose-Einstein condensate (BEC), which therefore cannot be explained by classical means. Indeed it is a macroscopic manifestation of quantum mechanics, realized as a thermodynamic phase. This implies that the wave-like properties of matter are observable on a macroscopic level, making quantum effects much more accessible as they are realized by many particles coherently occupying a single quantum state.

An intuitive way to determine the critical condensation temperature $T_c$, is to consider the thermal de Broglie wavelength $\lambda_{dB}$ associated with quantum mechanical matter waves in relation to the mean interparticle spacing, which is on the order of $n^{-1/3}$, where $n$ is the volume density of the particles. In free space it can be shown that the lowest temperature for which all particles still reside in excited states, in the thermodynamic limit is implicitly given via the relation $\lambda_{dB}^3 n = \zeta(3/2) \approx 2.612$ (as e.g. discussed Chap. 2 of [PS08]), where the appearance of the Riemann zeta function $\zeta(\alpha)$ results from the geometry of the system. Conventionally the thermal de Broglie wavelength has the following definition:

$$\lambda_{dB} = \sqrt{\frac{2\pi\hbar^2}{m k_B T}}. \tag{1.1}$$

It is given in terms of the reduced Planck's constant $\hbar = h/2\pi$, the mass $m$ of a particle, the Boltzmann constant $k_B$ and the temperature $T$. Solving the condensation criterion for $T_c$ yields the relation $T_c \propto n^{2/3}/m$. Thus in order to achieve a BEC, one can either reduce the temperature or increase the density, while it also helps to use (bosonic) particles of lower mass. But the method of increasing the density is actually very limited from above. As the density is increased, atoms start to interact more and more. For example if we consider densities common in day-to-day context these interactions usually result in the formation of either solids or liquids at very low temperature, with only few exceptions, such as the superfluid phase [1], which we will discuss in Sec. 1.1.1. The first experimental realization of a true non-interacting Boes-Einstein condensation was therefore not realized prior to 1995, which was 70 years after its initial prediction, as no sufficiently efficient cooling technique existed before.

These experiments were performed with dilute atomic gases achieving temperatures well below the $\mu$K range using cooling techniques, which we will discuss in Sec. 1.3. The first experiments were conducted for vapors of rubidium-87 [And+95], sodium-23 [Dav+95], and lithium-7 [Bra+95; BSH97]. They marked the beginning of a new field of research, the study of (ultracold) quantum gases, and led to the first nobel price in physics awarded in this field. Cornell and Wieman [And+95], and Ketterle [Dav+95] received this price in 2001 for their pioneering experiments in 1995. For the alkali atoms used in these early experiments, they achieved densities on the order of $10^{13}\text{cm}^{-3}$, while current experiments can reach values as high as $10^{-15}\text{cm}^{-3}$. These values illustrate the dilute character of the used gases, as air molecules at room temperature and atmospheric pressure have a density of about $10^{19}\text{cm}^{-3}$, while the density of atoms in liquids and solids is on the order of $10^{22}\text{cm}^{-3}$.

Besides the (non-)interacting ultracold atomic gases, strongly interacting BECs have been observed as early as 1937. In January of the following year two papers were published side by side, one by Kapitza [Kap38], and the other by Allen and

[1] Which besides ultracold atom systems has so far only been observed in both helium isotopes $^3$He and $^4$He and via spectroscopic signatures in small clusters of para-hydrogen [Gre+00].

Misner [AM38]. Both works presented their authors respective and independent results on the observed vanishing viscosity of liquid helium-4 ($^4$He) below the lambda-point[2] at $T = 2.17K$. Due to the corresponding possibility of dispersionless flow of this liquid this state is now known as superfluid helium. While it can be understood phenomenologically in the framework of Bose-Einstein condensation, it cannot exactly be described as a simple BEC, for which all particles would occupy the ground-state at $T = 0$. Instead the fraction of condensed $^4$He atoms cannot grow above 8%, as has been shown by Penrose and Onsager [PO56]. In the presence of interactions the ground-state of a bosonic system can no longer be represented as a product state, thus invalidating the original criterion for a BEC. Instead they proposed a more general definition, based on the single particle density matrix $\rho_{ij} = \langle \hat{a}_i^\dagger \hat{a}_j \rangle$, where the **second-quantized** operator $\hat{a}_i^\dagger$ ($\hat{a}_i$) creates (annihilates) a boson in the single particle orbital $|i\rangle$. The expectation value can be calculated either for a pure state or in a statistical ensemble. Considering the eigenvalues of this Hermitian matrix, they suggested that if the largest eigenvalue $\lambda_0$ scales extensively and thus is macroscopic, while all other eigenvalues do not, the many-body state can be considered a BEC. $\lambda_0$ also is a measure for the number of particles in the condensate orbital implying a definition for the **condensate fraction** $f_c = \lambda_0/N$, where $N$ is the total number of particles. The condensate orbital is then given as the corresponding eigenvector $|\psi_{\text{BEC}}\rangle = \sum_i v_i^0 |i\rangle$, as defined via the eigenvector coefficients $v_i^0$ of $\lambda_0$.

Common alternative criteria include the definition via a $U(1)$-symmetry breaking, where the expectation value $\langle \hat{a}_i \rangle$ has a non-zero value in the presence of a BEC [PS08], and the concept of off-diagonal long range order (ODLRO), as introduced by Yang [Yan62]. While the $U(1)$-symmetry breaking fails to give an exact picture of a BEC in a finite system of fixed particle number [LS91], for which $\langle \hat{a}_i \rangle$ always vanishes, this can often be mitigated by assuming the presence of a particle reservoir. Yang's ODLRO, on the other hand, also follows from the definition by Penrose and Onsager applied to homogeneous systems with repulsive interactions and does not generally extend to inhomogeneous systems. While the single-particle density matrix method thus gives the best description, $U(1)$-symmetry breaking is often used preferentially due to its simplicity, especially on a mean-field level, where the system is effectively treated as its own particle reservoir.

In addition to the mentioned systems, there also exist a few other contenders for BEC. A peculiar example are fermionic condensates. As fermions by themselves obey Fermi-Dirac statistics, which forbids multiple occupation of any single-particle orbital, condensation seems counterintuitive in such systems. But in the presence of sufficiently strong attractive interactions they can form (weakly) bound pairs, thus forming composite bosons, which subsequently can condensate. A famous realization is superconductivity of electrons in a solid, as described by the theory of Bardeen, Cooper and Schrieffer (BCS-theory) [BCS57] for weakly attractive interactions. In that case the bond length vastly exceeds the typical interparticle spacing. For increasing interaction strength the bond length decreases resulting in the BCS-BEC crossover [Che+05]. Another example is the magnon BEC, which is the condensation of quantized many-body excitations of collective spin precisions or magnons. But as there are no magnon excitations of zero energy, condensation can only be achieved in a driven non-equilibrium system [Dzy+07]. For further examples see *Bose-Einstein condensation* by [GSS95].

[2] This name derives from the characteristic shape of the graph for the specific heat capacity as a function of temperature in the vicinity of the normal to superfluid transition.

### 1.1.1 Superfluidity

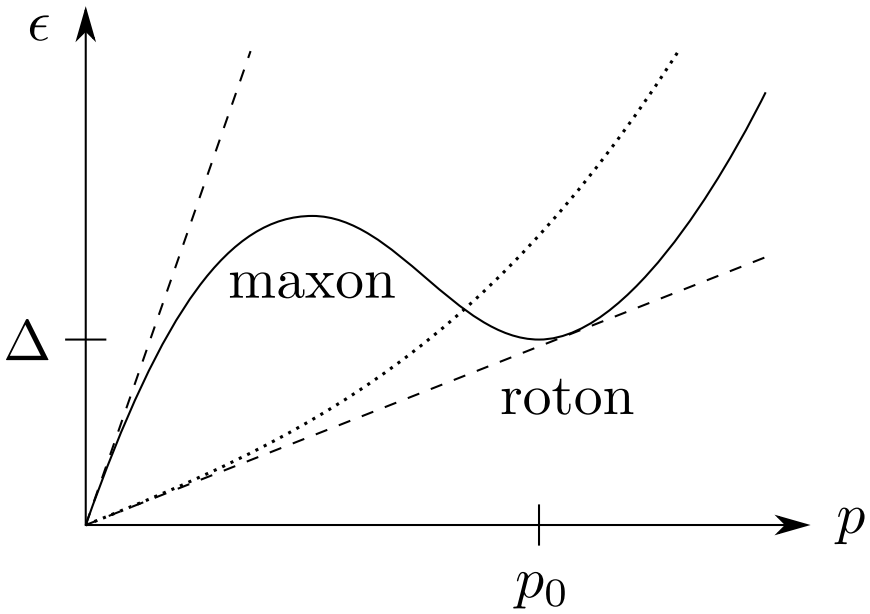


FIGURE 1.1: General features of typical excitation spectra for elementary excitations in a cooled bosonic many-body system. The black line corresponds to excitations in superfluid $^4$He. The minimum roton energy is given by $\Delta$ at the momentum $p_0$. The dotted line corresponds to a weakly interacting bose gas, as realized in quantum gas experiments. Dashed lines correspond to the maximum and minimum phase velocity $\epsilon(p)/p$ for each case, as long as they exist.

As has been mentioned earlier, **superfluidity** is a phenomenon first observed in $^4$He cooled below the lambda-point. It describes the property of a fluid that has zero viscosity. This property implies that the liquid can flow through narrow channels without any friction. A first model to explain the specific behavior in $^4$He was introduced by Tisza [TIS38] in 1938[3], as a response to Londons considerations [Lon38] along similar lines. In effect they describe a model of two interpenetrating fluids (**two fluid model**), consisting of one normal and one superfluid component, both with corresponding individual velocity fields. However it was Landau [Lan41], who pointed out that the normal component consists of **quasiparticles**, a concept he introduced to quantize elementary excitations of quantum fluids. At very low temperatures the density of the superfluid, which has zero viscosity and zero entropy, approaches that of the entire liquid, while the normal density, which is viscous and carries entropy, approaches zero. Therefore the superfluid density has to be discerned from the condensate density, which is limited to a fraction of the total density in $^4$He as has been mentioned before. When approaching the transition to the normal state by increasing the temperature the reverse behavior is observed: the superfluid density vanishes at the lambda-point, such that the fraction of the normal component becomes one.

The properties of this system are related to its elementary excitations. In a uniform ideal gas they correspond to the addition of a single particle in a momentum eigenstate. For sufficiently small interactions these states remain approximate eigenstates with a finite lifetime and still well-defined energies. In liquid $^4$He they exist

[3] See *The discovery of superfluidity* by Balibar [Bal07] for a remarkable account of the discovery in its intense historical context.

for small momenta in the form of **phonons** (sound waves) with a linear dispersion relation $\epsilon(p)$ (see Fig. 1.1) given in terms of the speed of sound $c$.

$$\epsilon(p) = cp \tag{1.2}$$

The dispersion shows a slight downward curvature for pressures above $18$ bar, and an upward curvature for pressures below this value. This low pressure regime is similar to a weakly interacting Bose gas, while the linear regime vanishes completely for a non-interacting gas, for which the dispersion becomes that of a free particle $\propto p^2$. At even larger momenta the dispersion relation of liquid $^4$He exhibits a local maximum, with the **maxon** modes, followed by a local minimum, which carries the **roton** modes[4]. In the vicinity of the minimum, $\epsilon(p)$ has the approximate form

$$\epsilon(p) = \Delta + \frac{(p-p_0)^2}{2m^*}. \tag{1.3}$$

In the limit of zero pressure the effective mass $m^*$ is $0.16$ times the mass of the $^4$He atoms. The excitations become less defined for energies above twice the roton energy $\Delta$, as they can decay into two rotons.

#### Landau's criterion for superfluidity

The hallmark feature of a superfluid is the absence of dissipative flow. In 1941 Landau published a remarkably simple criterion for the onset of dissipation [Lan41]. Let us consider a stationary obstacle, which the fluid flows past at a speed $\mathbf{v}$. We take the frame of reference in which the particle is stationary. Therefore we have to consider the Galilean transformation of energy and momentum, starting with the reference frame $K$ in which $E$ and $\mathbf{P}$ are the energy and momentum of the bose fluid. Expressing both quantities in a moving frame $K'$, which has a relative velocity $\mathbf{V}$, yields the relations

$$\mathbf{P}' \equiv \mathbf{P} - M\mathbf{V}, \tag{1.4}$$

$$E' \equiv \frac{|\mathbf{P}'|^2}{2M} = \frac{1}{2M}|\mathbf{P} - M\mathbf{V}|^2 = E - \mathbf{P}\cdot\mathbf{V} + \frac{M}{2}|\mathbf{V}|^2. \tag{1.5}$$

Here $E = |\mathbf{P}^2|/2M$, while $M$ is the total mass of the bosons. Let us now assume that dissipation of the flow around the particle takes place through creation of elementary excitations, as given by $\epsilon(\mathbf{p})$. We now consider $K$ as the reference frame in which the bosons are at rest, so $\mathbf{P} = 0$, then $E' = E + M|\mathbf{V}|^2/2$ in the frame for which the obstacle is at rest. But when a single elementary excitation of momentum $\mathbf{p}$ is created, the energy of the bosons in the reference frame $K$ becomes $E + \epsilon(\mathbf{p})$, while its momentum changes to $\mathbf{p}$. In the reference frame with the obstacle at rest, which moves with the velocity $-\mathbf{v}$ relative to the fluid, we have to set $\mathbf{V} = -\mathbf{v}$ in (1.4) and (1.5), so we obtain

[4] The name was meant to suggest a relation to vortex excitations, but actually they should be considered as short-wavelength phonon-like excitations.

$$\mathbf{P}' = \mathbf{p} + M\mathbf{v}, \tag{1.6}$$

$$E' = E + \epsilon(\mathbf{p}) + \mathbf{p}\cdot\mathbf{v} + \frac{M}{2}|\mathbf{v}|^2. \tag{1.7}$$

Comparing the situation with and without an assumed scattering event, we obtain a difference in energy and momentum given by $\epsilon(\mathbf{p}) + \mathbf{p}\cdot\mathbf{v}$ and $\mathbf{p}$ respectively. As the spontaneous creation of elementary excitations and therefore energy dissipation can only occur if and only if the corresponding process is energetically favorable. Therefore we conclude that the change in energy in the frame of the obstacle (which is at rest in both cases, thereby fulfilling a thermal equilibrium condition) has to be negative for dissipation to occur

$$\epsilon(\mathbf{p}) + \mathbf{p}\cdot\mathbf{v} < 0. \tag{1.8}$$

For any given excitation mode, dissipation is thus possible for every velocity that is equal or greater in absolute value than the phase velocity of the respective mode, or $|\mathbf{v}| \geq \epsilon(\mathbf{p})/|\mathbf{p}|$, and of opposite direction to the mode as all excitation energies are positive, so $\mathbf{p}\cdot\mathbf{v} < 0$. By considering all modes, we can find the minimum velocity $v_c$ for which dissipation occurs. It is given by

$$v_c = \min\left(\frac{\epsilon(\mathbf{p})}{\mathbf{p}}\right). \tag{1.9}$$

This expression is referred to as the **Landau critical velocity**. For velocities below this value it is impossible to create excitations, thereby allowing for superfluid behavior. For weakly interacting bosons this leads to a critical velocity given by $v_c = s$ due to (1.2), while in a strongly interacting system one obtains $v_c \approx \sqrt{\frac{2\Delta}{m^*}}$, for $p_0^2/2\Delta m \to 0$, which can be significantly less then the sound velocity $c$ as can be seen in Fig. 1.1. More generally for (1.3) one finds

$$v_c = \sqrt{\frac{\Delta}{2m^*}}\left(\frac{1 + (1 + \frac{x}{2} - \sqrt{x})^2}{1 + \frac{x}{2}}\right), \quad \text{where} \quad x = \frac{p_0^2}{2\Delta m} \ll 1. \tag{1.10}$$

As a final remark we note that $v_c = 0$ for a non-interacting system exhibiting the dispersion relation $\epsilon(p) = p^2/2m$, which implies the absence of superfluidity in a non-interacting BEC.

### The two-dimensional system

For a two-dimensional ideal Bose gas, one can easily derive the relation between the density $n_{2D} = N/A$, where $N$ is the total number of particles and $A$ is the area of the system, and the chemical potential $\mu$ determining $N$.

$$\mu = k_B T \ln\left(1 - e^{-T_{2D}/T}\right), \quad \text{where} \quad T_{2D} = \frac{2\pi\hbar^2 n_{2D}}{m k_B}. \tag{1.11}$$

As the two-dimensional density of states of free non-interacting particles is constant, starting at the lowest energy states, the total number of particles in the ground-state can be obtained by simply inserting the given chemical potential into the Bose distribution $n_B(\epsilon_i)$ for the ground-state $\epsilon_i = 0$, where $i$ denotes the different possible eigenstates of a free boson:

$$n_B(\epsilon_i) = \frac{1}{e^{(\epsilon_i-\mu)/k_BT} - 1}. \tag{1.12}$$

Thus we obtain

$$N_0 = \frac{1}{\left(1 - e^{-T_{2D}/T}\right)^{-1} - 1} = e^{T_{2D}/T} - 1. \tag{1.13}$$

$N_0$ therefore only becomes on the order of $N$ if $T \lesssim T_{2D}/\ln N$. But this term becomes vanishingly small compared to $N$ when taking the thermodynamic limit, where $N, A \to \infty$ and $n_{2D} \to$ constant. This leads to the conclusion that for any non-zero temperature a BEC of a uniform two-dimensional system is forbidden in the limit of large system size.

A more thorough analysis (see e.g. Chap. 15 of [PS08]) reveals that the behavior of the single-particle density matrix $\rho(\mathbf{r}', \mathbf{r}'') = \rho(\mathbf{r})$ of a homogeneous two-dimensional system of linear size $L$, with $\mathbf{r} = \mathbf{r}'' - \mathbf{r}'$, is given by

$$\rho(\mathbf{r}) \propto \left(\frac{r_m}{r}\right)^{\eta}. \tag{1.14}$$

Here the exponent is given by $\eta \equiv T/T_{2D}$ and $r_m$ corresponds to the length scale for which the long-wavelength approximation for the fluctuation spectrum, used in the derivation of (1.14), fails. The density matrix thus tends to zero at large distances, implying the absence of phase correlations over the whole system and thus of Bose-Einstein condensation. But due to the power law behavior there still exist finite regions where the phase is well correlated and also the superfluid density is non-zero. One thus speaks of a **quasicondensate**. The transition temperature for this system has been predicted by Berezinskii [Ber71; Ber72] and by Kosterlitz and Thouless [KT73], who were the first to stress that not only phonons determine the finite temperature behavior, emphasizing the crucial role of vortex lines in two-dimensional systems. Vortices are nodal points at the center of which the condensate wave function vanishes, thus reducing the superfluid density locally. Within Gross-Pitaevskii theory one can determine the energy of a vortex [PS08], which is given by

$$E \approx \pi n_{2D} \frac{\hbar^2}{m} \ln(L/\xi). \tag{1.15}$$

$L$ is the linear dimension of the system, while $\xi$ is the **healing length** of the wave function describing the required distance from a localized perturbation over which the wave function returns to its bulk behavior. Due to their non-zero energy, vortices are exponentially suppressed at small temperatures, but they become significant in number at a certain temperature, which leads to a sudden drop in the superfluid density at higher temperature referred to as the Berezinskii-Kosterlitz-Thouless transition. The critical temperature can be determined from the free energy $F = E - TS$,

where $S$ is the entropy of a vortex. It is given by $S = k \ln \nu$, with $\nu$ being the number of distinct configurations of the vortex. It can be estimated by the ratio of the total area of the system $A = L^2$ and the approximate area of the vortex core $\sim \pi\xi^2$, resulting in $\nu \sim (L/\xi)^2$. Thus we obtain $S \approx 2k \ln(L/\xi)$ for sufficiently large values of $L$, resulting in the free energy

$$F \approx \left( \frac{\pi n_{2D} \hbar^2}{m} - 2k_B T \right) \ln(L/\xi). \tag{1.16}$$

It is thus favorable to create vortex excitations when the temperature exceeds the critical temperature $T_{BKT}$:

$$T_{BKT} = \frac{\pi n_{2D} \hbar^2}{m 2k_B} = \frac{T_{2D}}{4}. \tag{1.17}$$

At this temperature the system undergoes a phase transition, from a quasicondensate with power-law decaying phase correlations for temperatures below $T_{BKT}$, to a normal state for temperatures above, in which the single-particle density matrix instead decays exponentially in space, as has been observed in the context of cold dilute gases [Had+06], while the corresponding superfluid behavior was observed in [Des+12].

### 1.1.2 Supersolidity

As the roton gap, which is present in a bosonic system with sufficiently strong long-range interactions such as in liquid $^4$He, is softened by reducing $\Delta$, one has to assume that the occupation of finite momentum states can become favorable, leading to the prediction of a peculiar quantum crystal state with superfluid properties, namely a **supersolid**. It was first predicted by Andreev and Lifshitz [AL69] in 1969, and in the following year by Matsuda and Tsuneto [MT70], discussing the coexistence of diagonal long-range order, associated with crystalline order, and ODLRO in the single-particle density matrix[5], as well as by Chester [Che70] and Leggett [Leg70], who used a wave function ansatz.

Andreev and Lifshitz consider a type of tight binding limit, starting with a crystal of bosonic particles containing defects which are described as quantum particles[6] (**defectons**) that can hop through the rigid lattice. These quasiparticles have a quasimomentum $\mathbf{k}$ and an associated dispersion $\epsilon(\mathbf{k})$ with the bandwidth $\Delta\epsilon$ which is proportional to the tunneling of the defectons. For a supersolid to be present in this picture the quasiparticles need to be sufficiently delocalized and present in equilibrium. Non-locality depends on their interaction with other crystalline excitations or defects. Assuming a sufficiently low temperature for quasiparticles to persist, Andreev and Lifshitz find a criterion such that the defects are not localized at any specific site,

[5] As they assume an unusual quantization, realizing hard-core bosons via local fermionic commutation and non-local bosonic commutation relations, we will not discuss their results in the context of this thesis.

[6] The quantum statistics these quasiparticles obey depends on the statistics of the crystal's constituent atoms and the defect itself.

$$na^3 \ll \left(\frac{\Delta\epsilon}{mc^2}\right)^{3/4}. \tag{1.18}$$

In this expression $n$ is the defect density and $a$ is the lattice spacing, while $m$ is the mass of the lattice constituents and $c$ is the speed of sound. To derive this result they assume a cubic interaction potential $\phi \sim mc^2(a/r)^3$ between the defects. They further argue that this relation has to be corrected under the assumption that the quasiparticles may still be localized in macroscopic regions forming a superlattice. For a delocalization of the defects it is thus necessary that the superlattice is unstable. This is the case if the potential barrier $\phi \sim mc^2na^3$ is less than $\Delta\epsilon$ or $na^3 \ll \Delta\epsilon/mc^2$.

In order to argue in favor of stability, they go on to consider the defecton energy $\epsilon(\mathbf{k})$, which they assume to have a minimum $\epsilon_0$ at $\mathbf{k} = 0$ in the simplest case. So

$$\epsilon(\mathbf{k}) = \epsilon_0 + \mathbf{k^2}/2m^*, \tag{1.19}$$

where $m^*$ is an associated effective mass. Further considerations about the volume dependence of $\epsilon_0$ on the pressure, and as such on the volume $V$ of the solid, combined with the assumption that the bosonic defectons condense in the $\mathbf{k} = 0$ state, so they contribute with the energy of a dilute Bose gas at $T = 0$, leads them to an expression for the energy contribution $E$ of the defectons to the total energy of the crystal,

$$E = \lambda\frac{V_0 - V}{V_0}N + \frac{2\pi a}{m^*}\frac{N^2}{V}. \tag{1.20}$$

Here $\lambda$ is an expansion coefficient for $\epsilon_0$ as a function of $V$, which is assumed to be positive, $V_0$ is the value of $V$ where $\epsilon_0$ may vanish, $a$ is the scattering amplitude of the defectons and $N$ is their total number. For repulsive defect interactions ($a > 0$), this energy has a minimum $E_0$ as a function of $N$. Thus the presence of non-localized bosonic defectons with repulsive interactions may lower the total energy of the solid by

$$E_0 = -V\frac{}{m^*\lambda^2}8\pi a\left(\frac{V - V_0}{V_0}\right)^2. \tag{1.21}$$

Note however that their considerations heavily rely on the presence of defects, which can only be created or destroyed at the surface of the solid. Prokof'ev and Svistunov reinforced this observation in 2005 by showing analytically that the presence of either zero-point vacancies or interstitial atoms is a necessary condition for the formation of a supersolid [PS05], thereby especially ruling out the possibility of superfluidity occurring in commensurate solids breaking a continuous symmetry in the absence of symmetry between vacancies and interstitials. Their arguments are based on the topology of particle trajectories within a Monte-Carlo description, which have to include the generation and annihilation of vacancy-interstitial pairs for the superfluid density to be non-zero. They therefore stretch the requirement of topological ODLRO for the existence of superfluidity.

Consider that Chaudhuri et al. [CPC99] have predicted an energy of approximately $15.6 \pm 4.2$K (in agreement with X-Ray scattering experiments [FGS89]) for

the generation of a single vacancy in a hexagonal close-packed (hcp) lattice of $^4$He, while Ceperly and Bernu [CB04] have predicted that the energy for the generation of an interstitial is about 48K in hcp $^4$He. Both values were calculated at the melting density. This implies that there is no macroscopically large number of vacancies or interstitials present in the typical temperature ranges considered in experiments, thus demanding a different mechanism for supersolidity in $^4$He, if it can exist at all. But the outlook is less pessimistic in the case of quantum optical systems, as we will see at the end of this section.

But for now let us briefly discuss the theoretical analysis as brought forth by Chester [Che70] and Leggett [Leg70]. Chester starts with the ansatz of a bosonic Jastrow wave function $\psi_N = \exp(-\frac{1}{2}\sum_{i\neq j} u(\mathbf{r}_i - \mathbf{r}_j))$. The function $u(\mathbf{r})$ is an arbitrary pseudopotential, that is hard-core, bounded from below and has a finite range. He furthermore notes that he can choose $u(\mathbf{r})$ such that the probability distribution corresponding to $\psi_N$ mimics a classical Gibbs distribution. As such distributions can represent crystalline systems at sufficiently low temperatures he concludes that the wave function will also correspond to a crystalline state. Furthermore using a theorem by Reatto, he is able to show that such a wave function can also describe a BEC. He concludes that the proposed Jastrow function should work as a good approximation for solid $^4$He. Notably he also suggests that condensation in a crystal might only be possible if a macroscopic number of vacancies is present.

Leggett further builds on Chester's results, proposing that a solid containing superfluid constituents should exhibit a **non-classical rotational inertia**. He suggests that a fraction of the mass of solid $^4$He effectively decouples, condensing in a superfluid that can acquire angular momentum only in discrete quanta. He thereby suggests the use of a rotational pendulum in order to probe the presence of a supersolid phase in $^4$He, which, in the end, showed no signs of supersolidity [KC04a; KC04b; KC12].

### Supersolidity in cold gases

As it turns out, the realization of the supersolid state is much less debated in systems of cold dilute Bose gases, as it is in systems of solid Helium (see Introduction). Only recently there have been two experimental groups reporting on the observation of signatures of supersolid order breaking a continuous translational symmetry in the former systems [Léo+17b; Li+17]. This is in contrast to lattice-supersolids which instead break a discrete translational symmetry pre-imposed by an OL (see e.g. [Ott+95; IF09; CS+10; Pol+10; SSS14; Bai+16]). These lattice-supersolids are the primary focus of this thesis and their experimental observation still remains an open challenge to date.

Lénoard et al. [Léo+17b] on the one hand realize the continuous $U(1)$ symmetry to be broken in the condensate phase via two discrete spatial symmetries generated in two crossed optical cavities, by symmetrically coupling a BEC to the modes of both, leading to the emergence of an order parameter exhibiting a continuous symmetry, which is expressed via the relative coherent field amplitudes of the cavities. They subsequently show that the ground-state of this system spontaneously breaks this symmetry, which simultaneously amounts to the spontaneous formation of a density wave pattern breaking the translational symmetry. The observed random nature of the phase of the order parameter proves the high ground-state degeneracy associated with the breaking of a continuous symmetry. Note that the symmetry breaking in this system is realized by internal forces, as the coupling of the BEC to the modes of an optical cavity effectively induces an infinite range interaction for

the BEC constituents. They further report on the observation of associated gapless Goldstone and gapped Higgs amplitude modes in [Léo+17a].

Li et al. [Li+17] on the other hand realize a spin-orbit coupling in a two-dimensional optical double-well lattice, using Raman induced tunneling between the two wells, while the particle movement remains free along the third direction. States in either of the two wells can be considered as effective spin states. The induced spin-orbit coupling leads to the formation of density modulations along this third dimension via interference of the spin manifolds with one another due to the coupling. The existence of a (weakly interacting) BEC in this system leads to a zero momentum peak in time-of-flight images (see Sec. 1.4.1), while the interference pattern breaking the spatial translation symmetry leads to a finite momentum peak in the static structure factor, which they observe using Bragg-scattering (see Sec. 1.4.4). We note that the formation of the density wave can be understood as a perturbation of the superfluid BEC, as the interference can be controlled by the strength of the spin orbit coupling, while even an arbitrarily small coupling generates a proportional amount of counter-propagating fractions of the condensate that interfere.

As a last example let us consider optical lattice systems, as will be introduced in further detail in Sec. 1.2.2. For these systems there are multiple ways one could introduce long-range interactions such that roton modes can form which may induce spontaneous symmetry breaking, as driven by internal forces. Common examples are polar molecules (see [Bar+12] for a review) or atoms with strong magnetic interactions such as chromium [Lah+07], dysprosium [LYL10] or erbium [Bai+16]. Regarding theoretical works see for example [IF09; CS+10; Pol+10; Bar+12; Lu+15]. But in the scope of this thesis we will focus on the formation of lattice-supersolids via long-range interactions as induced by Rydberg excitations. As suggested by Pupillo et al. [Pup+10] and others [HNP10; Hon+10] Rydberg atoms make for a versatile tool to induces long-range interactions that might eventually lead to the realization of supersolid order in a trapped atom cloud (see also Sec. 8.2.3). More details relevant in the context of this thesis are given in Chap. 2, which is about the essential physics of Rydberg atoms in cold atom experiments.

## 1.2 Manipulation and control

In this section we discuss the influence of external fields and thus methods to manipulate the behavior of the dilute atom gases. In experiment one primarily relies on the optical dipole force, which is induced by the AC-Stark effect.

### 1.2.1 AC-Stark effect

An electric field $\mathbf{E}(t) = E_0\hat{\mathbf{e}}\cos(\omega t)$, that oscillates in time, induces the AC-Stark effect in an atom it interacts with. This leads to an induced dipole moment $\mathbf{d}(t)$ in the atom, which also oscillates with the frequency $\omega$. In the description of this effect we will follow [PS08]. It is well known, that a linear response treatment yields a simple relation between the dipole moment and the electric field: $\mathbf{d}(t) = \alpha(\omega)\mathbf{E}(t)$, where $\alpha(\omega)$ is the complex polarization.

We consider an effective two-level atom, consisting of a ground state $|g\rangle$, and an excited state $|e\rangle$ with energies $E_g$ and $E_e$. This is a good approxmiation as long as the excitation frequency $\omega$ lies within the linewidth of a single dipole allowed transition, as is often the case. The wave function is given by the ansatz

$$|\psi(t)\rangle = a_g(t)e^{-\frac{i}{\hbar}E_g t}|\psi\rangle + a_e(t)e^{-\frac{i}{\hbar}E_e t}|\psi\rangle, \tag{1.22}$$

which is given in terms of time-dependent complex amplitudes $a_g(t)$ and $a_e(t)$. The Hamiltonian describing the dynamics of the system is given as follows:

$$H = H_0 + H_{\text{dip}}(t) = H_0 - \mathbf{d}\cdot\mathbf{E}(t). \tag{1.23}$$

$H_0$ is the unperturbed Hamiltonian, which is given in terms of the eigenstates $|g\rangle$ and $|e\rangle$ and eigenenergies $E_g$ and $E_e$. The dipole Hamiltonian $H_{\text{dip}}(t)$ on the other hand amounts to a perturbation. Thus considering up to first order in perturbation theory we obtain the time-dependent amplitude of the excited state

$$a_e^{(1)} = \frac{E_0}{2\hbar}\langle e|\mathbf{d}\cdot\hat{\mathbf{e}}|g\rangle\left[\frac{e^{i(\omega_{eg}+\omega)t}-1}{\omega_{eg}+\omega} + \frac{e^{i(\omega_{eg}-\omega)t}-1}{\omega_{eg}-\omega}\right]. \tag{1.24}$$

Here $\omega_{eg} = (E_e - E_g)/\hbar$. By averaging the expectation value $\langle H_{\text{dip}}(t)\rangle_t$ over time, where $\langle\cdot\rangle_t$ denotes an average of the expectation value over one period, one obtains the following value for the time-averaged energy shift

$$\Delta E = \frac{E_0^2}{4\hbar}\left[\frac{1}{\omega_{eg}+\omega} + \frac{1}{\omega_{eg}-\omega}\right]|\langle g|\mathbf{d}\cdot\hat{\mathbf{e}}|e\rangle|^2. \tag{1.25}$$

Thus the polarizability can be derived from $\Delta E$, as $\Delta E = -\frac{1}{2}\langle E^2(t)\rangle_t\alpha(\omega) = -\frac{1}{2}\frac{E_0^2}{2}\alpha(\omega)$:

$$\alpha(\omega) = |\langle g|\mathbf{d}\cdot\hat{\mathbf{e}}|e\rangle|^2\left[\frac{1}{E_e - E_g + \hbar\omega} + \frac{1}{E_e - E_g - \hbar\omega}\right]. \tag{1.26}$$

In this expression so far we have assumed an infinite lifetime for the excited state. But we can take this effect into account phenomenologically by giving the excited state a complex valued energy where the imaginary part corresponds to the spontaneous loss rate $\Gamma_e$. Thus one has to replace $E_e \mapsto E_e - \frac{i\hbar}{2}\Gamma_e$. We furthermore assume that $\omega$ is close to the transition frequency, which also allows to limit our scope to a single excitation level. Thus we may apply the rotating wave approximation (see also Sec. 2.2.1) by only considering the term with the smallest energy denominator. We then obtain our final approximation for the polarizability

$$\alpha(\omega) \approx \frac{|\langle g|\mathbf{d}\cdot\hat{\mathbf{e}}|e\rangle|^2(E_e - E_g - \hbar\omega)}{(E_e - E_g - \hbar\omega)^2 + (\hbar\Gamma_e/2)^2} + i\frac{|\langle g|\mathbf{d}\cdot\hat{\mathbf{e}}|e\rangle|^2\hbar\Gamma_e/2}{(E_e - E_g - \hbar\omega)^2 + (\hbar\Gamma_e/2)^2}. \tag{1.27}$$

Let us define the detuning $\delta$ and the Rabi frequency $\Omega$, as

$$\delta = \omega - \omega_{eg} \quad \text{and} \quad \Omega = E_0\frac{|\langle e|\mathbf{d}\cdot\hat{\mathbf{e}}|g\rangle|}{2\hbar}. \tag{1.28}$$

The dipole shift of the potential energy is then given by

$$V_{\text{dip}} = -\frac{1}{2}\text{Re}[\alpha(\omega)]\langle \mathbf{E}^2(t)\rangle_t = \frac{\hbar\Omega^2\delta}{\delta^2 + \Gamma_e^2/4}, \tag{1.29}$$

while the rate with which atoms are lost from the ground state $\Gamma_g$ is of Lorentzian shape:

$$\Gamma_g = \frac{\text{Im}[\alpha(\omega)]}{\hbar}\langle \mathbf{E}^2(t)\rangle_t = \frac{\Omega^2\Gamma_e}{\delta^2 + \Gamma_e^2/4}. \tag{1.30}$$

The dipole shift is negative or attractive for $\delta < 0$ (**red detuning**) and positive or repulsive for $\delta > 0$ (**blue detuning**). Note that both quantities are proportional to the intensity $I = |\mathbf{E}|^2 = E_0^2$ of the electric field. Thus in order to minimize scattering due to $\Gamma_g$ in experiment, which causes heating of the cloud, the laser intensity and $\delta$ have to be set as large as possible. The heating rate is therefore commonly restricted by the available laser power.

As we have seen, there is no explicit dependency on the internal hyperfine state of the atoms with regard to the generation of an optical dipole potential. Using circular polarized light on the other hand, allows for the generation of optical potentials which behave differently for each internal state.

Note that the perturbative treatment presented above is valid only as long as the admixture of the excited state is small. In first order of perturbation theory it is given by the ratio between the matrix element of the perturbation and the excitation energy of the intermediate state which effectively has the magnitude $\hbar(\delta^2 + \Gamma_e^2/4)^{1/2}$. Thus the condition for a valid perturbative description is $\hbar(\delta^2 + \Gamma_e^2/4)^{1/2} \gg E_0|\langle e|\mathbf{d}\cdot\hat{\mathbf{e}}|g\rangle| = \hbar\Omega$. Thus one either has to go for large detuning when increasing the electric field strength, or go beyond simple perturbation theory (as discussed in Chap. 8 where near resonant excitations are considered).

### 1.2.2 Optical lattices

As we have seen, the AC-Stark effect can be used to generate arbitrary shifts in the potential energy of the atoms in a cloud. Using the same concept let us now show how to generate a one-dimensional lattice, which can straightforwardly be generalized to higher dimensional lattices. We start with the electric field generated by a monochromatic laser which is given by $\mathbf{E}_1(\mathbf{r},t) = E_0\hat{\mathbf{e}}\cos(\mathbf{kr} - \omega t)$, where $k_L = |\mathbf{k}| = 2\pi/\lambda_L$ is the angular wavenumber and $\lambda_L$ the corresponding wavelength. To generate a standing wave laser field the beam is either reflected by a mirror, or a second counterpropagating laser is used, which has to be phase locked to the first one. As a result we have the additional electrical field $\mathbf{E}_2(\mathbf{r},t) = E_0\hat{\mathbf{e}}\cos(\mathbf{kr} + \omega t)$. The total electrical field is thus given by

$$\mathbf{E}(\mathbf{r},t) = \mathbf{E}_1(\mathbf{r},t) + \mathbf{E}_2(\mathbf{r},t) = 2E_0\hat{\mathbf{e}}\cos(\omega t)\cos(\mathbf{kr}). \tag{1.31}$$

With the same considerations, which lead to a value for the local dipole potential shift $V_{\text{dip}}$, we thus obtain a one-dimensional optical lattice (OL) potential. By setting $\mathbf{k} = k_L\hat{\mathbf{e}}_x$ we get

$$V(x) = -V_{\text{dip}} \cos^2(k_L x). \tag{1.32}$$

The lattice spacing $a$ of this optical lattice is therefore given by $a = \lambda_L/2$. If one generalizes this method to higher dimensional lattices, it might seem at first as if great care has to be put in the relative polarizations of the additional lasers. But as it turns out the far simpler way to create separable hypercubic lattices is by tuning the lasers to slightly different frequencies. On the relevant time scale this completely decouples each optical dipole potential, while the experimental realization is far easier [Bis12].

As the laser setup is not limited to perpendicular orientations leading to the mentioned hypercubic lattices most common in experiments, other setups allow for more complex (e.g. frustrated) lattice geometries. Some examples are triangular and hexagonal lattices [Bec+10; Tar+12] which can be tuned from one another in a crossover via the orientation of the laser polarization, but also kagome lattices [Jo+12], all of which have been realized to date.

Optical lattices are much more versatile compared to solid state lattices. For example by using circularly polarized lasers, as mentioned in Sec. 1.2.1, it is possible to engineer potentials and therefore lattices that are spin-dependent [Gad+10]. In addition optical lattices have an inherent high tunability even in the course of an experiment. Furthermore the time scale of the optical and electronic devices controlling the configuration of the dipole potentials is far beyond the time scale of the atomic motion, as given by tunneling rates in an OL which are usually less than 1kHz. The specific tuning knobs which make the quantum optics toolbox so versatile are

1. the intensity of each individual lattice laser (determining the potential depth),
2. the polarization of each beam (allowing for fine control of individual hyperfine levels, which may act as effective spin states),
3. the frequency of each laser (e.g. allowing for moving lattices by using slightly detuned counterpropagating lasers),
4. permanent control of all above parameters on a very fast time scale throughout the experiment (e.g. allowing for many-body interference experiments, such as quantum state tomography, see Sec. 1.4.6).

The high degree of control in the time domain also allows for spectroscopic probing via lattice modulation [End+12b], while lattice shaking allows for the generation of effective gauge fields [Hau+12] which would otherwise not be present for neutral atoms.

### 1.2.3 Local interactions

While cold quantum gases seem to lack strong long-range interactions due to the absence of Coulomb forces between the neutral atoms, their internal structure actually allows for a rich variety of interactions because of the polarizability of the outermost electron shell. The description of these interactions typically is very simple as particle separations are commonly on the order of a few 100nm, which is one order of magnitude larger than the length scale associated with the atom-atom interactions[7]. Due to the very low temperatures and thus very low kinetic energies in combination

[7] This also makes three-body interactions mostly irrelevant.

with the isotropic nature of the interaction, only long wavelength $s$-wave scattering is relevant in these systems. It is therefore possible to describe the effective (short-range) interaction $U(\mathbf{r}-\mathbf{r}')$ for two atoms of mass $m$ at the positions $\mathbf{r}$ and $\mathbf{r}'$ by a single parameter, the scattering length $a_s$, which is typically two orders of magnitude greater than the size of the typically used alkali atoms:

$$U(\mathbf{r}-\mathbf{r}') = \frac{4\pi\hbar^2 a_s}{m}\delta(\mathbf{r}-\mathbf{r}'). \tag{1.33}$$

Note that the locality of this interaction implies enhanced interactions in a deep optical lattice for which the atomic wave functions are strongly localized. We now consider a short discussion on the origin of this interaction and how the sign and strength of the interaction can be changed to nearly arbitrary values using Feshbach resonances.

**Van der Waals interaction**

As neutral atoms do not interact via the Coulomb interaction directly, but instead via mutually induced spontaneous electric dipole momenta, we have to consider the electric dipole-dipole interaction between atoms:

$$V_{\text{dip}} = \frac{1}{4\pi\epsilon_0 r^3}\left[\mathbf{d_1}\cdot\mathbf{d_2} - 3(\mathbf{d_1}\cdot\hat{\mathbf{r}})(\mathbf{d_2}\cdot\hat{\mathbf{r}})\right] = \frac{d_{1x}d_{2x} + d_{1y}d_{2y} - 2d_{1z}d_{2z}}{4\pi\epsilon_0 r^3}. \tag{1.34}$$

In this expression $\epsilon_0$ is the electric constant, $\mathbf{d}_1$ and $\mathbf{d}_2$ are the electric dipole moment operators for each atom, and $\hat{\mathbf{r}} = \mathbf{r}/r$, where $\mathbf{r}$ is the displacement vector between the atoms and $r = |\mathbf{r}|$. In the last step we define the orientation of the cartesian reference system via $\hat{\mathbf{r}} \equiv \hat{\mathbf{e}}_z$. As the atomic ground states of atoms can be considered eigenstates of the parity operator, all diagonal matrix elements of the electric dipole operator vanish. Consequently the leading contribution to the interaction energy is given via the second order in perturbation theory

$$U(r) = -\frac{6}{(4\pi\epsilon_0)^2 r^6}\sum_{n,n'}\frac{|\langle n|d_z|0\rangle|^2|\langle n'|d_z|0\rangle|^2}{E_n + E_{n'} - 2E_0}. \tag{1.35}$$

By considering the long wavelength scattering, as described by a wave function for the relative motion, which is given by the sum of an ingoing plane wave $\propto \exp(ikz)$ and an outgoing spherical wave $\propto \exp(ikr)/r$, one can deduce a theoretical prediction for the scattering length $a_s$, which corresponds to an effective phase shift $\delta_s(k)$ in the scattered state defined as $a_s^{-1} = -\lim_{k\to 0} k\cot(\delta_s(k))$ where $k$ is the wavenumber of the scattered state. We note that the long wavelength scattering does not depend on the specific details of the interaction potential[8], so it can be described with this single parameter and we can replace (1.35) by (1.33) for the interaction of dilute gases of atoms in their electronic ground states. While the precise values of $a_s$ are very hard to predict *ab initio*, measurements reveal e.g. for $^{87}$Rb that its scattering length is $a_s^{(s)} = 106 \pm 4a_0$ for singlet scattering and $a_s^{(t)} = 90 \pm 1a_0$ for triplet scattering.

[8] E.g. the thus far neglected repulsive interaction at very small separations of a few Bohr radii $\mathcal{O}(a_0)$ due to the overlap of the electron clouds.

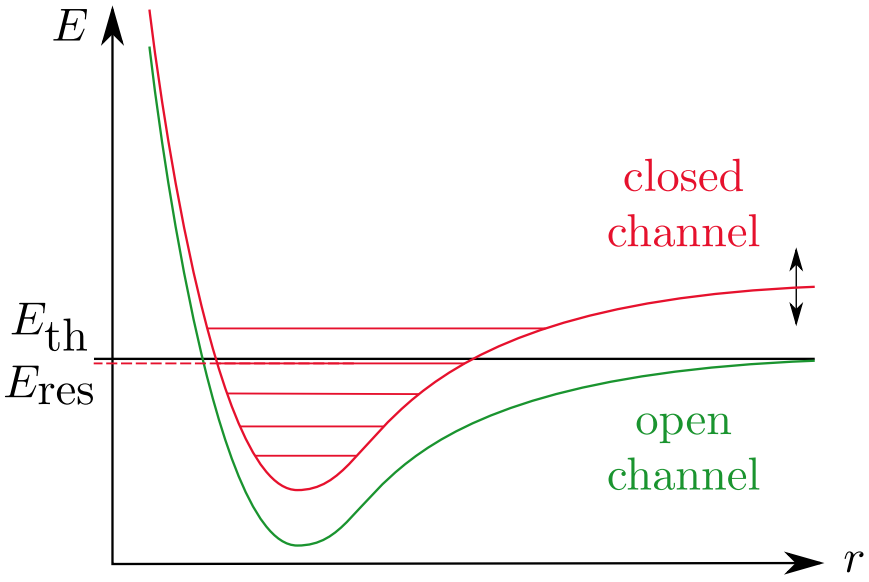


FIGURE 1.2: Schematic sketch of a Feshbach process. Depicted are two pair-potentials of an arbitrary pair of atoms as a function of their distance $r$. The threshold energy $E_{\mathrm{th}}$ of the open channel nearly matches the energy of a bound state $E_{\mathrm{res}}$ in a closed channel. Scattering between the channels induces an effective interaction in the open channel. The relative position of the closed channel in relation to the open channel can be tuned via external parameters.

**Feshbach resonances**

As introduced first by Feshbach in the context of nuclear physics [Fes62] it is possible to dramatically modify the elastic scattering behavior of particle pairs in the presence of a nearby bound state. In order to discuss these Feshbach resonances let us first introduce the notion of a **channel**. In a scattering event the internal state of the particles in the initial and final states are described by a set of quantum numbers (e.g. atomic species, state of excitation, spin). We refer to specific choice of these as a channel.

A Feshbach resonance appears when the total energy of an open channel, which is occupied by the pair of atoms, nearly matches the energy of a bound state $E_{\mathrm{res}}$ in a closed channel, which has a higher energy at infinite separation of the two atoms as illustrated in Fig. 1.2. The energy for which the pair of atoms is at rest at infinite separation in the open channel is the threshold energy $E_{\mathrm{th}}$. In presence of the closed channel the two particles in the open channel can scatter to an intermediate state in the aforementioned closed channel and subsequently decay into two particles in any of the open channels with positive non-zero rest energy at infinite separation. Assuming the presence of a single closed channel and a single open channel perturbation theory predicts that this second order process modifies the scattering length as follows:

$$\frac{4\pi\hbar^2}{m}a_s' = \frac{4\pi\hbar^2}{m}a_s + \frac{|\langle\psi_{\mathrm{res}}|H_{\mathrm{pert.}}|\psi_0\rangle|^2}{E_{\mathrm{th}} - E_{\mathrm{res}}}. \tag{1.36}$$

Here $a_s$ is the original scattering length in the absence of the closed channel and $H_{\mathrm{pert.}}$ is the perturbing Hamiltonian containing the off-diagonal matrix elements coupling the two channels. In principle it is therefore possible as a function of the

energy difference $E_{\text{th}} - E_{\text{res}}$ to obtain any value for the scattering length with either sign, thus allowing for any attractive and repulsive local interaction strength. The fact that the energies of the various channels depend on external parameters, such as the magnetic field, therefore implies a complete tunability of the local atom-atom interactions.

## 1.3 Preparation and cooling

Getting atoms to the cold temperatures required for Bose-Einstein condensation is a demanding multi-step process, as are the various methods required to trap the atomic vapor along the way. For this reason it took about 70 year from the prediction of such a state until the first realization in the lab. Let us consider a brief overview of the typical stages of the cooling and trapping procedure (for more details see e.g. [PS08]). A beam of atoms that emerges from an oven at a temperature $T \sim 10^2 - 10^3$K corresponding to a particle velocity $\sim 10^3$m/s, subsequently passes a so-called Zeeman slower reducing the velocity to about $30$m/s or a temperature of $1$K. After the Zeeman slower atoms are sufficiently slow to be captured in a magneto-optical trap (MOT) in which they are further cooled by means of laser cooling, whereby temperatures of order $100\mu$K are achieved due to the Doppler limit associated with this process. Sisyphus cooling then allows a further reduction to the order $10\mu$K, while evaporative cooling may further decrease temperatures well below $100$nK. In the following we briefly discuss the final stages of this cooling chain.

### 1.3.1 Laser cooling

Although it might seem counterintuitive it is possible to cool atom vapors by aiming a laser beam on it. Let us assume that the laser frequency is detuned below a dipole allowed electronic transition frequency. If an atom is moving towards the laser source the frequency is Doppler shifted to a higher frequency in the rest frame of the atom, while this shift increases for increased atom velocity. If this shift is sufficiently strong, such that the frequency is within the line width of the electronic transition, the atom is likely to absorb a photon from the laser. As a result the atom transitions into an internally excited state while the photon transfers a momentum kick in the opposite direction of the atom movement as seen in the lab frame. This leads to a slow down of the atom along this direction. As the direction of the photon subsequently emitted from the atom is random the transferred momentum over many such processes averages to zero. Thus by setting up counterpropagating pairs of laser beams for each spatial dimension, atoms in a specific range of kinetic energy can be cooled down.

To accommodate for the decreased population of high energy states the laser frequency is usually increased over time which is referred to as "chirping". The lowest temperature $T_L$ attainable by this procedure is thus given via the laser linewidth, as the right and left movers become indistinguishable by this process when the Doppler shift becomes less then half of the transition linewidth $\Gamma_e$ implying $k_B T_L = \hbar\Gamma_e/2$. Typical values for this Doppler limit are on the order of few $100\mu$K.

### 1.3.2 Sisyphus cooling

Despite the Doppler limit, experiments revealed another mechanism in the same setup which allows cooling to even lower energies at much greater detuning than predicted by the Doppler theory. It was also observed that this mechanism depends

on the use of linear polarization of the laser beam. Let us therefore discuss the general concepts behind this mechanism.

In the presence of two counter propagating lasers, the energies of the ground state hyperfine multiplet of a given atom species vary in space due to the interaction with the laser field (see Secs. 1.2.1 and 1.2.2). For a $^2S_{1/2}$ ground state manifold this leads to an effective spatial potential $V^{\pm}$ for each spin state which we will denote as the $g_-$ and $g_+$ state respectively. We have

$$V^{\pm}(z) = V_0\left[-2 \pm \sin(2qz)\right], \tag{1.37}$$

where $q$ is the wave number of the laser field, while the value of $V_0$ results from the dipole transitions to $^2P_{3/2}$ states induced by the laser and can be shown to have the value

$$V_0 = -\frac{2}{3}\frac{\hbar\Omega^2\delta}{\delta^2 + \Gamma_e^2/4}. \tag{1.38}$$

The prefactor is given by the sum of Clebsch-Gordan coefficients for the relevant transitions, while $\Omega$ is the Rabi frequency of the transition, which is proportional to the field strength. $\delta$ is the detuning of the laser frequency from resonance and leads to a positive value for $V_0$ if red detuned ($\delta < 0$) and $\Gamma_e$ is the spontaneous emission rate.

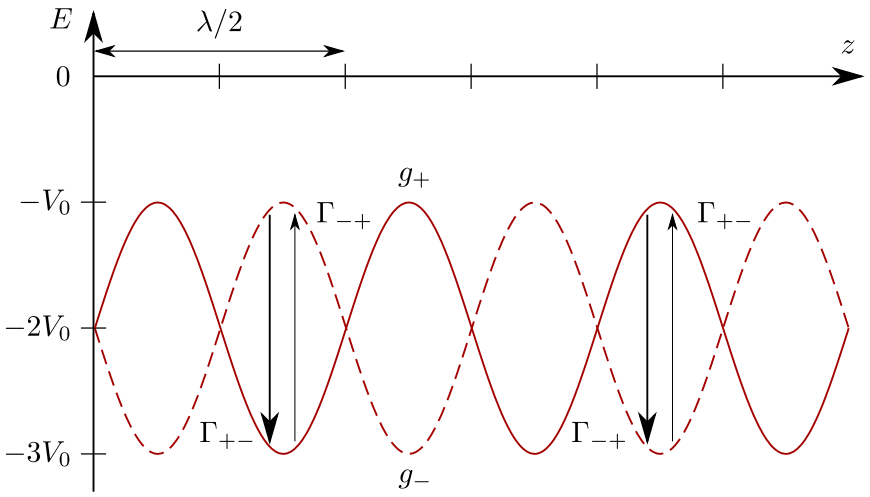


FIGURE 1.3: Energy of each spin state $g_+$ and $g_-$ of an atom as a function of the position for a red detuned laser field ($\delta < 0$). The zero of the energy scale is given by the energy of the atom in absence of the laser field. The pumping rates $\Gamma_{+-}$ and $\Gamma_{-+}$ are position dependent as depicted by the arrow size.

Due to the inhomogeneity of the standing wave laser field, the rate of optical pumping between the two ground states depends on the position. As the rate $\Gamma_{+-}$ of pumping an atom from the $g_-$ to the $g_+$ state is proportional to the intensity of the positively oriented circularly polarized component of the radiation, one finds

$$\Gamma_{+-} \propto \left[1 - \sin(2qz)\right]/2. \tag{1.39}$$

Conversely the opposite case is given by

$$\Gamma_{-+} \propto [1 + \sin(2qz)]/2. \tag{1.40}$$

Therefore pumping tends to move atoms from the spin state with higher energy to that with lower energy (see Fig. 1.3). Note that in order for both processes to occur both polarizations of the laser field need to be present, which implies the use of linear polarization. The Sisyphus mechanism can thus be understood in a semi-classical picture. We consider an atom that is moving away from a point where the energies of $g_-$ and $g_+$ are equal. If it is moving into a region where the enegy shift $V(z)$ is positive it loses kinetic energy due to conservation of its total energy, while its tendency to be pumped in the other state increases. In the opposite case if the atom moves into a region where the energy shift is negative it gains kinetic energy but has a reduced tendency to be pumped in the high energy state. As a result there is a net tendency for each atom to lose kinetic energy in the long run, in a perpetual process of loss in kinetic energy followed by optical pumping to the low energy spin state[9].

Due to the coupling to the laser field, this process is ultimately limited by the **recoil energy**

$$E_r = \frac{(\hbar q)^2}{2m}. \tag{1.41}$$

This is the kinetic energy transferred to an atom of mass $m$ at rest as it absorbs a photon of momentum $\hbar q$. Therefore the minimum reachable kinetic energy will be on the order of this energy scale. As it turns out, in the limit of large detuning $|\delta| \gg \Gamma_e$ the minimum achievable kinetic energy is on the order of $30E_r$ [GSS95] or about $10\mu$K.

### 1.3.3 Evaporative cooling

In this last step the atoms are usually held in a magnetic dipole trap. The process itself is very similar to a common method for cooling a hot beverage. There the energetic distribution of the water molecules is given by a classical Boltzmann distribution. Water molecules at the surface with sufficiently high kinetic energy can leave the liquid, locally increasing the vapor pressure above, while molecules from the vapor can enter the liquid again. This leads to a dynamic equilibrium between molecules leaving and entering the liquid. But as the considered example is an open system, more high energy molecules leave which in effect reduces the mean kinetic energy of the remaining molecules. Trapped atom gases can be cooled by an analogous mechanism, by creating a "hole" at a certain potential energy in the trapping potential such that particles with at least this evaporation threshold energy $\epsilon_{\text{ev}}$ can escape the system. The loss of high energy particles leads to a reduction in the average energy, thus reducing the temperature via rethermalization processes mediated by interatomic interactions[10]. This method is fundamentally limited due to the particle loss. However note that the cooling efficiency depends on the phase space

[9] This process reminded Dalibard and Cohen-Tannoudji of the Greek myth of Sisyphus, who was condemned to eternal punishment in Tartarus, where his task to push a heavy rock up a hill was made futile as the rock had the tendency to slip from his grip shortly before reaching the top. Thus they coined the term *Sisyphus cooling*.

[10] This comes as a problem when cooling fermions, usually mitigated by the use of sympathetic cooling [Mya+97].

density $\rho_p = n\lambda_{\mathrm{dB}}^3$ which can be manipulated by the confining potential. Thus using dimple traps [MFC04] to confine the cloud can increase the cooling efficiency significantly in relation to the commonly used dipole traps. As a result temperatures on the order of few 100 nK are possible [Gar+11].

Further techniques are still being devised in order to reach even lower temperatures for which some of the most peculiar quantum phases, such as spin glass [SS11] or spin ice [Gla+14] are predicted. Spin temperatures as low as 50pK have already been reached in experiments utilizing spin gradient demagnetization cooling [Med+11; Li+12].

## 1.4 Detection

Cold atoms are primarily detected by absorption imaging. A probing laser beam shines on the cloud with a frequency resonant to a suitable electronic transition. In opposition to the laser beam a CCD- or CMOS-camera collects and amplifies the photon signal after passing the atom cloud. Due to resonance the photons have a certain probability to be scattered diffusively by the atoms via spontaneous emission. Thereby the beam intensity gets reduced in direct proportion to the density of the atoms integrated along the path. Note that multiple measurements are thus required to obtain a three dimensional image. Furthermore, a sufficiently high density may block the beam entirely.

As we will see, it is possible to extract a wide range of properties by only measuring the (integrated) density $n(\mathbf{r}) = \langle \hat{b}^\dagger(\mathbf{r})\hat{b}(\mathbf{r})\rangle$. This is due to the fact that quantum optical experiments have a high degree of dynamical control throughout the experiment (as discussed in Sec. 1.2.2), so the design of the measurement protocol determines the measured property.

### 1.4.1 Time-of-flight Imaging

One of the most commonly used methods to determine the momentum distribution $n(\mathbf{k}) = \langle \hat{b}^\dagger(\mathbf{k})\hat{b}(\mathbf{k})\rangle$ in a many-body state is the **time-of-flight** imaging. Given a many-body state to be imaged all trapping potentials (e.g. dipole traps) are suddenly switched off. The cloud is subsequently imaged after a certain time $t_{\mathrm{tof}}$ has passed in which the atom cloud expands freely. As the density decreases throughout the expansion, interactions become decreasingly relevant. It is thus typically approximated that interactions can be neglected entirely during the expansion. Also assuming that the initial cloud size is negligible in comparison to the final size when the cloud is imaged, it can be shown that the finally measured real-space density profile $n(\mathbf{r})$ after the flight time $t$ is directly related to the momentum distribution $n(\mathbf{k})$ just before the release. It thus follows immediately from the free ballistic expansion of the cloud [BZ08] that

$$n(\mathbf{r}) = \left(\frac{m}{\hbar t}\right)^3 |w(\mathbf{k})|^2 n(\mathbf{k}). \tag{1.42}$$

In this expression $\mathbf{k}$ is related to $\mathbf{r}$ by $\mathbf{k} = m\mathbf{r}/\hbar t$, while $m$ is the mass of the atoms and $w(\mathbf{k})$ is the Fourier transform of the Wannier function corresponding to the trapping potential just before the release (see Sec. 3.1.3 for more details). The prefactor stems from the transformation of the volume elements $d^3k \mapsto d^3r$. Furthermore, in order to

guarantee the assumed free expansion, near Feshbach resonances one often ramps back to the zero crossing of the scattering length before the release.

### 1.4.2 Optical quantum gas microscope

It is also possible to measure the site-resolved density distribution of the cloud directly in an optical lattice by using high resolution optics. This technique is known as **optical quantum gas microscopy** [Bak+09], which describes an optical setup that operates close to fundamental optical limits. It allows for the observation of individual atoms on a submicrometer resolution and thus of single lattice sites (see also [Sch+12; Sch+15]).

### 1.4.3 Noise correlation measurement

It is important to realize that in each experimental image only a single realization of the density is observed and not the average. Depending on the imaging resolution each pixel records on average a number $N$ of atoms. Thus in each single realization of an experiment the number of atoms recorded will exhibit shot-noise fluctuations on the order of $1/\sqrt{N}$. As first proposed by Altman et al. [ADL04], it is possible to extract density-density correlations from these statistical fluctuations, which stem from the bosonic counting statistics as predicted by Hanbury Brown and Twiss [HBT56]. This method can be used to extract real-space density-density correlations $\langle n(\mathbf{r})n(\mathbf{r}')\rangle$ in-situ, or the static structure factor $\langle n(\mathbf{k})n(\mathbf{k}')\rangle$ after time-of-flight as first realized by Fölling et al. [Föl+05].

### 1.4.4 Bragg spectroscopy

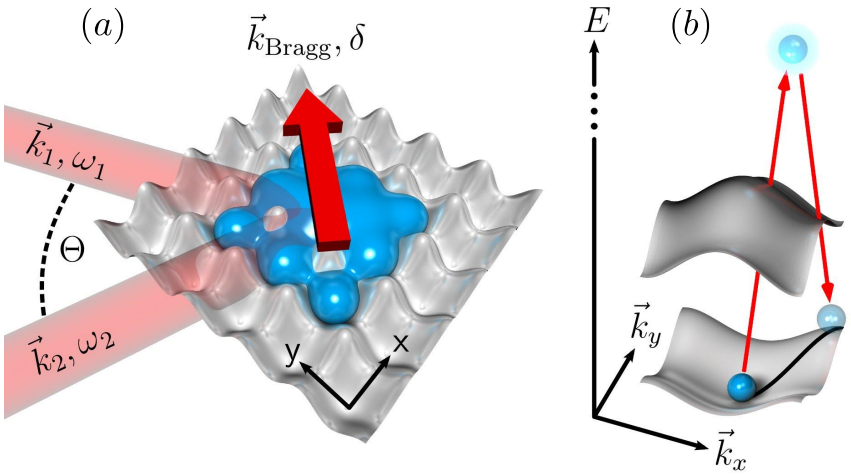


FIGURE 1.4: Schematic sketch of the Bragg process in real and momentum space. $(a)$ In real space two laser beams with momentum $\hbar\mathbf{k}_i$ and energy $\hbar\omega_i$ crossing at an angle $\Theta$ excite an ensemble of atoms trapped in an OL. The spectrum of available excitations of the atoms can be seen in momentum space $(b)$. There the Bragg process transfers energy and momentum via a two-photon process. It leads to the population of a different state whereby it reveals information on the excitation spectrum. In $(a, b)$ an excitation in $[1, 1]$-direction close to the edge of the Brillouin zone is shown. This figure is taken from [Ern+10].

In order to gain insight into the inherent properties of a many-body state as encoded in the excitation spectrum, one usually has to perturb the equilibrium state

of the system shifting it out of equilibrium as a result. The kind of perturbation in combination with the measured quantity (usually any of the aforementioned) determine the specific correlation function that is measured. An early example is lattice modulation spectroscopy, which generates perturbations over a wide range of momenta [Stö+04; Bis12]. A more selective method that will be of interest to us is Bragg spectroscopy. Let us introduce the method as described in [Ern+10].

In quantum gases it is based on a two-photon process which directly transfers energy and momentum to an atomic ensemble by inducing a collective excitation. Two phase-coherent lasers with wavevectors $\mathbf{k}_1$ and $\mathbf{k}_2$, and frequencies $\omega_1$ and $\omega_2$ intersect on the sample as shown in Fig. 1.4. Energy and momentum conservation imply that initial and final states with energy difference $\hbar\delta = \hbar(\omega_2 - \omega_1)$ and momentum difference $\hbar\mathbf{k}_{\text{Bragg}}$ are coupled resonantly by this process [see Fig. 1.4$(b)$ for a visualization in momentum space]. The momentum imprinted onto the sample is freely tunable by changing the angle $\Theta$ between the two beams, so

$$\hbar\mathbf{k}_{\text{Bragg}} = \hbar(\mathbf{k}_1 - \mathbf{k}_2) \approx 2\hbar k \sin(\Theta/2) \cdot (\hat{\mathbf{e}}_1 - \hat{\mathbf{e}}_2). \tag{1.43}$$

The unit vectors $\hat{\mathbf{e}}_1$ and $\hat{\mathbf{e}}_2$ correspond to the propagation direction of each laser beam respectively and $|\mathbf{k}_1| \approx |\mathbf{k}_2| = k$ for small $\delta$. As the energy transfer $\hbar\delta$ can be tuned independently via the two laser frequencies, it is possible to scan the complete excitation spectrum over the entire Brillouin zone.

### 1.4.5 Scanning electron beam microscopy

A well known method for the single atom resolved imaging of (conducting) condensed matter surfaces is the scanning tunneling microscopy. In analogy an electron beam can also be used to image quantum gas experiments. By scanning a tightly focused electron beam over the cloud atoms are locally ionized. An electrostatic field is used to subsequently extract the ions in order to count them in a channeltron detector which reveals the density distribution line by line. The focus of the electron beam, which is on the order of 100nm, in combination with the peak width in the time-of-flight ion counting signal determines the possible spatial resolution and scan time. In a typical image sequence a few hundred atoms are detected at a scan time of 100 ms, while the overall detection efficiency is limited by the ratio of ionizing to elastic collisions as well as the detector efficiency, in combination amounting to $10 - 20\%$ [SO15].

### 1.4.6 Interferometric methods

Interferometry is a family of techniques which are used in quantum gases in order to extract information about correlations, especially in the dynamical regime. It usually involves one or multiple **quenches** (sudden changes in one or multiple experimental parameters) applied to a well defined initial state, commonly an eigenstate of the Hamiltonian corresponding to the initial system. After the quench the initial state is no longer an eigenstate but instead amounts to a linear combination in the new eigenbasis. The subsequent time evolution leads to a dephasing of the partial amplitudes resulting in oscillations (**Ramsey fringes**) in observables, such as the spin-polarization [Zei+15] or the zero-momentum peak of a BEC [Gre+02a], which usually decay as the ratios of the relevant eigenfrequencies amount to irrational numbers. In certain cases rational or even integer ratios are possible leading to the collapse and revival of Ramsey fringes (see e.g. [Gre+02a; Zei+17]) as a subset

of partial amplitudes realign their phases. It thus serves as a method to investigate the spectrum of a given Hamiltonian.

Some experiments also include a spin-echo sequence in which a $\pi/2$-pulse is applied at the halfway point of the time evolution reversing the order of the partial phases on the equator of the Bloch sphere. In this way it is possible to cancel unwanted phases shifts due to single-particle effects such as the AC-Stark shift [Zei+17].

### 1.4.7 Electromagnetically induced transparency

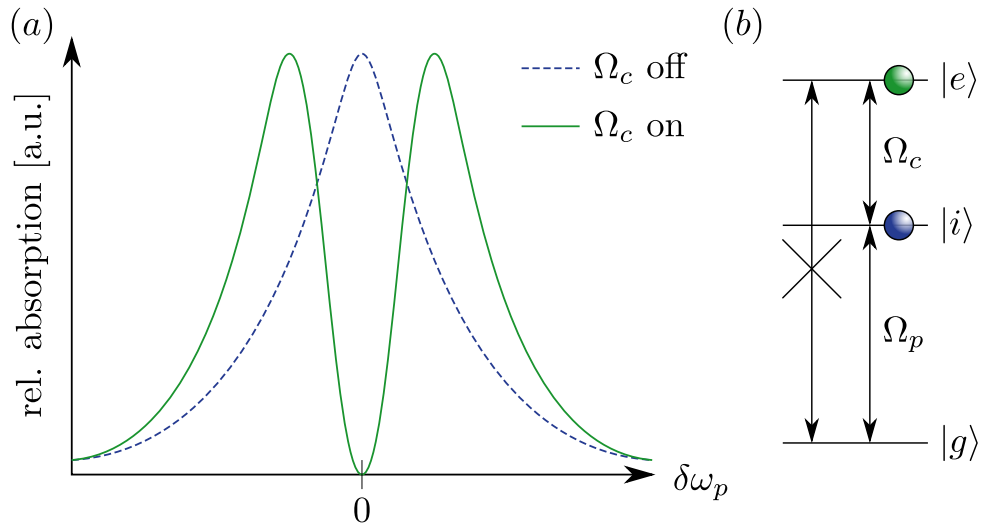


FIGURE 1.5: Schematic sketch of electromagnetically induced transparency. $(a)$ Three level ladder scheme $|g\rangle - |i\rangle - |e\rangle$, where the transition $|g\rangle \leftrightarrow |e\rangle$ is dipole forbidden. The transition $|g\rangle \leftrightarrow |i\rangle$ is driven by the probing laser field with Rabi frequency $\Omega_p$, while the transition $|i\rangle \leftrightarrow |e\rangle$ $(b)$ is driven by the control laser with Rabi frequency $\Omega_c$ which can be switched off. The absorption spectrum of the probe transition is shown in $(b)$. In the absence of the coupling laser the spectrum has the typical Lorentzian line shape (blue dashed line) of an atomic transition. With the control laser switched on (green line) a transparent window opens in the probe transition centered at the position of the original spectral line.

Electromagnetically induced transparency (EIT) describes the effect that a medium can be made transparent in a narrow window inside an otherwise absorbing spectral line (see [FIM05] for a review). To induce this effect one has to introduce a coherent optical nonlinearity. For this we have to consider an effective three level atom where one of the transitions is dipole forbidden and can thus neither absorb or emit a photon. Without loss of generality let use assume the ladder scheme shown in Fig. 1.5 where we have a ground state $|g\rangle$, an intermediate state $|i\rangle$ and an excited state $|e\rangle$ with corresponding energies $E_g < E_i < E_e$. The transition $|g\rangle \leftrightarrow |e\rangle$ is dipole forbidden while the remaining transitions are driven by two Rabi lasers with the Rabi frequencies $\Omega_p$ coupling the probe transition $|g\rangle \leftrightarrow |i\rangle$ and $\Omega_c$ coupling the control transition $|i\rangle \leftrightarrow |e\rangle$. The intermediate state further has a finite lifetime given by the decay rate $\Gamma$. For a resonant driving of the control transition and $\Omega_c > \Gamma$, a transparent window starts to open in the absorption spectrum of the probe transition where the strongest reduction of the absorption can be observed at resonance $\delta\omega_p = \omega_p - \omega_{gi} = 0$. Here $\omega_p$ is the frequency of the probe laser and $\omega_{gi}$ is the probe transition frequency.

While this effect can also be used to optimize cooling schemes [MEK00], we discuss it in the context of this thesis as it can also be used for a real-space imaging technique. The main idea is that the position of the transparency window depends on the detuning $\delta\omega_c = \omega_c - \omega_{ie}$ of the control laser frequency $\omega_c$ with regard to the control transition frequency $\omega_{ie}$. Let us consider the case when both transitions are driven on resonance. It is then possible that strong (long-range) interactions with an impurity atom, for example via Rydberg-Rydberg van der Waals (see Chap. 2) or Rydberg-Rydberg dipole interactions [Gün+13], induce a shift of $E_e$ in the vicinity of the impurity thus breaking the EIT condition. Under these circumstances the medium becomes opaque in a region surrounding the impurity. It is thus possible to image the position and dynamics of said impurity in an otherwise absorbing medium using previously mentioned imaging techniques.

# Chapter 2

# Many-body Rydberg systems

Despite the high versatility of ultracold atomic systems as analog quantum emulators, experimental realization of strong long-range correlations still represents an important challenge in the field. While Feshbach resonances give access to tunable local interactions [BZ08], progress has been made towards the trapping, cooling and control of ultracold polar molecules [Car+09], as well as magnetic [Lah+07] and Rydberg atoms [SWM10]. The significance of Rydberg excitations for creating strong non-local correlations has been pointed out numerous times, e.g. by [Wei+08; Hon+10], especially in the context of quantum computing [Luk+01; SWM10; Saf16].

Recent experiments have studied the statistical properties of dissipative Rydberg gases [Mal+14; Sch+14], especially in the superatom regime [Zei+15; Web+15], where the Rydberg blockade effect was analyzed. Using electromagnetically induced transparency (see Sec. 1.4.7), the occurrence of diffusive **Förster** excitation transport has been shown [Gün+13]. Also, ultralong-range Rydberg molecule formation [GDS00] has already been observed [Ben+09], realizing bound states with exotic orbital wave-function shapes, for example trilobite molecules which are bound predominantly via the $s$-wave channel [Boo+15] or butterfly states which are bound predominantely via the $p$-wave channel [Nie+16]. Crystallization of Rydberg atoms has been achieved up to a small number of excitations in the **frozen** limit [Sch+12; Sch+15]. There the system behaves like a spin-$\frac{1}{2}$ model with imbalanced interactions, as analyzed in numerous theoretical works [Ver+15; PDL10; LG14; Sch+10a], predicting a series of lattice incommensurate ordered phases (**devil's staircase**, see also [CS+10; Rad+13]). The opposite limit of weak (off-resonant) Rydberg dressing has extensively been investigated in theory [JR10; Hon+10; Pup+10; Cin+10; Hsu+12; CBP14; MSC14], predicting the formation of (droplet) supersolids (SS), while its experimental realization remains an open challenge [Bal+14; Nie+15]. Only recently coherent short-range correlations have been observed for the first time for a pair of atoms [Jau+16] and in a two-dimensional spin lattice [Zei+16], as well as coherent collapse and revival dynamics in a one dimensional spin chain [Zei+17; Ber+17].

In this chapter we will discuss the key concepts of Rydberg excitations, as well as some of their peculiar properties, which are most relevant in the context of this thesis. Because of these, Rydberg states are a versatile tool for realizing exotic types of quantum matter in cold quantum gas systems. Throughout our considerations we will roughly follow [SWM10] and [Löw+12].

## 2.1 Rydberg atoms

Rydberg atoms is a term used for atoms which have at least one of its electrons excited to a level of large principle quantum number $n \gtrsim 10$, which is a region where the electronic state becomes increasingly independet of the core electrons.

Thus the states behave very similar to hydrogen, especially for alkali atoms with their single valence electron, and for sufficiently high angular momentum states $l > 3$ [Löw+12]. The basic properties of Rydberg atoms have also been discussed extensively [SWM10] (and references therein). In this section we will focus on those aspects, which are of most relevance for many-body systems. First and foremost, these are the strong long-range interactions among neutral particles, which is the most prominent feature of Rydberg atoms. It is best summarized by comparing the energy scales of various relevant two-body interactions between the atoms, as exemplarily shown for rubidium in Fig. 2.1.

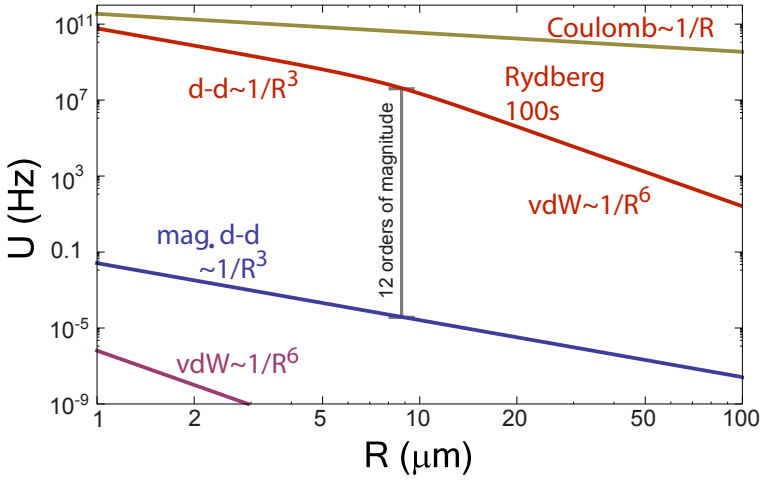


FIGURE 2.1: Two-body interaction strength for ground state Rb atoms (Van der Waals and magnetic dipole dipole), Rb atoms excited to the $100s$ level and ions. The figure is taken from [SWM10].

The two-particle interaction of ground state atoms is dominated by $1/r^6$ Van der Waals (VdW) forces, while $1/r^3$ magnetic dipole-dipole forces dominate for distances below about $30nm$, where $r$ is the inter particle distance. In typical optical lattices with a spacing of $0.5 - 1.0\mu$m, both couplings are negligibly small for neighboring sites, with the Van der Waals coupling even orders of magnitude below $1$ Hz in frequency units. As typical hopping rates are on the order of $100$ Hz, these interactions may not break the lattice symmetry in the many-body ground-state. As Coulomb interactions among ions are larger by many orders of magnitude, crystallization effects usually suppress itinerant physics. We also note that while trapping of ions in optical lattices has been demonstrated [Sch+10b], the realization of an itinerant ion gas in a lattice remains a challenging task due to heating effects and trapping times [End+12a; Lin+12]. But if we consider rubidium atoms excited to the $100s$ Rydberg level, a more than 12 orders of magnitude increase of the long-range non-magnetic interaction can be observed. While its short-range behavior is dominated by $1/r^3$ scaling because of dipole-dipole interactions (1.34), depending on the principle quantum number there is a crossover length scale beyond which the character changes to an $1/r^6$ Van der Waals tail. This length scale is strongly related to the radius $R$ of a Rydberg atom, which scales as $R \propto n^2$. The actual value of the interaction also strongly depends on the principal quantum number $n$, as will be discussed in the following sections, which will show the tremendous potential of introducing long-range and widely scalable interactions to neutral ultracold gas experiments via Rydberg atoms.

### 2.1.1 Level energies

In order to understand the strength of the long-range interaction among Rydberg atoms, we first consider their energy level structure. Particularly, we consider low angular momentum states, as these are readily accessible via optical excitation from the atomic ground state and thus optimal for common experimental setups. Assuming sufficiently small external fields, the energy levels are represented by the principle quantum number $n$, the orbital angular momentum $l$, the spin angular momentum $s$ and the total angular momentum $j$. Sufficiently high energy levels are accurately described by simple hydrogen-like energies

$$E_{nlj} = -\frac{\mathrm{Ry}'}{(n - \delta(n,j,l))^2}. \tag{2.1}$$

Here we introduce the specific Rydberg constant $\mathrm{Ry}' = \mathrm{Ry}/(1 + m_e/m_{\mathrm{nucleus}})$, which is given in terms of the mass of the electron $m_e$ and the nucleus $m_{\mathrm{nucleus}}$, while $\mathrm{Ry} = 109737.315685\mathrm{cm}^{-1}$ in atomic units, corresponding to $\mathrm{Ry} = 20670.412594\mathrm{THz}$ in natural units with $\hbar = 1$, as used throughout this thesis, if not specified otherwise. The quantum defect $\delta(n,j,l)$ is a slowly varying function[1], which mostly depends on $l$. Except for low-lying $s$ states, hyperfine interaction can in general be neglected.

### 2.1.2 Interactions

For large distances $r > n_{\mathrm{eff}}^2 a_0$, where $n_{\mathrm{eff}} = n - \delta(n,j,l)$ and $a_0$ is the Bohr radius, the interaction is determined by a Van der Waals interaction $V_{\mathrm{vdW}} = -C_6/r^6$. The van der Waals coefficient can be obtained by second-order perturbation theory. For the sake of simplicity let us consider the Van der Waals interaction between two isotropic and fully degenerate Rydberg $nS$-levels:

$$V_{\mathrm{vdW}}(r) = -\frac{6}{(4\pi\epsilon_0)^2 r^6} \sum_{j,j'} \frac{|\langle j|d_z|nS\rangle|^2 |\langle j'|d_z|nS\rangle|^2}{E_j + E_{j'} - 2E_n} \equiv -\frac{C_6}{r^6}. \tag{2.2}$$

Here we us the collective index $j$ for the quantum numbers of the electronic states of the atom[2]. This expression is primarily dominated by two-atom states in the energetic vicinity of the considered $|nS\rangle|nS\rangle$ state, while the sign is determined by relative deviations in the energy. Thus the main difference to the ground state Van der Waals interaction stems from the presence of energy levels above *and* below the considered two-atom energy. As it turns out, this expression yields a negative $C_6$ for Rb atoms where $30 \leq n \leq 95$ [Sin+05], implying repulsive Van der Waals interactions for the Rydberg atoms.

Furthermore, we can obtain the dominant scaling behavior of $C_6$ as a function of $n$. As the largest matrix elements of the transition dipole moment for nearby $s$ and $p$ states are generally of order $(0.5 - 1.5)n_{\mathrm{eff}}^2 a_0$, while the level spacing $\Delta E_{n+1} - E_n \propto (n+1)^{-2} - n^{-2}$ scales as $n^{-3}$ for large $n$, the overall leading behavior is given as $C_6 \propto n^{11}$. Via more precise calculations, the following scaling law has been derived in [Sin+05] for Rb, which is given in atomic units.

[1] In the case of rubidium the defect is in lowest order given by $\delta(l = 0) = 3.13$ and quickly decays to zero for increasing $l$, so $\delta(l > 3) \approx 0$ [Löw+12].

[2] Besides the principal quantum number $n$, these are the angular orbital momentum $l$ and its $z$-projection $m$.

$$C_6 = n^{11}\left(11.97 - 0.8486n + 3.385\times10^{-3}n^2\right). \tag{2.3}$$

For the $35S$ state we thus find $C_6 = -1.312\times10^{18}\text{au} \equiv -\hbar\times189.5\text{MHz}\mu\text{m}^6$. Rydberg atoms thus introduce enormous interactions in an optical lattice with typical lattice spacings of $0.532\mu$m, when compared to typical local interactions which are on the order of a few kHz.

As a final remark, we note that the second-order perturbation theory is only valid for distances, where the Van der Waals interaction is less than the Förster defect $\delta E = E_j + E_{j'} - 2E_n$. For smaller distances we are in the limit of a small Förster defect, leading to a Förster resonance [WS08] and thus a resonant coupling between $s$ and $p$ state. Thus the interaction $V(r)$ takes on a dipolar character $V(r)\propto 1/r^3$, as can be seen in Fig- 2.1. In Rb this is highly relevant when exciting Rydberg $p$ states, for which the channel $np_{3/2}+np_{3/2}\leftrightarrow(n+1)s_{1/2}+ns_{1/2}$ has a defect of just $\delta E/2\pi = -4.1$MHz for $n=38$. But as we will primarily consider the excitation of an individual $s$ state, the only relevant channels are of the type $ns_{1/2}+ns_{1/2}\leftrightarrow n_1p_j+n_2p_{j'}$, but those do not exhibit a Förster resonance for any $n<100$. Specifically $\delta E<-3$GHz for $n<45$, which also implies the repulsive character of the Van der Waals interaction between rubidum Rydberg $s$ states.

### 2.1.3 Lifetimes

The realization of coherent many-body ground-states is fundamentally limited by the lifetime $\tau$ of the considered Rydberg states. $\tau$ is determined by radiative decay to lower lying levels and blackbody radiation-induced transitions to predominantly nearby levels. Absorption and stimulated emission of thermal infrared photons, which induce transitions to neighboring states, start dominating the lifetime for $n\gtrsim40$ at room temperature (300K). But this effect can efficiently be eliminated in a cryogenic environment [Bet+09; Bou+17], as has been realized in cavity QED experiments, for example in [RBH01] the experimental setup was cooled to about $1K$.

Considering any pair of initial state $i$ and final state $f$, with an energy difference $\hbar\omega_{if}$, the transition rate between the two is generally given by an Einstein coefficient

$$A(\omega_{if}) = \frac{2e^2\omega_{if}^3}{3\epsilon_0c^3h}|\langle i|d_z|f\rangle| \tag{2.4}$$

for spontaneous decay and an Einstein coefficient $B(\omega)=A(\omega)N(\omega)$ for stimulated emission and absorption of blackbody radiation. Both coefficients depend on the transition dipole matrix element $|\langle i|d_z|f\rangle|$, while $B$ also depends on the number of blackbody photons $N(\omega)$ in each mode at temperature $T$, as given by the Bose statistics:

$$N(\omega) = \frac{1}{e^{\hbar\omega/k_BT}-1}. \tag{2.5}$$

We thus find the total lifetime of the state $|i\rangle$ by summing over all final states $|f\rangle$, so

$$\frac{1}{\tau_i} = \sum_{f<i} A(\omega_{if}) + \sum_f A(\omega_{if}) N(\omega_{if}) = \frac{1}{\tau_i^{(0)}} + \frac{1}{\tau_i^{(\mathrm{BBR})}}. \tag{2.6}$$

Note that the first sum only includes dipole allowed transitions to states with energies below the Rydberg state, while the second sum is only limited by the dipole selection rule. At $T = 0$K the radiative lifetime is given by

$$\tau_i^{(0)} = \tau_{nl}^{(0)} = \tau_l^{(0)} (n_{\mathrm{eff}})^{\alpha_l}. \tag{2.7}$$

The prefactor in general depends on the angular momentum, while for all alkali atoms one can use $\alpha_l \simeq 3$. The blackbody rate for large $n$ takes the following simple form, which also includes the effect of ionizing transitions to the continuum,

$$\frac{1}{\tau_i^{(\mathrm{BBR})}} = \frac{4\alpha^3 k_B T}{3\hbar n^2} \tag{2.8}$$

where $\alpha \approx \frac{1}{137}$ is the fine-structure constant. For example we obtain $\tau_i^{(\mathrm{BBR})} = 60\mu$s at 300K for $n = 35$. In combination with the spontaneous decay, which is of the same order, we thus find a combined lifetime of $\tau_{n=35} \approx 30\mu$s compared to the experimental result of $\tau_{n=35}^{(\mathrm{exp.})} \approx 28\mu$s for the Rb $35S$ Rydberg state [Bra+10; Bou+17].

## 2.2 Rydberg excitation in a many-body system

As we have seen, Rydberg atoms can be used to induce strong long-range interactions to a neutral quantum gas. Most commonly a two-photon excitation scheme is used to generate transitions to Rydberg states. Using light of opposed circular polarizations, this allows for the exclusive generation of Rydberg $s$-states, yielding isotropic VdW interactions. But also a direct transition to Rb $p$-states has been realized, although with the caveat of having to use ultraviolet lasers, as these transitions require light at 297 nm [Zei+16]. Let us consider the most typical two-photon ladder scheme $5s - 5p - ns$, which can also be used to realize EIT imaging (discussed in Sec. 1.4.7). The two transitions are excited using light of 780 and 480 nm (see Fig. 2.2).

As the intermediate $5p$ state has a lifetime of $26ns$ for $^{87}$Rb, the population of this state has to be suppressed, which can be achieved by detuning the

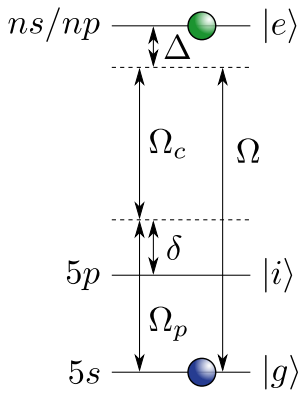


FIGURE 2.2: Typical three-level and (reduced) two-level scheme for the Rydberg excitation of Rb. The electronic ground state $|g\rangle$ (blue) is usually first excited to an intermediate state $|i\rangle$, with a Rabi frequency $\Omega_p$ and a detuning $\delta$. Subsequently $|i\rangle$ is excited to a Rydberg state $|e\rangle$ (green), at a Rabi frequency $\Omega_c$ and with the overall detuning $\Delta$. For large $\delta$ one obtains an effective two level system $|g\rangle \leftrightarrow |e\rangle$ with effective Rabi frequency $\Omega$ and detuning $\Delta$. A two-level scheme can also be realized, by directly exciting a Rydberg $np$-state.

red laser far from resonance. For sufficiently large detuning $\delta$ one can eliminate the intermediate state from further considerations. This reduces the system to an effective two-level system, exhibiting the total Rabi coupling $\Omega = |\Omega_p||\Omega_c|/2|\delta|$, which is determined by the individual Rabi couplings $\Omega_p$ (for $5s - 5p$) and $\Omega_c$ (for $5p - ns$), as well as the intermediate state detuning $\delta$. The detuning in the reduced two-level scheme is given by the total detuning $\Delta$. One also obtains a two-level system by directly exciting to a Rydberg $np$-state instead.

### 2.2.1 Rabi driving in the rotating frame

As stated before, we introduce excited electronic states of the atoms via a coherent driving of optical transitions to Rydberg levels. This yields Rabi oscillations which we can effectively describe by a static Hamiltonian, where fast oscillations are eliminated using the rotating wave approximation. The dynamical process is described by the interaction with the light field (see for example equation (A.11) in Chap. V of [CT04]). We therefore introduce the following *time-dependent* Hamiltonian in second quantized form, describing the effective two-level system, where we use natural units ($\hbar = 1$) and the interaction picture ($I$):

$$\hat{H}_R^{(I)} = -\hat{\mathbf{d}} \cdot \mathbf{E}_0 \cos(\omega_L t) = \frac{\Omega}{2}\left(e^{-i\omega_L t} + e^{i\omega_L t}\right)\hat{\sigma}^+(t) + \frac{\Omega^*}{2}\left(e^{-i\omega_L t} + e^{i\omega_L t}\right)\hat{\sigma}^-(t). \quad (2.9)$$

The time dependence of the (pseudo) spin-flip $\hat{\sigma}^\pm$-operators, which generate spin-flips between the ground state $g$ and the excited state $e$, is given by the transition frequency $\omega_0 = \omega_e - \omega_g$, while $\omega_L$ is the frequency of the light field. If we thus insert $\hat{\sigma}^\pm = \hat{\sigma}_0^\pm e^{\pm i\omega_0 t}$ into (2.9), while also replacing $\hat{\sigma}_0^\pm$ by appropriate products of bosonic creation (annihilation) operators $\hat{b}_g^\dagger/\hat{b}_e^\dagger$ ($\hat{b}_g/\hat{b}_e$), representing the electronic ground/excited states of the atoms, we find the full expression in the interaction picture:

$$\hat{H}_R^{(I)} = \frac{\Omega}{2}\left(e^{-i\Delta t} + e^{i(\omega_L+\omega_0)t}\right)\hat{b}_e^\dagger\hat{b}_g + \frac{\Omega^*}{2}\left(e^{-i(\omega_L+\omega_0)t} + e^{i\Delta t}\right)\hat{b}_g^\dagger\hat{b}_e. \quad (2.10)$$

Let us now assume that the effective Rabi frequency $\Omega$, as given by the corresponding dipole matrix element and the strength of the light fields (1.28), is a real quantity. The detuning $\Delta = \omega_L - \omega_0$ defines the slow time scale ($\Delta \ll \omega_L, \omega_0$). For $\Delta \ll \omega_L + \omega_0$, the terms oscillating with fast frequencies can be discarded, which corresponds to the **rotating wave approximation** [RH05]. The time independent Hamiltonian in the co-rotating frame follows from the time dependent unitary transformation matrix $\hat{U} = \hat{U}(t) = \hat{b}_g^\dagger\hat{b}_g + e^{i\Delta t}\hat{b}_e^\dagger\hat{b}_e$:

$$\hat{H}_R = \hat{U}\hat{H}_R^{(I)}\hat{U}^{-1} + i\frac{d\hat{U}}{dt}\hat{U}^{-1} = \frac{\Omega}{2}\left(\hat{b}_g^\dagger\hat{b}_e + \hat{b}_e^\dagger\hat{b}_g\right) - \Delta\hat{n}^e. \quad (2.11)$$

This transformation for a time dependent unitary transformation follows straight from the commutator $[\hat{U}, \frac{\partial}{\partial t}] = -(\frac{\partial\hat{U}}{\partial t})$, which has to be inserted into the Schrödinger equation $\hat{H}_R^{(I)}|\psi\rangle = i\frac{\partial}{\partial t}|\psi\rangle$, while keeping in mind that the wave function transforms as $|\tilde{\psi}\rangle = \hat{U}|\psi\rangle$. We can thus include the effect of the Rabi driving in a static Hamiltonian.

### 2.2.2 Blackbody radiation-induced avalanche dephasing

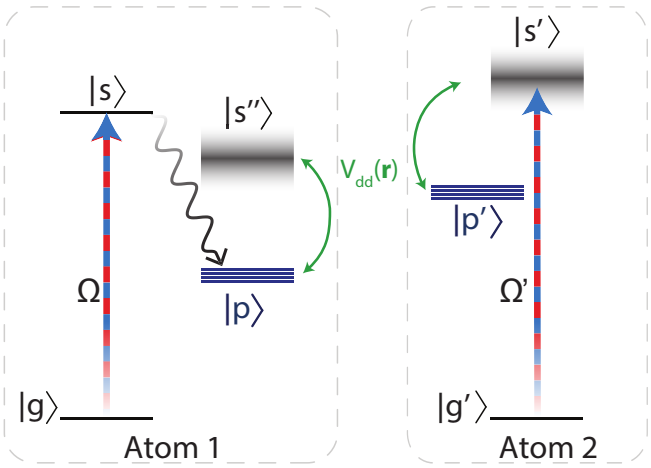


FIGURE 2.3: Blackbody-dominated decay from the Rydberg $s$-state $|s\rangle$ leads to a population of nearby $p$-states $|p\rangle$. These allow for off-diagonal dipole-exchange interactions: $|p, s'\rangle \leftrightarrow |s'', p'\rangle$. This process generates a dipole-dipole interaction between two different Rydberg $s$-states. It can bring atom 2 into resonance, thus enhancing the excitation. The corresponding energy shift broadens the transition (depicted by the gray shading). Figure taken from [Bou+17].

Before we discuss the relevant interaction potentials, we first have to consider another effect, which is induced by blackbody scattering from the coupled Rydberg $s$-state to nearby $p$-states of opposite parity[3] (see Fig. 2.3 for a sketch of this process). A thus produced $|p\rangle$ can subsequently trigger an off-diagonal dipole-exchange interaction of the form $|p, s'\rangle \rightarrow |s'', p'\rangle$. Such processes are referred to as Förster resonances and can induce energy transport, as observed in [Gün+13]. It thus leads to a dipole-dipole exchange interaction between two different Rydberg $s$-states. At a certain orientation and distance of the dipoles to each other, the second dipole is in resonance, so the excitation is enhanced. The dipole-dipole energy shift thereby broadens the transition in the sample inhomogeneously (represented by the gray shading of $|s'\rangle$ and $|s''\rangle$ in Fig. 2.3). For $|s\rangle = |s'\rangle$ this leads to **self-broadening**, where a single $s$-state transition is subsequently broadened due to the cascade of $p$-states it creates. We note that the effect relies on the occurrence of certain distances between atoms, so we expect a density dependence of the resulting line broadening, which indeed has been observed in [Gol+16; Ama+16].

As this process happens on a MHz timescale due to the strength of the dipole interaction, for example $C_3 = 2\pi \times 35\text{MHz}\,\mu\text{m}^3$ for the $18S$ state of rubidium [Bou+17], it can be considered to happen instantaneous in relation to the itinerant dynamics in typical optical lattices (≤kHz), as soon as a contaminant state has been created. We therefore consider the average time $\tau_c$ until the first contaminant excitation appears, as it provides an estimate of the actual coherent time available before the avalanche is triggered. For a system of $N$ atoms, the corresponding rate can well be approximated by the collective number of Rydberg excitations $N_e = \sum_i^N \langle \hat{n}_{e,i} \rangle = \sum_i n_{e,i}$, where $\hat{n}_{e,i} = \hat{b}_{e,i}^\dagger \hat{b}_{e,i}$ is the local density operator, multiplied by the rate at which the state decays to contaminant states:

[3] The parity of an electronic state is calculated as $P = (-1)^{\sum_i l_i}$, where the sum is taken over the orbital angular momentum quantum number $l_i$ for each electron $i$.

$$\tau_c = \tau_0 \left( b \sum_i \langle \hat{n}_{e,i} \rangle \right)^{-1} . \tag{2.12}$$

Here we introduce the sum of branching ratios $b = b_{nl}$ from the Rydberg state (with principal quantum number $n$ and the angular momentum $l$) to the contaminant states. As the branching ratios result from blackbody induced transitions, they strongly dependent on temperature, which can be seen in Fig. 2.4.

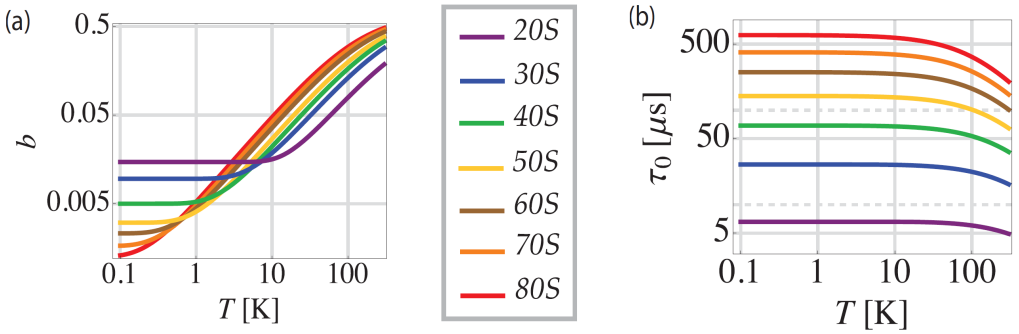


FIGURE 2.4: (a) Temperature dependence of the sum of branching ratios $b$ from different $nS$ states to contaminant $nP$ states playing a significant role in the avalanche dephasing process. (b) Effective lifetime $\tau_0$ (determined by spontaneous emission *and* blackbody radiation-induced transitions) for different $nS$ $^{87}$Rb Rydberg states as a function of the ambient temperature. This figure is taken from [Bou+17].

Therefore (2.12), in combination with the nature of the avalanche effect, implies multiple pathways to an increased coherence time [Bou+17]:

1. reduce the temperature (while $b_{35S} \approx 20\%$ is a typical value at room temperature, it reduces to below $5\%$ at 10K),
2. use an off-resonant cavity with a cavity length less than the wavelength of spontaneous emission to nearby states, so the spontaneous decay of the Rydberg excitation is suppressed,
3. reduce the effective number of Rydberg excitations in the system (either by using off resonant excitations, or by self-blocking of Rydberg excitations via long-range interactions, inducing an energy shift in the excited levels),
4. reduce the system size, either dimensional, as orientation plays an important role in the cascade of dipole-dipole exchanges, or by decreasing the particle number (see previous statement),
5. use stroboscopic excitation, by pulsing the Rabi driving on a sufficiently short timescale $t_p$ (which inversely scales with the system size $N$), followed by an extended dark time $t_d$ (which is a fixed multiple of the lifetime), in order to allow for decay of any contaminant excitation (this method implies an upper bound for the total atom number $N_c = b_e/\bar{n}_e$ in terms of the average local Rydberg fraction $\bar{n}_e$, above which stroboscopic approaches significantly diminish the dressing potential strength),
6. use post-selection (as in [Zei+16]), in order to select for contaminant-free data, which is possible as the avalanche induces a rapid ground state loss, significantly changing its counting statistics.

We note that in strontium a different dressing scheme can be realized that possibly reduces the relevance of avalanche dephasing. This EIT dressing scheme, discussed in [Gau+16], allows for a tenfold increase in the interaction strength of the dressed atoms, which implies that less atoms are necessary to achieve similar interaction energies as in the classical scheme.

### 2.2.3 Off-resonant dressing vs. near-resonant excitation

For Rydberg excitation at near resonant detuning, we expect a non-vanishing Rydberg fraction in the system, which may only be suppressed due to repulsive Rydberg-Rydberg interactions pushing nearby Rydberg levels out of resonance. This effect is called **Rydberg blockade**. In that case the coherent driving of Rydberg atoms effectively introduces a second particle species with three additional terms in the second quantized Hamiltonian. The first two are given by the Rabi driving (2.11), while the term essential for the generation of pronounced long-range correlations consists of the long-range interaction, which we will refer to as **bare** interaction in the following chapters:

$$\hat{H}_{VdW} = \frac{1}{2}\sum_{i\neq j}\hat{n}_i^e\hat{n}_j^e V_{VdW}\left(\mathbf{r}_i-\mathbf{r}_j\right), \quad \text{where} \quad V_{VdW}(\mathbf{r}) = \frac{C_6}{\mathbf{r}^6}. \tag{2.13}$$

But if we consider off-resonant dressing with $\Delta \gg \Omega$ and red detuning $\Delta < 0$ for a repulsive VdW interaction, such that facilitated excitations [LG14; Urv+15] are suppressed, we can remove $|e\rangle$ from the Hamiltonian in favor of a dressed ground state $|\tilde{g}\rangle \approx |g\rangle + \beta|e\rangle$, where $\beta = \Omega/2\Delta$ [Zei+16]. This leads to an effective two-body potential, which can be derived via a many-body perturbation expansion in $\beta$ of a Born-Oppenheimer treatment of the many-body interaction potential. In this case the interaction is instead given by the **dressed** pair-potential

$$\tilde{V}\left(\mathbf{r}_{ij}\right) = \tilde{C}_6/(r^6 + R_c^6), \tag{2.14}$$

where $R_c$ is the critical radius given by $R_c = (C_6/2\Delta)^{1/6}$ and $\tilde{C}_6$ is the rescaled interaction constant given by $\tilde{C}_6 = (\Omega/2\Delta)^4 C_6$. As a typical value for $C_6$ in natural units is given by $C_6 = 2\pi \times 241\text{MHz}\ \mu\text{m}^6$ [Li+17], we find for $\Omega = 2\pi \times 1\text{MHz}$ and $\Delta/\Omega = -7$ that $R_c/a \approx 3.0$ and $\tilde{C}_6/a^6 = 2\pi \times 0.28\text{MHz}$ for $a = 0.532\mu\text{m}$ corresponding to a typical lattice spacing in an optical lattice. So we have $\tilde{V}(0) = (\Omega/2\Delta)^3\Omega = 2\pi \times 0.36\text{kHz}$, which is on the order of typical local interactions discussed in Sec. 3.1.4. Also note that due to the explicit absence of $|e\rangle$ there will be no Rabi driving term (2.11) in this limit.

#### Hartree ansatz for the interaction

Many-body simulations using mean field methods require an efficient treatment of the long-range interaction term in either detuning limit discussed in the previous section. A typical method is the Hartree ansatz $\hat{n}_e^i\hat{n}_e^j = \langle\hat{n}_e^i\rangle\hat{n}_e^j + \hat{n}_e^i\langle\hat{n}_e^j\rangle - \langle\hat{n}_e^i\rangle\langle\hat{n}_e^j\rangle + \mathcal{O}(\delta\hat{n}_e^2)$, where $\delta\hat{n}_e^i = \hat{n}_e^i - \langle\hat{n}_e^i\rangle$. Let us test how this ansatz performs in describing the ground-state manifold of a small number of atoms. We define the Van der Waals constant $V = C_6/a^6$ in units of an arbitrary lattice spacing $a$. For two atoms at fixed positions **1** and **2** with $r = |\mathbf{r}_1 - \mathbf{r}_2|$, we find the simple Hamiltonian

$$\hat{H}(r) = \sum_{i=1}^{2} \hat{H}_{R,i} + V \times V(\mathbf{r}_{12} = r), \quad \text{with} \quad V(r) = \frac{1}{(r/a)^6}. \tag{2.15}$$

Let us further compare the exact ground-state of this Hamiltonian to the result obtained via a Hartree ansatz for the interaction term. Defining $E_0$ as the lowest eigenenergy of (2.15), we consider $E_{\text{pot}}(r) = E_0(r) - E_0(\infty)$. For two particles this pair-state energy shift as a function of their distance should correspond to the effective pair-potential (2.14) in the limit of red detuning. Here we consider the case of $V = 1000\Omega$, while other values only lead to a shift of the soft-core radius $R_c$.

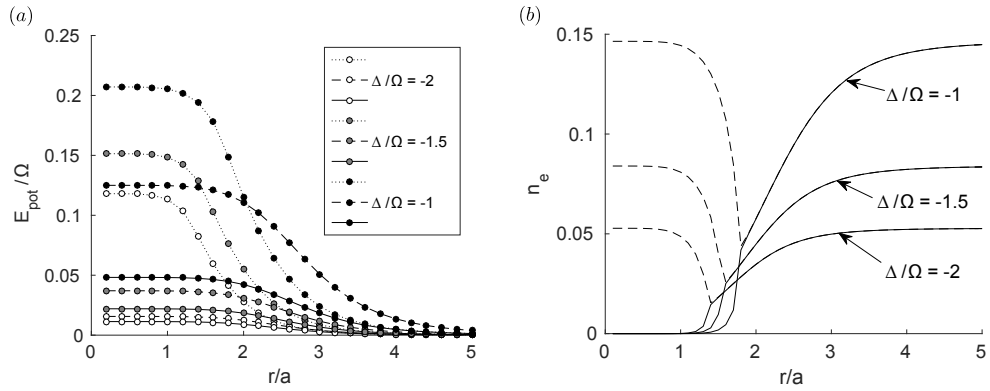


FIGURE 2.5: $(a)$ Ground-state energies $E_{\text{pot}}$ of (2.15) calculated exactly (solid lines), given by dressed potential (dashed lines) or obtained in the Hartree ansatz (dotted lines), for various values of the detuning shown in the legend. $(b)$ depicts the self-consistent values of the Rydberg state occupation $n_e^i = \langle \hat{n}_e^i \rangle$ obtained in the Hartree ansatz. The values for the site 1 (solid lines) and 2 (dashed lines) start to differ from one another below a certain critical distance, resulting in a softening of the interaction energy at smaller distances.

As can be seen in Fig. 2.5, the ground-state energy becomes well approximated by the pair-potential (2.14) for $\Delta/\Omega \ll -1$, while the Hartree approximation tends to underestimate the core radius and thus overestimates the interaction energy. Note that we can see the blockade effect at short distances qualitatively realized in the Hartree ansatz.

If detuning instead tends towards single particle resonance corresponding to $|\Delta/\Omega| \lesssim 1$, the pair-potential ansatz starts to fail as shown in Fig. 2.6, which is expected for $\Delta/\Omega \gtrsim -1$. The Hartree ansatz on the other hand yields a far better approximation of the energy, although it overestimates the interaction energy at small distances. The excitation blockade is once more realized at short distances. Close to resonance one can also observe that the Rydberg fraction obtained in the exact calculation starts to posses a spatial dependence revealing the blockade effect. Note that the mean-field result necessarily breaks the symmetry between the particles, while it is retained in the exact result, which can approximately be understood as a linear combination of all permutations of the Hartree result, as its value tends to the average value of the Hartree ansatz.

Going beyond resonance into the blue detuned regime, as shown in Fig. 2.7, the dressed pair-potential is no longer applicable, while the Hartree ansatz leads to an almost exact representation of $E_0$. Also the average occupation number of the exact and the mean field result nearly match.

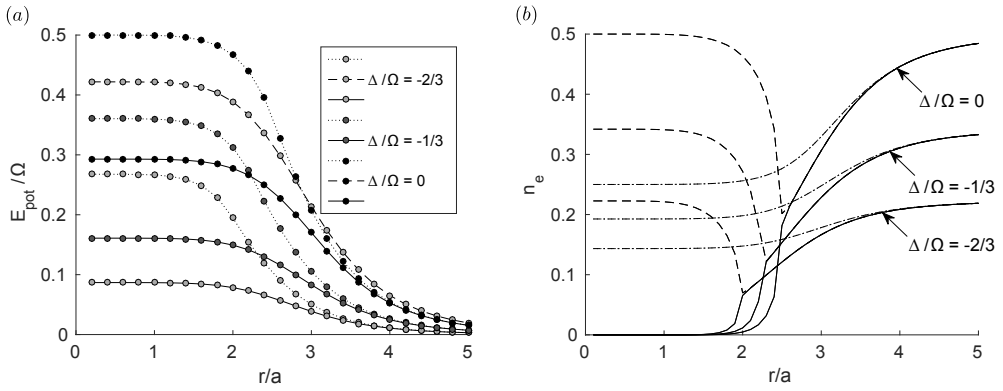


FIGURE 2.6: $(a)$ Ground-state energies $E_{\text{pot}}$ of (2.15) calculated exactly (solid lines), given by the dressed potential (dashed lines - not all are shown as some are out of range) or obtained in the Hartree ansatz (dotted lines), for various values of the detuning shown in the legend. $(b)$ depicts the self-consistent values of the Rydberg state occupation $n_e^i$ (solid and dashed lines). They start to differ from one another below a certain radius. Additionally, $n_e$ as obtained in the exact calculation is given by the dot-dashed line.

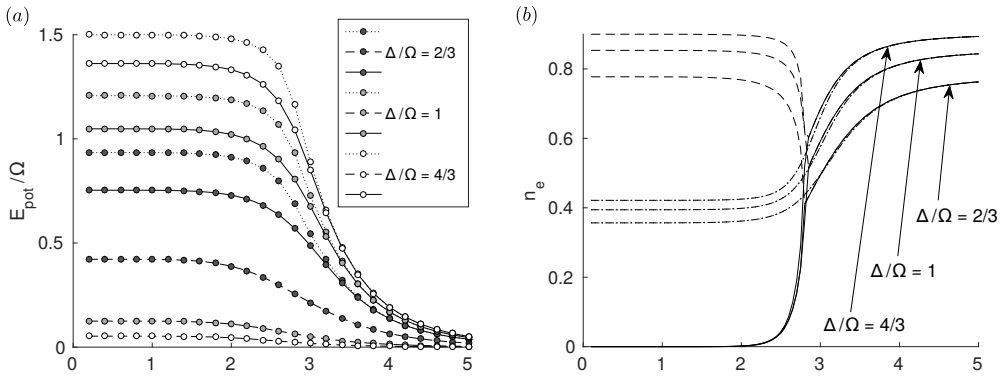


FIGURE 2.7: $(a)$ Ground-state energies $E_{\text{pot}}$ of (2.15) calculated exactly (solid lines), given by the dressed potential (dashed lines) or obtained in the Hartree ansatz (dotted lines), for various values of the detuning shown in the legend. $(b)$ depicts the self-consistent values of the Rydberg state occupation $n_e^i$ (solid and dashed lines). They start to differ from one another below a certain critical radius. Additionally $n_e$ as obtained in the exact case is given by the dot-dashed line.

Finally we want to know how these observations generalize to higher particle numbers. Let us therefore consider an ensemble of four atoms, which are either arranged in a square or on a line with periodic boundary conditions, while nearest neighbor distances are given by $r/a$ in both geometries. In the latter case the interaction is truncated for distances $r/a > 2$. As can be seen in Fig. 2.8 the Hartree ansatz in the larger ensemble is in very good qualitative agreement with the exact result for all considered values of the detuning in the near resonant regime, although it still tends to overestimate interaction energies at short distances. The dressed pair-potential on the other hand fails in this regime, as it cannot account for the blockade of Rydberg excitations.

To probe the blockade effect we also compare the density-density correlations $\langle \hat{n}_e^i \hat{n}_e^j \rangle$ obtained in the exact result to those derived in the Hartree ansatz. We consider the two cases when $i$ and $j$ are either nearest (NN) or next-nearest neighbors (NNN). As shown in Fig. 2.9 there is a good qualitative agreement between both in

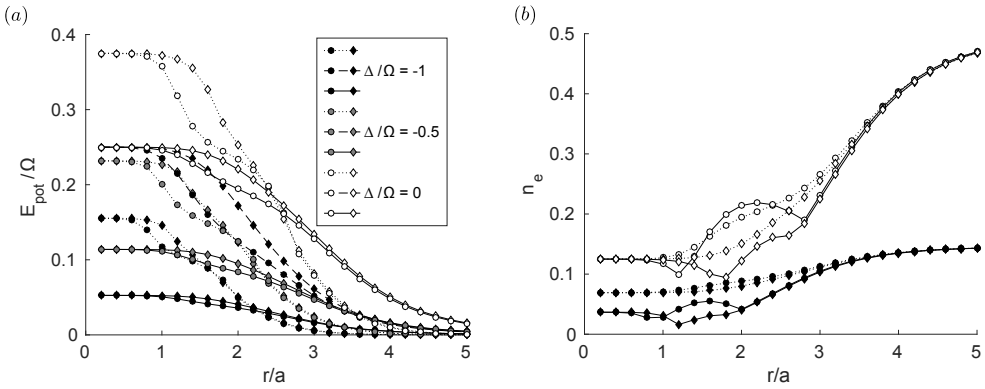


FIGURE 2.8: $(a)$ Ground-state energies $E_{\text{pot}}$ of (2.15) calculated exactly (solid lines), given by the dressed potential (dashed lines - not all are shown as some are out of range) or obtained in the Hartree ansatz (dotted lines), for various values of $\Delta/\Omega$ given in the legend. Here a 4-site system with two different geometries is considered: a square system (diamond symbols) or a linear system with periodic boundary conditions (circle symbols). $(b)$ depicts self-consistent values of the average Rydberg state occupation $n_e = \sum_i n_e^i/4$ (black lines) and as obtained in the exact calculation (dotted lines). The shaded symbols represent geometry and detuning as in $(a)$. Below a certain distance the mean-field results start to differ from the exact result, while qualitatively following the same behavior.

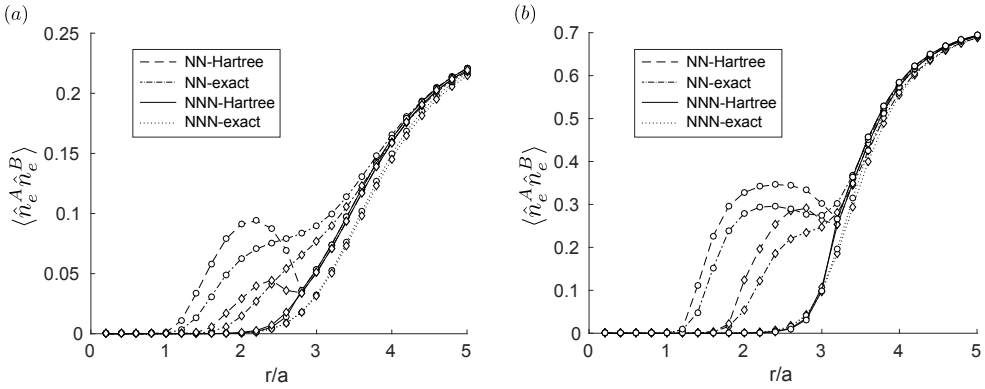


FIGURE 2.9: Occupation number correlation functions for nearest neighbors (NN) and next-nearest neighbors (NNN) as obtained in an exact calculation and in the Hartree approximation (see legend) for two values of $\Delta/\Omega = \{0, 1\}$ respectively shown in $(a)$ and $(b)$. The geometry of the considered 4-site system is given by symbol type: square geometry (diamond symbols) and linear system with periodic boundaries (circle symbols).

the vicinity of resonant excitation, while the blockade radius where correlations are suppressed entirely almost exactly coincides in both treatments.We thus conclude that the Hartree ansatz yields a very good approximation for a many-body system in the regime of near resonant Rydberg excitation.

We note that also the dressed pair-potential (2.14), which we have to consider in the weak (off-resonant) dressing regime, will be treated in a Hartree approach when we consider much larger systems, where exact methods can no longer be applied. It is the better choice in this limit, as long-range pair-entanglement is readily included via the dressed potential, while it is always absent in a Hartree ansatz for the bare interaction potential.

# Chapter 3

# Extended Bose-Hubbard model

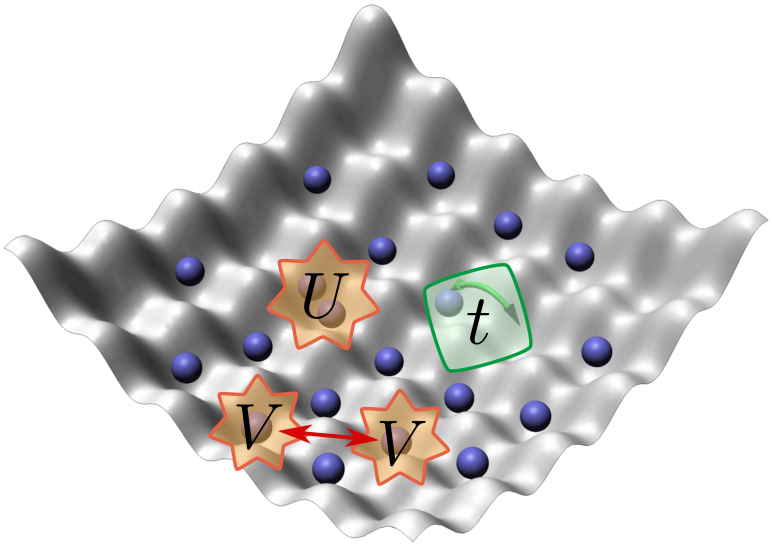


FIGURE 3.1: Dynamic processes of ultracold atoms in an optical lattice trap with harmonic confinement, as described by the extended Bose-Hubbard model. Particles can travel between nearest neighboring lattice sites at a tunneling rate $t$. If they encounter one another on a given site, they experience the local Hubbard interaction $U$. The presence of Rydberg excitations due to the Rabi driving (not shown) even allows for long-range interactions $V$ due to induced Van der Waals (or dipole-dipole) interactions.

One could describe the Hubbard model as the standard model of condensed matter physics. Albeit its minimalistic nature, describing the tunneling of quantum particles, such as electrons, atoms or molecules, between different lattice sites versus local interactions between the particles on each site, it gives rise to a vast range of non-trivial quantum phenomena. It has its roots in solid-state physics where it was independently and nearly simultaneously proposed by Gutzwiller, Hubbard, and Kanamori in 1963 (see [Mon92] for collected reprints). While its applicability is limited in the case of electrons in actual solid state systems due to the complex ("dirty") structure of real matter, it is especially useful for cold atoms in optical lattices. Its underlying approximations – particularly the assumption of narrow energy bands – can be realized in such systems close to perfection. Above all else the various involved energy scales can easily be tuned in optical lattice systems over orders of magnitude and even independently, by utilizing Feshbach resonances or Rabi processes (see Chap. 1).

Applying the Hubbard model also to bosons was first suggested by Fisher et al. in 1989 [Fis+89], while Jaksch et al. subsequently proposed realizing such a

model using ultracold atomic gases trapped in optical lattices [Jak+98]. The corresponding superfluid-Mott transition was first realized experimentally by Greiner et al. [Gre+02a] in three spatial dimensions, thus paving the way towards the vast toolbox of strongly correlated ultracold atomic lattice gases, which nowadays exists (see e.g. [BZ08] for an introduction).

In this chapter we will discuss the derivation of the (Bose)-Hubbard model in an optical lattice system, starting from a microscopic picture and thus allowing us to relate the (effective) Hubbard parameters to the various experimental parameters such as laser wavelength and intensity, atomic mass and scattering length, electronic states and transition matrix elements of the atoms, just to name a few.

As a starter we will first review the single particle and thus non-interacting physics in periodic potentials. Introducing non-local and thus extended Bloch states we then derive the emergence of a band structure in the tight binding limit. Subsequently these states will be used as a basis for the construction of (maximally) localized basis states within the individual bands, which are the Wannier states. While our focus will be on the standard formalism, we will briefly review an alternate definition put forward by Kivelson in 1982 [Kiv82] and discussed in great detail by Bissbort in 2012 [Bis12]. The latter method relies on the fact that the band projected position operator can be reduced to a simple form, yielding a numerically efficient method to determine the then unique Wannier states even in inseparable lattice potentials. Finally we will use the Wannier functions to determine the tunneling matrix elements as well as the local interaction strength. Combining all these elements then concludes the construction of the (Bose-)Hubbard model.

In addition to this basic derivation we will finish this chapter with a discussion of a long-range interaction extension of the (Bose-)Hubbard model, as realized by coherent Rydberg dressing discussed in Chap. 2. The relevant additions will be the inclusion of a second atomic component, given by atoms which are driven by a single – or multiple – Rabi lasers to high lying electronic states, namely Rydberg states. Due to the high polarizability of these states this will introduce strong long-range interactions to the model, the discussion of which concludes this chapter.

## 3.1 Derivation of the Bose-Hubbard model

The optimal framework for quantum many-body systems is quantum field theory which utilizes second quantization. As we will see this yields a very convenient quantum theory for many-body systems with strong correlations as induced by interactions. A quantum many-body system of interacting particles trapped in a spatially periodic potential $V(\mathbf{r})$, as for example given by atoms in an optical lattice, has a second quantized Hamiltonian of the form

$$\hat{H} = \int \hat{\psi}^\dagger(\mathbf{r}) \left( -\frac{\hbar^2 \nabla^2}{2m} + V(\mathbf{r}) \right) \hat{\psi}(\mathbf{r}) d^3\mathbf{r} + \iint \hat{\psi}^\dagger(\mathbf{r}) \hat{\psi}^\dagger(\mathbf{r}') \frac{U(\mathbf{r}-\mathbf{r}')}{2} \hat{\psi}(\mathbf{r}') \hat{\psi}(\mathbf{r}) d^3\mathbf{r} d^3\mathbf{r}'. \tag{3.1}$$

In this notation $\hat{\psi}^\dagger(\mathbf{r})$ and $\hat{\psi}(\mathbf{r})$ are quantum field operators which respectively either create or annihilate a quantum particle at position $\mathbf{r}$. The first term corresponds to the kinetic energy as given by $\hat{\mathbf{p}}^2/2m$, where $\hat{\mathbf{p}}$ is the momentum operator given in terms of the Nabla operator in position representation, so $\hat{\mathbf{p}} = -i\hbar\nabla$. The second term yields the external potential energy given by $V(\mathbf{r})$, while the last represents any two-particle interaction terms.

### 3.1.1 Bloch theorem

For vanishing two-particle interactions (3.1) can easily be separated into single particle Hamiltonians $\hat{H}_{\mathrm{sp}}$, which is due the lack of entanglement induced by the interaction among the particles:

$$\hat{H}_{\mathrm{sp}} = \int \hat{\psi}^{\dagger}(\mathbf{r}) \left( -\frac{\hbar^2}{2m} \nabla^2 + V(\mathbf{r}) \right) \hat{\psi}(\mathbf{r}) d^3\mathbf{r}. \tag{3.2}$$

Due to this separability we may thus obtain from $\hat{H}_{\mathrm{sp}}$ a basis representation which already incorporates the periodic properties of the system, thereby defining a useful starting point before also considering interaction effects. Let us now introduce an arbitrary real space lattice vector $\mathbf{R} = \sum_i n_i \mathbf{a}_i$, where $n_i \in \mathbb{Z}$ are arbitrary integers and $\mathbf{a}_i$ are the primitive lattice vectors, so the lattice spacing along individual directions is $a_i = |\mathbf{a}_i|$. The periodic property of the trapping potential implies the relation

$$V(\mathbf{r}) = V(\mathbf{r} + \mathbf{R}). \tag{3.3}$$

In order to determine the eigenvalues and eigenstates for a Hamiltonian of this general form, we have to consider how this discrete translational invariance is reflected by a corresponding symmetry of the Hamiltonian (3.2):

$$\hat{T}^{\dagger}(\mathbf{R}) \hat{H}_{\mathrm{sp}} \hat{T}(\mathbf{R}) = \hat{H}_{\mathrm{sp}}. \tag{3.4}$$

Here $\hat{T}(\mathbf{r}) = \exp(-i\mathbf{r} \cdot \hat{\mathbf{p}}/\hbar)$ is the translation operator which is defined by the generators of translations $\hat{p}_i$ and thus by the components of the momentum operators. Given a position state $|\mathbf{r}\rangle$, $\hat{T}(\mathbf{r}')|\mathbf{r}\rangle = |\mathbf{r} + \mathbf{r}'\rangle$. We can see that any translation of the Hamiltonian (3.1) by an arbitrary lattice vector $\mathbf{R}$ maps $\hat{H}_{\mathrm{sp}}$ back onto itself. Therefore, these translations and the Hamiltonian commute with one another, implying that both share the same set of eigenstates, which are the **Bloch states**. If $|\phi\rangle$ is an eigenstate of $\hat{H}_{\mathrm{sp}}$ with the eigenvalue $\lambda_\phi$, then $\hat{T}(\mathbf{a}_i)|\phi\rangle$, which is the state translated by one unit of a single primitive lattice vector, is an eigenstate as well. Assuming a non-degenerate spectrum[1] of $\hat{H}_{\mathrm{sp}}$, this also implies that both $|\phi\rangle$ and $\hat{T}(\mathbf{R})|\phi\rangle$ are identical up to a constant complex phase factor $\exp(i\phi)$. The real-space representation of these states are the **Bloch functions** $\psi_\phi(\mathbf{r}) = \langle \mathbf{r}|\phi\rangle$. Thus from multiple applications of the translation operator we can conclude the relation

$$\left\langle \mathbf{r} \left| \left(\hat{T}(\mathbf{a}_i)\right)^n \right| \phi \right\rangle = \psi_\phi(\mathbf{r} - n\mathbf{a}_i) = e^{in\phi} \psi_\phi(\mathbf{r}). \tag{3.5}$$

There is only one ansatz that satisfies these relations for any value of both $\mathbf{r}$ and $n$:

$$\psi_{\mathbf{k},\alpha}(\mathbf{r}) = e^{i\mathbf{k}\cdot\mathbf{r}} u_{\mathbf{k},\alpha}(\mathbf{r}). \tag{3.6}$$

Here $u_{\mathbf{k},\alpha}(\mathbf{r})$ is a complex-valued function of the same periodicity as that of the underlying lattice, so

[1] Even in case of degeneracy one can choose a suitable set of eigenstates, so all the relations are fulfilled exactly.

$$u_{\mathbf{k},\alpha}(\mathbf{r}) = u_{\mathbf{k},\alpha}(\mathbf{r}+\mathbf{R}). \tag{3.7}$$

We furthermore relabel the states by introducing the **quasimomentum** $\mathbf{k}$, which is a three dimensional vector of quantum numbers, corresponding to the state's change in phase under translations in any of the lattice directions. Its relation to the phase factor is given by $\phi = -\mathbf{k}\cdot\mathbf{a}_i + 2\pi n$, with $n \in \mathbb{Z}$. As there generally may be more than one state fulfilling the relations stated above, we introduce another quantum number $\alpha$, which will turn out to be the band index. In combination the set $\{\mathbf{k},\alpha\}$ uniquely specifies every individual energy eigenstate.

However, note that due to the periodicity $2\pi$ of the exponential function the quasimomenta $\mathbf{k}$ are not unique. This implies the existence of different $\mathbf{k}$, all of which yield the same transformation relation (3.5). But we can determine all values of $\mathbf{k}$ corresponding to the same transformation behavior, in order to subsequently link each unique eigenstate to a single representative $\mathbf{k}$. To do so we first have to introduce the reciprocal lattice generated by the primitive reciprocal lattice vectors $\mathbf{b}_j$. These are implicitly defined via the relation

$$\mathbf{a}_i \cdot \mathbf{b}_j = 2\pi\delta_{i,j}. \tag{3.8}$$

Given the set of $\{\mathbf{a}_i\}$, the $\mathbf{b}_j$ are obtained by inversion of the matrix which contains the primitve lattice vectors in its columns. Bloch states in an individual band $\alpha$ and for the two quasimomenta $\mathbf{k}$ and $\mathbf{k}' = \mathbf{k}+\mathbf{G}$ are identical states when both quasimomenta are related via a translation by the reciprocal lattice vector $\mathbf{G} = \sum_i n_i\mathbf{b}_i$. Thus the infinity of quantum numbers $\{\mathbf{k}+\mathbf{G},\alpha\}$ all refer to the same state for an arbitrary reciprocal lattice vector $\mathbf{G}$. In order to uniquely specify each state by the set $\{\mathbf{k},\alpha\}$ we introduce a requirement so each state has a single representative $\mathbf{k}$. Typically one requires that the euclidean norm of each representative $\mathbf{k}$ is less than for any other candidate $\mathbf{k}+\mathbf{G}$. All such $\mathbf{k}$ constitute the first Brillouin zone (1.BZ) and each set of $\mathbf{k}$ and $\alpha$ then uniquely refers to different physical Bloch states.

### 3.1.2 Bloch states and bands

Inserting the Bloch ansatz (3.6) into the time-independent Schrödinger equation corresponding to the Hamiltonian (3.1) yields an effective Schrödinger equation for the functions $u_{\mathbf{k},\alpha}(\mathbf{r})$:

$$\left[-\frac{\hbar^2}{2m}\left(-i\nabla+\mathbf{k}\right)^2 + V(\mathbf{r})\right] u_{\mathbf{k},\alpha}(\mathbf{r}) = E_{\mathbf{k},\alpha}u_{\mathbf{k},\alpha}(\mathbf{r}). \tag{3.9}$$

Due to the discrete translational symmetry of the potential $V(\mathbf{r})$ as well as the functions $u_{\mathbf{k},\alpha}(\mathbf{r})$, it is most straightforward to express both as Fourier series

$$V(\mathbf{r}) = \sum_{\{n_i\}} V_{n_1,n_2,n_3} e^{i\left(\sum_{j=1}^3 n_j\mathbf{b}_j\right)\cdot\mathbf{r}}, \tag{3.10}$$

$$u_{\mathbf{k},\alpha}(\mathbf{r}) = \sum_{\{n_i\}} c^{(\mathbf{k},\alpha)}_{n_1,n_2,n_3} e^{i\left(\sum_{j=1}^3 n_j\mathbf{b}_j\right)\cdot\mathbf{r}}. \tag{3.11}$$

The individual coefficients $V_{n_1,n_2,n_3}$ are obtained from the inverse transformation of the potential, which can be computed via an integration over the unit cell of the periodic potential. Thus only the coefficients $c^{(\mathbf{k},\alpha)}_{n_1,n_2,n_3}$ have to be determined. The effective Schrödinger equation reduces to a simple set of linear, algebraic equations when the Fourier series are inserted:

$$E_r \left( \frac{\mathbf{k} + \sum_{i=1}^{3} n_i \mathbf{b}_i}{k_L} \right)^2 c^{(\mathbf{k},\alpha)}_{n_1,n_2,n_3} + \sum_{\{n_i'\}} V_{\mathbf{n}-\mathbf{n}'} c^{(\mathbf{k},\alpha)}_{n_1',n_2',n_3'} = E_{\mathbf{k},\alpha} c^{(\mathbf{k},\alpha)}_{n_1,n_2,n_3}. \tag{3.12}$$

In this expression we have introduced the recoil energy $E_r = \hbar^2 k_L^2 / 2m$, which is the kinetic energy gained by an atom absorbing a photon of the lattice laser beams (see Sec. 1.3.2) and is given by the lattice quasimomentum $k_L = \pi/a$, where $a$ is the lattice spacing. If the potential is sufficiently smooth, for example when given by a sum of cosine functions as in a simple and thus separable hyper-cubic lattice, its corresponding coefficients $V_{n_1,n_2,n_3}$ decay rapidly for increasing frequency components. Correspondingly also the $c^{(\mathbf{k},\alpha)}_{n_1,n_2,n_3}$ will decay rapidly for the low energy states. Therefore we can truncate the high frequency terms at some $|n_1^m|$,$|n_2^m|$ and $|n_3^m|$, so we only need to consider the terms $\mathbf{n} = (n_1, n_2, n_3)$, where $|n_i| < |n_i^m|$. In that case (3.12) further reduces to a finite-dimensional eigenvalue problem:

$$H^{(\mathbf{k})} \begin{pmatrix} c^{(\mathbf{k},\alpha)}_{-n_1,-n_2,-n_3} \\ \vdots \\ c^{(\mathbf{k},\alpha)}_{n_1,n_2,n_3} \end{pmatrix} = E_{\mathbf{k},\alpha} \begin{pmatrix} c^{(\mathbf{k},\alpha)}_{-n_1,-n_2,-n_3} \\ \vdots \\ c^{(\mathbf{k},\alpha)}_{n_1,n_2,n_3} \end{pmatrix}. \tag{3.13}$$

The individual non-zero elements of the matrix are given by

$$H^{(\mathbf{k})}_{\mathbf{n}\mathbf{n}'} = \left( \mathbf{k} + \sum_{i=1}^{3} n_i \mathbf{b}_i \right)^2 \frac{E_r}{k_L^2} \delta_{\mathbf{n},\mathbf{n}'} + V_{\mathbf{n}-\mathbf{n}'} \tag{3.14}$$

The diagonal of this matrix is given by kinetic energy terms, while the off-diagonal terms couple the different plane wave states via the Fourier components of the lattice potential, analogous to a scattering of the plane waves. Due to the periodic potential, only quasimomentum states in the same equivalence class are coupled, making the matrix block-diagonal with individual blocks indexed by the quasimomentum $\mathbf{k}$.

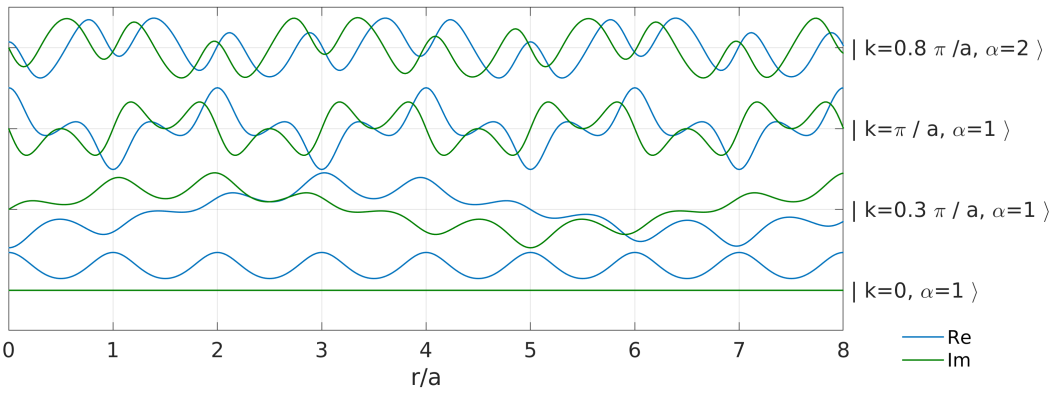


FIGURE 3.2: Examples of one-dimensional Bloch functions for $V_0/E_r = 5$.

For a given truncation the diagonalization of $H^{(\mathbf{k})}$ can be evaluated numerically for each $\mathbf{k}$, which results in the eigenenergies $E_{\mathbf{k},\alpha}$ for different bands $\alpha$. The corresponding eigenvectors contain the coefficients $c^{(\mathbf{k},\alpha)}_{n_1,n_2,n_3}$ determining $u_{\mathbf{k},\alpha}(\mathbf{r})$ of the Bloch functions. As Bloch functions are extended, they are normalized over the unit cell of volume $V_{\mathrm{uc}}$, which implies the normalization of the coefficients:

$$\int_{V_{\mathrm{uc}}} \left|\psi_{\mathbf{k},\alpha}(\mathbf{r})\right|^2 d^3\mathbf{r} = \int_{V_{\mathrm{uc}}} \left|u_{\mathbf{k},\alpha}(\mathbf{r})\right|^2 d^3\mathbf{r} = V_{\mathrm{uc}} \sum_{\{n_i\}} \left|c^{(\mathbf{k},\alpha)}_{n_1,n_2,n_3}\right|^2 = 1. \tag{3.15}$$

Then the Bloch states are given by

$$|\mathbf{k},\alpha\rangle = \int d^3\mathbf{r} \sum_{\{n_i\}} c^{(\mathbf{k},\alpha)}_{n_1,n_2,n_3} e^{i(\sum_{i=1}^3 n_i\mathbf{b}_i - \mathbf{k})\cdot\mathbf{r}} |\mathbf{r}\rangle\,. \tag{3.16}$$

As all Bloch states constitute the complete set of eigenstates of $\hat{H}_{\mathrm{sp}}$, they make up an orthonormal basis of the single-particle Hilbert space, so

$$\left\langle \mathbf{k},\alpha|\mathbf{k}',\alpha'\right\rangle = \delta_{\mathbf{k},\mathbf{k}'}\delta_{\alpha,\alpha'} \quad \text{and} \quad \mathbb{1} = \sum_{\mathbf{k},\alpha} |\mathbf{k},\alpha\rangle\langle\mathbf{k},\alpha|\,. \tag{3.17}$$

Let us now consider the simple example of a one-dimensional optical lattice as generated by a typical laser setup (see Sec. 1.2.2). We get the potential

$$V(r) = V_0\left(\sin^2(k_L r) - \frac{1}{2}\right) = -\frac{V_0}{4}\left(\exp(i2k_L r) + \exp(-i2k_L r)\right), \tag{3.18}$$

where $V_0$ is the lattice depth. As $V(r)$ consists only of two Fourier components (3.14) yields a tridiagonal matrix $H^{(k)}$ with matrix elements

$$H^{(k)}_{n,n'} = E_r\left(\frac{k}{k_L} + 2n\right)^2 \delta_{n,n'} - \frac{V_0}{4}(\delta_{n,n'+1} + \delta_{n,n'-1}). \tag{3.19}$$

Plotting the resulting eigenenergies $E_{k,\alpha}$ as a function of $k$ for each $\alpha$ reveals the single particle band structure. For $V_0 = 0$ the lattice potential vanishes and we expect a free particle dispersion relation. Due to the equivalence argument for the quasimomenta, this relation is folded back into the first Brillouin zone as shown in Fig. 3.3. Increasing the lattice depth to a finite value the potential couples all momentum states corresponding to the same quasimomentum lying on a vertical line in the back folded dispersion relation. States with energy differences on the order of the coupling by the potential start to hybridize, which opens up band gaps. Thus avoided crossings appear where the free particle energies intersect, leading to the formation of separate bands. In a finite lattice of $L$ sites there are $L$ individual Bloch states and each band is discrete, while only in the limit $L \to \infty$ the bands become continuous.

Note that the low temperature physics of bosons in such systems are dominated by the lowest band as long as the temperature and average interaction energies are well below the energy gap to higher bands.

In the limit of a deep lattice $V_0/E_r \gg 1$ the bands generally become cosine shaped,

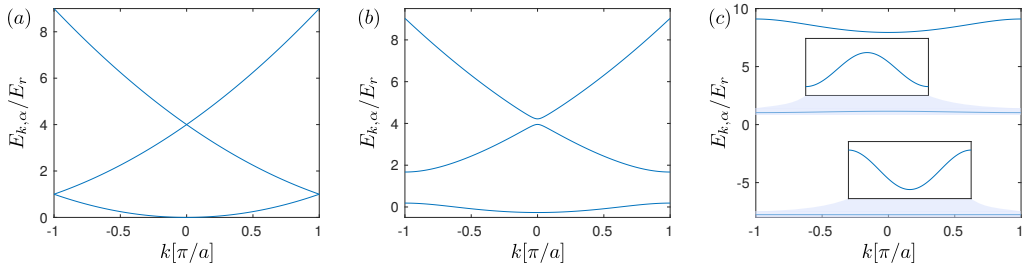


FIGURE 3.3: One dimensional single particle dispersion relations generated by an optical lattice potential with three different potential strengths $V_0/E_r = \{0, 3, 25\}$ $(a, b, c)$. Individual points on each band correspond to unique Bloch states with eigenenergies $E_{k,\alpha}$ described by the quantum numbers quasimomentum $k$ and band index $\alpha$. $(a)$ The quadratic dispersion of a free particle is folded back into the first Brillouin zone. For increasing lattice depth $V_0$ band gaps open up $(b)$, while the bands approach the tight binding limit for $V_0 \gg E_r$ $(c)$.

where the lowest band becomes proportional to $(1 - \cos(ka))$ with a positive effective mass $m^* = \left( \frac{\partial^2 E_{k,\alpha=0}}{\partial k^2}\Big|_{k=0} \right)^{-1}$. As can be seen in Fig. 3.3, the signs of these effective masses alternate from band to band in the one dimensional example. In this so called **tight-binding** limit the corresponding Wannier functions are strongly localized, so only Wannier states on nearest neighbor sites overlap sufficiently to generate a considerable tunneling amplitude $t$, as we will discuss in the following sections. Furthermore the tight-binding limit can be used to approximate the band gaps, as the states in low lying bands can be assumed to be localized primarily close to the minima of the lattice potential. Let us consider the minimum $r = 0$ of $V'(r) = V(r) + \frac{V_0}{2}$:

$$V'(r) \approx V_0 k_L^2 r^2 = \frac{m\omega^2 r^2}{2} \quad \text{with} \quad \omega = \sqrt{\frac{2V_0}{m}} k_L = 2\sqrt{\frac{\hbar^2 k_L^2}{2m}} \frac{\sqrt{V_0}}{\hbar} = 2\sqrt{\frac{V_0}{E_r}} \frac{E_r}{\hbar}. \tag{3.20}$$

In that limit the potential behaves approximately as a harmonic potential with eigenenergies that are spaced by $\Delta E = \omega\hbar = 2\sqrt{\frac{V_0}{E_r}} E_r$, which translates to the approximate band spacing of the low-lying bands in the tight-binding limit.

### 3.1.3 Wannier state construction

Commonly, the local Wannier state centered at a site $i$ corresponding to the position $\mathbf{R}_i$ in the band $\alpha$, is defined as the discrete Fourier transform of the Bloch states in the same band:

$$|\mathbf{R}_i, \alpha\rangle = \frac{1}{\sqrt{L}} \sum_{\mathbf{k}\epsilon 1.\mathrm{BZ}} e^{-i\mathbf{k}\cdot\mathbf{R}_i} |\mathbf{k}, \alpha\rangle. \tag{3.21}$$

In contrast to its apparent uniqueness this definition actually hides the importance of the individual phases of each Bloch state, all of which can have arbitrary values in the general case. Thus in order to find a unique Wannier basis, either an algorithm is needed to determine the complex phases or a more precise definition should be considered. With regard to the former, a typical approach is to focus on the maximally localized Wannier functions. The Wannier functions are thus uniquely defined as those states $|\mathbf{R}_i, \alpha\rangle$ for which the Bloch state phases are chosen such that

$\langle \mathbf{R}_i, \alpha|\hat{\mathbf{r}}^2|\mathbf{R}_i, \alpha\rangle - \langle \mathbf{R}_i, \alpha|\hat{\mathbf{r}}|\mathbf{R}_i, \alpha\rangle^2$ is minimized. While this method is numerically feasible for simple lattice geometries, using methods for the minimization of the energy of a variational state, the variational landscape may contain local minima, especially in more complex lattice geometries. Thus it also has to be guaranteed by the algorithm that the global minimum is always found, which adds further complications.

But based on the idea by Kivelson [Kiv82], one may instead define Wannier functions as the eigenstates of the band projected position operator, which he uses in the context of disordered systems. While Kivelson's work focuses on the one-dimensional case, Bissbort gives a thorough introduction of this concept in [Bis12] generalized to arbitrary lattice geometries at higher dimensions, even including the scenario of an inhomogeneous system.

### 3.1.4 Evaluation of Hubbard parameters

Using either the Bloch states $\psi_{\mathbf{k},\alpha}$ or the corresponding band-projected Wannier states $w_{\mathbf{R}_i,\alpha}$, we can represent the Hamiltonian (3.1) using either basis representation of the field operators:

$$\hat{\psi}(\mathbf{r}) = \sum_{\mathbf{k},\alpha} \psi_{\mathbf{k},\alpha}(\mathbf{r})\hat{b}_{\mathbf{k},\alpha}, \tag{3.22}$$

$$\hat{\psi}(\mathbf{r}) = \sum_{i,\alpha} w_{\mathbf{R},\alpha}(\mathbf{r})\hat{b}_{\mathbf{R}_i,\alpha}. \tag{3.23}$$

Here the operators $\hat{b}_{\mathbf{k},\alpha}$ and $\hat{b}_{\mathbf{R}_i,\alpha}$ correspondingly annihilate a particle in a Bloch state of quasimomentum $\mathbf{k}$ in band $\alpha$ and in a Wannier state at site $\mathbf{R}_i$ in band $\alpha$. For temperatures and average particle interactions below the energy gap of the Bloch bands (at least $V_0 > 3E_r$) this representation can be limited to the lowest band index $\alpha = 0$. Thus, omitting the band index in the operators $\hat{b}$ and $\hat{b}^\dagger$, the Hamiltonian (3.1) can be written as

$$\begin{aligned}\hat{H} = &\sum_{i,j} \hat{b}_i^\dagger \hat{b}_j \int w^*_{\mathbf{R}_i,0}(\mathbf{r}) \left(-\frac{\hbar^2\Delta}{2m} + V(\mathbf{r})\right) w_{\mathbf{R}_j,0}(\mathbf{r}) d^d\mathbf{r} \\ &+ \frac{1}{2}\sum_{i,i',j,j'} \hat{b}_i^\dagger \hat{b}_{i'}^\dagger \hat{b}_{j'} \hat{b}_j \iint w^*_{\mathbf{R}_i,0}(\mathbf{r}) w^*_{\mathbf{R}_{i'},0}(\mathbf{r}') U(\mathbf{r}-\mathbf{r}') w_{\mathbf{R}'_j,0}(\mathbf{r}') w_{\mathbf{R}_j,0}(\mathbf{r}) d^d\mathbf{r} d^d\mathbf{r}'.\end{aligned} \tag{3.24}$$

From this expression we separate individual terms starting from the on-site energy:

$$\varepsilon_i = \int w^*_{\mathbf{R}_i,0}(\mathbf{r}) \left(-\frac{\hbar^2\Delta}{2m} + V(\mathbf{r})\right) w_{\mathbf{R}_i,0}(\mathbf{r}) d^d\mathbf{r}. \tag{3.25}$$

The tunneling matrix elements in general are defined for any pair of sites $\mathbf{R}_i$ and $\mathbf{R}_j$ with site indices $i \neq j$:

$$t_{ij} = -\int w^*_{\mathbf{R}_i,0}(\mathbf{r}) \left(-\frac{\hbar^2\Delta}{2m} + V(\mathbf{r})\right) w_{\mathbf{R}_j,0}(\mathbf{r}) d^d\mathbf{r}. \tag{3.26}$$

Finally we also get the interaction terms between pairs of atoms:

$$U_{ii',jj'} = \iint w^*_{\mathbf{R}_i,0}(\mathbf{r}) w^*_{\mathbf{R}_{i'},0}(\mathbf{r}') U(\mathbf{r}-\mathbf{r}') w_{\mathbf{R}'_j,0}(\mathbf{r}') w_{\mathbf{R}_j,0}(\mathbf{r}) d^d\mathbf{r} d^d\mathbf{r}'. \tag{3.27}$$

As the Wannier functions are typically localized on each site with an approximately exponential decay away from the site [BZ08], the tunneling amplitudes $t_{ij}$ are exponentially suppressed for increasing distance. This implies that only nearest neighbor (NN) tunneling will be relevant in a sufficiently deep lattice, while the remaining long-range tunneling processes can be neglected. Thus the kinetic terms can be restricted to a summation over NN only, which we will denote by $\sum_{\langle i,j\rangle}$. The value of this hopping in an isotropic lattice with $a_i = a$ is given as follows, where $i$ and $j$ are any of the nearest neighbor pairs:

$$t = -\int w^*_{\mathbf{R}_i,0}(\mathbf{r}) \left( -\frac{\hbar^2\Delta}{2m} + V(\mathbf{r}) \right) w_{\mathbf{R}_j,0}(\mathbf{r}) d^d\mathbf{r}. \tag{3.28}$$

Regarding the derivation of the standard Bose-Hubbard model we further assume that the interaction potential is given by a short-ranged pseudo-potential $U(\mathbf{r}-\mathbf{r}') = \frac{4\pi\hbar^2 a_s}{m}\delta(\mathbf{r}-\mathbf{r}')$, effectively describing the contact interactions between atoms in ultracold gases as introduced in Sec. 1.2.3. Furthermore, for sufficiently deep lattices the Wannier functions are primarily localized to the vicinity of a single site, so the dominant contributions are given for the case where all lattice indices coincide. Thus we obtain the Hubbard interaction

$$U = \frac{4\pi\hbar^2 a_s}{m} \int \left| w_{\mathbf{R}_i,0}(\mathbf{r}) \right|^2 \left| w_{\mathbf{R}_i,0}(\mathbf{r}) \right|^2 d^d\mathbf{r}. \tag{3.29}$$

Even though we only consider the most dominant matrix element, this approach is sufficient to describe most physical phenomena arising from the two-particle interactions.

### Asymptotic behavior

For sufficiently deep lattices $(V_0, V_0^\perp) \gg E_r$, one can obtain the tunneling rate $t$ as an exact expression given by the width $W \approx 4t$ of the lowest Bloch band in the 1d Mathieu equation [Zwe03; Sla52] (effectively two-dimensional system for $V_0^\perp \gg V_0$):

$$t = \frac{4}{\sqrt{\pi}} E_r \left( \frac{V_0}{E_r} \right)^{\frac{3}{4}} e^{-2\sqrt{\frac{V_0}{E_r}}}. \tag{3.30}$$

Regarding the local interaction, one can show that the overlap $|\langle \mathbf{R}_0, 0 | \psi_{\text{Gauss}} \rangle|^2$ between the exact Wannier state and the Gaussian ground state, corresponding to an harmonic approximation of the potential for a given lattice site, deviates from one by less than 3% for $V_0/E_r = 3$ [BZ08] and approaches unity for increasing lattice depths. Therefore one can use the Gaussian ground state to obtain a very accurate approximation of the local interaction ($V_0^\perp \gg V_0$ for a two-dimensional system)

$$U = \sqrt{\frac{8}{\pi}} k_L a_s E_r \left( \frac{V_0}{E_r} \right)^{\frac{2}{4}} \left( \frac{V_0^\perp}{E_r} \right)^{\frac{1}{4}}. \tag{3.31}$$

**Standard form of the Bose-Hubbard model**

Finally that we have everything together, let us write down the Bose-Hubbard model in its standard form using second quantization:

$$\hat{H}_{\mathrm{BH}} = -t \sum_{\langle i,j \rangle} \left( \hat{b}_i^\dagger \hat{b}_j + \mathrm{h.c.} \right) + \frac{U}{2} \sum_i \hat{n}_i \left( \hat{n}_i - 1 \right) + \sum_i \varepsilon_i \hat{n}_i, \tag{3.32}$$

where we introduce the local density operator or occupation number operator $\hat{n}_i = \hat{b}_i^\dagger \hat{b}_i$.

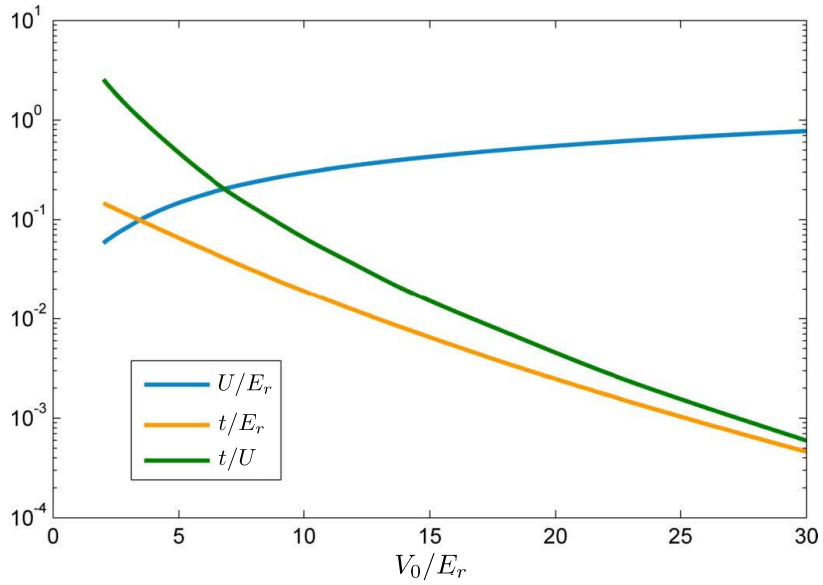


FIGURE 3.4: The Bose-Hubbard parameters $t$ and $U$, as well as their ratio as a function of the lattice depth $V_0/E_r$ for $^{87}$RB in an 812nm optical lattice. This figure is adapted from [Bis12].

In actual experiments the optical lattice potential is typically deformed by an additional external harmonic trap, resulting in a spatially inhomogeneous potential $V(\mathbf{r})$ without its discrete translational symmetry. For a sufficiently weak external confinement we may assume that the lattice symmetry remains approximately valid locally, such that the lowest Wannier functions mostly remain the same. In that case the external trap simply yields a shift of the local energies proportional to the confining potential $V_c(\mathbf{r}_i) = V_c^0 \mathbf{r}_i^2$, where $V_c^0$ is the strength of the harmonic trap. If we furthermore investigate such a system in the grand canonical ensemble ($\hat{H}_{\mathrm{BH}} \to \hat{H}_{\mathrm{BH,G}}$), we also have to introduce the term $\hat{N}\mu$, where $\hat{N} = \sum_i \hat{n}_i$ and $\mu$ is the global chemical potential controlling the total number of bosons in the system. So with $\varepsilon_i = V_c(\mathbf{r}_i) - \mu$ we obtain

$$\hat{H}_{\mathrm{BH,G}} = -t \sum_{\langle i,j \rangle} \left( \hat{b}_i^\dagger \hat{b}_j + \mathrm{h.c.} \right) + \frac{U}{2} \sum_i \hat{n}_i \left( \hat{n}_i - 1 \right) + \sum_i (V_c(\mathbf{r}_i) - \mu) \hat{n}_i. \tag{3.33}$$

The Bose-Hubbard model is the simplest interacting bosonic lattice model. It describes the competition between a repulsive on-site interaction $U$, disfavoring high local occupancies while favoring localization via suppression of particle number fluctuations, versus the kinetic energy $t$, favoring delocalization of particles as

long as delocalized particles do not interact too strongly. While it was initially proposed for a description of liquid helium in porous media [Fis+89], ultracold bosonic atoms in optical lattices allow for an almost perfect realization of the model [Jak+98; Gre+02a; Gre+02b; Zwe03; BZ08]. Especially noteworthy is the possibility to tune the ratio $U/t$ over orders of magnitude by varying the lattice depth $V_0$, which itself depends on the laser power of the lattice laser. This allows for a wide range of parameters for which experiments can implement the Bose-Hubbard model, especially considering the possibility to tune local interactions independently using Feshbach resonances (see Sec. 1.2.3).

## 3.2 Rydberg extension of the model

A downside of the Bose-Hubbard model presented thus far is the absence of long-range interactions, which could generate long-range entanglement, possibly leading to a broken lattice symmetry associated with exotic phases of matter such as the lattice-supersolid or a devil's staircase of density wave ordered phases. Among the various suggested methods, such as polar molecules [GSL02; MTL07; CS+10; Pol+10] and magnetic dipole interactions [BB11; Bai+16], we focus on the use of Rydberg excitations discussed in Chap. 2. As Rydberg excitations have a huge polarizability (scaling $\propto n^3$ in the principle quantum number), neutral isotropic Rydberg atoms exhibit strong Van der Waals interactions ($\propto n^{11}$). But in order to generate coherent Rydberg excitations one has to coherently drive a Rydberg excitation via a Rabi-laser.

Commonly there are two pathways to generate a Rydberg excitation in typical quantum gas experiments. In most cases alkaline (e.g. $^{87}$Rb) but also alkaline-earth atoms (e.g. Sr as discussed in [Muk+11]) are used to generate Rydberg excitations. Note that the presence of a second valence electron in the alkaline-earth atoms allows for a simultaneous magic wavelength trapping of ground *and* excited states [Muk+11], while Rydberg excited atoms by themselves commonly exhibit an optical lattice of opposite sign in relation to the ground state. By limiting the excited Rydberg fraction, one can limit this effect in practice. In both cases a single electron from the $s$-valence shell is excited to a high lying Rydberg state $n \gtrsim 20$ in a Rabi-scheme. Either the transition is driven directly using a UV-laser, resulting in a state with $p$-wave symmetry, also for the resulting long-range interaction, or an intermediate state is used so the final Rydberg excitation may either be an $s$- or $d$-state.

As we are primarily interested in isotropic interactions we focus on the latter case, while the former may also behave isotropic, either in the absence of a quantization axes (as induced by polarizing fields), or in a two-dimensional system when an external field guarantees a perpendicular alignment. One can show that this two-photon process can effectively be mapped onto a single-photon process, coupling the $s$-wave ground state to an $s$-wave Rydberg state (see Sec. 2.2 for further details). Thus one obtains an effective two level system consisting of the ground state atom $|g\rangle$ and the Rydberg excitation $|e\rangle$[2]. Both are coupled via an (effective) Rabi frequency $\Omega$, while the total detuning $\Delta$ of the laser frequencies with regard to the excitation energies generates an effective offset for the chemical potential of the Rydberg component.

Following the derivation presented in Sec. 2.2.1 we obtain an extended two component Bose-Hubbard model of the form

[2]Note that the use of electronic states makes it possible to generate arbitrary spin models by mapping each state onto an effective spin orientation.

$$\hat{H} = \hat{H}_{2BH,kin} + \sum_{i}^{N} \left( \hat{H}_{2BH,loc,i} + \hat{H}_{R,i} + \hat{H}_{int,i} \right), \tag{3.34}$$

where

$$\hat{H}_{2BH,kin} = -t \sum_{\langle i,j \rangle} \left( \hat{b}^{\dagger}_{\sigma,i} \hat{b}_{\sigma,j} + \eta \hat{b}^{\dagger}_{\nu,i} \hat{b}_{\nu,j} + h.c. \right), \tag{3.35}$$

$$\hat{H}_{2BH,loc,i} = U \left( \frac{\hat{n}^{\sigma}_i}{2} (\hat{n}^{\sigma}_i - 1) + \lambda \hat{n}^{\sigma}_i \hat{n}^{\nu}_i + \tilde{\lambda} \frac{\hat{n}^{\nu}_i}{2} (\hat{n}^{\nu}_i - 1) \right) - \mu \left( \hat{n}^{\sigma}_i + \hat{n}^{\nu}_i \right), \tag{3.36}$$

$$\hat{H}_{R,i} = \frac{\Omega}{2} \left( \hat{b}^{\dagger}_{\sigma,i} \hat{b}_{\nu,i} + \hat{b}^{\dagger}_{\nu,i} \hat{b}_{\sigma,i} \right) - \Delta \hat{n}^{\nu}_i, \tag{3.37}$$

$$\hat{H}_{int,i} = \frac{V}{2} \sum_{j \neq i} \hat{n}^{\nu}_i \hat{n}^{\nu}_j V \left( \mathbf{r}_i, \mathbf{r}_j \right). \tag{3.38}$$

Throughout this thesis we consider two interpretations of this model (see Fig. 3.5). In the first case we consider the situation of far off-resonant driving (**weak dressing**), for which the $\sigma$ species corresponds to a bare hyperfine level $|b\rangle$ in the atomic ground state manifold, while the $\nu$ species is given by another hyperfine ground state $|d\rangle$, which is coupled far off-resonantly to a Rydberg excitation, with $\Omega \ll |\Delta_{\text{far}}|$. Thus it represents a coherent mixture of the form $|\tilde{d}\rangle = |d\rangle + \varepsilon|e\rangle$, where $\varepsilon = \Omega/2|\Delta_{\text{far}}|$ determines the Rydberg fraction $\varepsilon^2$ of this single-particle dressing. For repulsive interactions the driving has to be red detuned, such that the long-range interaction does not facilitate additional excitations. Only then is it allowed to consider the dressing as a single-particle effect.

In contrast, near resonant excitation of Rydberg states with $|\Delta_{\text{near}}| = \mathcal{O}(\Omega)$ induces an effective detuning of the Rabi transition, which is proportional to the total long-range interaction energy. We therefore consider near resonant excitation (**strong dressing**) of the Rydberg state as a second case, where the two components $\sigma$ and $\nu$ are given by an atomic ground state $|g\rangle$ and a Rydberg excited state $|e\rangle$ respectively.

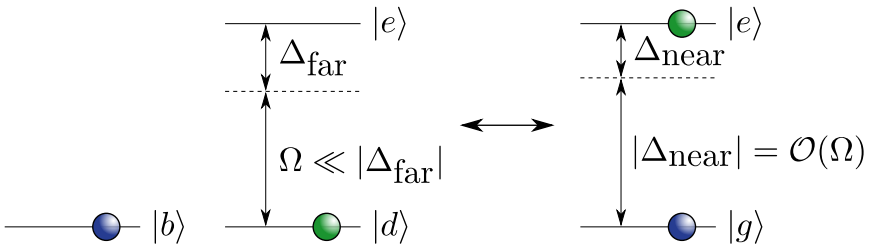


FIGURE 3.5: The extended Bose-Hubbard model with two components can be achieved in two ways using Rydberg excitations. *Left:* For far off-resonant excitation of Rydberg states, one hyperfine ground state $|d\rangle$ (green) becomes weakly dressed by a Rydberg state $|e\rangle$, while the bare hyperfine state $|b\rangle$ (blue) can interact with the dressed species only via a local inter-species Hubbard interaction. *Right:* At near resonant excitation of the Rydberg state, the two components are given by the ground state $|g\rangle$ (blue) and the Rydberg state $|e\rangle$ (green) that is addressed by the Rabi process.

The main difference between these two cases therefore lies in the shape of the long-range interaction. For near resonant dressing one has to consider the bare Van der Waals (VdW) interaction, which, using the notation $\mathbf{r}_{ij} \equiv \mathbf{r}_i - \mathbf{r}_j$, has the form $V\left(\mathbf{r}_{ij}\right) \propto 1/\mathbf{r}^6_{ij}$, while the weak dressing case leads to an effective soft-core interaction $V\left(\mathbf{r}_{ij}\right) \propto 1/(\mathbf{r}^6_{ij} + R^6_c)$, where $R_c$ is the soft-core radius (see Sec. 2.2.3).

### 3.2.1 Parameters of the extended Bose-Hubbard model

Many of the parameters of the extended Bose-Hubbard model (3.34) are easily adjustable in experiments, some even over several orders of magnitude. The Rabi parameters can be controlled directly via the laser intensity determining the Rabi frequency $\Omega$, which also depends on the matrix elements of the chosen transition, and the laser detuning $\Delta$ [BZ08], while the VdW interaction is determined by the choice of principle quantum number $n$ for the Rydberg level ($C_6 \propto n^{11}$, see Sec. 2.1.2). We have $V(\mathbf{r}_i, \mathbf{r}_j) = V(\mathbf{r}_{ij}) = a^6/|\mathbf{r}_{ij}|^6$ and $V = C_6/a^6$, where $a$ is the lattice spacing. A typical value for $C_6$ is 240MHz $\mu$m$^6$ [Li+18], so in a typical lattice where $a = 0.532$nm, $V \approx 15$GHz. From here on we consider spatial vectors $\mathbf{r}_i$ to be in units of lattice spacings $a$. Although the ground state hopping and interaction are determined by the lattice depth, they can be tuned independently using Feshbach resonances, as discussed in Sec. 1.2.3. The remaining parameters are not as simple to control. The hopping of Rydberg-excited atoms is not yet an experimentally well-controlled parameter, since the OL, trapping the ground state ($g$) atoms, is not the same for Rydberg states by default. Often it is even of opposite sign [Dut+00; You+10; YAR10], while proposals have been made to counter this effect via so called magic-wavelength trapping [ZRS11]. A noteworthy example are alkaline-earth atoms such as strontium with two valence electrons [Muk+11], one of which generates the Rydberg excitations while the other can be used to achieve simultaneous trapping of the Rydberg and the ground state at the magic wavelengths $\lambda_m = 323.4$ nm and $\lambda_m = 418.6$ nm. In the presented work we focus on the limiting case $\eta = 0$, motivated by the fact that the Rydberg part of the Hilbert space is dominated by the VdW interaction and the Rabi frequency, while the total kinetic energy contribution from $|e\rangle$ will be small compared to $|g\rangle$ due to low Rydberg fractions (similar to [Hon+10], see App. D.1). As the Rydberg states are perturbed by the Rabi process, their localization will anyway be lifted due to hybridization of $|e\rangle$ with $|g\rangle$.

The remaining local interactions on the other hand are fixed by considering the quantum Zeno effect [MS77; GR+09; VCH14]. It describes the observation that loss channels with a bare loss rate $\gamma_0 \gg U$ are strongly suppressed in the lattice, as this corresponds to a strong measurement of the lossy states, thus keeping them fixed at zero occupation. Experiments have shown the large cross section of molecular ion formation in Rydberg gases [Nie+15]. Due to the different electronic structure of such ions, they are not trapped by the confining potential, implying a large bare loss rate $\gamma_0$. The local quantum states susceptible to molecule formation or ionization correspond to Fock states of the form $|n_g \geq 0, n_e > 0\rangle$. We can model their loss-induced suppression by choosing "arbitrarily" large values[3] for the parameters $\lambda$ and $\tilde{\lambda}$ in (3.36).

With regard to the second interpretation of (3.34), both $g$ and $e$ are replaced by two different atomic hyperfine ground states $b$ (bare) and $d$ (dressed), the second of which is far off-resonantly dressed by a Rydberg state. In this case we can consider the local interactions and the tunneling rates to be identical for both species, at least as long as no spin-dependent lattices are used. As we do not consider driving between the two hyperfine levels, we can neglect the Rabi mixing term in (3.37) and consider two separate chemical potentials $\mu_b = \mu$ and $\mu_d = \mu + \Delta$ for each independent species instead.

[3] A valid alternative is to neglect the corresponding part of the local Hilbert space instead.

# Chapter 4

# Bosonic Dynamical mean-field theory

Mean-field methods commonly only include a static mean-field. This implies that any quantum-fluctuations are neglected, even if they might become important, as for example in the vicinity of a quantum phase transition. There the fluctuations may destabilize either of the phases with regard to the others and thus the actual phase transition is shifted with regard to a static mean-field prediction. Conceptually speaking, in order to include fluctuation effects, one has to generalize the idea of a static mean-field to a dynamical mean-field, thereby introducing a frequency dependency of such a mean-field.

In this chapter we will derive the basic concepts of the **bosonic dynamical mean-field theory** (B-DMFT) [BV08; HSH09; And+10; STH11; And+11], in its real-space representation (RB-DMFT). We will see that B-DMFT naturally follows from an expansion in powers of correlation functions, starting with the lowest order, which is the condensate order parameter $\phi = \langle \hat{b} \rangle$ defined as the expectation value of the annihilation operator $\hat{b}$. In contrast to the fermionic systems [Geo+96], this expectation value does not vanish in general. The next higher order correlation functions are Green's functions of the general form $\propto \langle \hat{b}_i^{(\dagger)} \hat{b}_j^{(\dagger)} \rangle$, where $(\dagger)$ signifies the general possibility to consider an arbitrary combination of creation and annihilation operators. The non-number-conserving combinations are usually called **anomalous Green's functions** and naturally arise in bosonic systems. The indices $i$ and $j$ correspond to any selection of modes, most commonly corresponding to a pair of neighboring sites. In the Heisenberg picture these Green's functions obviously become time dependent, even for a static Hamiltonian. They will therefore naturally serve as dynamical Weiss-Green's function[1], and as they arise from the tunneling term in the Hamiltonian, they describe the first order effect of nearest-neighbor correlations on the many-body behavior. We will furthermore see that DMFT is non-perturbative with regard to local interactions, resulting in an exact consideration of local fluctuations. The corresponding self-consistent loop is sketched in Fig. 4.1, while the various quantities will be introduced in the course of this chapter.

Regarding the basic concepts of B-DMFT, we will be following the formulations and notations, as introduced by Michiel Snoek and Walter Hofstetter in *Quantum Gases: Finite Temperature and Non-Equilibrium Dynamics* (Vol. 1 Cold Atoms Series) [SH13], using natural units $\hbar = 1$ throughout this chapter. Thus energies will be in units of radial frequencies $\omega$.

[1] In the same sense, as the condensate order parameter $\phi$ serves as a static Weiss-mean-field.

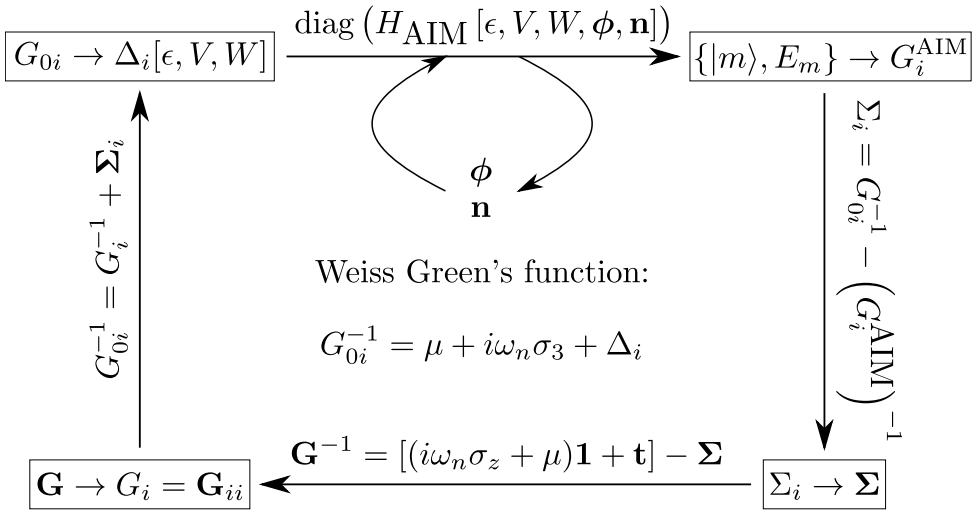


FIGURE 4.1: Schematic depiction the self-consistent loop of RB-DMFT for an extended Hamiltonian in the Hartree approximation. Note that the whole loop applies just as well, when using connected quantities instead.

## 4.1 Effective impurity action

The first step, in order to find the local dynamical mean-field, which will be given by a self-consistent Weiss-Green's function, is to introduce an effective local action. This can be achieved by tracing out all degrees of freedom (DOF) in a given lattice system, but those of a given site. The remaining action will thus contain all dynamic properties of the full system while effectively describing a single site. Let us derive this effective description for an extended Bose-Hubbard model of $N$ bosonic flavors, as we will be using for the description of a Rydberg system, given in a grand-canonical ensemble:

$$\hat{H} = -\sum_{i,j,\sigma,\gamma} t_{ij}^{\sigma\gamma} \hat{b}_{i\sigma}^{\dagger} \hat{b}_{j\gamma} + \frac{1}{2} \sum_{i,\sigma,\gamma} U_{\sigma\gamma} \hat{n}_{i\sigma} (\hat{n}_{i\gamma} - \delta_{\sigma,\gamma}) - \sum_{i,\sigma} \mu_\sigma \hat{n}_{i\sigma} + \sum_{i \neq j,\sigma} V_\sigma(i,j) \hat{n}_{i\sigma} \hat{n}_{j\sigma}. \quad (4.1)$$

The hopping matrices $t_{ij}^{\sigma\gamma}$ generally have to obey the relation $t_{ij}^{\sigma\gamma} = t_{ji}^{\gamma\sigma *}$. In our case they are only non-zero either for nearest neighbors of the same flavor $\sigma = \gamma$, or when both $\sigma \neq \gamma$ *and* $i = j$ are fulfilled simultaneously, where the latter case corresponds to the Rabi terms, so $t_{ii}^{\sigma\gamma} = \Omega_{\sigma\gamma}/2$ for $\sigma \neq \gamma$. For the two component system considered in this work, it is thus given by $\Omega_{ge} = \Omega_{eg} = \Omega$. Furthermore we only assume long-range interactions of the form $V_\sigma(i,j) = V_\sigma(\mathbf{r}_i - \mathbf{r}_j = \mathbf{r})$ (and no singular i.e. divergent behavior for any $\mathbf{r}$ possible on a given lattice). We will therefore use the shorthand expression $V_\sigma(i) \equiv V_\sigma(i,0)$. As is well known (see e.g. Sec. 4.2 'Field integral for the quantum partition function' in *Condensed Matter Field Theory* by Altland and Simons [AS10]), the partition function ($Z$) can be expressed as a Feynman path integral in terms of the total action $S[\mathbf{b}^*, \mathbf{b}]$, which is given in the coherent state representation. So

$$Z = \int \mathcal{D}[\mathbf{b}^*]\mathcal{D}[\mathbf{b}] \exp\left(-S[\mathbf{b}^*, \mathbf{b}]\right). \quad (4.2)$$

Here we use the abbreviated notation $\int \mathcal{D}[\mathbf{b}^*]\mathcal{D}[\mathbf{b}] = \int \prod_{i,\sigma} \mathcal{D}[b_{i\sigma}^*]\mathcal{D}[b_{i\sigma}]$, while the $b_{i\sigma}(\tau)$ are the (complex-valued) fields, corresponding to the coherent state representation. The total action in turn is given by

$$S[\mathbf{b}^*, \mathbf{b}] = \int_0^\beta d\tau \left( \sum_{i,\sigma} b^*_{i\sigma}(\tau) \frac{\partial b_{i\sigma}(\tau)}{\partial \tau} + H(\tau) \right). \tag{4.3}$$

The expression $H(\tau)$ is constituted by the Hamiltonian describing the system (4.1), but with all annihilation and creation operators ($\hat{b}_{i\sigma}/\hat{b}^\dagger_{i\sigma}$) replaced correspondingly by the fields and the complex-conjugate fields ($b_{i\sigma}(\tau)/b^*_{i\sigma}(\tau)$). Let us now consider a given site, which we will call site 0 from now on, and split the action into three parts, following the **cavity** method, as also used in the derivation of the fermionic DMFT equations [Geo+96],

$$S = S_0 + S_{(0)} + \Delta S. \tag{4.4}$$

$S_0$ contains all terms only related to site 0, while $S_{(0)}$ is the remaining system *excluding* any terms which include site 0. The latter is commonly referred to as the **cavity system**. All other terms connecting site 0 to the cavity system are included in $\Delta S$. Defining $b^*_{i\sigma} b_{i\sigma} = n_{i\sigma}$ we thus have

$$S_0 = \int_0^\beta d\tau \sum_\sigma \left( b^*_{0\sigma} \frac{\partial b_{0\sigma}}{\partial \tau} - \mu_\sigma b^*_{0\sigma} b_{0\sigma} \right) + \sum_{\sigma,\gamma} \left( \frac{\Omega_{\sigma\gamma}}{2} (b^*_{0\sigma} b_{0\gamma} + b_{0\sigma} b^*_{0\gamma}) + \frac{U_{\sigma\gamma}}{2} |b_{0\sigma}|^2 |b_{0\gamma}|^2 \right), \tag{4.5}$$

$$\Delta S = \int_0^\beta d\tau \left( \sum_{\langle 0,i\rangle,\sigma} -(t^\sigma_{0i} b^*_{0\sigma} b_{i\sigma} + c.c.) + \sum_{i\neq 0,\sigma} V_\sigma(i) n_{i\sigma} n_{0\sigma} \right). \tag{4.6}$$

Let us now define $\int \mathcal{D}_{(0)}[\mathbf{b}^*]\mathcal{D}_{(0)}[\mathbf{b}] = \int \prod_{i\neq 0,\sigma} \mathcal{D}[b^*_{i\sigma}]\mathcal{D}[b_{i\sigma}]$ and $\int \mathcal{D}[\mathbf{b}^*_0]\mathcal{D}[\mathbf{b}_0] = \int \prod_\sigma \mathcal{D}[b^*_{0\sigma}]\mathcal{D}[b_{0\sigma}]$, in order to introduce the cavity partition function $Z_{(0)}$, as well as the effective partition function $Z^0_{\text{eff}} \equiv Z/Z_{(0)}$, which defines the effective action $S^0_{\text{eff}}$. Thus we define

$$Z_{(0)} = \int \mathcal{D}_{(0)}[\mathbf{b}^*]\mathcal{D}_{(0)}[\mathbf{b}] \exp(-S_{(0)}), \tag{4.7}$$

$$Z^0_{\text{eff}} \equiv \int \mathcal{D}[\mathbf{b}^*_0]\mathcal{D}[\mathbf{b}_0] \exp(-S^0_{\text{eff}}) \equiv Z/Z_{(0)}. \tag{4.8}$$

As $Z^0_{\text{eff}} = Z^{-1}_{(0)} \int \mathcal{D}[\mathbf{b}^*_0]\mathcal{D}[\mathbf{b}_0] \exp(-S_0) \int \mathcal{D}_{(0)}[\mathbf{b}^*]\mathcal{D}_{(0)}[\mathbf{b}] \exp(-S_{(0)} - \Delta S)$ we introduce the cavity expectation value

$$\langle x \rangle_{(0)} = \frac{\int \mathcal{D}_{(0)}[\mathbf{b}^*]\mathcal{D}_{(0)}[\mathbf{b}] x \exp(-S_{(0)})}{Z_{(0)}}. \tag{4.9}$$

We thus find the following implicit definition of the effective action $S^0_{\text{eff}}$:

$$Z^0_{\text{eff}} = \int \mathcal{D}[\mathbf{b}^*_0]\mathcal{D}[\mathbf{b}_0] \exp(-S_0) \langle \exp(-\Delta S) \rangle_{(0)} \equiv \int \mathcal{D}[\mathbf{b}^*_0]\mathcal{D}[\mathbf{b}_0] \exp(-S^0_{\text{eff}}). \tag{4.10}$$

Defining $\exp(-y) \equiv \langle \exp(-\Delta S) \rangle_{(0)}$, we may explicitly write down the effective action as

$$S^0_{\text{eff}} = S_0 + y. \tag{4.11}$$

Due to the exponential function, $y$ is given as a series of cavity expectation values of $\Delta S$ in all its moments. This is commonly considered as an expansion in $1/z$ via a rescaled hopping $t_{ij}^{\sigma} \to \tilde{t}_{ij}^{\sigma}/z$ [SH13], where $z$ is the number of nearest neighbors. Such a rescaling guarantees retaining a non-trivial mean-field description in the infinite dimensional limit ($z \to \infty$). In a system with homogeneous hopping amplitudes $t_{ij}^{\sigma}$, its value can be computed from the hopping matrix as $z = \sum_{i\neq 0} t_{i0}^{\sigma}/\max_{i\neq 0}(t_{i0}^{\sigma})$. For the case of the long-range interaction this implies that we consider a similarly defined effective number of (nearest) neighbors $z_{\text{eff}} \equiv \sum_{i\neq 0} V_{\sigma}(i)/\max_{i\neq 0}(V_{\sigma}(i))$[2], when rescaling the interaction terms $V_{\sigma}(i) \to \tilde{V}_{\sigma}(i)/z_{\text{eff}}$. It also has a roughly linear scaling in terms of the spatial dimension $d$, as long as for $|\mathbf{r}_i - \mathbf{r}_0|/a > 1$ (with lattice spacing $a$), $V_{\sigma}(\mathbf{r}) \propto \mathbf{r}^{-(d+\varepsilon)}$, where $\varepsilon > 1$. The proper infinite dimensional limit $d \to \infty$ should thus be obtained by simultaneously keeping $\varepsilon$ fixed. For common infinite range interactions, such as dipolar or Van der Waals interactions, $z_{\text{eff}}$ is greater than $z$, as it is not limited to the nearest neighbors[3]. The expansion of $y$ up to third order in $\Delta S$ (and thus in according products of $1/z$ and $1/z_{\text{eff}}$) can be derived as follows.

$$\begin{aligned} y &= -\ln\langle e^{-\Delta S}\rangle_{(0)} = -\ln\left(1 - \sum_{k=1}^{\infty} \frac{\langle \Delta S^k\rangle_{(0)}(-1)^{k-1}}{k!}\right) \\ &= \langle \Delta S\rangle_{(0)} - \frac{\langle \Delta S^2\rangle_{(0)}}{2} + \frac{\langle \Delta S^3\rangle_{(0)}}{6} + \frac{\langle \Delta S\rangle_{(0)}^2}{2} - \frac{\langle \Delta S^2\rangle_{(0)}\langle \Delta S\rangle_{(0)}}{2} + \frac{\langle \Delta S\rangle_{(0)}^3}{3} + \mathcal{O}(\Delta S^4) \\ &= \langle \Delta S\rangle_{(0)} - \frac{1}{2}\left(\langle \Delta S^2\rangle_{(0)} - \langle \Delta S\rangle_{(0)}^2\right) \\ &\quad + \frac{1}{6}\left(\langle \Delta S^3\rangle_{(0)} - 3\langle \Delta S\rangle_{(0)}\langle \Delta S^2\rangle_{(0)} + 2\langle \Delta S\rangle_{(0)}^3\right) + \mathcal{O}(\Delta S^4) \end{aligned} \tag{4.12}$$

Here we have used $-ln(1-x) = \sum_{n=1}^{\infty} x^n/n$. Within the common B-DFMT cavity construction, one focuses on the low order correlation functions, as they contribute in leading orders of $1/z$ (and $1/z_{\text{eff}}$). These correspond to the first two terms in (4.12),

$$\langle \Delta S\rangle_{(0)} = \int_0^{\beta} d\tau \left( \sum_{\langle 0,i\rangle,\sigma} -\left(t_{0i}^{\sigma} b_{0\sigma}^{*}\langle b_{i\sigma}\rangle_{(0)} + c.c.\right) + \sum_{i\neq 0,\sigma} V_{\sigma}(i)\langle n_{i\sigma}\rangle_{(0)} n_{0\sigma} \right). \tag{4.13}$$

For convenience in writing down higher order terms, we combine all components in a vector, so for the $N$ components $\sigma = 1,\ldots,N$ we write $\mathbf{b}_i = (b_{i0},\ldots,b_{iN})$ and use Nambu notation.

$$\begin{aligned} \langle \Delta S^2\rangle_{(0)} - \langle \Delta S\rangle_{(0)}^2 = \int_0^{\beta} d\tau \int_0^{\beta} d\eta \Big( &\left(\mathbf{b}_0^{*}(\tau)\,\mathbf{b}_0(\tau)\right)\mathbf{M}(\tau,\eta)\left(\mathbf{b}_0(\eta)\,\mathbf{b}_0^{*}(\eta)\right)^T \\ &+ \left(\mathbf{b}_0^{*}(\tau)\,\mathbf{n}_0(\tau)\right)\mathbf{F}(\tau,\eta)\left(\mathbf{b}_0(\eta)\,\mathbf{n}_0(\eta)\right)^T \Big) \end{aligned} \tag{4.14}$$

Here we have introduced the $2N \times 2N$ matrices $\mathbf{M}(\tau,\eta)$ and $\mathbf{F}(\tau,\eta)$. In terms of the various bosonic species $(\sigma,\gamma)$, these matrices have the following entries in Nambu notation:

[2] Strong long-range interactions tend to enhance mean-field like behavior, as can be seen in the dimensional scaling of $z_{\text{eff}}$ as discussed in App. B for various relevant cases of interaction potentials.

[3] Note, that the use of dipolar interactions also implies $d < 3$, for such a scaling to work, see App. B.

$$
\begin{aligned}
M_{11}^{\sigma\gamma}(\tau,\eta) &= \sum_{i,j} t_{0i}^{\sigma} t_{0j}^{\gamma *} \left( \langle b_{i\sigma}(\tau) b_{j\gamma}^{*}(\eta) \rangle_{(0)} - \langle b_{i\sigma}(\tau) \rangle_{(0)} \langle b_{j\gamma}^{*}(\eta) \rangle_{(0)} \right), \\
M_{22}^{\sigma\gamma}(\tau,\eta) &= \sum_{i,j} t_{0i}^{\sigma *} t_{0j}^{\gamma} \left( \langle b_{i\sigma}^{*}(\tau) b_{j\gamma}(\eta) \rangle_{(0)} - \langle b_{i\sigma}^{*}(\tau) \rangle_{(0)} \langle b_{j\gamma}(\eta) \rangle_{(0)} \right), \\
M_{12}^{\sigma\gamma}(\tau,\eta) &= \sum_{i,j} t_{0i}^{\sigma} t_{0j}^{\gamma} \left( \langle b_{i\sigma}(\tau) b_{j\gamma}(\eta) \rangle_{(0)} - \langle b_{i\sigma}(\tau) \rangle_{(0)} \langle b_{j\gamma}(\eta) \rangle_{(0)} \right), \\
M_{21}^{\sigma\gamma}(\tau,\eta) &= \sum_{i,j} t_{0i}^{\sigma *} t_{0j}^{\gamma *} \left( \langle b_{i\sigma}^{*}(\tau) b_{j\gamma}^{*}(\eta) \rangle_{(0)} - \langle b_{i\sigma}^{*}(\tau) \rangle_{(0)} \langle b_{j\gamma}^{*}(\eta) \rangle_{(0)} \right).
\end{aligned}
\tag{4.15}
$$

The long-range interaction leads to additional contributions, which correspond to interaction vertices,

$$
\begin{aligned}
F_{11}^{\sigma\gamma}(\tau,\eta) &= 0, \\
F_{12}^{\sigma\gamma}(\tau,\eta) &= -2 \sum_{i\neq 0,j} V_{\sigma}(i) t_{0j}^{\gamma} \left( \langle n_{i\sigma}(\tau) b_{j\gamma}(\eta) \rangle_{(0)} - \langle n_{i\sigma}(\tau) \rangle_{(0)} \langle b_{j\gamma}(\eta) \rangle_{(0)} \right), \\
F_{21}^{\sigma\gamma}(\tau,\eta) &= -2 \sum_{i\neq 0,j} V_{\sigma}(i) t_{0j}^{\gamma *} \left( \langle n_{i\sigma}(\tau) b_{j\gamma}^{*}(\eta) \rangle_{(0)} - \langle n_{i\sigma}(\tau) \rangle_{(0)} \langle b_{j\gamma}^{*}(\eta) \rangle_{(0)} \right), \\
F_{22}^{\sigma\gamma}(\tau,\eta) &= \sum_{i\neq 0,j\neq 0} V_{\sigma}(i) V_{\gamma}(j) \left( \langle n_{i\sigma}(\tau) n_{j\gamma}(\eta) \rangle_{(0)} - \langle n_{i\sigma}(\tau) \rangle_{(0)} \langle n_{j\gamma}(\eta) \rangle_{(0)} \right).
\end{aligned}
\tag{4.16}
$$

In order to find a closed formulation, using only second order correlation functions[4] (i.e. second order in the number of field operators), we now have to introduce an approximation for (4.16). A common method is the Hartree ansatz[5]. In this approximation one replaces the occupation number (operators) for every site *except* site 0 by their expectation values $n_{j\sigma}(\eta) = \langle n_{j\sigma}(\eta) \rangle$. Correspondingly all terms (4.16) will vanish exactly.

The thus derived effective action (4.11) (via (4.5) and (4.12)) has a Hamiltonian representation $\hat{H}_{\mathrm{AIM}}^{\mathrm{eff}}$, which can be written as follows. Note that from here onwards we omit the site index for the local impurity site ($\hat{b}_{0\sigma} \to \hat{b}_{\sigma}$ and $\hat{n}_{0\sigma} \to \hat{n}_{\sigma}$), so

$$
\begin{aligned}
\hat{H}_{\mathrm{AIM}}^{\mathrm{eff}} = &- \sum_{\sigma} \mu_{\sigma} \hat{n}_{\sigma} + \sum_{\sigma\gamma} \frac{U_{\sigma\gamma}}{2} \hat{n}_{\sigma} \left( \hat{n}_{\gamma} - \delta_{\sigma,\gamma} \right) + \frac{\Omega}{2} \left( \hat{b}_{g}^{\dagger} \hat{b}_{e} + \mathrm{h.c.} \right) \\
&+ \sum_{\sigma} \left[ \hat{n}_{\sigma} \sum_{i\neq 0} V(i) \langle \hat{n}_{i\sigma} \rangle_{(0)} - \left( \hat{b}_{\sigma}^{\dagger} \sum_{\langle 0,i \rangle} t_{0i}^{\sigma\sigma} \langle \hat{b}_{i\sigma} \rangle_{(0)} + \mathrm{h.c.} \right) \right] \\
&+ \underbrace{\sum_{l=1}^{L} \left( \epsilon_{l} \hat{a}_{l}^{\dagger} \hat{a}_{l} + \sum_{\sigma} \left( V_{l,\sigma} \hat{a}_{l}^{\dagger} \hat{b}_{\sigma} + V_{l,\sigma}^{*} \hat{a}_{l} \hat{b}_{\sigma}^{\dagger} + W_{l,\sigma} \hat{a}_{l} \hat{b}_{\sigma} + W_{l,\sigma}^{*} \hat{a}_{l}^{\dagger} \hat{b}_{\sigma}^{\dagger} \right) \right)}_{\hat{H}'_{\mathrm{AIM}}}.
\end{aligned}
\tag{4.17}
$$

Here we have introduced $L$ bath orbitals (in $\hat{H}'_{\mathrm{AIM}}$) with corresponding bosonic creation (annihilation) operators $\hat{a}_{l}^{\dagger}(\hat{a}_{l})$[6], as well as their energies $\epsilon_{l}$. They are coupled

[4] These correlation functions are the single-particle Green's functions, which we introduce in Sec. 4.3

[5] See App. A for considerations about the Hartree-Fock treatment, while the use of the Hartree method is motivated in Sec. 2.2.3.

[6] Note the absence of a spin degree of freedom $\sigma$. As the coupling terms $V$ and $W$ are determined self-consistently, it is left to the solver whether they only couple one or multiple bath orbitals to each spin component of the impurity, implicitly determining the spin structure of the bath orbitals.

to the impurity site via normal hopping amplitudes $V_{l,\sigma}$ and anomalous hopping amplitudes $W_{l,\sigma}$.

## 4.2 Hybridization functions

We will now show how the effective Anderson impurity Hamiltonian (4.17) reproduces the effective action (4.11) or more precisely the matrices (4.15). As all fields $b_{i\sigma}(\tau)$ and $a_l(\tau)$ are periodic in $\beta$, we now introduce their Fourier transforms, which works analogously for all complex fields $b_{i\sigma}(\tau)$ and $a_l(\tau)$:

$$a_{n,l} \equiv a_l(i\omega_n) = \int_0^\beta d\tau \exp(i\omega_n\tau) a_l(\tau) \qquad a_l(\tau) = \frac{1}{\beta}\sum_{n=-\infty}^{\infty} \exp(-i\omega_n\tau) a_{n,l}, \tag{4.18}$$

$$a^*_{n,l} \equiv a^*_l(i\omega_n) = \int_0^\beta d\tau \exp(-i\omega_n\tau) a^*_l(\tau) \qquad a^*_l(\tau) = \frac{1}{\beta}\sum_{n=-\infty}^{\infty} \exp(i\omega_n\tau) a^*_{n,l}. \tag{4.19}$$

Here we have also introduced the Matsubara frequencies $\omega_n = \frac{2\pi n}{\beta}$ (see e.g. Sec. 4.2 in [AS10]). Within this transformation let us now focus only on those contributions to the action generated by $\hat{H}'_{\mathrm{AIM}}$ in (4.17), which include the orbital fields $a_l(\tau)$ and $a_l(\tau)^*$ and call it $S'_{\mathrm{AIM}}$. In the following we have to complete the square in terms of the complex valued fields.

$$\begin{aligned} S'_{\mathrm{AIM}} =& \frac{1}{\beta}\sum_{l,n}\Bigg( (\epsilon_l - i\omega_n) a^*_{n,l} a_{n,l} \\ &\qquad + \sum_\sigma \left( V_{l,\sigma} a^*_{n,l} b_{n,\sigma} + V^*_{l,\sigma} a_{n,l} b^*_{n,\sigma} + W_{l,\sigma} a_{n,l} b_{-n,\sigma} + W^*_{l,\sigma} a^*_{n,l} b^*_{-n,\sigma} \right) \Bigg) \\ =& \frac{1}{\beta}\sum_{l,n}\left[ a^*_{n,l} + \sum_\sigma \left( \frac{V^*_{l,\sigma}}{\epsilon_l - i\omega_n} b^*_{n,\sigma} + \frac{W_{l,\sigma}}{\epsilon_l - i\omega_n} b_{-n,\sigma} \right) \right] \\ &\qquad (\epsilon_l - i\omega_n)\left[ a_{n,l} + \sum_\gamma \left( \frac{V_{l,\gamma}}{\epsilon_l - i\omega_n} b_{n,\gamma} + \frac{W^*_{l,\gamma}}{\epsilon_l - i\omega_n} b^*_{-n,\gamma} \right) \right] - X \end{aligned} \tag{4.20}$$

The remainder is incorporated into $X$, which we write in Nambu notation and has a form very similar to (4.14).,

$$X = \frac{1}{2\beta}\sum_n \sum_{\sigma,\gamma} \left( b^*_{n,\sigma} b_{-n,\sigma} \right) \begin{pmatrix} \Delta^{\sigma\gamma}_{11}(i\omega_n) & \Delta^{\sigma\gamma}_{12}(i\omega_n) \\ \Delta^{\sigma\gamma}_{21}(i\omega_n) & \Delta^{\sigma\gamma}_{22}(i\omega_n) \end{pmatrix} \begin{pmatrix} b_{n,\gamma} \\ b^*_{-n,\gamma} \end{pmatrix}. \tag{4.21}$$

Note the appearance of the prefactor $1/2$, which is due to double counting of the individual terms in this representation. We call the matrices $\boldsymbol{\Delta}^{\sigma\gamma}(i\omega_n)$ **hybridization** functions. Their individual terms $[\boldsymbol{\Delta}^{\sigma\gamma}(i\omega_n)]_{ij} = \Delta^{\sigma\gamma}_{ij}(i\omega_n)$ are given as

$$\begin{aligned}
\Delta_{11}^{\sigma\gamma}(i\omega_n) &= \sum_l \left( \frac{V_{l,\sigma}^* V_{l,\gamma}}{\epsilon_l - i\omega_n} + \frac{W_{l,\sigma}^* W_{l,\gamma}}{\epsilon_l + i\omega_n} \right), \\
\Delta_{22}^{\sigma\gamma}(i\omega_n) &= \sum_l \left( \frac{W_{l,\gamma}^* W_{l,\sigma}}{\epsilon_l - i\omega_n} + \frac{V_{l,\gamma}^* V_{l,\sigma}}{\epsilon_l + i\omega_n} \right), \\
\Delta_{12}^{\sigma\gamma}(i\omega_n) &= \sum_l \left( \frac{V_{l,\sigma}^* W_{l,\gamma}^*}{\epsilon_l - i\omega_n} + \frac{W_{l,\sigma}^* V_{l,\gamma}^*}{\epsilon_l + i\omega_n} \right), \\
\Delta_{21}^{\sigma\gamma}(i\omega_n) &= \sum_l \left( \frac{W_{l,\sigma} V_{l,\gamma}}{\epsilon_l - i\omega_n} + \frac{V_{l,\sigma} W_{l,\gamma}}{\epsilon_l + i\omega_n} \right).
\end{aligned} \tag{4.22}$$

In the next step one solves the path integrals over all bath fields $a_{n,l}$ and $a_{n,l}^*$ in the partition function. Due to (4.20) all those integrals are "generalized" Gaussian integrals, given in Matsubara frequencies where the action of a time independent Hamiltonian is diagonal. Thus, presuming properly normalized $\mathcal{D}[\mathbf{a}^*]\mathcal{D}[\mathbf{a}]$, they have the following form:

$$\int \mathcal{D}[\mathbf{a}^*]\mathcal{D}[\mathbf{a}] \exp(-\mathbf{a}^\dagger A \mathbf{a}) = \det A^{-1}. \tag{4.23}$$

The integrals therefore simply yield a constant factor in the partition function. So when self-consistency has been achieved, it will hold that $\mathbf{\Delta}^{\sigma\gamma}(i\omega_n) \equiv \mathbf{M}^{\sigma\gamma}(i\omega_n)$ and (4.20) will be an exact representation of (4.14) (including the prefactor $1/2$), while the first two lines of (4.17) obviously yield (4.5) and (4.13) respectively.

To show this let us explicitly consider the relation between the individual matrices $\mathbf{\Delta}^{\sigma\gamma}(i\omega_n)$ and $\mathbf{M}^{\sigma\gamma}(i\omega_n)$ (the Fourier transform of $\mathbf{M}^{\sigma\gamma}(\tau - \eta)$). From (4.18) and (4.19) it already follows that $\mathbf{M}(\tau, \eta) = \mathbf{M}(\tau - \eta)$. From the defining relations of $\mathbf{M}(\tau, \eta)$ in (4.15) we furthermore get the relations

$$M_{22}^{\sigma\gamma}(\tau - \eta) = M_{11}^{\sigma\gamma}(\tau - \eta)^*, \tag{4.24}$$
$$M_{22}^{\sigma\gamma}(\tau - \eta) = M_{11}^{\gamma\sigma}(\eta - \tau), \tag{4.25}$$
$$M_{21}^{\sigma\gamma}(\tau - \eta) = M_{12}^{\sigma\gamma}(\tau - \eta)^*, \tag{4.26}$$
$$M_{12}^{\sigma\gamma}(\tau - \eta) = M_{12}^{\gamma\sigma}(\eta - \tau). \tag{4.27}$$

Considering the Matsubara representation, while applying the Fourier transformations (4.18) and (4.19) (also for $\mathbf{M}(\tau - \eta)$, as it is periodic in $\beta$ in the same way the bosonic fields are), this yields

$$\int_0^\beta d\tau \int_0^\beta d\eta\, b^*_\sigma(\tau) M^{\sigma\gamma}_{11}(\tau-\eta) b_\gamma(\eta) =$$
$$= \int_0^\beta \int_0^\beta \frac{d\tau d\eta}{\beta^3} \sum_{n_1,n_2,n_3} e^{i\omega_{n_1}\tau - i\omega_{n_3}(\tau-\eta) - i\omega_{n_2}\eta} b^*_{\sigma n_1} M^{\sigma\gamma}_{11}(i\omega_{n_3}) b_{\gamma n_2}$$
$$= \frac{1}{\beta}\sum_n b^*_{\sigma n} M^{\sigma\gamma}_{11}(i\omega_n) b_{\gamma n}, \tag{4.28}$$

$$\int_0^\beta d\tau \int_0^\beta d\eta\, b_\sigma(\tau) M^{\sigma\gamma}_{22}(\tau-\eta) b^*_\gamma(\eta) = \int_0^\beta d\tau \int_0^\beta d\eta\, b_\sigma(\tau) M^{\sigma\gamma}_{11}(\eta-\tau)^* b^*_\gamma(\eta)$$
$$= \frac{1}{\beta}\sum_n b^*_{\sigma n} M^{\sigma\gamma}_{11}(i\omega_n)^* b_{\gamma n}, \tag{4.29}$$

$$\int_0^\beta d\tau \int_0^\beta d\eta\, b^*_\sigma(\tau) M^{\sigma\gamma}_{12}(\tau-\eta) b^*_\gamma(\eta) = \frac{1}{\beta}\sum_n b^*_{\sigma n} M^{\sigma\gamma}_{12}(i\omega_n) b^*_{\gamma -n}, \tag{4.30}$$

$$\int_0^\beta d\tau \int_0^\beta d\eta\, b_\sigma(\tau) M^{\sigma\gamma}_{21}(\tau-\eta) b_\gamma(\eta) = \frac{1}{\beta}\sum_n b_{\sigma n} M^{\sigma\gamma}_{12}(i\omega_n)^* b_{\gamma -n}. \tag{4.31}$$

Accordingly we can translate the aforementioned relations to the Matsubara frequencies,

$$M^{\sigma\gamma}_{22}(i\omega_n) = M^{\sigma\gamma}_{11}(i\omega_n)^* \quad \longleftrightarrow \quad \Delta^{\sigma\gamma}_{22}(i\omega_n) = \Delta^{\sigma\gamma}_{11}(i\omega_n)^*, \tag{4.32}$$
$$M^{\sigma\gamma}_{22}(i\omega_n) = M^{\gamma\sigma}_{11}(-i\omega_n) \quad \longleftrightarrow \quad \Delta^{\sigma\gamma}_{22}(i\omega_n) = \Delta^{\gamma\sigma}_{11}(-i\omega_n), \tag{4.33}$$
$$M^{\sigma\gamma}_{21}(i\omega_n) = M^{\sigma\gamma}_{12}(i\omega_n)^* \quad \longleftrightarrow \quad \Delta^{\sigma\gamma}_{21}(i\omega_n) = \Delta^{\sigma\gamma}_{12}(i\omega_n)^*, \tag{4.34}$$
$$M^{\sigma\gamma}_{12}(i\omega_n) = M^{\gamma\sigma}_{12}(-i\omega_n) \quad \longleftrightarrow \quad \Delta^{\sigma\gamma}_{12}(i\omega_n) = \Delta^{\gamma\sigma}_{12}(-i\omega_n). \tag{4.35}$$

When compared to (4.22), it is immediately apparent that all these relations are mirrored by the hybridisation functions. Therefore the comparison of (4.21) to (4.14) implies that after self-consistency has been reached, we will indeed find $\mathbf{\Delta}^{\sigma\gamma}(i\omega_n) \equiv \mathbf{M}^{\sigma\gamma}(i\omega_n)$.

### 4.2.1 Bosonic correction of the condensate order parameter

So far we have seen, that one may tackle a lattice system with strong (local) correlations, as given by (4.1), in terms of local impurity Hamiltonians (4.17). In this representation some special care has to be taken, due to the required cavity expectation values $\langle\cdot\rangle_{(0)}$. This expectation value is especially relevant for the condensate order parameter in the neighborhood of the 0-site, which we aim to transform to an effective Anderson type impurity model. But as the cavity system is missing a neighboring site at those very sites, one might expect a substantial deviation of the cavity expectation from its regular expectation value. Let us thus explicitly derive the cavity expectation value of the condensate order parameter of such a site, in order to determine the relation to its full expectation value.

$$
\begin{aligned}
Z^0_{\text{eff}}[J_{j\gamma}, J^*_{j\gamma}] &= \frac{Z[J_{j\gamma}, J^*_{j\gamma}]}{Z_{(0)}} \\
&= \int \frac{\mathcal{D}[\mathbf{b}^*]\mathcal{D}[\mathbf{b}]}{Z_{(0)}} \exp\left(-S[\mathbf{b}^*, \mathbf{b}] + \int d\tau (b^*_{j\gamma}(\tau) J_{j\gamma}(\tau) + b_{j\gamma}(\tau) J^*_{j\gamma}(\tau))\right) \\
&= \int \mathcal{D}[\mathbf{b}^*_0]\mathcal{D}[\mathbf{b}_0] \exp(-S_0 - y[J_{j\gamma}, J^*_{j\gamma}])
\end{aligned} \tag{4.36}
$$

First we start by generalizing the partition function (using (4.7) and (4.8)) to a generating functional, by introducing source fields $S_J = \int d\tau (b^*_{j\gamma} J_{j\gamma} + b_{j\gamma} J^*_{j\gamma})$ as shown above, so we may derive the expectation value in the cavity system as follows. Note that in the case of self-consistency, one can compute local expectation values using the effective action (4.8).

$$
\begin{aligned}
\langle b_{j\gamma}(\eta)\rangle &= \left.\frac{\delta \ln Z[J_{j\gamma}, J^*_{j\gamma}]}{\delta J^*_{j\gamma}(\eta)}\right|_{J^*_{j\gamma}, J_{j\gamma}\to 0} = \left.\frac{\delta \ln Z^0_{\text{eff}}[J_{j\gamma}, J^*_{j\gamma}]}{\delta J^*_{j\gamma}(\eta)}\right|_{J^*_{j\gamma}, J_{j\gamma}\to 0} \\
&= -\int \mathcal{D}[\mathbf{b}^*_0]\mathcal{D}[\mathbf{b}_0] \frac{\exp(-S_0 - y[0,0])}{Z^0_{\text{eff}}} \left.\frac{\delta y[J_{j\gamma}, J^*_{j\gamma}]}{\delta J^*_{j\gamma}(\eta)}\right|_{J^*_{j\gamma}, J_{j\gamma}\to 0} \\
&= -\left\langle \left.\frac{\delta y[J_{j\gamma}, J^*_{j\gamma}]}{\delta J^*_{j\gamma}(\eta)}\right|_{J^*_{j\gamma}, J_{j\gamma}\to 0} \right\rangle_0
\end{aligned} \tag{4.37}
$$

In the last line we have used that for $J^*_{j\gamma}, J_{j\gamma} \to 0, y[J_{j\gamma}, J^*_{j\gamma}] \to y$, so we may directly use the impurity expectation value $\langle\cdot\rangle_0$, defined as

$$
\langle x\rangle_0 = \frac{\int \mathcal{D}[\mathbf{b}^*_0]\mathcal{D}[\mathbf{b}_0] x \exp(-S^0_{\text{eff}})}{Z^0_{\text{eff}}}. \tag{4.38}
$$

Similar to (4.12) we now also expand $y[J_{j\gamma}, J^*_{j\gamma}]$ up to second order in either of its defining terms.

$$
\begin{aligned}
y[J^*_{j\gamma}, J_{j\gamma}] =& -\ln\langle \exp\left(-\Delta S + S_J\right)\rangle_{(0)} \\
=& \langle \Delta S\rangle_{(0)} - \langle S_J\rangle_{(0)} - \frac{1}{2}\left(\langle(\Delta S - S_J)^2\rangle_{(0)} - \langle \Delta S - S_J\rangle^2_{(0)}\right) + \dots \\
=& \langle \Delta S\rangle_{(0)} - \langle S_J\rangle_{(0)} - \frac{1}{2}\Bigg(\langle \Delta S^2\rangle_{(0)} - 2\langle \Delta S S_J\rangle_{(0)} + \underbrace{\langle S^2_J\rangle_{(0)}}_{\to 0} \\
& - \langle \Delta S\rangle^2_{(0)} + 2\langle \Delta S\rangle_{(0)}\langle S_J\rangle_{(0)} - \underbrace{\langle S_J\rangle^2_{(0)}}_{\to 0}\Bigg) + \dots \\
=& y - \langle S_J\rangle_{(0)} + \left(\langle \Delta S S_J\rangle_{(0)} - \langle \Delta S\rangle_{(0)}\langle S_J\rangle_{(0)}\right) + \dots
\end{aligned} \tag{4.39}
$$

Note that all but the terms of linear order in $S_J$ will give a vanishing contribution in (4.37), so we may neglect the indicated terms. The thus remaining relevant terms are given as

$$\langle S_J\rangle_{(0)} = \int_0^\beta d\tau \left(\langle b^*_{j\gamma}\rangle_{(0)} J_{j\gamma}(\tau) + \langle b_{j\gamma}\rangle_{(0)} J^*_{j\gamma}(\tau)\right), \tag{4.40}$$

$$\begin{aligned}\langle \Delta S S_J\rangle_{(0)} = \int_0^\beta \int_0^\beta d\tau d\eta \Big\langle &- \sum_{\langle 0,i\rangle,\sigma} \left(t^\sigma_{0i} b^*_{0\sigma}(\tau) b_{i\sigma}(\tau) + \text{c.c.}\right)\left(b^*_{j\gamma}(\eta) J_{j\gamma}(\eta) + \text{c.c.}\right) \\ &+ \sum_{i\neq 0,\sigma} V_\sigma(i) n_{0\sigma}(\tau) n_{i\sigma}(\tau)\left(b^*_{j\gamma}(\eta) J_{j\gamma}(\eta) + \text{c.c.}\right)\Big\rangle_{(0)}.\end{aligned} \tag{4.41}$$

When computing (4.37), only terms linear in $J^*_{j\gamma}$ need to be considered. Thus we can derive the following relation.

$$\begin{aligned}\langle b_{j\gamma}(\eta)\rangle &= \left\langle \left( \frac{\delta\langle S_J\rangle_{(0)}}{\delta J^*_{j\gamma}(\eta)} - \frac{\delta}{\delta J^*_{j\gamma}(\eta)} \left(\langle \Delta S S_J\rangle_{(0)} - \langle \Delta S\rangle_{(0)}\langle S_J\rangle_{(0)}\right)\right)\Big|_{J^*_{j\gamma}, J_{j\gamma}\to 0}\right\rangle_0 \\
&= \langle b_{j\gamma}\rangle_{(0)} \\
&\quad + \sum_{\langle 0,i\rangle,\sigma} \int_0^\beta d\tau \left(t^\sigma_{0i}\langle b^*_{0\sigma}(\tau)\rangle_0 \langle b_{i\sigma}(\tau) b_{j\gamma}(\eta)\rangle_{(0)} + t^{\sigma *}_{0i}\langle b_{0\sigma}(\tau)\rangle_0 \langle b^*_{i\sigma}(\tau) b_{j\gamma}(\eta)\rangle_{(0)}\right) \\
&\quad - \sum_{\langle 0,i\rangle,\sigma} \int_0^\beta d\tau \left(t^\sigma_{0i}\langle b^*_{0\sigma}(\tau)\rangle_0 \langle b_{i\sigma}(\tau)\rangle_{(0)} + t^{\sigma *}_{0i}\langle b_{0\sigma}(\tau)\rangle_0 \langle b^*_{i\sigma}(\tau)\rangle_{(0)}\right)\langle b_{j\gamma}(\eta)\rangle_{(0)} \\
&\quad - \sum_{i\neq 0,\sigma} \int_0^\beta d\tau V_\sigma(i)\langle n_{0\sigma}(\tau)\rangle_0 \left(\langle n_{i\sigma}(\tau) b_{j\gamma}(\eta)\rangle_{(0)} - \langle n_{i\sigma}(\tau)\rangle_{(0)}\langle b_{j\gamma}(\eta)\rangle_{(0)}\right) \\
&= \langle b_{j\gamma}\rangle_{(0)} \\
&\quad + \sum_{\langle 0,i\rangle,\sigma} \int_0^\beta d\tau \Big(t^\sigma_{0i}\langle b^*_{0\sigma}(\tau)\rangle_0 \left[\langle b_{i\sigma}(\tau) b_{j\gamma}(\eta)\rangle_{(0)} - \langle b_{i\sigma}(\tau)\rangle_{(0)}\langle b_{j\gamma}(\eta)\rangle_{(0)}\right] \\
&\qquad\qquad + t^{\sigma *}_{0i}\langle b_{0\sigma}(\tau)\rangle_0 \left[\langle b^*_{i\sigma}(\tau) b_{j\gamma}(\eta)\rangle_{(0)} - \langle b^*_{i\sigma}(\tau)\rangle_{(0)}\langle b_{j\gamma}(\eta)\rangle_{(0)}\right]\Big) \\
&\quad - \sum_{i\neq 0,\sigma} \int_0^\beta d\tau V_\sigma(i)\langle n_{0\sigma}(\tau)\rangle_0 \left[\langle n_{i\sigma}(\tau) b_{j\gamma}(\eta)\rangle_{(0)} - \langle n_{i\sigma}(\tau)\rangle_{(0)}\langle b_{j\gamma}(\eta)\rangle_{(0)}\right]\end{aligned} \tag{4.42}$$

This expression can be simplified by including the sum of all nearest neighbors of the extracted impurity site multiplied by the corresponding hopping amplitudes, as needed for (4.17) while using (4.15) and (4.16):

$$\begin{aligned}\sum_j t^\gamma_{0j}\langle b_{j\gamma}\rangle &= \sum_j t^\gamma_{0j}\langle b_{j\gamma}\rangle_{(0)} \\
&\quad + \sum_\sigma \int_0^\beta d\tau \left(\phi^*_{0\sigma} M^{\sigma\gamma}_{12}(\tau,\eta) + \phi_{0\sigma} M^{\sigma\gamma}_{22}(\tau,\eta) + \frac{n_{0\sigma}}{2} F^{\sigma\gamma}_{12}(\tau,\eta)\right) \\
&= \sum_j t^\gamma_{0j}\langle b_{j\gamma}\rangle_{(0)} + \sum_\sigma \left(\phi^*_{0\sigma} M^{\sigma\gamma}_{12}(i\omega_n = 0) + \phi_{0\sigma} M^{\sigma\gamma}_{22}(0) + \frac{n_{0\sigma}}{2} F^{\sigma\gamma}_{12}(0)\right).\end{aligned} \tag{4.43}$$

Here we have introduced the impurity condensate order parameters $\phi^*_{0\sigma} \equiv \langle b^*_{0\sigma}\rangle_0$ and $\phi_{0\sigma} \equiv \langle b_{0\sigma}\rangle_0$ as well as the impurity occupation number $n_{0\sigma} \equiv \langle b^*_{0\sigma} b_{0\sigma}\rangle_0$, all of which

are independent of the imaginary time $\eta$ for the time independent Hamiltonian. This is of course equally true for the expression $\sum_j t_{0j}^{\gamma}\langle b_{j\gamma}\rangle_{(0)}$. If the Hamiltonian also describes a homogeneous lattice, we have $t_{ij}^{\gamma} = t^{\gamma}$ and can simply solve for the total cavity condensates of all NN sites. For a converged self-consistent impurity model $\langle b_{j\gamma}\rangle = \phi_{j\gamma}$. Once again the last term of (4.43) vanishes in the Hartree limit, while it would be retained in a Hartree-Fock type treatment. We note that due to the integral over the whole period, all integral expressions yield the Fourier transformed values at $n = 0$, so at $\omega_n = 0$, and are thus independent of $\eta$. Furthermore one can obtain a similar relation to (4.43) for $b_{j\gamma}^*$ by taking the functional derivative with regard to $J_{j\gamma}$ instead. But as the results are simply related by a complex conjugation, the derivation can be omitted.

### 4.2.2 Bosonic correction of the local occupation number

On the other hand, a similar treatment of the occupation number leads to corresponding correction terms for its cavity expectation value in relation to its full expectation value. Again we first generalise the partition function to a generating functional, but this time in a way to extract occupation numbers instead, by introducing the source fields $S_N = \int d\tau b_{i\sigma}^* b_{i\sigma} N_{i\sigma}$.

$$\begin{aligned} Z_{\text{eff}}^0[N_{i\sigma}] &= \frac{Z[N_{i\sigma}]}{Z_{(0)}} \\ &= \frac{1}{Z_{(0)}} \int \mathcal{D}[\mathbf{b}^*]\mathcal{D}[\mathbf{b}] \exp\left(-S[\mathbf{b}^*,\mathbf{b}] + \int d\tau b_{i\sigma}^*(\tau) b_{i\sigma}(\tau) N_{i\sigma}(\tau)\right) \\ &= \int \mathcal{D}[\mathbf{b}_0^*]\mathcal{D}[\mathbf{b}_0] \exp(-S_0 - y[N_{i\sigma}]) \end{aligned} \tag{4.44}$$

The occupation number, as another local observable, can again be computed in the effective action when self-consistency has been reached.

$$\begin{aligned} \langle n_{i\sigma}(\tau)\rangle &= \left.\frac{\delta \ln Z[N_{i\sigma}]}{\delta N_{i\sigma}^*(\tau)}\right|_{N_{i\sigma}\to 0} = \left.\frac{\delta \ln Z_{\text{eff}}^0[N_{i\sigma}]}{\delta N_{i\sigma}(\tau)}\right|_{N_{i\sigma}\to 0} \\ &= -\int \mathcal{D}[\mathbf{b}_0^*]\mathcal{D}[\mathbf{b}_0] \frac{\exp(-S_0 - y[0])}{Z_{\text{eff}}^0} \left.\frac{\delta y[N_{i\sigma}]}{\delta N_{i\sigma}(\tau)}\right|_{N_{i\sigma}\to 0} \\ &= -\left\langle \left.\frac{\delta y[N_{i\sigma}]}{\delta N_{i\sigma}(\tau)}\right|_{N_{i\sigma}\to 0} \right\rangle_0 \end{aligned} \tag{4.45}$$

In the last line we have used, that for $N_{i\sigma} \to 0, y[N_{i\sigma}] \to y$, so we may once more use the impurity expectation value (4.38). Again we expand $y[N_{i\sigma}]$ up to second order in either of its defining terms.

$$\begin{aligned} y[N_{i\sigma}] &= -\ln\langle \exp\left(-\Delta S + S_N\right)\rangle_{(0)} \\ &\vdots \\ &= y - \langle S_N\rangle_{(0)} + \left(\langle \Delta S S_N\rangle_{(0)} - \langle \Delta S\rangle_{(0)}\langle S_N\rangle_{(0)}\right) + \dots \end{aligned} \tag{4.46}$$

Note that once more all but the terms of linear order in $S_N$ will give a vanishing contribution in (4.45). Using the notation $n_{i\sigma}(\eta) = b_{i\sigma}^*(\eta) b_{i\sigma}(\eta)$, the relevant terms are given as

$$\langle S_N\rangle_{(0)} = \int_0^\beta d\tau \langle n_{i\sigma}\rangle_{(0)} N_{i\sigma}(\tau), \tag{4.47}$$

$$\begin{aligned}\langle \Delta S S_N\rangle_{(0)} = \int_0^\beta \int_0^\beta d\tau d\eta \Bigg\langle &- \sum_{\langle 0,j\rangle,\gamma} \left(t_{0j}^\gamma b_{0\gamma}^*(\tau) b_{j\gamma}(\tau) + \text{c.c.}\right) n_{i\sigma}(\eta) N_{i\sigma}(\eta) \\ &+ \sum_{j\neq 0,\gamma} V_\gamma(j) n_{0\gamma}(\tau) n_{j\gamma}(\tau) n_{i\sigma}(\eta) N_{i\sigma}(\eta)\Bigg\rangle_{(0)}.\end{aligned} \tag{4.48}$$

When computing (4.45), only terms of linear order in $N_{i\sigma}$ need to be considered. Thus we derive the following relation.

$$\begin{aligned}\langle n_{i\sigma}(\tau)\rangle =& \left\langle \left( \frac{\delta\langle S_N\rangle_{(0)}}{\delta N_{i\sigma}(\tau)} - \frac{\delta}{\delta N_{i\sigma}(\tau)} \left( \langle \Delta S S_N\rangle_{(0)} - \langle \Delta S\rangle_{(0)} \langle S_N\rangle_{(0)} \right) \right) \Bigg|_{N_{i\sigma}\to 0} \right\rangle_0 \\ =& \langle n_{i\sigma}\rangle_{(0)} \\ &+ \sum_{\langle 0,j\rangle,\gamma} \int_0^\beta d\eta \Big( t_{0j}^\gamma \langle b_{0\gamma}^*(\eta)\rangle_0 \left[ \langle b_{j\gamma}(\eta) n_{i\sigma}(\tau)\rangle_{(0)} - \langle b_{j\gamma}(\eta)\rangle_{(0)} \langle n_{i\sigma}(\tau)\rangle_{(0)} \right] \\ &\qquad + t_{0j}^{\gamma *} \langle b_{0\gamma}(\eta)\rangle_0 \left[ \langle b_{j\gamma}^*(\eta) n_{i\sigma}(\tau)\rangle_{(0)} - \langle b_{j\gamma}^*(\eta)\rangle_{(0)} \langle n_{i\sigma}(\tau)\rangle_{(0)} \right] \Big) \\ &- \sum_{j\neq 0,\gamma} \int_0^\beta d\eta V_\gamma(j) \langle n_{0\gamma}(\eta)\rangle_0 \left[ \langle n_{j\gamma}(\eta) n_{i\sigma}(\tau)\rangle_{(0)} - \langle n_{j\gamma}(\eta)\rangle_{(0)} \langle n_{i\sigma}(\tau)\rangle_{(0)} \right]\end{aligned} \tag{4.49}$$

This expression can be simplified in analogy to (4.43) by considering the interaction term of the Hamiltonian for the impurity site 0 with the rest of the system, as required in (4.17) while using (4.16):

$$\begin{aligned}\sum_{i\neq 0} V_\sigma(i) \langle n_{i\sigma}\rangle =& \sum_{i\neq 0} V_\sigma(i) \langle b_{i\sigma}\rangle_{(0)} \\ &- \sum_\gamma \int_0^\beta d\tau \left( n_{0\gamma} F_{22}^{\sigma\gamma}(\tau,\eta) + \frac{\phi_{0\gamma}^*}{2} F_{12}^{\sigma\gamma}(\tau,\eta) + \frac{\phi_{0\gamma}}{2} F_{21}^{\sigma\gamma}(\tau,\eta) \right) \\ =& \sum_{i\neq 0} V_\sigma(i) \langle n_{i\sigma}\rangle_{(0)} - \sum_\gamma \left( n_{0\gamma} F_{22}^{\sigma\gamma}(i\omega_n = 0) + \frac{\phi_{0\gamma}^*}{2} F_{12}^{\sigma\gamma}(0) + \frac{\phi_{0\gamma}}{2} F_{21}^{\sigma\gamma}(0) \right).\end{aligned} \tag{4.50}$$

This time we can see that all correction terms stem from (4.16), which we neglect in a Hartree approximation, meaning that *no corrections* of the occupation number will be considered in our case, as we use a Hartree treatment. Also note that $\langle n_{i\sigma}\rangle = n_{i\sigma}$ for a converged self-consistent impurity model.

## 4.3 Green's functions

In this section we shortly introduce some basics of the many-body Green's function formalism with a focus on single-particle (also called two-point) Green's functions, as these are most relevant for the DMFT method. Given a quantum mechanical

system described by a grand canonical Hamiltonian (e.g. (4.1) or (4.17)), the single-particle or (more precisely) two-point causal Green's function in imaginary time for any two field operators $\hat{a}$ and $\hat{b}$ is defined as

$$G(\tau,\eta) = -\langle \mathcal{T}_{\tau,\eta}\{\hat{a}(\tau)\hat{b}(\eta)\}\rangle = -\theta(\tau-\eta)\langle \hat{a}(\tau)\hat{b}(\eta)\rangle - \theta(\eta-\tau)\langle \hat{b}(\eta)\hat{a}(\tau)\rangle. \tag{4.51}$$

Here we have introduced the time ordering operator $\mathcal{T}_{\tau,\eta}$, which specifies that all field operators following it have to be reordered, such that their times increase from right to left[7]. Regarding the time dependence of the field operators, note that their time evolution is given similar to the definition of the Heisenberg picture:

$$\hat{a}(\tau) = \exp(\tau\hat{H})\hat{a}\exp(-\tau\hat{H}), \quad \tau \in [-\beta,\beta]. \tag{4.52}$$

They are thus defined via the grand-canonical Hamiltonian $\hat{H}$. Furthermore, note that the imaginary-time creation operator is not simply the Hermitian conjugate of the annihilation operator, as

$$(\hat{a}(\tau))^\dagger = \hat{a}^\dagger(-\tau) \neq \hat{a}^\dagger(\tau). \tag{4.53}$$

Finally the Green's functions are defined in terms of a quantum mechanical thermal expectation value, which for a given observable $\hat{O}$ is defined by

$$\langle \hat{O}\rangle = \frac{1}{Z}\mathrm{Tr}\left(\exp(-\beta\hat{H})\hat{O}\right), \quad Z = \mathrm{Tr}\left(\exp(-\beta\hat{H})\right). \tag{4.54}$$

For a time–independent Hamiltonian, it holds that $G(\tau,\eta) \equiv G(\tau-\eta)$. So assuming $\tau > \eta$ without loss of generality, this can be shown as follows.

$$\begin{aligned} G(\tau,\eta) = -\langle \hat{b}(\tau)\hat{a}(\eta)\rangle &= -\frac{1}{Z}\mathrm{Tr}\left(\exp(-\beta\hat{H})\exp(\tau\hat{H})\hat{b}\exp(-\tau\hat{H})\exp(\eta\hat{H})\hat{a}\exp(-\eta\hat{H})\right) \\ &= -\frac{1}{Z}\mathrm{Tr}\left(\exp(-\beta\hat{H})\exp((\tau-\eta)\hat{H})\hat{b}\exp(-(\tau-\eta)\hat{H})\hat{a}\right) \\ &= -\langle \hat{b}(\tau-\eta)\hat{a}(0)\rangle = G(\tau-\eta,0) \equiv G(\tau-\eta) \end{aligned} \tag{4.55}$$

Furthermore one can show that $G(\tau-\eta)$ is periodic in $\beta$ thus limiting the relevant interval to $\tau-\eta \in [-\beta,\beta]$. Here we also allow for negative values, in order for the time ordering operator to be able to lead to both possible orders of the field operators. However we will show, that periodicity allows us to trivially take into account what happens for $\tau < 0$ via complex conjugation. To show the periodicity we may assume that $-\beta < \tau < 0$ in the following derivation.

[7] For two times only, one can easily define it in terms of the Heaviside step function $\theta(\tau)$, so $\mathcal{T}_{\tau,\eta}\{\hat{a}(\tau)\hat{b}(\eta)\} \equiv \theta(\tau-\eta)\hat{a}(\tau)\hat{b}(\eta) + \theta(\eta-\tau)\hat{b}(\eta)\hat{a}(\tau)$

$$\begin{aligned} G(\tau) = -\langle \hat{b}(0)\hat{a}(\tau)\rangle &= -\frac{1}{Z}\mathrm{Tr}\left(\exp(-\beta\hat{H})\hat{b}\exp(\tau\hat{H})\hat{a}\exp(-\tau\hat{H})\right) \\ &= -\frac{1}{Z}\mathrm{Tr}\left(\exp(-\beta\hat{H})\exp((\tau+\beta)\hat{H})\hat{a}\exp(-(\beta+\tau)\hat{H})\hat{b}\right) \\ &= -\langle \hat{a}(\tau+\beta)\hat{b}(0)\rangle = G(\tau+\beta) \end{aligned} \tag{4.56}$$

Thus the periodicity stems from the cyclic property of the trace. For the case $0 < \tau < \beta$ one can repeat the above derivation and show the similar property

$$G(\tau-\beta) = G(\tau). \tag{4.57}$$

Note however that for $\tau > 0$ one in general has $G(\tau+\beta) \neq G(\tau)$, but as we never need this part of the function, we may restrict ourselves to the interval $[-\beta, \beta]$. Due to this $\beta$ periodicity (which is specific to bosonic systems[8]), one can decompose the Green's functions via a Fourier transformation onto the discrete set of bosonic Matsubara frequencies $\omega_n$, which guarantees the shown periodic property:

$$G(i\omega_n) = \int_0^\beta d\tau \exp(i\omega_n\tau)G(\tau), \quad \omega_n = \frac{2\pi n}{\beta}, \quad n \in \mathbb{Z}. \tag{4.58}$$

Using this transformation let us now derive the Lehmann representation of the bosonic single-particle Green's functions[9]. Here it is useful to introduce the eigenbasis $\{|n\rangle\}$ of the given Hamiltonian $\hat{H}$, so $\hat{H}|n\rangle = E_n|n\rangle$, which yields a representation of the identity operator $\mathbb{1} = \sum_m |m\rangle\langle m|$.

$$\begin{aligned} G(i\omega_n) &= -\frac{1}{Z}\int_0^\beta d\tau \exp(i\omega_n\tau)\mathrm{Tr}\left(\exp(-\beta\hat{H})\exp(\tau\hat{H})\hat{a}\exp(-\tau\hat{H})\hat{b}\right) \\ &= -\frac{1}{Z}\sum_{m,m'}\int_0^\beta d\tau \exp((i\omega_n + E_{m'} - E_m)\tau)\exp(-\beta E_{m'})\langle m'|\hat{a}|m\rangle\langle m|\hat{b}|m'\rangle \\ &= -\frac{1}{Z}\sum_{m,m'}\frac{\exp(-\beta E_{m'}) - \exp(-\beta E_m)}{E_{m'} - E_m + i\omega_n}\langle m'|\hat{a}|m\rangle\langle m|\hat{b}|m'\rangle \\ &= \frac{1}{Z}\sum_{m,m'}\frac{\exp(\beta(E_{m'} - E_m)) - 1}{E_{m'} - E_m + i\omega_n}\exp(-\beta E_{m'})\langle m'|\hat{a}|m\rangle\langle m|\hat{b}|m'\rangle \end{aligned} \tag{4.59}$$

In the second to last step we have used $\exp(i\omega_n\beta) = \exp(i2n\pi) = 1$, which applies due to the Matsubara frequencies. As we will be using Nambu notation and have $N$ bosonic species (denoted by the Greek letters $\sigma, \gamma$) in the considered system, any local Green's function will be a $2N \times 2N$ matrix, which can be decomposed into the $2 \times 2$ Nambu matrices

$$\mathbf{G}^{\sigma\gamma}(\tau) = -\left\langle T_{\tau,0}\begin{pmatrix} \hat{b}_\sigma(\tau)\hat{b}^\dagger_\gamma(0) & \hat{b}_\sigma(\tau)\hat{b}_\gamma(0) \\ \hat{b}^\dagger_\sigma(\tau)\hat{b}^\dagger_\gamma(0) & \hat{b}^\dagger_\sigma(\tau)\hat{b}_\gamma(0) \end{pmatrix}\right\rangle. \tag{4.60}$$

[8] For fermionic systems on additionally gets a minus sign due to the anticommutator, so $G_{\text{fermion}}(\tau) = -G_{\text{fermion}}(\tau+\beta)$

[9] Note that one obtains the connected Green's function from this by removing the disconnected part (see Sec. 4.3.1) from the zero frequency part. In the zero temperature limit this can also be achieved by omitting the diagonal terms at zero frequency, when computing the Lehmann representation.

The diagonal entries are commonly referred to as the normal Green's functions ($G^n$), while the off diagonal terms are the anomalous Green's functions ($G^a$), which are related to superfluid behavior. Keeping (4.53) in mind, one can easily verify the relations

$$\begin{aligned} G_{11}^{\sigma\gamma}(\tau) &= G_{11}^{\gamma\sigma *}(\tau) \qquad & G_{11}^{\sigma\gamma}(\tau) &= G_{22}^{\gamma\sigma}(-\tau), \\ G_{12}^{\sigma\gamma}(\tau) &= G_{21}^{\gamma\sigma *}(\tau) \qquad & G_{12}^{\sigma\gamma}(\tau) &= G_{12}^{\gamma\sigma}(-\tau). \end{aligned} \tag{4.61}$$

For completeness let us briefly consider the derivation of one of these relations, namely $G_{12}^{\sigma\gamma}(\tau) = G_{21}^{\gamma\sigma *}(\tau)$. Without loss of generality we may assume $\tau > 0$ in the following derivation.

$$\begin{aligned} G_{12}^{\sigma\gamma *}(\tau) &= -\langle \mathcal{T}_{\tau,0}\{b_\sigma(\tau) b_\gamma(0)\}\rangle^* \\ &= -\langle b_\gamma^\dagger(-0) b_\sigma^\dagger(-\tau)\rangle \\ &= -\langle \mathcal{T}_{\tau,0}\{b_\gamma^\dagger(\tau) b_\sigma^\dagger(0)\}\rangle = G_{21}^{\gamma\sigma}(\tau) \end{aligned} \tag{4.62}$$

In the Matsubara representation of the Green's functions, one can then find analogous relations. To show that this is very intuitive, let us briefly consider the following transformation.

$$\begin{aligned} -\sum_n \frac{1}{\beta^2} \langle b_{\sigma n} b_{\gamma n}^* \rangle e^{-i\omega_n \tau} &= -\frac{1}{\beta^2} \sum_n \iint \langle b_\sigma(\tau') b_\gamma^*(\tau'')\rangle e^{i\omega_n(\tau' - (\tau+\tau''))} d\tau' d\tau'' \\ &= -\frac{1}{\beta} \iint \delta(\tau' - (\tau+\tau'')) \langle b_\sigma(\tau') b_\gamma^*(\tau'')\rangle d\tau' d\tau'' \\ &= -\frac{1}{\beta} \int \langle b_\sigma(\tau+\tau'') b_\gamma^*(\tau'')\rangle d\tau'' \\ &= -\frac{1}{\beta} \int \langle b_\sigma(\tau) b_\gamma^*(0)\rangle d\tau'' = G_{11}^{\sigma\gamma}(\tau) \end{aligned} \tag{4.63}$$

In the last step, the cyclic property of the trace has been used. Therefore the Green's function matrix in Matsubara frequencies can be decomposed into $2 \times 2$ Nambu matrices similar to (4.60):

$$\mathbf{G}^{\sigma\gamma}(i\omega_n) = -\frac{1}{\beta} \left\langle \begin{pmatrix} b_{\sigma n} b_{\gamma n}^* & b_{\sigma n} b_{\gamma n} \\ b_{\sigma n}^* b_{\gamma n}^* & b_{\sigma n}^* b_{\gamma n} \end{pmatrix} \right\rangle. \tag{4.64}$$

For its matrix elements, the relations (4.61) yield the symmetry relations

$$\begin{aligned} G_{11}^{\sigma\gamma *}(i\omega_n) &= G_{11}^{\gamma\sigma}(i\omega_n) \qquad & G_{11}^{\sigma\gamma}(i\omega_n) &= G_{22}^{\gamma\sigma}(-i\omega_n), \\ G_{12}^{\sigma\gamma *}(i\omega_n) &= G_{21}^{\gamma\sigma}(i\omega_n) \qquad & G_{12}^{\sigma\gamma}(i\omega_n) &= G_{12}^{\gamma\sigma}(-i\omega_n). \end{aligned} \tag{4.65}$$

These expressions imply the further simplified relations

$$G_{11}^{\sigma\gamma *}(i\omega_n) = G_{22}^{\sigma\gamma}(-i\omega_n), \qquad G_{12}^{\sigma\gamma *}(i\omega_n) = G_{21}^{\sigma\gamma}(-i\omega_n). \tag{4.66}$$

From (4.66) it is immediately apparent, that at most half of the $2N \times 2N$ functions are actually independent expressions. (4.65) further limits this to the diagonal and all

above diagonal terms with regard to the components. So there are at most $\frac{N(N-1)}{2\cdot 2}$ independent bosonic two point Green's functions to be considered in a system of $N$ bosonic species.

### 4.3.1 Connected Green's functions

The term **connected** implies that disconnected parts contributing to the full Green's function have to be extracted, while keeping in mind the sign convention (4.51), so

$$\mathbf{G}^{\sigma\gamma C}(\tau) = \begin{pmatrix} G_{11}^{\sigma\gamma}(\tau) + \phi_{0\sigma}\phi_{0\gamma}^{*} & G_{12}^{\sigma\gamma}(\tau) + \phi_{0\sigma}\phi_{0\gamma} \\ G_{21}^{\sigma\gamma}(\tau) + \phi_{0\sigma}^{*}\phi_{0\gamma}^{*} & G_{22}^{\sigma\gamma}(\tau) + \phi_{0\sigma}^{*}\phi_{0\gamma} \end{pmatrix}. \tag{4.67}$$

Thus it is given by extracting the constant offset generated by the static mean-field condensate order parameters $\phi_{0\sigma}$. In the Matsubara frequencies this simply generates a shift for the zeroth mode:

$$\mathbf{G}^{\sigma\gamma C}(i\omega_n) = \mathbf{G}^{\sigma\gamma}(i\omega_n) + \delta_{0,n}\beta \begin{pmatrix} \phi_{0\sigma}\phi_{0\gamma}^{*} & \phi_{0\sigma}\phi_{0\gamma} \\ \phi_{0\sigma}^{*}\phi_{0\gamma}^{*} & \phi_{0\sigma}^{*}\phi_{0\gamma} \end{pmatrix}. \tag{4.68}$$

## 4.4 Self-consistency via Dyson equations

To close the DMFT loop, the last remaining step is to derive the relevant Dyson equations, which will grant the self-consistency and reveal the primary approximation of the DMFT method. Let us first consider the local problem in order to derive the local Dyson equation. For this we start with the non-interacting Green's function, as generated by the effective impurity system (4.17) (so neglecting the various interaction terms). Due to (4.20) integrating over all bath orbital fields $a_{n,l}$ yields the following contributions from the non-interacting part of the local action, where we also consider the hybridization functions (4.21):

$$\begin{aligned} S_{\mathrm{AIM}}^{0} = &- \frac{1}{\beta}\sum_{n>0}\sum_{\sigma\gamma}\left[(\mu_\sigma + i\omega_n)b_{n,\sigma}^{*}b_{n,\sigma} + (\mu_\sigma - i\omega_n)b_{-n,\sigma}b_{-n,\sigma}^{*}\right] \\ &- \frac{1}{2\beta}\sum_{\sigma\gamma}\left[\mu_\sigma b_{0,\sigma}^{*}b_{0,\sigma} + \mu_\sigma b_{-0,\sigma}b_{-0,\sigma}^{*}\right] - X. \end{aligned} \tag{4.69}$$

Note that we now only sum over all $n \geq 0$, so all terms appear only once in the summation, which necessitates to consider the zero frequency separately. Via the use of functional derivatives of the partition function, akin to (4.37) and (4.45), we may now analytically derive the Green's function corresponding to this action. To do so we first have to introduce the source fields $J_{\pm n,\sigma}^{*}$ and $J_{\pm n,\sigma}$, which for $n > 0$ are given by

$$\bar{\mathbf{J}} \equiv (J_{n,1}^{*}, \ldots, J_{n,N}^{*}, J_{-n,1}, \ldots, J_{-n,N})^{\mathrm{T}}, \tag{4.70}$$

$$\mathbf{J} \equiv (J_{n,1}, \ldots, J_{n,N}, J_{-n,1}^{*}, \ldots, J_{-n,N}^{*}). \tag{4.71}$$

To avoid double counting for the case $n = 0$, we have to use slightly different source terms for $n = 0$,

$$\bar{\mathbf{J}}_0 \equiv (J^*_{0,1}, \ldots, J^*_{0,N}, J_{0,1}, \ldots, J_{0,N})^{\mathrm{T}}/2, \tag{4.72}$$

$$\mathbf{J}_0 \equiv (J_{0,1}, \ldots, J_{0,N}, J^*_{0,1}, \ldots, J^*_{0,N})/2. \tag{4.73}$$

Thus we work in the Matsubara representation, where $N$ is the number of bosonic components and $n$ corresponds to the considered Matsubara frequency. In the same fashion, replacing the source fields $J$ by the physical fields $b$ in order to define $\bar{\mathbf{b}}$ and $\mathbf{b}$, one finds the following form for the relevant integration in (4.8), for which we here neglect the interaction terms. So in Matsubara frequencies (see e.g. Sec. 3.2, 'Construction of the path integral' in [AS10])

$$Z_n[\bar{\mathbf{J}}_n, \mathbf{J}_n] = \int d\bar{\mathbf{b}}_n d\mathbf{b}_n \exp(-\bar{\mathbf{b}}_n A_n \mathbf{b}_n + \bar{\mathbf{J}}_n \mathbf{b}_n + \bar{\mathbf{b}}_n \mathbf{J}_n) = C \exp\left(\bar{\mathbf{J}}_n A_n^{-1} \mathbf{J}_n\right). \tag{4.74}$$

Note that this expression is only a small part of the path integral representing the complete partition function, while the constant prefactor $C$ will not be relevant in the end, as it just is a part of the bare partition function without source fields. Due to the time independence of the Hamiltonian (4.1), the partition function factorizes in the Matsubara frequencies, so we may focus on a single Matsubara frequency at a time. The corresponding matrix elements of $A_n$ are given as

$$[A_n]^{\sigma\gamma}_{ij} = -\frac{1}{\beta}\left(\mu_\sigma \delta_{\sigma,\gamma}\delta_{i,j} + i\omega_n(-1)^{i+1}\delta_{\sigma,\gamma}\delta_{i,j} + \Delta^{\sigma,\gamma}_{i,j}(i\omega_n)\right) = -\frac{1}{\beta}[\tilde{A}_n]^{\sigma\gamma}_{ij}, \tag{4.75}$$

$$[A_0]^{\sigma\gamma}_{ij} = -\frac{1}{2\beta}\left(\mu_\sigma \delta_{\sigma,\gamma}\delta_{i,j} + \Delta^{\sigma,\gamma}_{i,j}(0)\right) = -\frac{1}{2\beta}[\tilde{A}_0]^{\sigma\gamma}_{ij}. \tag{4.76}$$

The individual terms of the Green's functions in Matsubara representation then simply follow from functional derivatives, while we note that regular derivatives suffice in this case. Let us derive the following example for $n > 0$.

$$\begin{aligned}
\langle b_{n,\sigma} b_{-n,\gamma}\rangle &= \frac{\delta}{\delta J^*_{n,\sigma}}\frac{\delta}{\delta J^*_{-n,\gamma}} \ln Z_{\mathrm{eff}}[\bar{\mathbf{J}}_n, \mathbf{J}_n]\Big|_{\bar{\mathbf{J}}_n, \mathbf{J}_n \to 0} = \frac{\delta}{\delta J^*_{n,\sigma}}\frac{\delta}{\delta J^*_{-n,\gamma}} \ln Z_n[\bar{\mathbf{J}}_n, \mathbf{J}_n]\Big|_{\bar{\mathbf{J}}_n, \mathbf{J}_n \to 0} \\
&= \frac{d}{dJ^*_{n,\sigma}}\frac{d}{dJ^*_{-n,\gamma}} \left[\ln(C) + \ln\exp\left(\bar{\mathbf{J}}_n A_n^{-1} \mathbf{J}_n\right)\right]\Big|_{\bar{\mathbf{J}}_n, \mathbf{J}_n \to 0} \\
&= \frac{d}{dJ^*_{n,\sigma}}\frac{d}{dJ^*_{-n,\gamma}} \left(\sum_{i,j} \bar{\mathbf{J}}^i_n \left[A_n^{-1}\right]_{ij} \mathbf{J}^j_n\right)\Big|_{\bar{\mathbf{J}}_n, \mathbf{J}_n \to 0} \\
&= \left[A_n^{-1}\right]^{\sigma\gamma}_{12} = -\beta\left[\tilde{A}_n^{-1}\right]^{\sigma\gamma}_{12} \equiv -\beta G^{\sigma\gamma C}_{12}(i\omega_n)
\end{aligned} \tag{4.77}$$

In the same fashion one also finds all remaining terms of the Green's function matrix,

$$G^{\sigma\gamma C}_{21}(i\omega_n) = \left[\tilde{A}_n^{-1}\right]^{\sigma\gamma}_{21}, \quad G^{\sigma\gamma C}_{11}(i\omega_n) = \left[\tilde{A}_n^{-1}\right]^{\sigma\gamma}_{11}, \quad G^{\sigma\gamma C}_{22}(i\omega_n) = \left[\tilde{A}_n^{-1}\right]^{\sigma\gamma}_{22}. \tag{4.78}$$

For completeness let us also consider the case of the zeroth Matsubara frequency.

$$\begin{aligned}
\langle b_{0,\sigma} b_{0,\gamma} \rangle &= \frac{\delta}{\delta J^*_{0,\sigma}} \frac{\delta}{\delta J^*_{0,\gamma}} \ln Z_{\text{eff}}[\bar{\mathbf{J}}_0, \mathbf{J}_0]\Big|_{\bar{\mathbf{J}}_0, \mathbf{J}_0 \to 0} = \frac{\delta}{\delta J^*_{0,\sigma}} \frac{\delta}{\delta J^*_{0,\gamma}} \ln Z_0[\bar{\mathbf{J}}_0, \mathbf{J}_0]\Big|_{\bar{\mathbf{J}}_0, \mathbf{J}_0 \to 0} \\
&= \frac{d}{dJ^*_{0,\sigma}} \frac{d}{dJ^*_{0,\gamma}} \left[ \ln(C) + \ln \exp\left( \bar{\mathbf{J}}_0 A_0^{-1} \mathbf{J}_0 \right) \right]\Big|_{\bar{\mathbf{J}}_0, \mathbf{J}_0 \to 0} \\
&= \frac{d}{dJ^*_{0,\sigma}} \frac{d}{dJ^*_{0,\gamma}} \left( \sum_{i,j} \bar{\mathbf{J}}_0^i \left[ A_0^{-1} \right]_{ij} \mathbf{J}_0^j \right)\Big|_{\bar{\mathbf{J}}_0, \mathbf{J}_0 \to 0} \\
&= \frac{d}{dJ^*_{0,\sigma}} \frac{d}{dJ^*_{0,\gamma}} \left[ \sum_{\sigma'\gamma'} \frac{J^*_{0,\sigma'}}{2} \left(2 - \delta_{\sigma'\gamma'}\right) \left[ A_0^{-1} \right]_{12}^{\sigma'\gamma'} \frac{J^*_{0,\gamma'}}{2} \right]\Bigg|_{J^*_{0,\sigma}, J^*_{0,\gamma} \to 0} \\
&= \frac{1}{2} \left[ A_0^{-1} \right]_{12}^{\sigma\gamma} = -\frac{2\beta}{2} \left[ \tilde{A}_0^{-1} \right]_{12}^{\sigma\gamma} \equiv -\beta G_{12}^{\sigma\gamma C}(0)
\end{aligned} \tag{4.79}$$

As some terms may now appear multiple times, we have written the last steps explicitly, keeping in mind the symmetry properties of the hybridisation functions (4.35), which translates to $[A_0]_{12}^{\sigma\gamma} = [A_0]_{12}^{\gamma\sigma}$ and thus to $[A_0^{-1}]_{12}^{\sigma\gamma} = [A_0^{-1}]_{12}^{\gamma\sigma}$. Furthermore considering (4.33), which implies $[A_0^{-1}]_{11}^{\sigma\gamma} = [A_0^{-1}]_{22}^{\gamma\sigma}$, we also find the remaining terms for the zeroth Matsubara frequency,

$$G_{21}^{\sigma\gamma C}(0) = \left[ \tilde{A}_0^{-1} \right]_{21}^{\sigma\gamma}, \quad G_{11}^{\sigma\gamma C}(0) = \left[ \tilde{A}_0^{-1} \right]_{11}^{\sigma\gamma}, \quad G_{22}^{\sigma\gamma C}(0) = \left[ \tilde{A}_0^{-1} \right]_{22}^{\sigma\gamma}. \tag{4.80}$$

*Note*: Here we have neglected all self-consistent cavity expectation values (second line in (4.17)). By neglecting the effective shift of the chemical potentials due to the Hartree terms, we simply move these terms into the self-energy, which will correctly carry their effect over to the interacting Green's function, as we will see shortly. Furthermore disregarding the contributions from the condensate order parameters implies that we will be using the connected Green's functions from here onwards. Thus for the local non-interacting problem (4.69) we obtain an analytic expression for the connected non-interacting local Green's function

$$\mathbf{G}_0^C(i\omega_n) = \left( \boldsymbol{\mu} \otimes \mathbb{1}_2 + i\omega_n \mathbb{1}_N \otimes \sigma_3 + \boldsymbol{\Delta}(i\omega_n) \right)^{-1}, \tag{4.81}$$

where the 0 specifies the non-interacting property, *not* the site. Here $\boldsymbol{\mu}$ is the diagonal $N \times N$ matrix, given by the chemical potentials of each bosonic species and $\sigma_3$ is one of the Pauli matrices.

### 4.4.1 Local Dyson equation

Now we extend our focus to the interacting case, in order to find the local Dyson equation, giving the relation between the connected (interacting and non-interacting) Green's functions and the self-energy. The most straightforward way is to start by considering the equation of motion for the imaginary time Heisenberg operators, in order to derive the corresponding equation of motion for the Green's functions,

$$\frac{d}{d\tau} \hat{A}(\tau) = \left[ \hat{H}, \hat{A}(\tau) \right] + \frac{\partial \hat{A}(\tau)}{\partial \tau}. \tag{4.82}$$

Considering (4.51), but using two general field operators $\hat{a}(\tau)$ and $\hat{b}(0) = \hat{b}$ (which can be any product of creation and annihilation operators), we introduce the abbreviated notation

$$G_{a,b}(\tau) = -\langle \mathcal{T}_{\tau,0}\{\hat{a}(\tau)\hat{b}(0)\}\rangle. \tag{4.83}$$

We thus derive the following equation of motion for the two-point Green's function of two arbitrary field operators $\hat{a}(\tau)$ and $\hat{b}(0) = \hat{b}$, which can be either creation or annihilation operators, where we have used $\frac{\partial}{\partial\tau}\theta(\tau) = \delta(\tau)$ and $\delta(-\tau) = \delta(\tau)$.

$$\begin{aligned}
\frac{d}{d\tau}G^C_{a,b}(\tau) &= -\frac{d}{d\tau}\left(\theta(\tau)\langle\hat{a}(\tau)\hat{b}(0)\rangle + \theta(-\tau)\langle\hat{b}(0)\hat{a}(\tau)\right) + \langle\frac{d}{d\tau}\hat{a}(\tau)\rangle\langle\hat{b}(0)\rangle \\
&= -\delta(\tau)\langle\hat{a}(0)\hat{b}(0) - \hat{b}(0)\hat{a}(0)\rangle - \left(\theta(\tau)\langle\frac{d\hat{a}(\tau)}{d\tau}\hat{b}(0)\rangle + \theta(-\tau)\langle\hat{b}(0)\frac{d\hat{a}(\tau)}{d\tau}\rangle\right) \\
&= -\delta(\tau)\langle[\hat{a}(0),\hat{b}(0)]\rangle - \left(\theta(\tau)\langle[\hat{H},\hat{a}](\tau)\hat{b}(0)\rangle + \theta(-\tau)\langle\hat{b}(0)[\hat{H},\hat{a}](\tau)\rangle\right) \\
&= -\delta(\tau)\langle[\hat{a}(0),\hat{b}(0)]\rangle + G_{[H,a],b}(\tau)
\end{aligned} \tag{4.84}$$

Note that the time-dependence can be taken out of the commutator, as the time-evolution operator, which defines the Heisenberg operators, commutes with the Hamiltonian. Furthermore due to the cyclic property of the trace, the derivative of the condensate order parameter vanishes, thus it only yields a constant shift of the connected Green's function with regard to the full Green's function. By a Fourier transformation the differential equation can be simplified to a regular equation, which leads to the Matsubara representation, as

$$\begin{aligned}
\frac{1}{\beta}\sum_n \exp(-i\omega_n\tau)(-i\omega_n)G^C_{a,b}(i\omega_n) &= -\frac{1}{\beta}\sum_n \exp(-i\omega_n\tau)\left[\langle[\hat{a}(0),\hat{b}(0)]\rangle + G_{[H,a],b}(i\omega_n)\right], \\
-i\omega_n G^C_{a,b}(i\omega_n) &= -\langle[\hat{a}(0),\hat{b}(0)]\rangle + G_{[H,a],b}(i\omega_n), \\
\langle[\hat{a}(0),\hat{b}(0)]\rangle &= i\omega_n G^C_{a,b}(i\omega_n) + G_{[H,a],b}(i\omega_n).
\end{aligned} \tag{4.85}$$

Note that this expression also holds for $G_{a,b}(i\omega_n)$, which can be seen by subtracting $i\omega_n\beta\phi$ In order to evaluate the full Green's function matrix (4.60) we need to explicitly consider all Green's functions, generated by the commutator with the (effective impurity) Hamiltonian (4.17). Regarding the two-point Green's function we are interested in for the DMFT loop, the relevant commutators are

$$\begin{aligned}
\left[\hat{H}^{\text{eff}}_{\text{AIM}},\hat{b}_\sigma\right] =& \tilde{\mu}_\sigma\hat{b}_\sigma - \sum_\gamma\left(U_{\sigma\gamma}\hat{b}^\dagger_\gamma\hat{b}_\gamma\hat{b}_\sigma + \frac{\Omega_{\sigma\gamma}}{2}\hat{b}_\gamma\right) \\
&+ \sum_{\langle 0,i\rangle} t^{\sigma\sigma}_{0i}\langle\hat{b}_{i\sigma}\rangle_{(0)} - \sum_l\left(V^*_{l,\sigma}\hat{a}_l + W^*_{l,\sigma}\hat{a}^\dagger_l\right),
\end{aligned} \tag{4.86}$$

$$\begin{aligned}
\left[\hat{H}^{\text{eff}}_{\text{AIM}},\hat{b}^\dagger_\sigma\right] =& -\tilde{\mu}_\sigma\hat{b}_\sigma + \sum_\gamma\left(U_{\sigma\gamma}\hat{b}^\dagger_\sigma\hat{b}^\dagger_\gamma\hat{b}_\gamma + \frac{\Omega_{\sigma\gamma}}{2}\hat{b}^\dagger_\gamma\right) \\
&- \sum_{\langle 0,i\rangle} t^{\sigma\sigma}_{0i}\langle\hat{b}^\dagger_{i\sigma}\rangle_{(0)} + \sum_l\left(V_{l,\sigma}\hat{a}^\dagger_l + W_{l,\sigma}\hat{a}_l\right).
\end{aligned} \tag{4.87}$$

Here we have used the commutators $[\hat{b}^\dagger_{\sigma_1}\hat{b}^\dagger_{\sigma_2}\hat{b}_{\sigma_2}\hat{b}_{\sigma_1},\hat{b}^\dagger_\gamma] = \hat{b}^\dagger_{\sigma_1}\hat{b}^\dagger_{\sigma_2}\hat{b}_{\sigma_2}\delta_{\sigma_1,\gamma}+\hat{b}^\dagger_{\sigma_1}\hat{b}^\dagger_{\sigma_2}\hat{b}_{\sigma_1}\delta_{\sigma_2,\gamma}$ and $[\hat{b}^\dagger_{\sigma_1}\hat{b}_{\sigma_2},\hat{b}_\gamma] = -\hat{b}_{\sigma_2}\delta_{\sigma_1,\gamma}$ as well as the corresponding hermitian conjugate expressions. Furthermore, we have introduced the modified chemical potential $\tilde{\mu}_\sigma \equiv \mu_\sigma + \sum_{i\neq 0} V_\sigma(i)\langle\hat{n}_{i\sigma}\rangle_{(0)} \equiv \mu_\sigma + \mu^{(0)}_\sigma$, which includes the self-consistent Hartree shift. These expressions all contain a dependence on the bath orbitals, which we want to eliminate in the end. To do so we also need to consider the commutators

$$\left[\hat{H}^{\text{eff}}_{\text{AIM}},\hat{a}_l\right] = -\sum_\sigma\left(V_{l,\sigma}\hat{b}_\sigma + W^*_{l_\sigma}\hat{b}^\dagger_\sigma\right) - \epsilon_l\hat{a}_l, \tag{4.88}$$

$$\left[\hat{H}^{\text{eff}}_{\text{AIM}},\hat{a}^\dagger_l\right] = \sum_\sigma\left(V^*_{l,\sigma}\hat{b}^\dagger_\sigma + W_{l_\sigma}\hat{b}_\sigma\right) + \epsilon_l\hat{a}^\dagger_l. \tag{4.89}$$

Also considering $\langle[\hat{b}_\sigma,\hat{b}^\dagger_\gamma]\rangle = \delta_{\sigma,\gamma}$, we may now evaluate (4.85) for the case of the normal Green's function,

$$\begin{aligned}(i\omega_n+\tilde{\mu}_\sigma)\,G_{b_\sigma,b^\dagger_\gamma} = &\sum_l\left(V^*_{l,\sigma}G_{a_l,b^\dagger_\gamma} + W^*_{l,\sigma}G_{a^\dagger_l,b^\dagger_\gamma}\right) + \delta_{\sigma,\gamma}\\ &+\sum_\lambda\left(U_{\sigma,\lambda}G_{b^\dagger_\lambda b_\lambda b_\sigma,b^\dagger_\gamma} + \frac{\Omega_{\sigma\lambda}}{2}G_{b_\lambda,b^\dagger_\gamma}\right) - \eta^{(0)}_\sigma G_{1,b^\dagger_\gamma}.\end{aligned} \tag{4.90}$$

In the last term we have introduced the sum of cavity condensate order parameters $\eta^{(0)}_\sigma \equiv \sum_{\langle 0,i\rangle} t^{\sigma\sigma}_{0i}\langle\hat{b}^\dagger_{i,\sigma}\rangle$ and also find a contribution by a single-point Green's function, which equates to

$$G_{1,b^\dagger_\gamma} = \int_0^\beta e^{i\omega_n\tau}(-\langle\mathbb{1}(\tau)\hat{b}^\dagger_\gamma\rangle)d\tau = -\beta\phi^*_\gamma\delta_{0,n}. \tag{4.91}$$

To eliminate the contributions from the bath orbitals, we also need to consider their corresponding equations of motion,

$$\begin{aligned}(i\omega_n-\epsilon_l)\,G_{a_l,b^\dagger_\gamma} &= \sum_\sigma\left(V_{l,\sigma}G_{b_\sigma,b^\dagger_\gamma} + W^*_{l,\sigma}G_{b^\dagger_\sigma,b^\dagger_\gamma}\right),\\ (i\omega_n+\epsilon_l)\,G_{a^\dagger_l,b^\dagger_\gamma} &= -\sum_\sigma\left(V^*_{l,\sigma}G_{b^\dagger_\sigma,b^\dagger_\gamma} + W_{l,\sigma}G_{b_\sigma,b^\dagger_\gamma}\right).\end{aligned} \tag{4.92}$$

Inserting (4.92) into (4.90), while also considering (4.22) leads to the following form, where the bath orbitals have been eliminated:

$$\begin{aligned}(i\omega_n+\tilde{\mu}_\sigma)\,G_{b_\sigma,b^\dagger_\gamma} = &-\sum_\lambda\left(\Delta^{\sigma\lambda}_{11}G_{b_\lambda,b^\dagger_\gamma} + \Delta^{\sigma\lambda}_{12}G_{b^\dagger_\lambda,b^\dagger_\gamma}\right) + \delta_{\sigma,\gamma}\\ &+\sum_\lambda\left(U_{\sigma,\lambda}G_{b^\dagger_\lambda b_\lambda b_\sigma,b^\dagger_\gamma} + \frac{\Omega_{\sigma\lambda}}{2}G_{b_\lambda,b^\dagger_\gamma}\right) + \beta\eta^{(0)}_\sigma\phi^*_\gamma\delta_{0,n}.\end{aligned} \tag{4.93}$$

A similar expression can be obtained for the case of the anomalous Green's function. To do so one simply needs to replace $b^\dagger_\gamma \to b_\gamma$ in (4.90) as well as in (4.92). Note that $\langle[b_\sigma,b_\gamma]\rangle = 0$ in this case. We find

$$
\begin{aligned}
(i\omega_n + \tilde{\mu}_\sigma)\, G_{b_\sigma, b_\gamma} = &- \sum_\lambda \left( \Delta_{11}^{\sigma\lambda} G_{b_\lambda, b_\gamma} + \Delta_{12}^{\sigma\lambda} G_{b_\lambda^\dagger, b_\gamma} \right) \\
&+ \sum_\lambda \left( U_{\sigma,\lambda} G_{b_\lambda^\dagger b_\lambda b_\sigma, b_\gamma} + \frac{\Omega_{\sigma\lambda}}{2} G_{b_\lambda, b_\gamma} \right) + \beta \eta_\sigma^{(0)} \phi_\gamma \delta_{0,n}.
\end{aligned} \tag{4.94}
$$

In Nambu notation both (4.93) and (4.94), as well as their counterparts for negative frequencies can be combined into a single expression, which is the local Dyson equation

$$
(i\omega_n \mathbb{1}_N \otimes \sigma_3 + \boldsymbol{\mu} \otimes \mathbb{1}_2 + \boldsymbol{\Delta})\mathbf{G} - [\mathbf{UF} + \beta \boldsymbol{\eta}^{(0)} \boldsymbol{\phi}^\dagger \delta_{0,n} - \mathbf{MG}] = \mathbb{1}_N \otimes \mathbb{1}_2. \tag{4.95}
$$

The various matrices we have introduced here denote contributions by the chemical potential $\boldsymbol{\mu} = \mathrm{diag}(\mu_1, \ldots, \mu_N)$, the well known hybridization functions $\boldsymbol{\Delta}$ [see (4.22)], terms containing higher order Green's functions $\mathbf{UF}$, products of the condensate order parameters $\boldsymbol{\eta}^{(0)T} = (\eta_1^{(0)}, \eta_1^{(0)*}, \ldots, \eta_N^{(0)}, \eta_N^{(0)*})$ and $\boldsymbol{\phi}^\dagger = (\phi_{01}^*, \phi_{01}, \ldots, \phi_{0N}^*, \phi_{0N})$, as well as the Rabi and Hartree terms, which are combined into $\mathbf{M}$. We have defined

$$
\mathbf{UF}^{\sigma\gamma} = \sum_\lambda U_{\sigma\lambda} \begin{pmatrix} G_{b_\lambda^\dagger b_\lambda b_\sigma, b_\gamma^\dagger} & G_{b_\lambda^\dagger b_\lambda b_\sigma, b_\gamma} \\ G_{b_\sigma^\dagger b_\lambda^\dagger b_\lambda, b_\gamma^\dagger} & G_{b_\sigma^\dagger b_\lambda^\dagger b_\lambda, b_\gamma} \end{pmatrix}, \tag{4.96}
$$

$$
\mathbf{M}^{\sigma\gamma} = \left[ \frac{\Omega_{\sigma\gamma}}{2}(1 - \delta_{\sigma,\gamma}) + \mu_\sigma^{(0)} \delta_{\sigma,\gamma} \right] \mathbb{1}_2. \tag{4.97}
$$

Multiplying (4.95) by the inverse of the interacting local Green's function from the right and identifying (4.81), we find the local Dyson equation in its standard form,

$$
\mathbf{G}^{-1}(i\omega_n) = \boldsymbol{\mu} \otimes \mathbb{1}_2 + i\omega_n \mathbb{1}_N \otimes \sigma_3 + \boldsymbol{\Delta}(i\omega_n) - \boldsymbol{\Sigma}(i\omega_n) = \mathbf{G}_0^{C-1}(i\omega_n) - \boldsymbol{\Sigma}(i\omega_n), \tag{4.98}
$$

$$
\mathbf{G}^{C-1}(i\omega_n) = \mathbf{G}_0^{C-1}(i\omega_n) - \boldsymbol{\Sigma}^C(i\omega_n). \tag{4.99}
$$

Here we introduce the (connected) local self-energy, which incorporates not only contributions from higher order Green's functions, but also some other terms, in order to retain a simple form for the non-interacting local Green's function,

$$
\boldsymbol{\Sigma}(i\omega_n) \equiv [\mathbf{UF}(i\omega_n) + \beta \boldsymbol{\eta}^{(0)} \boldsymbol{\phi}^\dagger \delta_{0,n}] \mathbf{G}^{-1}(i\omega_n) - \mathbf{M}, \tag{4.100}
$$

$$
\begin{aligned}
\boldsymbol{\Sigma}^C(i\omega_n) \equiv &[\mathbf{UF}(i\omega_n) + \beta(\boldsymbol{\eta}^{(0)} \boldsymbol{\phi}^\dagger - (\boldsymbol{\mu} \otimes \mathbb{1}_2 + \boldsymbol{\Delta})\boldsymbol{\phi}\boldsymbol{\phi}^\dagger)\delta_{0,n}] \mathbf{G}^{C-1}(i\omega_n) \\
&- \mathbf{MGG}^{C-1}(i\omega_n).
\end{aligned} \tag{4.101}
$$

As the local non-interacting Green's function is known analytically (4.81) and the local interacting Green's function can be computed via the Lehmann representation (4.59) – given the state spectrum of the **self-consistent** impurity problem (4.17) – one can thus calculate the local self-energy in a completely unperturbative fashion[10].

[10] Another - more direct approach - is to compute the higher order four point Green's functions using the corresponding Lehmann representation and directly apply (4.102) to obtain the self-energies. As this is computationally more demanding, while (4.99) yields the same result when self-consistency has been reached, the latter method is used in this work.

### 4.4.2 Lattice Dyson equation

If we now consider the case of the full lattice problem, for a system with a total number $L$ of lattice sites, we have to extend the Nambu notation to real-space, by defining

$$\mathcal{B}_n^\dagger \equiv \begin{pmatrix} b_{11,n} \\ \vdots \\ b_{LN,n} \\ b_{11,-n}^* \\ \vdots \\ b_{LN,-n}^* \end{pmatrix}, \quad \mathcal{B}_n \equiv \begin{pmatrix} b_{11,n}^*, & \dots, & b_{LN,n}^*, & b_{11,-n}, & \dots, & b_{LN,-n} \end{pmatrix}. \tag{4.102}$$

Thus we may write down the real-space Dyson equation, determining the relation between the connected interacting lattice Green's function $\mathbf{G}^C_{\text{latt}}(i\omega_n)$, the connected non-interacting lattice Green's function $\mathbf{G}^C_{\text{0latt}}(i\omega_n)$ and the connected lattice self-energy $\mathbf{\Sigma}^C_{\text{latt}}(i\omega_n)$, which has the generic form

$$\mathbf{G}^{C-1}_{\text{latt}}(i\omega_n) = \mathbf{G}^{C-1}_{\text{0latt}}(i\omega_n) - \mathbf{\Sigma}^C_{\text{latt}}(i\omega_n), \tag{4.103}$$

while the connected non-interacting lattice Green's function can be derived similar to the local non-interacting Green's functions (4.81), as

$$\mathbf{G}^{C-1}_{\text{0latt}}(i\omega_n) = \mathbb{1}_L \otimes \boldsymbol{\mu} \otimes \mathbb{1}_2 + i\omega_n \mathbb{1}_L \otimes \mathbb{1}_N \otimes \sigma_3 + \mathbf{t} \otimes \begin{pmatrix} 1 & 0 \\ 0 & 0 \end{pmatrix} + \mathbf{t}^\dagger \otimes \begin{pmatrix} 0 & 0 \\ 0 & 1 \end{pmatrix}. \tag{4.104}$$

Here we have introduced the hopping matrix $\mathbf{t}$ given by the matrix elements $[\mathbf{t}]_{ij}^{\sigma\gamma} = t_{ij}^{\sigma\gamma} - t_{ij}^{\sigma\gamma}\delta_{i,j}$, as the effect of the Rabi terms is already included in the self-energy. Note that this expression also applies to systems, which have a hopping that is accompanied by a phase shift, as in the presence of a gauge field, while we will only consider real-valued hopping amplitudes $\mathbf{t} = \mathbf{t}^\dagger$. If the lattice self-energy were known, we would have an exact description of the system. But as this requires an exact solution of the correlated many-body system, this is exponentially hard in the system size[11]. On the other hand, we have already shown that local self-energies can be obtained non-perturbatively in the DMFT-scheme. Thus we now introduce the **DMFT-approximation**, by assuming that the self-energy is diagonal in its real-space indices. Locality of the self-energy is the primary approximation of DMFT and it implies that only local correlations are treated beyond the mean-field level.

Let us take a brief look at individual entries of these Green's and show how to obtain static observables. Regarding the notation, we will use the convention that, when two lattice indices are included, we will refer to the lattice Green's function, while the use of a single lattice index will refer to the local Green's function of the corresponding site. We furthermore denote the normal and anomalous Green's functions by the letters $n$ and $a$, which correspond to the diagonal and off-diagonal terms in the Nambu notation. For example, an arbitrary normal two-point correlation can be obtained as

[11] Actually, even more so in a bosonic system without fixed particle number, where already the local Hilbert space is not finite. Thus any numerical implementation requires a Fock-space truncation. For a method to soften the truncation see Chap. 5

$$\langle \hat{b}^\dagger_{i\sigma}\hat{b}_{j\gamma}\rangle = \lim_{\varepsilon\to 0^-}\langle \mathcal{T}_{0,\varepsilon}\{\hat{b}^\dagger_{i\sigma}\hat{b}_{j\gamma}\}\rangle = -\lim_{\varepsilon\to 0^-} G^{\gamma\sigma,n}_{ji}(\varepsilon) = \frac{1}{\beta^2}\lim_{\varepsilon\to 0^+}\sum_n e^{-i\omega_n(-\varepsilon)}\langle \hat{b}^\dagger_{i\sigma,n}\hat{b}_{j\gamma,n}\rangle$$
$$= -\frac{1}{\beta}\left(G^{\gamma\sigma,n}_{ji}(i\omega_n=0) + \sum_{n>0}\left[e^{i\omega_n\varepsilon}G^{\gamma\sigma,n}_{ji}(i\omega_n) + e^{-i\omega_n\varepsilon}G^{\sigma\gamma,n}_{ij}(i\omega_n)\right]\right). \quad (4.105)$$

## 4.5 Kinetic energy and nearest neighbor fluctuations

Starting from the connected normal real-space Green's function at equal times, with time ordering fixed by the infinitesimal time difference $\epsilon < 0$, we find

$$\lim_{\epsilon\to 0^-} G^{Cn}_{\sigma,ji}(\epsilon,0) = -\left(\langle \hat{b}^\dagger_{\sigma,i}\hat{b}_{\sigma,j}\rangle - \langle \hat{b}^\dagger_{\sigma,i}\rangle\langle \hat{b}_{\sigma,j}\rangle\right) \quad (4.106)$$
$$= \lim_{\epsilon\to 0^+}\sum_{n=-\infty}^{\infty}\frac{e^{i\omega_n\epsilon}}{\beta}G^{Cn}_{\sigma,ji}(i\omega_n).$$

for the connected Green's functions $G^{Cn}_{\sigma,ji}(i\omega_n)$ in bosonic Matsubara frequencies. The anomalous part is accordingly given by

$$\lim_{\epsilon\to 0^-} G^{Ca}_{\sigma,ji}(\epsilon,0) = -\left(\langle \hat{b}_{\sigma,i}\hat{b}_{\sigma,j}\rangle - \langle \hat{b}_{\sigma,i}\rangle\langle \hat{b}_{\sigma,j}\rangle\right) \quad (4.107)$$
$$= \lim_{\epsilon\to 0^+}\sum_{n=-\infty}^{\infty}\frac{e^{i\omega_n\epsilon}}{\beta}G^{Ca}_{\sigma,ji}(i\omega_n).$$

Thus expressing the total kinetic energy in terms of connected real-space Green's functions yields

$$E_{kin} = -\sum_{ij\sigma} t^\sigma_{ij}\langle \hat{b}^\dagger_{\sigma,i}\hat{b}_{\sigma,j}\rangle$$
$$= \sum_{ij\sigma} t^\sigma_{ij}\left(\lim_{\epsilon\to 0^+}\sum_{n=-\infty}^{\infty}\frac{e^{i\omega_n\epsilon}}{\beta}G^{Cn}_{\sigma,ji}(i\omega_n) - \phi^*_{\sigma,i}\phi_{\sigma,j}\right).$$

where $\phi_{\sigma,i}$ is the local condensate order parameter of the atomic state $\sigma$ at lattice site $i$. This expression can be further simplified by employing both the local [(4.108) as in (36) of [Vas+15]] and lattice [(4.109) as in (37) of [Vas+15]] Dyson equations in Nambu notation, as regularly used within RB-DMFT. Here we suppress the state index $\sigma$, as this part of the derivation is independent of the atomic state. In Nambu notation for $n \geq 0$ the real-space lattice Green's functions are represented as $G^{Cn}_{ji}(+i\omega_n) = [\mathbf{G}^C_{ji}(i\omega_n)]_{11}$ and $G^{Cn}_{ji}(-i\omega_n) = [\mathbf{G}^C_{ji}(i\omega_n)]_{22}$, while the anomalous term is given by $G^{Ca}_{ji}(+i\omega_n) = [\mathbf{G}^C_{ji}(i\omega_n)]_{12} = G^{Ca}_{ji}(-i\omega_n)$ and $[\mathbf{G}^C_{ji}(i\omega_n)]_{12} = [\mathbf{G}^C_{ji}(i\omega_n)]^*_{21}$. So

$$\mathbf{G}^C_i(i\omega_n)^{-1} = i\omega_n\sigma_3 + \mu\mathbf{1}_2 + \mathbf{\Delta}_i(i\omega_n) - \mathbf{\Sigma}_i(i\omega_n), \quad (4.108)$$
$$[\mathbf{G}^C(i\omega_n)^{-1}]_{ij} = t_{ij}\mathbf{1}_2 + \delta_{ij}[i\omega_n\sigma_3 + \mu\mathbf{1}_2 - \mathbf{\Sigma}_i(i\omega_n)]. \quad (4.109)$$

where the Pauli matrix $\sigma_3$ is used due to Nambu notation. These equations are given in terms of local self-energies $\mathbf{\Sigma}_i(i\omega_n)$, the Anderson impurity hybridization function $\mathbf{\Delta}_i(i\omega_n)$ and the local impurity Green's function $\mathbf{G}^C_i(i\omega_n) \equiv [\mathbf{G}^C(i\omega_n)]_{ii}$

(**DMFT self-consistency**). Inserting $\mathbf{\Sigma}_i(i\omega_n)$ from (4.108) in (4.109), combined with a matrix multiplication by $\mathbf{G}^C(i\omega_n)$ from the right, where we are only interested in the diagonal elements, yields

$$\begin{aligned}&\sum_j [\mathbf{G}^C(i\omega_n)^{-1}]_{ij}[\mathbf{G}^C(i\omega_n)]_{ji} = \\ =&\sum_j \left[t_{ij}\mathbf{1}_2 - \delta_{ij}\left(\mathbf{\Delta}_i(i\omega_n) - \mathbf{G}_i^C(i\omega_n)^{-1}\right)\right][\mathbf{G}^C(i\omega_n)]_{ji}.\end{aligned}$$

Further using the self-consistency property of the impurity Green's function leads to the identities

$$\sum_j t_{ij}[\mathbf{G}^C(i\omega_n)]_{ji} = \mathbf{\Delta}_i(i\omega_n)\mathbf{G}_i^C(i\omega_n). \tag{4.110}$$

of which only the diagonal parts are of interest to us. Considering the symmetries in Nambu notation, they allow to transform the expression for $E_{kin}$ into a single sum over all sites $i$ as follows:

$$\begin{aligned}E_{kin} =&\frac{2}{\beta}\lim_{\epsilon\to 0^+}\sum_{i\sigma,n\geq 0}\mathrm{Re}\left(\left[\mathbf{\Delta}_i^{\sigma\sigma}(i\omega_n)\mathbf{G}_i^{\sigma\sigma C}(i\omega_n)\right]_{11}e^{i\omega_n\epsilon}\right)\\ &-\sum_{i\sigma}\frac{\mathrm{Tr}\left[\mathbf{\Delta}_i^{\sigma\sigma}(0)\mathbf{G}_i^{\sigma\sigma C}(0)\right]}{2\beta} - \sum_{ij\sigma}t_{ij}\phi^*_{\sigma,i}\phi_{\sigma,j}.\end{aligned} \tag{4.111}$$

Note that both $\mathbf{\Delta}_i^{\sigma\sigma}$ and $\mathbf{G}_i^{\sigma\sigma C}$ are local quantities, which can be obtained for each impurity individually. The remaining problem is due to the cutoff imposed on the Matsubara frequencies in the numerics, which implies that the limit of equal times is in general not simply given by setting $\epsilon = 0$ [12]. One can instead account for the cutoff by requiring that the particle number is given correctly:

$$-\frac{1}{\beta}\sum_n G_{ii}^{\sigma\sigma C}(i\omega_n)e^{i\omega_n\epsilon} + \phi^*_{\sigma,i}\phi_{\sigma,i} \stackrel{!}{=} \langle\hat{n}_i^\sigma\rangle_{AIM}. \tag{4.112}$$

For every site and species this yields a value of $\epsilon$ which can be used to calculate the kinetic energy in the local representation (4.111).

## 4.6 Spectral functions

As DMFT is a method based on Green's functions, it may also be used to obtain information about the spectral properties of a given system. The spectral function corresponding to a given (normal) two-point Green's function is obtained via the relation

$$\mathcal{A}_{i,j}(\omega) = -\frac{1}{\pi}\mathrm{Im}G_{b_i^\dagger,b_j}(\omega), \tag{4.113}$$

[12] In general it depends on the convergence behavior of the limits, whether they can be exchanged.

where $i$ and $j$ are different lattice sites in this case. This relation holds independently of the use of real or imaginary frequencies, but when computing the spectral function for real frequencies one has to keep in mind the imaginary offset $\eta = i0^+$ needed for the poles on the real axis. Thus for real frequencies one has to use the Lehmann representation (4.59) in the following form:

$$G_{a,b}(\omega) = -\frac{1}{Z}\sum_{m,m'}\frac{\exp(-\beta E_{m'}) - \exp(-\beta E_m)}{E_{m'} - E_m + \omega + \eta i}\langle n|\hat{a}|m\rangle\langle m|\hat{b}|n\rangle. \tag{4.114}$$

The analytic continuation from the imaginary Matsubara frequencies, which are used in the self-consistent DMFT loop where the Green's functions are given as analytic functions via the Lehmann representation, to real frequencies is thus straightforward. But there is a caveat when using exact diagonalization to solve the impurity model. In that case we model the effective bath contribution to the interacting local Green's function via an Anderson impurity Hamiltonian with a finite number of bath sites (4.17). While this yields a very high accuracy approximation in imaginary frequencies already for a very low number of orbitals (typically 3-4 are fine), the discreteness of the spectrum becomes strongly apparent in real frequencies, as shown in Fig. 4.2 for the local density of states $\mathcal{A}_{i,i}(\omega)$ in a homogeneous Mott state on a two-dimensional square lattice. We can furthermore see that the convergence observed in the imaginary frequencies does not necessarily translate to an equal convergence in real frequencies, also as a result of the discrete spectrum in the impurity spectral function versus an approximately continuous spectrum on the diagonal of the lattice spectral function. We furthermore note that $\eta$ has to be set to a small nonzero value, in order to obtain a smooth spectrum. Its value determines the width of the Lorentzian broadening of the otherwise delta-shaped peaks.

Due to the relation of the spectral function to the commutator (see Sec. 6.4.2) one finds the sum rule

$$\int \mathcal{A}_{i,j}(\omega)d\omega = \delta_{i,j}. \tag{4.115}$$

Therefore integrating the local density of states should always result in the value one. As can be seen this is only approximately the case in the DMFT result. The deviation for the impurity model spectral function ($G_i$ in Fig. 4.2) on the one hand stems from the broadening induced by $\eta$, as the considered interval cuts off part of the tail, while a direct sum of the spectral weights in the Lehmann representation exactly fulfills the sum rule. The mismatch in case of the diagonal part of the interacting Green's function ($G_{ii}$ in Fig. 4.2) on the other hand results from the discrete spectrum representation of the self-energy used in the lattice Dyson-equation versus the continuous spectrum in its non-interacting part.

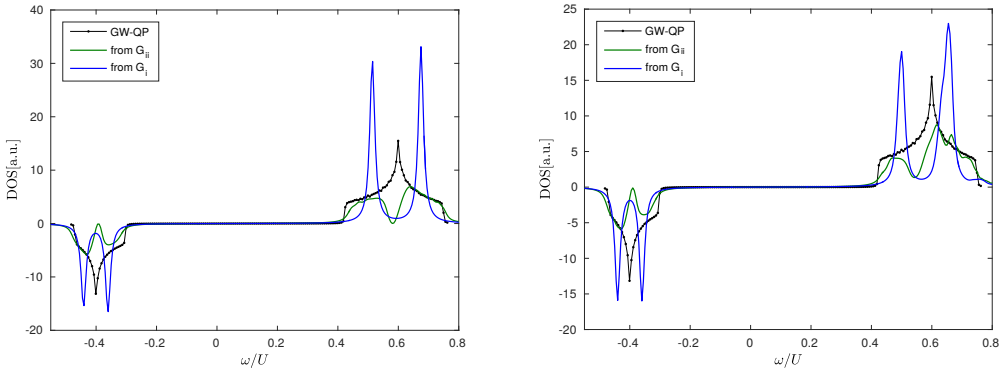


FIGURE 4.2: Spectra obtained either via the quasiparticle method (GW-QP, discussed in Chap. 6) or from a converged real-space DMFT result using an exact diagonalization solver. For DMFT two versions of the DOS are shown: one given by the impurity Green's function $G_i$ and the other corresponding to the local part of the interacting lattice Green's function $G_{ii}$. Here we use the parameters $\eta/U = 0.01$ as well as $\mu/U = 0.4$ and $t/U = 0.02$ within a simple single-component Bose-Hubbard model on a two-dimensional square lattice, corresponding to an insulating Mott state with unit filling. For the DMFT result we consider two cases: 2 bath orbitals for the impurity model in a system of $16 \times 16$ sites (*left*) where the sum-rule yields $0.9891$ (blue) and $0.7792$ (green), as well as 4 orbitals for the impurity in a system of $8 \times 8$ sites (*right*) where the sum-rule yields $0.9891$ (blue) and $0.8978$. The quasiparticle description yields $1.0000$ in the sum rule, when using a Fock-space truncation of at least $n = 10$.

# Chapter 5

# Truncation of the bosonic Fock basis

Applying any diagonalization-based method to a bosonic lattice system, which is not entirely in an insulating phase, often requires the use of a truncation scheme for the local Hilbert space. This is most evident for methods which are based on variational wave functions, as for example the bosonic Gutzwiller state (GS) [Gut63; Gut64; Gut65; RK91; KCB92] $|\psi\rangle = \prod_i |\psi_i\rangle$, because any numerical implementation requires a finite number of variational constants, which is realized by employing a truncation scheme. Related examples are the density matrix renormalization group (DMRG) [Whi92; Sch05; Hal06] and derived methods such as matrix product states [ÖR95; VMC08; Sch11; Orú14], projected entangled pair states [VMC08; MVC07; Orú14], as well as time-evolving block decimation [Vid03; Vid04; VGRC04; ZV04], which all require a truncation of the local occupation number basis to several lowest number states. The same is correspondingly true for bosonic single-impurity Anderson models [LBB10] as used in numerical renormalization-group [GI07] approaches and dynamical mean-field theory (DMFT) [MV89; GK92; Geo+96; KV04; And+11]. DMFT relies on either mapping a correlated many-body problem onto bosonic Anderson impurity models [HSH09; SH13] or directly solving the action via truncation-free stochastic methods [BV08; And+11] such as the continous-time Monte Carlo method [Gul+11]. Nevertheless some effort has been made within DMRG, going beyond the simple truncation, by implementing an "optimal phonon basis" [ZJW98] which is conceptually similar to the ansatz we will discuss in this chapter.

To a varying degree, all these methods will suffer from an insufficient truncation, while an increased basis size requires a corresponding increase in computing power. While matrix size can be limited independent of this truncation in DMRG methods, these usually describe states in terms of a locally truncated number basis. Therefore the cutoff $N_c$ also determines the possible overall truncation error. Furthermore, whenever solving a quantum impurity system by diagonalization, the corresponding matrices scale as $\prod_i M_i^2$, where $i$ represents internal degrees of freedom (IDOF) and $M_i$ is the size of each corresponding Hilbert space requiring a truncation for bosonic IDOF. The same relation is true for the variational GS for which $i$ represents all sites and IDOF under consideration.

As we will show for the cases of DMFT and the GS, the use of a single additional variational basis state, which we denote as **coherent-tail** state (CTS), can strongly increase the accuracy as compared to the common truncation scheme. Especially for DMFT the CTS is highly efficient: even strongly reduced Hilbert spaces suffice to well approximate the (quasi-)exact DMFT results obtained by using a Hilbert space more than three times as large. Due to this reduction in computational complexity, this scheme is accompanied by a more than tenfold increase in numerical efficiency, as was shown in [GH17], which this chapter is based upon.

## 5.1 The coherent-tail state

In any numerical second quantized method utilizing the grand canonical ensemble of an interacting Bose gas on a lattice, at some point it becomes necessary to approximate the infinite local Fock basis in order to allow for results within a finite algorithm. As a test case, let us consider the standard Bose-Hubbard model [GK63; Fis+89; Jak+98]

$$H = -t \sum_{\langle i,j \rangle} (\hat{b}_i^\dagger \hat{b}_j + \hat{b}_j^\dagger \hat{b}_i) + \frac{U}{2} \sum_i \hat{n}_i(\hat{n}_i - 1) - \mu \sum_i \hat{n}_i. \tag{5.1}$$

We use the common notation, where $\hat{b}_i$ ($\hat{b}_i^\dagger$) is the annihilator (creator) of a boson at site $i$, while $\hat{n}_i$ is the corresponding particle number operator $\hat{n}_i = \hat{b}_i^\dagger \hat{b}_i$. The tunneling rate $t$ [BZ08] and the local Hubbard interaction $U$ [BZ08] are tunable by Feshbach resonances [Fes58; Cou+98; Ino+98], while the chemical potential $\mu$ determines the total particle number.

Numerous techniques have been applied to investigate this model, ranging from the Gross-Pitaevskii equation [PSG02; KHS15], Bogoliubov theory [TAV07; Kol07; HP15] and variational mean-field methods such as the GS [She+93; Buo+09] to more advanced techniques including Monte Carlo methods [CS+08; KK09; Pol13] and bosonic DMFT (B-DMFT) [BV08; HSH09; SH13; And+11]. For numerical simulations in any of these methods, one needs to limit the infinite local Fock basis of bosons by a finite occupation number cutoff $N_c$. While $N_c$ can be arbitrarily high in principle, some methods require a comparatively low $N_c$ in order to limit the numerical effort. Let us now focus on the GS and B-DMFT, which both become exact in the atomic limit $t/U \to 0$ as well as the non-interacting limit $U/t \to 0$. In between these limits both are also exact in the infinite dimensional limit, while the latter method also includes the effect of non-local fluctuations up to first order in $1/z$, where $z$ is the number of nearest neighbor sites. In the non-interacting case, the exact ground-state can be written as a product of coherent states over the lattice sites $i$, so

$$|\psi\rangle = \prod_i |\alpha_i\rangle\,, \tag{5.2}$$

which also corresponds to the macroscopic condensate wave function $\Psi(i) = \langle \psi | \hat{b}_i | \psi \rangle$ solving the Gross-Pitaevskii equation. Despite some effort [KN11] this correspondence is yet to be fully investigated.

For now we will focus on the intermediate superfluid regime, where for fixed chemical potential an increase in $t/U$ will result in an increasing mean particle number. In order to keep track of the ground-state, one would generally need to include a proportionally increasing number of Fock states in any method that requires a $N_c$. This is true for both GS and B-DMFT. In order to retain a small set of basis states, one should now switch to an optimized basis set similar to [ZJW98], but we also want to limit the computational cost. Therefore let us propose the following truncation scheme, where we simply replace the highest included number state by a variational state $|\alpha_{N_c}\rangle$, given as a linear combination of all remaining Fock states. Further requiring $\hat{b}\,|\alpha_{N_c}\rangle$ to be given as an exact linear combination of the new basis, thus reducing "leakage" out of the basis, yields the coherent-tail state (CTS) $|\alpha_{N_c}\rangle$:

$$\widetilde{|\alpha_{N_c}\rangle} = \sum_{n=N_c}^{\infty} \frac{(\alpha_{N_c})^n}{\sqrt{n!}} |n\rangle\,. \tag{5.3}$$

This is a coherent state with the lower occupation numbers projected out. In order to act as a proper basis state it therefore has to be normalized:

$$|\alpha_{N_c}\rangle = c_{N_c}\widetilde{|\alpha_{N_c}\rangle}, \quad \text{where} \quad c_{N_c} = \left(\sum_{n=N_c}^{\infty} |\alpha_{N_c}|^{2n}/n!\right)^{-1/2}. \tag{5.4}$$

This state extends the finite basis of $N_c$ Fock states $\{0, 1, 2, \ldots, N_c - 1\}$, which in the following we denote as $N_c$-Fock basis, to $\{0, 1, 2, \ldots, N_c - 1, \alpha_{N_c}\}$. As the CTS are no longer actually coherent, and as such not eigenstates of the annihilation operator, they instead satisfy relations of the form

$$\hat{b}\,|\alpha_{N_c}\rangle = c_{N_c}\frac{(\alpha_{N_c})^{N_c}}{\sqrt{(N_c-1)!}}\,|N_c - 1\rangle + \alpha_{N_c}\,|\alpha_{N_c}\rangle\,, \qquad N_c > 1; \tag{5.5}$$

$$\begin{aligned}\hat{b}\hat{b}\,|\alpha_{N_c}\rangle =& c_{N_c}\frac{(\alpha_{N_c})^{N_c}}{\sqrt{(N_c-2)!}}\,|N_c - 2\rangle \\ &+ \alpha_{N_c}\left(c_{N_c}\frac{(\alpha_{N_c})^{N_c}}{\sqrt{(N_c-1)!}}\,|N_c - 1\rangle + \alpha_{N_c}\,|\alpha_{N_c}\rangle\right), \qquad N_c > 2; \\ &\vdots\end{aligned} \tag{5.6}$$

These expressions are necessary to calculate additional matrix elements beyond those already given in the Fock basis. In principle one can derive these properties for any number of annihilation operators, but as most considered systems only require two particle terms at most, for example the system of main focus in this thesis as discussed in Sec. 3.2, let us only consider the relations above.

Note that matrix elements within this basis will be as sparse as in the original representation, even in multi-component or cluster simulations [AKL11; Lüh13]. In the following sections we will see how this soft bosonic truncation allows for significantly improved numerical accuracy in both GS and B-DMFT and for a dramatically reduced calculation time at fixed accuracy within B-DMFT.

## 5.2 Gutzwiller mean-field state

We now consider the GS which is given by the ansatz $|\psi_G\rangle = \prod_i |\psi_i\rangle$, where $|\psi_i\rangle$ is usually written as a linear combination of the $N_c$-Fock basis states, while in our case this basis will be extended by the CTS. Due to the factorized wave function the effective Hamiltonian has the form

$$H_G = -t\sum_{\langle i,j\rangle}(\hat{b}_i^\dagger\phi_j + \text{h.c.}) + \frac{U}{2}\sum_i \hat{n}_i(\hat{n}_i - 1) - \mu\sum_i \hat{n}_i, \tag{5.7}$$

where $\phi_i = \langle\hat{b}_i\rangle$. It is thus a set of local many-body problems coupled by the self-consistent fields $\phi_i$ (commonly called condensate order parameter). The ground-state energy of this simplified Hamiltonian is found by variation of these fields. In a homogeneous system where every site has $z$ nearest neighbors and in the absence of spontaneous symmetry breaking, the problem reduces to a single variable $\phi$, thus further simplifying (5.7):

$$H_{\mathrm{G}}^{\mathrm{local}} = -tz(\hat{b}^{\dagger}\phi + \phi^{*}\hat{b}) + \frac{U}{2}\hat{n}(\hat{n}-1) - \mu\hat{n}. \tag{5.8}$$

In general this problem can be solved in an arbitrary local basis, but any numerical implementation requires a truncation, for example to the common finite $N_c$-Fock basis, or in our case the CTS extended $N_c$-Fock basis. Within this basis we utilize the properties (5.5) and (5.6) to calculate additional matrix elements of $H_{\mathrm{G}}^{\mathrm{local}}$. Note that the CTS acts as the Fock state $|N_c\rangle$ for $\alpha_{N_c} \to 0$. Now one only needs to find the minimum of $E_{\mathrm{tot}}^{\mathrm{G}} = \langle\psi_{\mathrm{G}}|H_{\mathrm{G}}^{\mathrm{local}}|\psi_{\mathrm{G}}\rangle$ by simultaneous variation of the physical parameter $\phi$ and the non-physical CTS-parameter $\alpha_{N_c}$. Since the final result has to be independent of the truncation scheme, a comparison for various $N_c$ and $\alpha_{N_c}$ at given values of $\mu/U = t/U = 0.4$ reveals the limited efficiency of the CTS (see Fig. 5.1). Thus we can now tell how a CTS-extended basis with reduced cutoff compares to a large $N_c$-Fock basis.

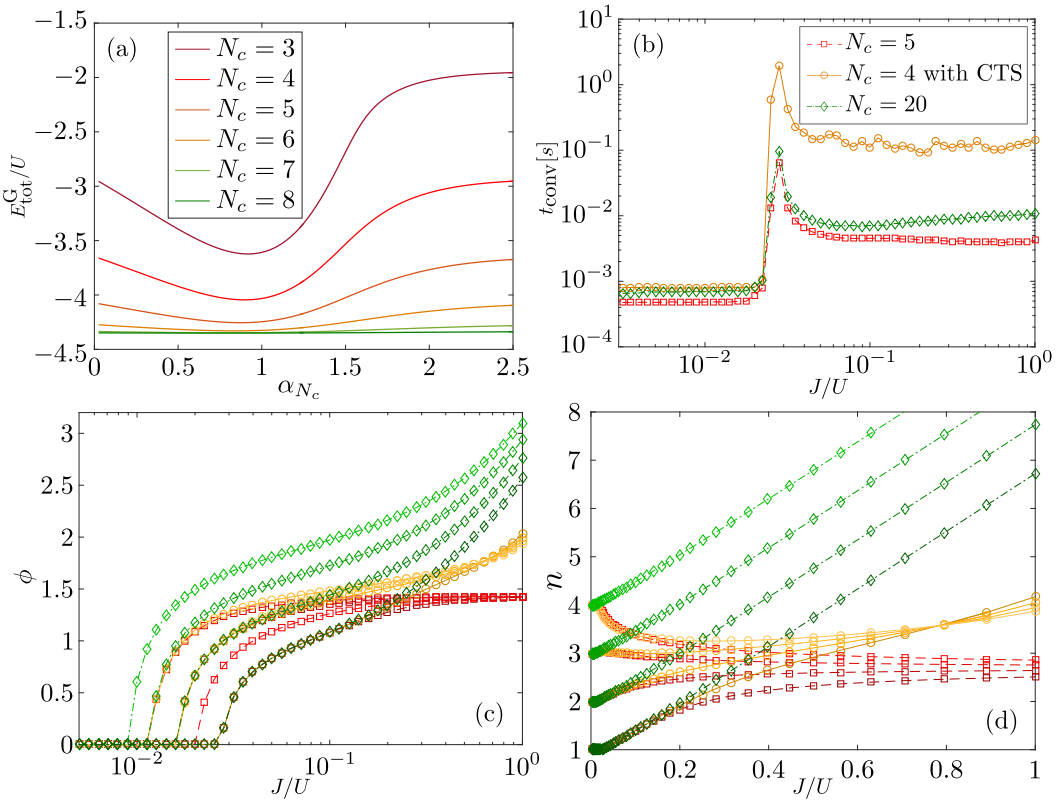


FIGURE 5.1: (a) Possible reduction of $E_{\mathrm{tot}}^{\mathrm{G}} = \langle\psi_{\mathrm{G}}|H_{\mathrm{G}}^{local}|\psi_{\mathrm{G}}\rangle$ via variation of $\alpha_{N_c}$, for various truncations denoted by $N_c$, with $t/U = \mu/U = 0.4$ and $z = 6$. (b) Convergence time of the GS for various truncation schemes, as given in the legend, and $\mu/U = 1.5$. Graphs (c,d) depict the expectation values of the observables $\langle\hat{b}\rangle$ and $\langle\hat{n}\rangle$ for various $\mu = 0.5, 1.5, 2.5, 3.5$ (dark to bright colors; corresponding to the Mott lobes $n = 1, 2, 3, 4$) and truncations as in legend (b).

At any truncation level, if the CTS is added to the $N_c$-Fock basis $E_{\mathrm{tot}}^{\mathrm{G}}$ is improved in comparison to a simple additional Fock state, corresponding to $\alpha_{N_c} \to 0$ in Fig. 5.1(a) [also consider Fig. 5.1(c,d)]. One even improves upon the mean-field Mott transition for Mott lobes $n = \langle\hat{n}\rangle = N_c$ at the limit of the Fock basis with cutoff $N_c + 1$ [see Fig. 5.1(c,d)]. But due to the necessary optimization of $\alpha_{N_c}$, this comes at an additional computational cost [see Fig. 5.1(b)]. The GS thus does not benefit much from

the CTS, as far as computational effort is considered. But as we will show, within B-DMFT the CTS truncation scheme leads to a significant speed-up paired with the increased accuracy.

## 5.3 Bosonic dynamical mean-field theory

For B-DMFT the CTS extended Fock basis can be used by the impurity solver within the self-consistent loop. Its implementation is most straightforward in the exact diagonalization method. In that case, the lattice Hamiltonian is mapped onto an effective Anderson impurity model [HSH09; SH13], which is an extended version of the GS Hamiltonian (5.7) as can be seen in Sec. 4.1,

$$\begin{aligned}\mathcal{H}^{\text{eff}}_{\text{AIM}} =& \frac{U}{2}\hat{n}_0\left(\hat{n}_0-1\right)-\mu\hat{n}_0+\sum_l \epsilon_l \hat{a}_l^\dagger \hat{a}_l - t\left(\hat{b}_0^\dagger\left(\sum_{\langle i,0\rangle}\langle\hat{b}_i\rangle_C\right)+\hat{b}_0\left(\sum_{\langle i,0\rangle}\langle\hat{b}_i^\dagger\rangle_C\right)\right)\\ &+\sum_l\left(V_l\hat{a}_l^\dagger\hat{b}_0+V_l^*\hat{a}_l\hat{b}_0^\dagger+W_l\hat{a}_l\hat{b}_0+W_l^*\hat{a}_l^\dagger\hat{b}_0^\dagger\right).\end{aligned} \tag{5.9}$$

The additional terms including the annihilation (creation) operators $\hat{a}_l$ ($\hat{a}_l^\dagger$) describe effective bath orbitals which self-consistently mimic the action of the lattice sites surrounding the given site $j = 0$ in the Hubbard model (5.1). They do so via the orbital energies $\epsilon_l$, normal hoppings $V_l$ and anomalous hoppings $W_l$. For an optimal representation of this action, increasing the number of bath orbitals is favorable over increasing bath truncations. They are therefore treated as hard-core bosons. The cavity expectation value $\langle . \rangle_C$ is computed in a system where the impurity site has been removed, which is required due to the mapping onto the effective model as discussed in Sec. 4.1. In the case of a homogeneous lattice gas, used here for benchmarking purposes easily allowing for comparisons with truncations as high as $N_c = 20$, the term containing the self-consistent cavity order parameter simplifies to $\sum_i \langle b_i \rangle_C = z \cdot \phi_C$, where $z$ is the number of nearest neighbours, and $\phi_C$ is the cavity expectation value of the condensate order parameter.

Within this implementation, a choice of $\alpha_{N_c}$ to compute the ground-state of the full system, is efficiently obtained by minimizing the energy $E_{\text{AIM}} = \langle 0|\mathcal{H}^{\text{eff}}_{\text{AIM}}|0\rangle$ for the lowest energy eigenstate $|0\rangle$ of the self-consistent $\mathcal{H}^{\text{eff}}_{\text{AIM}}$ with regard to the variational parameter $\alpha_{N_c}$. This yields the optimal representation for the low energy spectrum of $\mathcal{H}^{\text{eff}}_{\text{AIM}}$ which determines the interacting Green's function in the Lehmann representation (4.59). Another way of optimization would be the minimization of the self-consistently converged DMFT expectation value $E_{\text{tot}}(\alpha_{N_c}) = \langle H \rangle$ in relation to $\alpha_{N_c}$, where we define $E^{\text{DMFT}}_{\text{tot}}$ as this minimum. Let us emphasize that the optimal $E_{\text{tot}}(\alpha_{N_c})$ should not depend on the choice of basis, so neither a variation in $N_c$ nor in $\alpha_{N_c}$ should result in a significant change of its self-consistent value, as is indeed verified exemplarily for $\mu/U = t/U = 0.4$ in Fig. 5.2(a). Then the optimal CTS state allows for a remarkably good approximation of the total BDMFT energy even at a very low Fock space truncation $N_c$ [see Figs. 5.2(a) and 5.3(c)].

A further look at the convergence times reveals the numerical benefit of replacing a large number of Fock states (all those with $n \geq N_c$) by the single variational state $|\alpha_{N_c}\rangle$. We have simulated the Bose-Hubbard-model (5.1) within B-DMFT using a Bethe lattice with $z = 6$ for $0 \leq \mu/U \leq 3.5$ and $0 < t/U \leq 1$. The convergence times for various truncation schemes are shown in Fig. 5.2(b) for $\mu/U = 0.4$. Note the above 10-fold decrease in convergence times when using the CTS-extended Fock

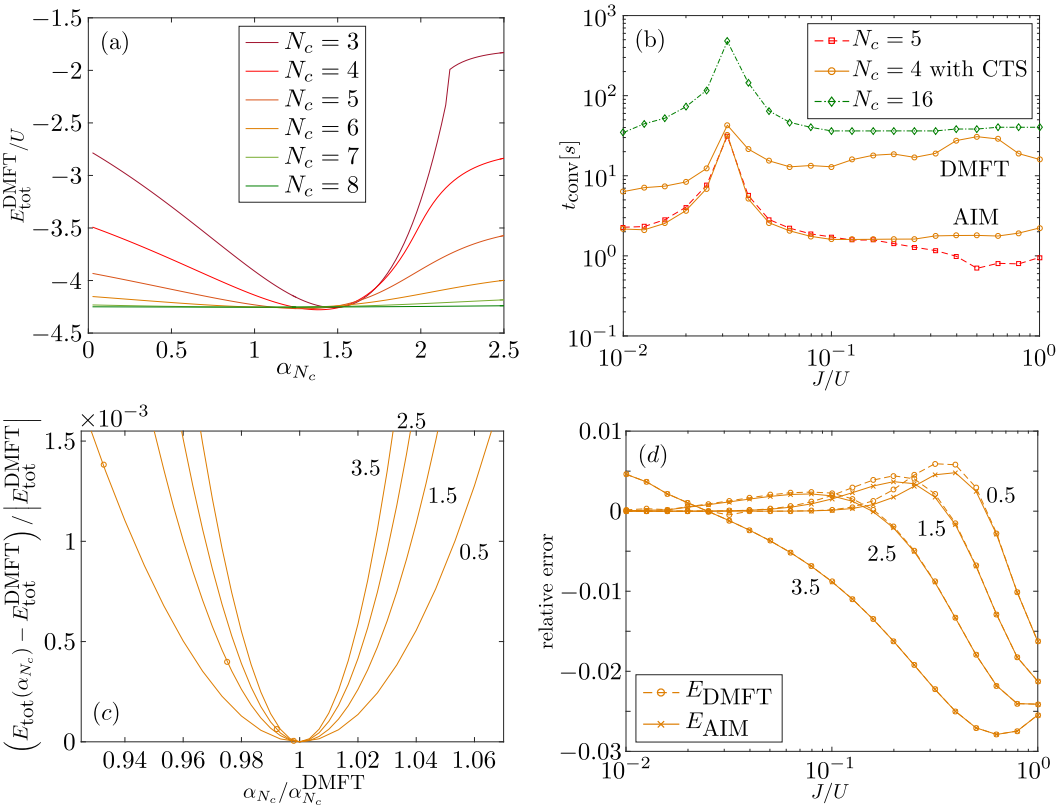


FIGURE 5.2: (a) Reduction of $E_{\mathrm{tot}}^{\mathrm{DMFT}}$ achieved by variation of the CTS via $\alpha_{N_c}$ for various values of $N_c$. Shown are self-consistent BDMFT results for $\mu/U = t/U = 0.4$ and $z = 6$ (also used in (b,c,d)). (b) Comparison of convergence times of BDMFT for various truncation schemes, as given in the legend and annotation, with $\mu$ chosen as in (a). The two optimization schemes described in the text are compared in (c,d). (c) depicts the relative deviation of $E_{\mathrm{tot}}(\alpha_{N_c})$ from its minimum, while the value found via minimization of $E_{\mathrm{AIM}}$ is given by each marker. The corresponding simulations are performed for $t/U = 0.3162$. In (d) the resulting total energies, found by minimizing either $E_{\mathrm{AIM}}$ or $E_{\mathrm{DMFT}} = E_{\mathrm{tot}}^{\mathrm{DMFT}}$, are compared to the exact energies, as calculated for a regular cutoff $N_c = 20$. The used values of $\mu/U$ are given in each graph (c,d).

basis compared to the regular Fock basis with a high $N_c$, as used for the (quasi-)exact solution. While this speed-up is only possible over the full range of parameters when optimizing $E_{\mathrm{AIM}}$, this simplified scheme leads to negligible deviations in the energy [as shown in Figs. 5.2(c,d)]. Also note the additional time loss of the CTS scheme compared to a truncation of equal basis size at large $t/U$, which is due to the need to optimize $\alpha_{N_c}$, by finding either the minimum of $E_{\mathrm{AIM}}$ or of $E_{\mathrm{tot}}$, while the latter also requires multiple runs of fully converged DMFT simulations. Due to these minor differences we now focus on results obtained via the first scheme.

Regarding physical observables, we have calculated local observables such as the condensate order parameter $\phi = \langle \hat{b} \rangle$ and the occupation number $n = \langle \hat{n} \rangle$, as well as the non-local non-condensate fluctuations $G_c(t = 0) = -\left(\left\langle \hat{b}_i^\dagger \hat{b}_j \right\rangle - \left\langle \hat{b}_i^\dagger \right\rangle \left\langle \hat{b}_j \right\rangle\right)$, where $i$ and $j$ are nearest neighbors. This expression is more commonly denoted as the connected Green's function at equal times, which we can directly extract within B-DMFT as discussed in Sec. 4.5. Furthermore we also obtain the total energy $E_{\mathrm{tot}}$ and the kinetic energy $E_{\mathrm{kin}}^{\mathrm{con}}$ through the connected part of the Green's function, allowing

for a comparison of the quality of different truncation schemes:

$$E_{\text{kin}}^{\text{con}} = -tz\left(\left\langle \hat{b}_i^\dagger \hat{b}_j \right\rangle - \phi^* \phi\right) = tzG_c(t=0). \tag{5.10}$$

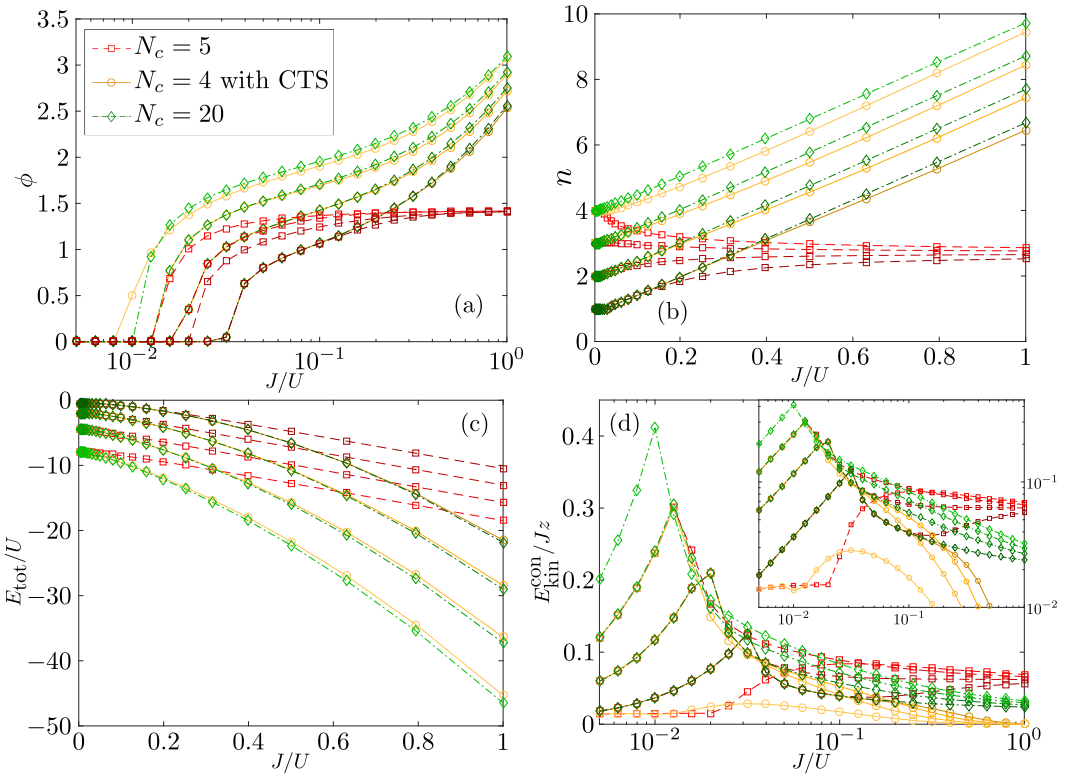


FIGURE 5.3: Results from converged BDMFT simulations, obtained for various truncation schemes, coded by colors and symbols shown in legend (a). Simulations were done for $\mu/U = 0.5, 1.5, 2.5, 3.5$ (dark to bright colors) and $z = 6$. Shown are the local observables $\phi$ (a), $n$ (b), the total energy per site $E_{\text{tot}} = \left\langle \hat{H} \right\rangle / L$ (c), where $L$ is the number of lattice sites, and the connected Green's function $G_c(t = 0)$ (d), as discussed in the main text (5.10). The inset of (d) shows the same data plotted on a double log-scale for a better overview.

As is visible from the local observables as well as the total energy, replacing the highest Fock state $|N_c\rangle$ by the CTS $|\alpha_{N_c}\rangle$ tremendously improves the results to almost the same accuracy as the (quasi-)exact result from the increased cutoff $N_c = 20$ [see Figs. 5.3(a)-(c)]. Remarkably, the CTS truncation even predicts the Mott transition for the Mott lobe $n = 4$ (for $\mu/U = 3.5$) almost exactly, as shown Fig. 5.3(a), while the regular cutoff $N_c = 5$ fails to do so. Both truncations also yield wrong values for the connected Green's function $G_c(t = 0)$ [see Fig. 5.3(d)]. Just about where the occupation number $n$ exceeds $N_c$, the high accuracy of local observables is lost as well. Differences between the three cases can be seen most clearly in the non-condensed contribution to the kinetic energy (5.10), which are due to non-local fluctuations described by the connected Green's function [see Fig. 5.3(d)]. These have a monotonously decreasing tail for $t/U \to \infty$ in the exact solution. Obviously the ratio of these fluctuations to the condensate fluctuations of the condensate order parameter ($\propto G_c(t = 0)/\|\phi\|^2$) vanishes in this limit. But a hard and low truncation results in an artificially increased value of the non-local non-condensate fluctuations beyond certain values of $t/U$, while the CTS leads to the opposite behaviour, where the tail is damped more than in the exact result, thus suppressing non-condensate

fluctuations early. This is likely a result of the CTS being more heavy-tailed than the Hubbard interaction would allow [KN11]. As non-condensate fluctuations only give a sub-leading contribution to the kinetic energy, it becomes clear why the CTS allows for the tremendous increase in accuracy and speed-up in numerical simulations compared to a simple high Fock space cutoff $N_c$ even for large $t/U$.

In conclusion, we see that the introduced truncation scheme based on the CTS (5.3) leads to an increase in the numerical accuracy and computational efficiency of GS and B-DMFT simulations. This increase is shown to be especially pronounced in B-DMFT. Therefore the method allows for B-DMFT simulations at much larger densities, but with reasonable computational effort. It is thus also a very promising method for accurate simulations of systems at higher filling per site. Furthermore cluster-based methods [AKL11; Lüh13] should especially benefit from this softened truncation, since the size of their Fock basis scales as $N_c^L$ with cluster size $L$. The concept of softening the hard cutoff, usually applied in the number basis, should thus more generally benefit a wide range of numerical simulations of bosonic lattice systems. Within this thesis it is used to reduce the local Fock space of the considered two-component models, see Sec. 3.2.

# Chapter 6

# Operator based quasiparticle theory of quantized fluctuations

In this chapter we will derive the generalized quasiparticle theory first introduced by Bissbort [Bis12; BBH14], which can be understood as an extension of the Bogoliubov theory [Bog47] (also discussed in [PS03; PS08]) beyond the limit of a single band of quasiparticle modes. It is based on linearized fluctuations of a variational many-body ground-state wave function, which in our case will be given by a Gutzwiller product wave function. We will show how this method can be extended to systems with multiple bosonic components in combination with interspecies hopping aka Rabi oscillations and long-range interactions, which also imply spontaneous breaking of translational symmetries, thus removing the assumption of a homogeneous ground-state utilized in [Bis12; BBH14].

Following [Bis12] in the introduction of the method, we will show how second order fluctuations, which are neglected in the Gutzwiller ansatz, can exactly be represented in the eigenbasis of the local Gutzwiller Hamiltonian. While it can be shown that this is analogous to a calculation of the linearized equations of motion [Bis12], here we will only consider the formulation in terms of fluctuation operators. Along the way we will go beyond [Bis12], by readily including the effect of the extended Bose-Hubbard-Hamiltonian which includes the effect of Rydberg states. The purpose of these calculations is the derivation of a second order expansion of the full Hamiltonian in terms of aforementioned fluctuation operators. Diagonalization of this Hamiltonian reveals the spectrum of quasiparticle excitations with the Gutzwiller ground-state as its quasi-vacuum. Due to the nature of this second order expansion, this extended description will only include non-interacting long-lived quasiparticles, while their zero-point energies lead to a renormalization of the

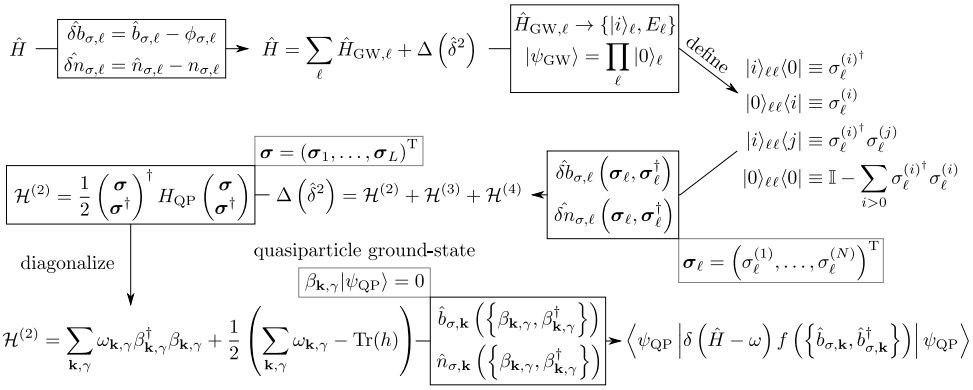


FIGURE 6.1: Schematic depiction of the work-flow of the quasiparticle method described in this chapter.

ground-state energy.

We will furthermore discuss how any local operator and thus arbitrary combinations of them can be represented in terms of the quasiparticle basis. This will allow for the derivation of many experimentally relevant observables, including the spectral function ($\mathcal{A}^{(2)}(\mathbf{k},\omega)$) and the dynamic structure factor (DSF, $S(\mathbf{k},\omega)$), among others. See Fig. 6.1 for a schematic depiction of the corresponding work-flow, starting from the Gutzwiller ground-state and going all the way to the calculation of the spectral functions. The various appearing quantities will be discussed throughout this chapter.

## 6.1 Derivation of the quasiparticle Hamiltonian

When deriving the quasiparticle representation we should keep in mind the Hamiltonian we are going to investigate, especially due to the various types of spontaneous symmetry breaking expected to be involved. As a reminder let us once more consider the general form of the Hamiltonian

$$\hat{H} = \hat{H}_{2BH,kin} + \sum_{\ell}^{N} \left( \hat{H}_{2BH,loc,\ell} + \hat{H}_{R,\ell} + \hat{H}_{int,\ell} \right). \tag{6.1}$$

The terms $\hat{H}_{2BH}$ correspond to the standard Bose Hubbard model for two particle components, while the terms $\hat{H}_R$ and $\hat{H}_{int}$ are extensions which introduce Rabi oscillations between the two components on the one hand and long-range interaction of the Rydberg states on the other. We assume a more general form for the interaction, thereby including models, where the interaction is given by the effective long-range interaction of a component far off resonantly dressed by a Rydberg state.

$$\hat{H}_{2BH,kin} = -t \sum_{\langle \ell,\ell' \rangle} \left( \hat{b}^{\dagger}_{g,\ell} \hat{b}_{g,\ell'} + \eta \hat{b}^{\dagger}_{e,\ell} \hat{b}_{e,\ell'} + \text{h.c.} \right), \tag{6.2}$$

$$\hat{H}_{2BH,loc,\ell} = U \left( \frac{\hat{n}^g_\ell}{2} (\hat{n}^g_\ell - 1) + \lambda \hat{n}^g_\ell \hat{n}^e_i + \tilde{\lambda} \frac{\hat{n}^e_\ell}{2} (\hat{n}^e_\ell - 1) \right) - \mu \left( \hat{n}^g_\ell + \hat{n}^e_\ell \right), \tag{6.3}$$

$$\hat{H}_{R,\ell} = \frac{\Omega}{2} \left( \hat{b}^{\dagger}_{g,\ell} \hat{b}_{e,\ell} + \hat{b}^{\dagger}_{e,\ell} \hat{b}_{g,\ell} \right) - \Delta \hat{n}^e_\ell, \tag{6.4}$$

$$\hat{H}_{int,\ell} = \frac{1}{2} \sum_{\ell \neq \ell'} \hat{n}^e_\ell \hat{n}^e_{\ell'} V\left(\mathbf{r}_\ell, \mathbf{r}_{\ell'}\right). \tag{6.5}$$

In order to determine the Gutzwiller ground-state of such a system let us first introduce the variational Gutzwiller wave function, which in the general case assumes an arbitrary site wise factorization of the many-body ground-state:

$$|\psi_G\rangle = \prod_{\otimes \ell}^{L} |\psi_\ell\rangle, \quad \text{with} \quad |\psi_\ell\rangle = \sum c^{(\ell)}_n |n_\ell\rangle. \tag{6.6}$$

Here the states $|n_\ell\rangle$ are local Fock-states for the site $\ell$ with the particle number $n_\ell$. The state (6.6) is thus defined via local sets of variational parameters given by the coefficients $c^{(\ell)}_n$ with the additional local normalization constraint $\sum_n \left| c^{(\ell)}_n \right|^2 = 1$.

Thus the straightforward way of finding an approximate ground-state within this ansatz is to minimize the total many-body energy $E_G$ of (6.1) as given by this

state via variation of the coefficients $c_n^{(\ell)}$:

$$E_G = \langle\psi_G|\,\hat{H}\,|\psi_G\rangle = \sum_l E_G^{(\ell)} = \sum_\ell \langle\psi_\ell|\,\hat{H}_{GW,\ell}\,|\psi_\ell\rangle\,. \tag{6.7}$$

Up to an irrelevant complex phase factor in all $c_n^{(\ell)}$ this yields a unique solution. But in an inhomogeneous system this could require a tremendous numerical effort, having to minimize an energy landscape of $N \times L$ dimensions, where $N$ is the size of the local Fock-space[1] and $L$ is the number of distinct sites, each with a different local Gutzwiller state $|\psi_\ell\rangle$. Also note that minimizing the expression (6.7) implies that each $|\psi_\ell\rangle$ is the lowest energy eigenstate of a local Gutzwiller eigenbasis. From here on we switch the notation denoting the local Gutzwiller eigenstates as $|i\rangle_\ell$, so $|0\rangle_\ell \equiv |\psi_\ell\rangle$, which are the eigenstates of the individual, local and self-consistent Gutzwiller Hamiltonians

$$\begin{aligned}\hat{H}_{GW,\ell'=0} = &-\sum_{\langle 0,\ell\rangle,\sigma} t_\sigma \left(\hat{b}^\dagger_{\sigma,0}\phi_{\sigma,\ell} - \frac{\phi^*_{\sigma,0}\phi_{\sigma,\ell}}{2} + h.c.\right) + \sum_{\sigma,\sigma'}\frac{U_{\sigma\sigma'}}{2}\left(\hat{b}^\dagger_{\sigma,0}\hat{b}^\dagger_{\sigma',0}\hat{b}_{\sigma',0}\hat{b}_{\sigma,0}\right)\\ &+\frac{\Omega}{2}\left(\hat{b}^\dagger_{g,0}\hat{b}_{e,0} + \hat{b}^\dagger_{e,0}\hat{b}_{g,0}\right) - \sum_\sigma \mu_\sigma \hat{n}^\sigma_0 + \sum_{\ell\neq 0}\left(\hat{n}^e_0 n^e_\ell + \frac{n^e_0 n^e_\ell}{2}\right) V\left(\mathbf{r}_0, \mathbf{r}_\ell\right).\end{aligned} \tag{6.8}$$

Depending on the component $\sigma = \{g, e\}$ we have $t_\sigma = \{t, \eta t\}$, $U_{\sigma\sigma'} = \delta_{\sigma,\sigma'}U_\sigma + (1 - \delta_{\sigma,\sigma'})U_{ge}$ where $U_\sigma = \{U, \tilde{\lambda}U\}$ and $U_{ge} = \lambda U$ as well as $\mu_\sigma = \{\mu, \mu + \Delta\}$. We have furthermore introduced the variational fields $\phi_{\sigma,\ell}$ and $n^\sigma_\ell$ which couple the local Hamiltonians amongst each another. These fields thus have to fulfill the self-consistency conditions

$$\phi_{\sigma,\ell} \equiv \left\langle \hat{b}^\dagger_{\sigma,\ell}\right\rangle \quad \text{and} \quad n^\sigma_\ell \equiv \langle \hat{n}^\sigma_\ell\rangle\,. \tag{6.9}$$

This implies a second method for determining the variational Gutzwiller ground-state via a simple iterative procedure. Starting with arbitrary values for $\phi_{\sigma,\ell}$ and $n^\sigma_\ell$ the expressions (6.9) determine updates of these values. These updates are then repeated until a self-consistent solution is found. It can be shown that the minimization procedure and the self-consistent updates yield equivalent results[2] [Bis12].

### 6.1.1 Gutzwiller fluctuation operators

Considering the mean-field Hamiltonian (6.8), we note that it also follows from an expansion of the full Hamiltonian (6.1) in terms of the **fluctuation operators**

$$\hat{\delta b}_{\sigma,\ell} = \hat{b}_{\sigma,\ell} - \phi_{\sigma,\ell} \quad \text{and} \quad \hat{\delta n}^\sigma_\ell = \hat{n}^\sigma_\ell - n^\sigma_\ell\,. \tag{6.10}$$

In order to obtain (6.8), in this expansion, we simply neglect terms beyond first order in any of the fluctuation operators. This corresponds to the assumption of vanishing

[1] $N$ is actually infinity for Bosons, therefore the Fock-basis has to be truncated in numerical simulations, as discussed in further detail in Chap. 5.

[2] While the minimization procedure is easy to optimize in the homogeneous case, it becomes increasingly hard in inhomogeneous systems, due to the increasing number of parameters $c_n^{(\ell)}$. Thus the self-consistent method was implemented throughout the simulations presented in this thesis.

contributions of second order (non-local) fluctuations in the variational energy (6.7), which in turn is the justification for the ansatz (6.6).

Furthermore keeping in mind that each local Gutzwiller mean-field Hamiltonian (6.8) defines a complete set of local basis states $\{|i\rangle_\ell\}$, we will now show how the effect of the second order fluctuations can be retained via this basis. Let us interpret each lowest local eigenstate as "Gutzwiller"-vacuum. Thus we can define transition operators, which annihilate excited Gutzwiller states aka **Gutzwiller fluctuations** $|i\rangle_\ell$ with $i > 0$, as follows:

$$\hat{\sigma}_\ell^{(i)} \equiv |0\rangle_{\ell\,\ell}\langle i| \otimes \prod_{\otimes \ell' \neq \ell} \mathbb{1}_{\ell'}. \tag{6.11}$$

This operator only acts on site $\ell$ where it transfers an excited eigenstate $|i\rangle_\ell$ of the local Gutzwiller basis to the local ground-state $|0\rangle_\ell$. For clarity in the notation we will omit the local unit operators $\mathbb{1}_{\ell'}$ from here onwards. The set of all such defined operators $\hat{\sigma}_\ell^{(i)}$ and their hermitian adjoint operators, in combination with the unit operator $\mathbb{1}_\ell$, are complete in the sense that any many-body operator can be expressed by them. It is sufficient to show this for an arbitrary local operator as any many-body operator can readily be expressed via a linear combination of products of local operators. Since the local Gutzwiller eigenstates constitute a complete local basis we can expand any local operator $\hat{O}^{(\ell)}$ in this basis:

$$\hat{O}^{(\ell)} = \sum_{i,j\geq 0} {}_\ell\langle i|\hat{O}^{(\ell)}|j\rangle_\ell\, |i\rangle_{\ell\,\ell}\langle j| \equiv \sum_{i,j\geq 0} O_{ij}^{(\ell)}\, |i\rangle_{\ell\,\ell}\langle j|. \tag{6.12}$$

By using this representation for the previously neglected higher order fluctuation terms we are able to retain their effect as an expansion in the creation and annihilation operators $\hat{\sigma}_\ell^{(i)^\dagger}$ and $\hat{\sigma}_\ell^{(i)}$ of Gutzwiller fluctuations. In total there are four qualitatively different cases when mapping the transition operators $|i\rangle_{\ell\,\ell}\langle j|$ onto these operators. The possibilities are as follows:

$$|i\rangle_{\ell\,\ell}\langle 0| \equiv \hat{\sigma}_\ell^{(i)^\dagger} \qquad \text{if } i > 0, \tag{6.13}$$

$$|0\rangle_{\ell\,\ell}\langle i| \equiv \hat{\sigma}_\ell^{(i)} \qquad \text{if } i > 0, \tag{6.14}$$

$$|i\rangle_{\ell\,\ell}\langle j| = \hat{\sigma}_\ell^{(i)^\dagger}\hat{\sigma}_\ell^{(j)} \qquad \text{if } i, j > 0, \tag{6.15}$$

$$|0\rangle_{\ell\,\ell}\langle 0| = \mathbb{1}_\ell - \sum_{i>0} \hat{\sigma}_\ell^{(i)^\dagger}\hat{\sigma}_\ell^{(i)}. \tag{6.16}$$

In principle one could represent the last relation (6.16) as any properly normalized linear combination of $\hat{\sigma}_\ell^{(i)}\hat{\sigma}_\ell^{(i)^\dagger}$, but by requiring all operators to appear in normal order the chosen representation (6.16) is unique.

### 6.1.2 Commutation relation and control parameter

An important property of the operators $\hat{\sigma}_\ell^{(i)^\dagger}$ and $\hat{\sigma}_\ell^{(i)}$ are their commutation relations which are easy to derive using (6.15) and (6.16).

$$\begin{aligned}\left[\hat{\sigma}_\ell^{(i)}, \hat{\sigma}_{\ell'}^{(j)^\dagger}\right] =& \delta_{i,j}\delta_{\ell,\ell'} |0\rangle_{\ell\,\ell}\langle 0| - \delta_{\ell,\ell'} |j\rangle_{\ell\,\ell}\langle i| \\ =& \delta_{i,j}\delta_{\ell,\ell'} - \delta_{\ell,\ell'}\left(\delta_{i,j}\sum_{j'>0}\hat{\sigma}_\ell^{(j')^\dagger}\hat{\sigma}_\ell^{(j')} + \hat{\sigma}_\ell^{(j)^\dagger}\hat{\sigma}_\ell^{(i)}\right) \end{aligned} \tag{6.17}$$

$$\left[\hat{\sigma}_\ell^{(i)^\dagger}, \hat{\sigma}_{\ell'}^{(j)^\dagger}\right] = \left[\hat{\sigma}_\ell^{(i)}, \hat{\sigma}_{\ell'}^{(j)}\right] = 0 \tag{6.18}$$

Thus we can see that they behave approximately bosonic, but contain a local second order correction proportional to the local number of fluctuations and a transition element, which both have to be small to justify the bosonic approximation. To make this point more apparent we need to transform to quasimomentum space. Considering a system of $L$ sites, one at first might be tempted to use the naive transformation $\frac{1}{\sqrt{L}}\sum_\ell e^{-i\mathbf{k}\cdot\mathbf{r}_\ell}$, where $\mathbf{r}_\ell$ is the position vector corresponding to site $\ell$. But as we will discuss more thoroughly in Sec. 6.3, a more general transformation is needed for the case of an inhomogeneous ground-state of reduced translational symmetry, which is expected to form in the presence of sufficiently strong long-range interactions. We thus use

$$\begin{aligned}\tilde{\sigma}_{\mathbf{k},s}^{(i)} =& \frac{1}{\sqrt{L_c}}\sum_l e^{-i\mathbf{k}\cdot(\mathbf{r}_l+\mathbf{r}_s)}\hat{\sigma}_{l,s}^{(i)}, \quad \hat{\sigma}_{l,s}^{(i)} = \frac{1}{\sqrt{L_c}}\sum_{\mathbf{k}\in 1.\mathrm{BZ}'} e^{i\mathbf{k}\cdot(\mathbf{r}_l+\mathbf{r}_s)}\tilde{\sigma}_{\mathbf{k},s}^{(i)}, \\ \tilde{\sigma}_{\mathbf{k},s}^{(i)^\dagger} =& \frac{1}{\sqrt{L_c}}\sum_l e^{i\mathbf{k}\cdot(\mathbf{r}_l+\mathbf{r}_s)}\sigma_{l,s}^{(i)^\dagger}, \quad \hat{\sigma}_{l,s}^{(i)^\dagger} = \frac{1}{\sqrt{L_c}}\sum_{\mathbf{k}\in 1.\mathrm{BZ}'} e^{-i\mathbf{k}\cdot(\mathbf{r}_l+\mathbf{r}_s)}\tilde{\sigma}_{\mathbf{k},s}^{(i)^\dagger}. \end{aligned} \tag{6.19}$$

Here $L_c$ is the number of unit cells which tile the full system in a periodic pattern. This implies that the number of independent quasimomenta is correspondingly restricted to a reduced Brillouin zone (1.BZ′). This notation furthermore splits the position vector $\mathbf{r}_\ell = \mathbf{r}_l + \mathbf{r}_s$ into a superlattice part $\mathbf{r}_l$ and the relative position $\mathbf{r}_s$ inside each unit cell denoted by $l$. In that case we find the commutation relations

$$\left[\tilde{\sigma}_{\mathbf{k}',s'}^{(j)}, \tilde{\sigma}_{\mathbf{k},s}^{(i)^\dagger}\right] = \delta_{i,j}\delta_{\mathbf{k},\mathbf{k}'}\delta_{s,s'} - \frac{\delta_{s,s'}}{L_c}R_{\mathbf{k},\mathbf{k}'}^{(i,j)}(s), \tag{6.20}$$

$$\left[\tilde{\sigma}_{\mathbf{k}',s'}^{(i)^\dagger}, \tilde{\sigma}_{\mathbf{k},s}^{(j)^\dagger}\right] = \left[\tilde{\sigma}_{\mathbf{k}',s'}^{(i)}, \tilde{\sigma}_{\mathbf{k},s}^{(j)}\right] = 0. \tag{6.21}$$

Here we introduce the operator $R_{\mathbf{k},\mathbf{k}'}^{(i,j)}(s)$, which describes the deviation from bosonic behavior. It is of the form

$$\begin{aligned} R_{\mathbf{k},\mathbf{k}'}^{(i,j)}(s) =& \sum_l e^{i(\mathbf{k}-\mathbf{k}')\cdot(\mathbf{r}_l+\mathbf{r}_s)}\left(\hat{\sigma}_{l,s}^{(i)^\dagger}\hat{\sigma}_{l,s}^{(j)} + \delta_{i,j}\sum_{j'>0}\hat{\sigma}_{l,s}^{(j')^\dagger}\hat{\sigma}_{l,s}^{(j')}\right) \\ =& \sum_{\mathbf{k}_1\in 1.\mathrm{BZ}'}\left(\tilde{\sigma}_{\lfloor\mathbf{k}-\mathbf{k}'+\mathbf{k}_1\rfloor,s}^{(i)^\dagger}\tilde{\sigma}_{\mathbf{k}_1,s}^{(j)} + \delta_{i,j}\sum_{j'>0}\tilde{\sigma}_{\lfloor\mathbf{k}-\mathbf{k}'+\mathbf{k}_1\rfloor,s}^{(j')^\dagger}\tilde{\sigma}_{\mathbf{k}_1,s}^{(j')}\right). \end{aligned} \tag{6.22}$$

The notation $\lfloor\cdot\rfloor$ describes the back folding of $\mathbf{k}$ to the first Brillouin zone (1.BZ), introduced due to equivalence relations between the quasimomentum space operators (6.19) (analogous to (6.37) discussed in Sec. 6.3). Back folding is achieved by

adding a suitable reciprocal lattice vector $\mathbf{G}$, such that $\lfloor \mathbf{k} \rfloor = \mathbf{k} + \mathbf{G}$ results in a quasi-momentum vector inside 1.BZ. The set of possible vectors $\mathbf{G}$ is implicitly defined as all vectors fulfilling $\mathbf{G} \cdot \mathbf{r}_\ell = 2\pi n$, where $n \in \mathbb{Z}$. Thus we can see that the first term on the right hand side of (6.20) corresponds to the regular bosonic part of order one, while the second term is of the order of the density of quasiparticles, especially notable for $\mathbf{k} = \mathbf{k}'$. But as this factor is scaled by the system size via the prefactor $L_c^{-1}$, the fluctuation operators $\tilde{\sigma}_{\mathbf{k}}^{(i)}$ are also approximately bosonic in the limit of a small density of occupied fluctuations. Therefore we may consider $\langle R_{\mathbf{k},\mathbf{k}'}^{(i,j)}(s) \rangle / L_c$ as a set of control parameters, the maximum of which serves as a figure of merit for the validity of the quasiparticle method.

### 6.1.3 Expansion in fluctuation operators

The mean-field Hamiltonian can thus be written as $H_{GW} = \sum_\ell \sum_{i>0} E_i^{(\ell)} \hat{\sigma}_\ell^{(i)^\dagger} \hat{\sigma}_\ell^{(i)} + \sum_\ell E_0^{(\ell)} (\mathbb{1} - \sum_{i>0} \hat{\sigma}_\ell^{(i)^\dagger} \hat{\sigma}_\ell^{(i)})$. So the full Hamiltonian has the form

$$\hat{H} = \hat{H}_{GW} + \hat{H}_\delta = \sum_\ell \sum_{i>0} \left( E_i^{(\ell)} - E_0^{(\ell)} \right) \hat{\sigma}_\ell^{(i)^\dagger} \hat{\sigma}_\ell^{(i)} + \sum_\ell E_0^{(\ell)} + H_\delta . \tag{6.23}$$

Here the term $\hat{H}_\delta$ includes all terms neglected in the definition of the mean-field Hamiltonian. Thus it consists of all terms with fluctuation operators in second order:

$$\hat{H}_\delta = - \sum_{\langle \ell,\ell' \rangle,\sigma} t_\sigma (\delta\hat{b}_{\sigma,\ell}^\dagger \delta\hat{b}_{\sigma,\ell'} + \delta\hat{b}_{\sigma,\ell'}^\dagger \delta\hat{b}_{\sigma,\ell}) + \frac{1}{2} \sum_{\ell \neq \ell'} \delta\hat{n}_\ell^e \delta\hat{n}_{\ell'}^e V(\mathbf{r}_\ell, \mathbf{r}_{\ell'}) . \tag{6.24}$$

One can now use the completeness of each local Gutzwiller basis set for every site, $\mathbb{1}_\ell = \sum_{i=0}^\infty |i\rangle_{\ell\,\ell} \langle i|$, in order to represent both, or more precisely any, local fluctuation operators appearing in (6.24):

$$\begin{aligned}
\delta\hat{b}_{\sigma,\ell} &= \hat{b}_{\sigma,\ell} - \phi_{\sigma,\ell} & \delta\hat{n}_\ell^\sigma &= \hat{n}_\ell^\sigma - n_\ell^\sigma \\
&= \sum_{i,j=0}^\infty \left( {}_\ell\langle i|\hat{b}_{\sigma,\ell}|j\rangle_\ell - \phi_{\sigma,\ell}\delta_{i,j} \right) |i\rangle_{\ell\,\ell}\langle j| & &= \sum_{i,j=0}^\infty \left( {}_\ell\langle i|\hat{n}_\ell^\sigma|j\rangle_\ell - n_\ell^\sigma \delta_{i,j} \right) |i\rangle_{\ell\,\ell}\langle j| \\
&\equiv \sum_{i,j=0}^\infty \left( B_{i,j}^{\sigma,(\ell)} - \phi_{\sigma,\ell}\delta_{i,j} \right) |i\rangle_{\ell\,\ell}\langle j| & &\equiv \sum_{i,j=0}^\infty \left( N_{i,j}^{\sigma,(\ell)} - n_\ell^\sigma \delta_{i,j} \right) |i\rangle_{\ell\,\ell}\langle j| \\
&\equiv \sum_{i,j=0}^\infty \tilde{B}_{i,j}^{\sigma,(\ell)} |i\rangle_{\ell\,\ell}\langle j| & &\equiv \sum_{i,j=0}^\infty \tilde{N}_{i,j}^{\sigma,(\ell)} |i\rangle_{\ell\,\ell}\langle j|
\end{aligned} \tag{6.25}$$

We note that the matrix elements $B_{0,0}^{\sigma,(\ell)} \equiv \phi_{\sigma,\ell}$ and $N_{0,0}^{\sigma,(\ell)} \equiv n_\ell^\sigma$ are both given by the values of the self-consistent fields, namely the local order parameters. Accordingly all matrix elements $\tilde{B}_{0,0}^{\sigma,(\ell)} = 0$ and $\tilde{N}_{0,0}^{\sigma,(\ell)} = 0$ vanish. Using these expansions we can exactly rewrite the fluctuation part of the Hamiltonian (6.24), which using the notation $\ell' = \ell + \delta\ell$ thus becomes

$$\begin{aligned}\hat{H}_\delta = &- \sum_{\langle \ell,\ell'\rangle,\sigma} t_\sigma \sum_{\substack{i_1,i_2\\ j_1,j_2}} \tilde{F}^{\sigma,(\ell,\ell')}_{i_1,i_2,j_1,j_2} |i_1\rangle_{\ell\,\ell}\langle j_1| \otimes |i_2\rangle_{\ell'\,\ell'}\langle j_2| \\ &+ \frac{1}{2}\sum_{\ell}\sum_{\delta\ell\neq 0} V(\mathbf{r}_\ell, \mathbf{r}_{\delta\ell}) \sum_{\substack{i_1,i_2\\ j_1,j_2}} \tilde{N}^{\sigma,(\ell)}_{i_1,j_1}\tilde{N}^{\sigma,(\ell+\delta\ell)}_{i_2,j_2} |i_1\rangle_{\ell\,\ell}\langle j_1| \otimes |i_2\rangle_{\ell'\,\ell'}\langle j_2|.\end{aligned} \tag{6.26}$$

In this expression we have introduced the following complex coefficients for the hopping terms:

$$\tilde{F}^{\sigma,(\ell,\ell')}_{i_1,i_2,j_1,j_2} = \tilde{B}^{\sigma,(\ell)*}_{j_1,i_1}\tilde{B}^{\sigma,(\ell')}_{i_2,j_2} + \tilde{B}^{\sigma,(\ell)}_{i_1,j_1}\tilde{B}^{\sigma,(\ell')*}_{j_2,i_2}. \tag{6.27}$$

Due to the definition (6.25), neither of the two terms has any contributions in either zeroth or first order of the $\sigma^{(i)}_\ell$. If we now use the representations (6.13)–(6.16) we find the full expansion of the Hamiltonian $\hat{H}$ in terms of $\sigma^{(i)}_\ell$. Using $E_0 = \sum_\ell E^{(\ell)}_0$,

$$\hat{H} = E_0 + \mathcal{H}^{(2)} + \mathcal{H}^{(3)} + \mathcal{H}^{(4)}. \tag{6.28}$$

In this expression no approximation has been made so far. Therefore it is an exact representation of the original Hamiltonian (6.24). The second order Hamiltonian $\mathcal{H}^{(2)}$ taken by itself determines the quasiparticle structure with all quasiparticles obtaining an infinite lifetime, while the higher order terms $\mathcal{H}^{(3)}$ and $\mathcal{H}^{(4)}$ generate couplings between those quasiparticles, invoking decay and interaction processes, ultimately limiting the lifetimes of the quasiparticles. These higher order terms are given explicitly in App. C. For now the most important part is the second order term which describes the bare quasiparticle modes. Before we write it out explicitly let us introduce the tunneling matrix $t^{\ell,\ell'}_\sigma$, which for a given particle component is given by the corresponding hopping amplitude $t_\sigma$ whenever the sites $\ell$ and $\ell'$ are nearest neighbors (NN). Then $\mathcal{H}^{(2)}$ has the following convenient form, where we have used the symmetry relation $\tilde{F}^{\sigma,(\ell',\ell)}_{i_2,i_1,j_2,j_1} = \tilde{F}^{\sigma,(\ell,\ell')}_{i_1,i_2,j_1,j_2}$:

$$\begin{aligned}\mathcal{H}^{(2)} = &\sum_\ell \sum_{i>0} E^{(l)}_i {\sigma^{(i)}_\ell}^\dagger \sigma^{(i)}_\ell \\ &- \frac{1}{2}\sum_{\ell,\ell',\sigma} t^{\ell,\ell'}_\sigma \sum_{i,j>0}\left[2\tilde{F}^{\sigma,(\ell,\ell')}_{i,0,0,j}{\sigma^{(i)}_\ell}^\dagger \sigma^{(j)}_{\ell'} + \tilde{F}^{\sigma,(\ell,\ell')}_{0,0,i,j}\sigma^{(i)}_\ell\sigma^{(j)}_{\ell'} + \tilde{F}^{\sigma,(\ell,\ell')}_{i,j,0,0}{\sigma^{(i)}_\ell}^\dagger{\sigma^{(j)}_{\ell'}}^\dagger\right] \\ &+ \frac{1}{2}\sum_{l,\delta\ell\neq 0} V(\mathbf{r}_\ell,\mathbf{r}_{\delta\ell}) \sum_{i,j>0}\tilde{N}^{e,(l)}_{0,i}\tilde{N}^{e,(\ell')}_{0,j}\left[2{\sigma^{(i)}_\ell}^\dagger\sigma^{(j)}_{\ell'} + \sigma^{(i)}_\ell\sigma^{(j)}_{\ell'} + {\sigma^{(i)}_\ell}^\dagger{\sigma^{(j)}_{\ell'}}^\dagger\right].\end{aligned} \tag{6.29}$$

This contribution to the Hamiltonian matrix is the main focus of the quasiparticle method and it has to be diagonalized in order to extend the results beyond the Gutzwiller level of approximation.

## 6.2 Hamiltonian quasiparticle matrix

Due to the second quantized form of (6.29), knowledge of its eigenmodes allows for the direct calculation of many experimentally relevant observables. But in order to

find the eigenmodes of (6.29) we have to find a form more suitable for diagonalization. We therefore introduce a Nambu-type notation, which is related to the simultaneous appearance of all conceivable pairs of creation and annihilation operators in (6.29), by defining the following (symplectic) vectors:

$$\boldsymbol{\sigma} = \begin{pmatrix} \boldsymbol{\sigma}_1 \\ \vdots \\ \boldsymbol{\sigma}_L \end{pmatrix}, \qquad \text{where} \qquad \sigma_\ell = \begin{pmatrix} \hat{\sigma}_\ell^{(1)} \\ \vdots \\ \hat{\sigma}_\ell^{(N_{\max})} \end{pmatrix}. \tag{6.30}$$

Here, $L$ is the total number of lattice sites in the considered system, while $N_{\max}$ is the cut-off in the Gutzwiller basis [3]. Before we can rewrite $\mathcal{H}^{(2)}$ (6.29) in matrix form, we first have to introduce the conjugate transposed vector

$$\begin{pmatrix} \boldsymbol{\sigma} \\ \boldsymbol{\sigma}^\dagger \end{pmatrix}^\dagger = \begin{pmatrix} \hat{\sigma}_1^{(1)} \\ \vdots \\ \hat{\sigma}_L^{(N_{\max})} \\ \hat{\sigma}_1^{(1)^\dagger} \\ \vdots \\ \hat{\sigma}_L^{(N_{\max})^\dagger} \end{pmatrix}^\dagger = \left( \hat{\sigma}_1^{(1)^\dagger}, \cdots, \hat{\sigma}_L^{(N_{\max})^\dagger}, \hat{\sigma}_1^{(1)}, \cdots, \hat{\sigma}_L^{(N_{\max})} \right). \tag{6.31}$$

Using these vectors the second order term $\mathcal{H}^{(2)}$ (6.29) can be brought into a simple bilinear matrix form. To obtain this form we assume exact bosonic behavior of the Gutzwiller fluctuation operators, in contrast to (6.17) but approximately valid for sufficiently small occupation of the fluctuation states. So $\mathcal{H}^{(2)}$ is found to be of the approximate form

$$\mathcal{H}^{(2)} = \frac{1}{2} \begin{pmatrix} \boldsymbol{\sigma} \\ \boldsymbol{\sigma}^\dagger \end{pmatrix}^\dagger \mathcal{H}_{\mathrm{QP}} \begin{pmatrix} \boldsymbol{\sigma} \\ \boldsymbol{\sigma}^\dagger \end{pmatrix} - \frac{1}{2} \mathrm{Tr}(h), \tag{6.32}$$

the validity of which can be verified in the end, by checking the actual deviation from bosonic behavior. The general form of the Hamiltonian quasiparticle matrix (6.32) is independent of whether the Gutzwiller ground-state is homogeneous or not. We find it to be of the following form:

$$\mathcal{H}_{\mathrm{QP}} = \begin{pmatrix} h & \Delta \\ \Delta^* & h^* \end{pmatrix}. \tag{6.33}$$

In a potentially inhomogeneous system consisting of numerous inequivalent sites for which we also consider multiple particle species, we have to differentiate these features using a multitude of indices. Thus to reduce confusion, let us restate the various indices used so far. We indicate the particle species using the greek letters $\sigma, \sigma'$, while lattice sites are signified by $\ell, \ell'$ and $i, j$ correspond to the local excitations of the Gutzwiller basis. With that in mind the entries of the on-diagonal and off-diagonal blocks directly follow from $\mathcal{H}^{(2)}$ as given by (6.29).

[3] Note that in principle $N_{\max}$ can be taken to vary from site to site, for example in a strongly inhomogeneous system.

$$h_{(i,\ell),(j,\ell')} = \delta_{\ell,\ell'}\delta_{i,j}E_i^{(\ell)} - \sum_\sigma t^\sigma_{\ell\ell'}\tilde{F}^{\sigma(\ell,\ell')}_{i00j} + V_{\ell\ell'}\tilde{N}^{\sigma(\ell)}_{i0}\tilde{N}^{\sigma(\ell')}_{0j} \tag{6.34}$$

$$\Delta_{(i,\ell),(j,\ell')} = -\sum_\sigma t^\sigma_{\ell\ell'}\tilde{F}^{\sigma(\ell,\ell')}_{ij00} + V_{\ell\ell'}\tilde{N}^{\sigma(\ell)}_{i0}\tilde{N}^{\sigma(\ell')}_{j0} \tag{6.35}$$

## 6.3 Diagonalization for inhomogeneous periodic order

From now on we assume the more general case of an inhomogeneous ground-state, which can be described by a periodic superlattice. Therefore we introduce equivalence classes of lattice sites which assign to every site index $\ell$ the index of its corresponding equivalence class $c(\ell)$ within the unit cell of the superlattice. For a superlattice spanned by the set of Bravais vectors $\mathcal{V}_d = \{\mathbf{a}_0, \ldots, \mathbf{a}_d\}$ in $d$ spatial dimensions, with each vector $\mathbf{a}_i$ given as integer vector in units of the lattice spacings $a_i$, the number of equivalence classes $N_c$ is given by the length of the wedge product (cross product) of these vectors corresponding to the size of the unit cell. In an OL with $L$ sites there are thus $L_c$ unit cells of size $N_c = L/L_c$. For a given equivalence class site index $s = c(\ell)$ all corresponding sites have identical local observables, which are equal to those of the representative site $s$. Together they form the representative unit cell which we place at the origin. The various equivalent sites $\{\ell | s = c(\ell)\}$ are reached by adding any integer linear combination of $\mathcal{V}_d$ to the position of the representative site.

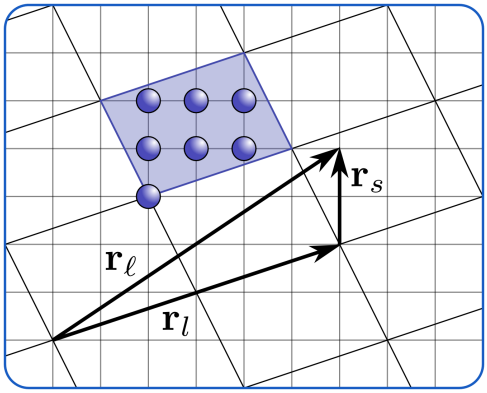


FIGURE 6.2: Decomposition of the positional vector $\mathbf{r}_\ell$. The various sites of the OL are given by the intersections of the grey lines. The superlattice is given by the black lines. An exemplary unit cell, containing seven lattice sites occupied by one atom each, is shown by the blue shaded area. $\mathbf{r}_\ell$ is decomposed into a linear combination of a superlattice vector $\mathbf{r}_l$ and the relative vector $\mathbf{r}_s$ of a given site $s$ inside the unit cell.

For the transformation to the space of quasimomenta we therefore have to keep these classes in mind. It will be useful to decompose the positional vector $\mathbf{r}_\ell$ into its superlattice part $\mathbf{r}_l$ (an integer linear combination of $\mathcal{V}_d$) and the relative position $\mathbf{r}_s$ of each representative site in the unit cell. Their relation is shown in Fig. 6.2. Using these relations a naive ansatz for a generalized unitary transformation matrix in analogy to the homogeneous case would be

$$K_{(i\ell),(j\mathbf{k}s)} \equiv \frac{1}{\sqrt{L_c}}\delta_{i,j}\delta_{s,c(\ell)}e^{i\mathbf{k}\mathbf{r}_\ell} \mathrel{\hat{=}} \frac{1}{\sqrt{L_c}}\delta_{i,j}\delta_{s,s'}e^{i\mathbf{k}(\mathbf{r}_l+\mathbf{r}_s)} \equiv K_{(ils),(j\mathbf{k}s')}. \tag{6.36}$$

Note that this defines an only partial transformation meaning it retains some spatial information for each equivalent site $s$. Thus we will obtain $N_c$ times the number bands compared to the homogeneous case, as the index $s$ simply reflects the possibility of $N_c$ times as many inequivalent Gutzwiller bases as in a homogeneous system.

At first glance is might seem as if the number of fluctuation operators in the first Brillouin zone of the OL also increases by a factor of $N_c$. This illusion stems from the fact that actually we only have to consider a reduced Brillouin zone given a superlattice structure. Its reciprocal lattice vectors $\mathbf{G}_r$ are implicitly defined via $\mathbf{G}_r \cdot \mathbf{r}_l = 2\pi n$ where $n \in \mathbb{Z}$. So the seemingly different operators $\tilde{\sigma}^{(i)}_{\mathbf{k},s}$ and $\tilde{\sigma}^{(i)}_{\mathbf{k}+\mathbf{G}_r,s}$ actually only differ by a trivial complex factor:

$$\tilde{\sigma}^{(i)}_{\mathbf{k}+\mathbf{G}_r,s} = \frac{1}{\sqrt{L_c}} \sum_l e^{-i(\mathbf{k}+\mathbf{G}_r)\cdot(\mathbf{r}_l+\mathbf{r}_s)} \hat{\sigma}^{(i)}_{l,s} = \tilde{\sigma}^{(i)}_{\mathbf{k},s} e^{-i\mathbf{G}_r\cdot\mathbf{r}_s}. \tag{6.37}$$

Therefore one might be tempted to omit this phase factor in the transformation altogether and instead define the generalized unitary transformation as $K'_{(ils),(j\mathbf{k}s')} = \frac{1}{\sqrt{L_c}}\delta_{i,j}\delta_{s,s'}e^{i\mathbf{k}\mathbf{r}_l}$, but due to the slightly more intuitive form (6.36) we stick to the original definition.

Before we continue with transforming the quasiparticle matrix (6.33), let us briefly discuss the relation of these transformations to the more common transformation $K_{(i\ell),(j\mathbf{k})} = \delta_{i,j}e^{i\mathbf{k}\mathbf{r}_\ell}/\sqrt{L}$, as used in a homogeneous system, by comparing how they transform the Gutzwiller fluctuation operators $\hat{\sigma}^{(i)}_\ell = \hat{\sigma}^{(i)}_{l,s}$. The usual transformation to quasimomentum space looks as follows:

$$\tilde{\sigma}^{(i)}_{\mathbf{k}} = \frac{1}{\sqrt{L}} \sum_\ell e^{-i\mathbf{k}\cdot\mathbf{r}_\ell} \hat{\sigma}^{(i)}_\ell = \frac{1}{\sqrt{N_c}} \sum_s \sum_l K^*_{(i\mathbf{k}s),(ils)} \hat{\sigma}^{(i)}_{l,s} \equiv \frac{1}{\sqrt{N_c}} \sum_s \tilde{\sigma}^{(i)}_{\mathbf{k},s} \tag{6.38}$$

To close the circle we also have to consider the transformation back to positional space, which is defined via the complete first Brillouin zone of the optical lattice:

$$\begin{aligned} \hat{\sigma}^{(i)}_\ell &= \frac{1}{\sqrt{L}} \sum_{\mathbf{k}\in 1.\mathrm{BZ}} e^{i\mathbf{k}\cdot\mathbf{r}_\ell} \tilde{\sigma}^{(i)}_{\mathbf{k}} \equiv \hat{\sigma}^{(i)}_{l,s} \\ &= \frac{1}{\sqrt{L}} \sum_{\mathbf{k}'\in 1.\mathrm{BZ}'} \sum_{\mathbf{G}_r} e^{i(\mathbf{k}'+\mathbf{G}_r)\cdot(\mathbf{r}_l+\mathbf{r}_s)} \frac{1}{\sqrt{N_c}} \sum_{s'} \tilde{\sigma}^{(i)}_{\mathbf{k}'+\mathbf{G}_r,s'} \end{aligned} \tag{6.39}$$

$$\hat{\sigma}^{(i)}_{l,s} = \frac{1}{\sqrt{L_c}} \sum_{\mathbf{k}\in 1.\mathrm{BZ}'} e^{i\mathbf{k}\cdot(\mathbf{r}_l+\mathbf{r}_s)} \tilde{\sigma}^{(i)}_{\mathbf{k},s} = \frac{1}{\sqrt{L_c}N_c} \sum_{\mathbf{k}\in 1.\mathrm{BZ}} e^{i\mathbf{k}\cdot(\mathbf{r}_l+\mathbf{r}_s)} \tilde{\sigma}^{(i)}_{\mathbf{k},s} \tag{6.40}$$

Here we have decomposed the quasimomenta $\mathbf{k}$ in the first Brillouin zone (1.BZ) analogous to the real space vectors $\mathbf{r}_\ell$. So $\mathbf{k} = \mathbf{k}' + \mathbf{G}_r$ where $\mathbf{G}_r$ is a reciprocal lattice vector of the superlattice. It is chosen such that $\mathbf{k}'$ lies within the first reduced Brillouin zone (1.BZ′) as generated by the set $\{\mathbf{G}_r\}$. We have furthermore used the translational symmetry of $\tilde{\sigma}^{(i)}_{\mathbf{k},s}$ in the quasimomenta (6.37), which also yields a convenient way to retain a formulation in the original Brillouin zone (6.40).

Using the transformation relation (6.40) we can bring $\mathcal{H}^{(2)}$ in (6.29) into the quasimomentum form. To do so let us consider its individual terms one at a time.

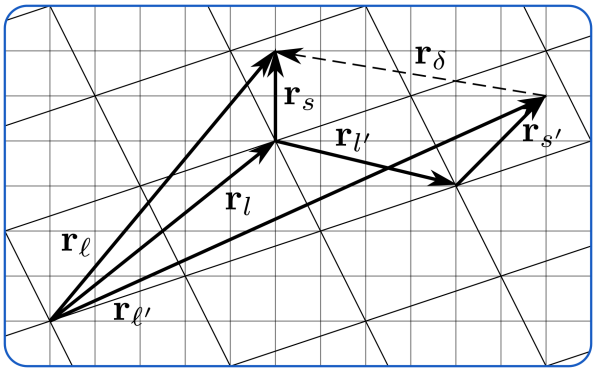


FIGURE 6.3: Decomposition of both positional vectors $\mathbf{r}_\ell$ and $\mathbf{r}_{\ell'}$. The sites of the underlying OL are given by the intersections of the grey lines, while the superlattice is given by the black lines. In equation (6.41) the positional vectors $\mathbf{r}_\ell$ and $\mathbf{r}_{\ell'}$ are decomposed into combinations of superlattice vectors $\mathbf{r}_l$ and $\mathbf{r}_{l'}$ as well as corresponding position vectors $\mathbf{r}_s$ and $\mathbf{r}_{s'}$ of the given sites $s$ and $s'$ inside each unit cell. The dashed vector marks the relative vector between the two considered sites $\ell$ and $\ell'$.

$$\begin{aligned}
&\sum_{\ell,\ell'} t_\sigma^{\ell\ell'} F_{i,0,0,j}^{\sigma,(\ell,\ell')} \hat{\sigma}_\ell^{(i)\dagger} \hat{\sigma}_{\ell'}^{(j)} \\
=&\frac{1}{L_c} \sum_{\substack{l,l' \\ s,s'}} \sum_{\mathbf{k},\mathbf{k}'\in 1.\mathrm{BZ}'} t_\sigma^{\mathbf{r}_s-\mathbf{r}_{s'}-\mathbf{r}_{l'}} F_{i,0,0,j}^{\sigma,(s,s')} e^{-i\mathbf{k}\cdot\mathbf{r}_\ell} e^{i\mathbf{k}'\cdot\mathbf{r}_{\ell'}} \tilde{\sigma}_{\mathbf{k},s}^{(i)\dagger} \tilde{\sigma}_{\mathbf{k}',s'}^{(j)} \\
=&\frac{1}{N_c} \sum_{s,s'} F_{i,0,0,j}^{\sigma,(s,s')} \sum_{\mathbf{k}\in 1.\mathrm{BZ}} t_\sigma^{(s,s')}(\mathbf{k}) \tilde{\sigma}_{\mathbf{k},s}^{(i)\dagger} \tilde{\sigma}_{\mathbf{k},s'}^{(j)}.
\end{aligned} \tag{6.41}$$

The two position vectors are decomposed as $\mathbf{r}_\ell = \mathbf{r}_l + \mathbf{r}_s$ and $\mathbf{r}_{\ell'} = \mathbf{r}_l + \mathbf{r}_{l'} + \mathbf{r}_{s'}$, where $\mathbf{r}_{l/l'}$ are superlattice vectors and $\mathbf{r}_{s/s'}$ are the positions inside of a given unit cell. Their relation is depicted in Fig. 6.3. This allows the subsequent summation over $l$ resulting in $L_c\delta_{\mathbf{k},\mathbf{k}'}$. We again use the translational symmetry to extend the summation to the original Brillouin zone, which will proof beneficial in the general case where we consider an arbitrary superlattice. Note that the tunneling matrix $t_\sigma^{\ell\ell'}$ can be expressed as a function of the relative vector $\mathbf{r}_\ell - \mathbf{r}_{\ell'} = \mathbf{r}_s - \mathbf{r}_{l'} - \mathbf{r}_{s'}$ between any pair of sites, so $t_\sigma^{\ell\ell'} = t_\sigma^{\mathbf{r}_s-\mathbf{r}_{s'}-\mathbf{r}_{l'}} = t_\sigma \delta_{|\mathbf{r}_s-\mathbf{r}_{s'}-\mathbf{r}_{l'}|,1}$ (in units of NN lattice spacings). We also define the expression $t_\sigma^{(s,s')}(\mathbf{k}) = \sum_l t_\sigma \delta_{|\mathbf{r}_s-\mathbf{r}_{s'}-\mathbf{r}_l|,1} \exp\left[-i\mathbf{k}\cdot(\mathbf{r}_s-\mathbf{r}_{s'}-\mathbf{r}_l)\right]$ in order to further simplify (6.41). Note that this sum in general yields a complex number even for real valued hopping amplitudes as $s$ and $s'$ are not always nearest neighbors for opposite directions. We thus have to keep in mind the symmetry relations $t_\sigma^{(s,s')}(-\mathbf{k}) = t_\sigma^{(s',s)}(\mathbf{k}) = t_\sigma^{(s,s')}(\mathbf{k})^*$, which simply follow from the definition and assuming real valued tunneling amplitudes.

In the same fashion we can also transform the anomalous hopping terms, for which we find

$$\sum_{\ell,\ell'} t_\sigma^{\ell\ell'} F_{0,0,i,j}^{\sigma,(\ell,\ell')} \hat{\sigma}_\ell^{(i)} \hat{\sigma}_{\ell'}^{(j)} = \frac{1}{N_c} \sum_{s,s'} F_{0,0,i,j}^{\sigma,(s,s')} \sum_{\mathbf{k}\in 1.\mathrm{BZ}} t_\sigma^{(s,s')}(\mathbf{k}) \tilde{\sigma}_{-\mathbf{k},s}^{(i)} \tilde{\sigma}_{\mathbf{k},s'}^{(j)}. \tag{6.42}$$

Regarding the normal contributions of the interaction we once more utilize a decomposition of the form $\mathbf{r}_{\ell'} = \mathbf{r}_\ell - \mathbf{r}_{\delta\ell}$. At this point we furthermore restrict our considerations to interactions of the form $V(\mathbf{r},\mathbf{r}') = V(\mathbf{r}-\mathbf{r}') = V(\mathbf{r}'-\mathbf{r})$, so we obtain

$$\sum_{\ell,\ell'} V(\mathbf{r}_{\delta\ell}) \tilde{N}_{0,i}^{e,(\ell)} \tilde{N}_{0,j}^{e,(\ell')} \hat{\sigma}_{\ell}^{(i)\dagger} \hat{\sigma}_{\ell'}^{(j)} = \frac{1}{N_c} \sum_{s,s'} \tilde{N}_{0,i}^{e,(s)} \tilde{N}_{0,j}^{e,(s')} \sum_{\mathbf{k}\in 1.\mathrm{BZ}} V^{(s,s')}(\mathbf{k}) \tilde{\sigma}_{\mathbf{k},s}^{(i)\dagger} \tilde{\sigma}_{\mathbf{k},s'}^{(j)}. \quad (6.43)$$

Here we have introduced the partial quasimomentum transformation of the long-range interaction $V^{(s,s')}(\mathbf{k}) = \sum_l V(\mathbf{r}_s - \mathbf{r}_{s'} - \mathbf{r}_l) \exp\left[-i\mathbf{k}\cdot(\mathbf{r}_s - \mathbf{r}_{s'} - \mathbf{r}_l)\right]$. Note that the relations $V^{(s,s')}(-\mathbf{k}) = V^{(s',s)}(\mathbf{k}) = V^{(s,s')}(\mathbf{k})^*$ are also fulfilled by the long-range (real valued) interaction. The reason for this is the simultaneous presence of an inversion symmetry in the interaction on the one hand and in the unit cell tiling of the system on the other. Correspondingly the anomalous interaction terms transform in the same way as the hopping terms (6.42):

$$\sum_{\ell,\ell'} V(\mathbf{r}_{\delta\ell}) \tilde{N}_{0,i}^{e,(\ell)} \tilde{N}_{0,j}^{e,(\ell')} \hat{\sigma}_{\ell}^{(i)} \hat{\sigma}_{\ell'}^{(j)} = \frac{1}{N_c} \sum_{s,s'} \tilde{N}_{0,i}^{e,(s)} \tilde{N}_{0,j}^{e,(s')} \sum_{\mathbf{k}\in 1.\mathrm{BZ}} V^{(s,s')}(\mathbf{k}) \tilde{\sigma}_{-\mathbf{k},s}^{(i)} \tilde{\sigma}_{\mathbf{k},s'}^{(j)}. \quad (6.44)$$

The only remaining terms are those on the diagonal which also result in diagonal terms of the quasimomentum representation *if* we assume exact bosonic commutation relations for the Gutzwiller operators.

$$\sum_{\ell} E_i^{\ell} \hat{\sigma}_{\ell}^{(i)\dagger} \hat{\sigma}_{\ell}^{(i)} = \frac{1}{2N_c} \sum_{s} E_i^{s} \sum_{\mathbf{k}\in 1.\mathrm{BZ}} \left( \tilde{\sigma}_{\mathbf{k},s}^{(i)\dagger} \tilde{\sigma}_{\mathbf{k},s}^{(i)} + \tilde{\sigma}_{\mathbf{k},s}^{(i)} \tilde{\sigma}_{\mathbf{k},s}^{(i)\dagger} \right) - \frac{1}{2N_c} \sum_{s} \sum_{\mathbf{k}\in 1.\mathrm{BZ}} E_i^{s} \quad (6.45)$$

Note that this transformation is very similar to the homogeneous case studied in [Bis12]. It is a first step in the diagonalization of the quasiparticle matrix, the transformation of which could also be expressed via the following generalized unitary transformation matrix

$$\mathcal{K} = \begin{pmatrix} K & 0 \\ 0 & K^* \end{pmatrix}. \quad (6.46)$$

The elements of the matrices $K$ are given by (6.36). Under the assumption of bosonic commutation relations, which can be checked *a posteriori*, for the $\tilde{\sigma}_{\mathbf{k},s}^{(i)}$ in momentum space and correspondingly in position space the transformation can thus be expressed as

$$\mathcal{K}^{\dagger} \mathcal{H}_{QP} \mathcal{K} = \begin{pmatrix} K^{\dagger} h K & K^{\dagger} \Delta^* K^* \\ K^T \Delta^* K & K^T h^* K^* \end{pmatrix}. \quad (6.47)$$

From this we can see that the transformation of the off-diagonal blocks leads to expressions that couple $\mathbf{k} \leftrightarrow -\mathbf{k}$ blocks of the size $N_c N \times N_c N$ for each $\mathbf{k}$. The factors of $N$ stem from the cutoff used for the local Fock basis representation of all components combined, while $N_c$ is the size of the unit cell. Reordering the thus coupled blocks results in the following $2D \times 2D$ block diagonal structure where $D = N_c N$:

$$\tilde{\mathcal{H}}_{\mathrm{QP}}(\mathbf{k}) = \begin{pmatrix} \tilde{h}(\mathbf{k}) & \tilde{\Delta}(\mathbf{k}) \\ \tilde{\Delta}(-\mathbf{k})^* & \tilde{h}(-\mathbf{k})^* \end{pmatrix}. \quad (6.48)$$

Its subsequent diagonalization reveals the quasiparticle mode structure. We have

already derived the individual terms via the direct transformation of the Gutzwiller fluctuation operators as shown in equations (6.41)–(6.45). The resulting matrix elements are given by

$$\tilde{h}_{(i,s),(j,s')}(\mathbf{k}) = -\sum_{\sigma} F^{\sigma(s,s')}_{i,0,0,j}\, t^{(s,s')}_{\sigma}(\mathbf{k}) + \tilde{N}^{e,(s)}_{i,0}\tilde{N}^{e,(s')}_{0,j} V^{(s,s')}(\mathbf{k}) + \delta_{s,s'}\delta_{i,j}E^{(s)}_{i}, \quad (6.49)$$

$$\tilde{\Delta}_{(i,s),(j,s')}(\mathbf{k}) = -\sum_{\sigma} F^{\sigma(s,s')}_{i,j,0,0}\, t^{(s,s')}_{\sigma}(\mathbf{k}) + \tilde{N}^{e,(s)}_{i,0}\tilde{N}^{e,(s')}_{j,0} V^{(s,s')}(\mathbf{k}). \quad (6.50)$$

In order to preserve the bosonic structure of the operators the final diagonalization has to be performed on the symplectic space[4], namely by diagonalizing $\Sigma\tilde{\mathcal{H}}_{QP}$ where $\Sigma = \mathrm{diag}(\mathbb{1}_{NL}, -\mathbb{1}_{NL})$ for the full Hamiltonian quasiparticle matrix or $\Sigma = \mathrm{diag}(\mathbb{1}_{D}, -\mathbb{1}_{D})$ for the $\mathbf{k}$ blocks.

### 6.3.1 Completeness relation

As can be seen from (6.48), the quasiparticle block-matrices corresponding to pairs of momenta $\mathbf{k}$ and $-\mathbf{k}$ are of the same general form, both in a homogeneous system (where $s = s' = 0$ in (6.49) and (6.50)) as well as in an inhomogeneous system with periodic superlattice order. Therefore $s$ and $s'$ effectively act as additional Fock base indices. Thus the eigenvalue and eigenvector structure of a homogeneous system is retained in our case. As has been discussed in App. (K.1.1) of [Bis12], eigenvalues for matrices of this form always appear in pairs $\omega_{\mathbf{k},\gamma}$ and $-\omega^{*}_{\mathbf{k},\gamma}$ where $\gamma$ is the quasiparticle mode index. They have corresponding eigenvectors $\mathbf{x}^{(\mathbf{k},\gamma)} = \begin{pmatrix} \mathbf{u}^{(\mathbf{k},\gamma)} \\ -\mathbf{v}^{(\mathbf{k},\gamma)} \end{pmatrix}$ and $\mathbf{y}^{(\mathbf{k},\gamma)} = \begin{pmatrix} -\mathbf{v}^{(\mathbf{k},\gamma)^*} \\ \mathbf{u}^{(\mathbf{k},\gamma)^*} \end{pmatrix}$ which are orthogonal with respect to $\Sigma$. The two vectors are furthermore linearly independent and have opposite sign in the pseudo norm generated by $\Sigma$. Due to the nature of the quasiparticle matrix, namely that it describes non-interacting infinitely lived quasiparticle modes, we expect to only find real eigenvalues with $\omega_{\mathbf{k},\gamma} = \omega^{*}_{\mathbf{k},\gamma}$. The appearance of imaginary eigenvalues in contrast implies the instability of the mean-field ground-state assumed prior to a quasiparticle analysis.

#### Non-diagonalizable sub-block of the condensate

In the condensate phase there exists one eigenvalue 0 in the sub-block of $\mathbf{k} = 0$ which does not possess a conjugate pair of eigenvectors, resulting in an incomplete basis of eigenvectors in this sub-block which therefore is non-diagonalizable. It can thus only be transformed into Jordan normal form. As we will see, this case leads to a qualitatively different Hamiltonian and as such requires special treatment. The unpaired eigenvector corresponding to the zero eigenvalue pair appearing in $\tilde{\mathcal{H}}_{\mathrm{QP}}(\mathbf{k} = 0)$ has the structure

$$\mathbf{p} = \begin{pmatrix} \mathbf{u}^{(0)} \\ -\mathbf{u}^{(0)^*} \end{pmatrix}. \quad (6.51)$$

[4] This is in accordance to an analogue derivation via the equation of motion as discussed in [Bis12].

Thus its pseudo norm $\mathbf{p}^\dagger\Sigma\mathbf{p} = 0$ vanishes, which corresponds to the case of $\mathbf{x}^{(\mathbf{k}=0,\gamma=1)}$ and $\mathbf{y}^{(\mathbf{k}=0,\gamma=1)}$ collapsing onto one another. Therefore we normalize this special vector with respect to the euclidean norm $\mathbf{p}^\dagger\mathbf{p} = 1$. This determines $\mathbf{p}$ up to a complex phase factor. Assuming no further vanishing eigenvalues exist, the remaining eigenvectors $\mathbf{x}^{(\mathbf{k}=0,\gamma>1)}$ and $\mathbf{y}^{(\mathbf{k}=0,\gamma>1)}$ span a (2D-2)-dimensional subspace of this block. They are mutually orthogonal and can be normalized with respect to $\Sigma$ for all higher mode indices $\gamma > 1$.

$$\mathbf{x}^{(\mathbf{k}=0,\gamma)^\dagger}\Sigma\mathbf{x}^{(\mathbf{k}=0,\alpha)} = \delta_{\gamma,\alpha} \tag{6.52}$$

$$\mathbf{y}^{(\mathbf{k}=0,\gamma)^\dagger}\Sigma\mathbf{y}^{(\mathbf{k}=0,\alpha)} = -\delta_{\gamma,\alpha} \tag{6.53}$$

$$\mathbf{x}^{(\mathbf{k}=0,\gamma)^\dagger}\Sigma\mathbf{y}^{(\mathbf{k}=0,\alpha)} = 0 \tag{6.54}$$

Furthermore, as they are eigenvectors of different eigenvalues, they are also orthogonal to $\mathbf{p}$ which is linearly independent of all other eigenvectors. So

$$\mathbf{p}^\dagger\Sigma\mathbf{x}^{(\mathbf{k}=0,\alpha)} = 0 \quad \text{and} \quad \mathbf{p}^\dagger\Sigma\mathbf{y}^{(\mathbf{k}=0,\alpha)} = 0. \tag{6.55}$$

Thus these vectors span almost the entire $2D$-dimensional subspace corresponding to $\mathbf{k} = 0$, but with a single basis vector missing to complete the basis. We denote this last vector by $\mathbf{q}$ and it can be implicitly defined via

$$\Sigma\tilde{\mathcal{H}}_{QP}(\mathbf{k} = 0)\mathbf{q} = -\frac{i}{\tilde{m}}\mathbf{p}. \tag{6.56}$$

Here $\tilde{m}$ is a mass-like real number that is not to be confused with the effective mass of the quasiparticle modes. Its value can be determined *a posteriori* and is fixed by the normalization condition. While $\mathbf{q}$ in principle can be any vector that is linear indepenent to $\mathbf{p}$ and lies within the generalized eigenspace corresponding to the eigenvalue zero, (6.56) determines $\mathbf{q}$ up to a scaling factor. In analogy to the form of $\mathbf{p}$ we can choose the form

$$\mathbf{q} = -i\begin{pmatrix}\mathbf{v}^{(0)}\\ \mathbf{v}^{(0)*}\end{pmatrix}. \tag{6.57}$$

This definition is compatible with (6.56) and linear independent to $\mathbf{p}$. Its $\Sigma$-norm vanishes as $\mathbf{q}^\dagger\Sigma\mathbf{q} = 0$. We thus normalize it via its relation to $\mathbf{p}$:

$$\mathbf{q}^\dagger\Sigma\mathbf{p} = i. \tag{6.58}$$

In conclusion we now have the complete set $\{\mathbf{x}^{(\mathbf{k}=0,\gamma>1)}, \mathbf{y}^{(\mathbf{k}=0,\gamma>1)}, \mathbf{p}, \mathbf{q}\}$ of basis vectors spanning the entire subspace corresponding to the block $\tilde{\mathcal{H}}_{QP}(\mathbf{k})$. In this basis $\Sigma\tilde{\mathcal{H}}_{QP}(\mathbf{k})$ can be transformed into Jordan normal form. Let us briefly write down the completeness relation corresponding to the $\mathbf{k} = 0$ subspace, which holds in a condensate state:

$$\mathbb{1}^{(\mathbf{k}=0)} = \sum_{\gamma>1}\left(\mathbf{x}^{(\mathbf{k}=0,\gamma)}\mathbf{x}^{(\mathbf{k}=0,\gamma)^\dagger} - \mathbf{y}^{(\mathbf{k}=0,\gamma)}\mathbf{y}^{(\mathbf{k}=0,\gamma)^\dagger}\right)\Sigma + i(\mathbf{q}\mathbf{p}^\dagger - \mathbf{p}\mathbf{q}^\dagger)\Sigma. \tag{6.59}$$

This representation of the unit operator can be checked by considering the orthogonality relations presented above while applying the unit operator to the set of basis vectors.

#### Insulator and diagonalizable sub-blocks

In case of an insulator state none of the eigenvalues vanish in any of the $\mathbf{k}$-blocks. Thus we always have a complete basis of eigenvectors $\{\mathbf{x}^{(\mathbf{k},\gamma)}, \mathbf{y}^{(\mathbf{k},\gamma)}\}$. This structure also applies to every $\mathbf{k} \neq 0$ block of $\Sigma\tilde{\mathcal{H}}_{QP}(\mathbf{k})$ in a condensate state. Therefore the unit operator simplifies in comparison to the $\mathbf{k} = 0$ block of the condensate:

$$\mathbb{1}^{(\mathbf{k})} = \sum_{\gamma>1} \left( \mathbf{x}^{(\mathbf{k},\gamma)} \mathbf{x}^{(\mathbf{k},\gamma)^\dagger} - \mathbf{y}^{(\mathbf{k},\gamma)} \mathbf{y}^{(\mathbf{k},\gamma)^\dagger} \right) \Sigma. \tag{6.60}$$

### 6.3.2 Quasiparticle mode operators

In order to conclude the diagonalization of the Hamiltonian quasiparticle matrix let us finally define the Bogoliubov-type **quasiparticle mode operators**.

#### Condensate

We first consider the condensate phase, for which the $\mathbf{k} = 0$ and $\gamma = 1$ mode has to be treated separately:

$$\beta_\alpha \equiv \mathbf{x}^{(\alpha)^\dagger} \Sigma \begin{pmatrix} \tilde{\boldsymbol{\sigma}} \\ \tilde{\boldsymbol{\sigma}}^\dagger \end{pmatrix} = \mathbf{u}^{(\alpha)^\dagger} \tilde{\boldsymbol{\sigma}} + \mathbf{v}^{(\alpha)^\dagger} \tilde{\boldsymbol{\sigma}}^\dagger, \tag{6.61}$$

$$\beta_\alpha^\dagger \equiv -\mathbf{y}^{(\alpha)^\dagger} \Sigma \begin{pmatrix} \tilde{\boldsymbol{\sigma}} \\ \tilde{\boldsymbol{\sigma}}^\dagger \end{pmatrix} = \mathbf{v}^{(\alpha)^t} \tilde{\boldsymbol{\sigma}} + \mathbf{u}^{(\alpha)^t} \tilde{\boldsymbol{\sigma}}^\dagger, \tag{6.62}$$

$$\mathcal{P} \equiv \mathbf{p}^\dagger \Sigma \begin{pmatrix} \tilde{\boldsymbol{\sigma}} \\ \tilde{\boldsymbol{\sigma}}^\dagger \end{pmatrix} = \sum_{i>0,s} \left( u_{i,s}^{(0)^*} \tilde{\sigma}_{\mathbf{k}=0,s}^{(i)} + u_{i,s}^{(0)} \tilde{\sigma}_{\mathbf{k}=0,s}^{(i)^\dagger} \right), \tag{6.63}$$

$$\mathcal{Q} \equiv -\mathbf{q}^\dagger \Sigma \begin{pmatrix} \tilde{\boldsymbol{\sigma}} \\ \tilde{\boldsymbol{\sigma}}^\dagger \end{pmatrix} = \sum_{i>0,s} \left( -i v_{i,s}^{(0)^*} \tilde{\sigma}_{\mathbf{k}=0,s}^{(i)} - i v_{i,s}^{(0)} \tilde{\sigma}_{\mathbf{k}=0,s}^{(i)^\dagger} \right). \tag{6.64}$$

Note that the lower half of each eigenvector $\mathbf{x}^{(\mathbf{k},\gamma)} = \begin{pmatrix} \mathbf{u}^{(\mathbf{k},\gamma)} \\ -\mathbf{v}^{(\mathbf{k},\gamma)} \end{pmatrix}$ and $\mathbf{y}^{(\mathbf{k},\gamma)} = \begin{pmatrix} -\mathbf{v}^{(\mathbf{k},\gamma)^*} \\ \mathbf{u}^{(\mathbf{k},\gamma)^*} \end{pmatrix}$ within a given block corresponding to $\Sigma\tilde{\mathcal{H}}_{QP}(\mathbf{k})$ implicitly refers to the $-\mathbf{k}$ sector, as

$$\mathbf{v}^{(\mathbf{k},\gamma)^\dagger} \tilde{\boldsymbol{\sigma}}^\dagger = \sum_{i>0,s} v_{i,s}^{(\mathbf{k},\gamma)^*} \tilde{\sigma}_{-\mathbf{k},s}^{(i)^\dagger} \quad \text{and} \quad \mathbf{u}^{(\mathbf{k},\gamma)^t} \tilde{\boldsymbol{\sigma}}^\dagger = \sum_{i>0,s} u_{i,s}^{(\mathbf{k},\gamma)} \tilde{\sigma}_{-\mathbf{k},s}^{(i)^\dagger}. \tag{6.65}$$

Thus one has to be careful about the distinction of the upper index $\mathbf{k}$ as used in $\mathbf{u}^{(\mathbf{k},\gamma)}$, representing a vector in the sub-space of the corresponding block, and its usage as a lower index $\mathbf{k}$ in $\mathbf{u}_{i,s,\mathbf{k}}^{(\alpha)}$, which is a vector in the entire space where the indices $(i, s, \mathbf{k})$ refer to a Gutzwiller fluctuation mode. With that in mind and assuming completely bosonic fluctuation operators (6.20) let us briefly derive the commutation relations of the quasiparticle mode operators. For $\mathbf{k}, \mathbf{k}' \in 1.\mathrm{BZ}'$

$$\begin{aligned}\left[\beta_{\mathbf{k},\alpha}, \beta^\dagger_{\mathbf{k}',\gamma}\right] &= \sum_{i,s}\sum_{j,s'}\left[u^{(\mathbf{k},\alpha)^*}_{i,s}\tilde{\sigma}^{(i)}_{\mathbf{k},s} + v^{(\mathbf{k},\alpha)^*}_{i,s}\tilde{\sigma}^{(i)^\dagger}_{-\mathbf{k},s}, u^{(\mathbf{k}',\gamma)}_{j,s'}\tilde{\sigma}^{(j)^\dagger}_{\mathbf{k}',s'} + v^{(\mathbf{k}',\gamma)}_{j,s'}\tilde{\sigma}^{(j)}_{-\mathbf{k}',s'}\right] \\ &= \delta_{\mathbf{k},\mathbf{k}'}\sum_{i,s}\left(u^{(\mathbf{k},\alpha)^*}_{i,s}u^{(\mathbf{k},\gamma)}_{i,s} - v^{(\mathbf{k},\alpha)^*}_{i,s}v^{(\mathbf{k},\gamma)}_{i,s}\right) = \delta_{\mathbf{k},\mathbf{k}'}\delta_{\alpha,\gamma}\end{aligned}$$

The equality in the last line stems from the orthogonality relations of $\mathbf{x}^{(\alpha)}$ and $\mathbf{y}^{(\alpha)}$.

The matrix $W$ corresponding to the generalized transformation, which diagonalizes the system, is defined using the eigenvectors as column vectors:

$$W \equiv \left[\mathbf{x}^{(1)}, \ldots, \mathbf{x}^{(\mathcal{D}-1)}, i\mathbf{p}, \mathbf{y}^{(1)}, \ldots, \mathbf{y}^{(\mathcal{D}-1)}, i\mathbf{q}\right]. \tag{6.66}$$

Here $\mathcal{D} = L_c N_c N = LN$ is given by the full size of the space of fluctuations as given by the number of unit cells $L_c$, the size of the unit cells $N_c$ and the local Fock space size $N$. Regarding the inverse matrix, which yields the explicit mode operators (6.61)–(6.64), we have to keep the symplectic nature of the representation in mind. Therefore we define

$$W^{-1} \equiv W^\dagger \Sigma W W^\dagger \Sigma = \tilde{\Sigma} W^\dagger \Sigma. \tag{6.67}$$

The matrix $\tilde{\Sigma}$ can be shown to have the following form, compatible with the definition of the quasiparticle mode operators introduced above:

$$\tilde{\Sigma} = \begin{pmatrix} \mathbb{1}_{\mathcal{D}-1} & & & \\ & 0 & \cdots & -i \\ & \vdots & -\mathbb{1}_{\mathcal{D}-1} & \vdots \\ & i & \cdots & 0 \end{pmatrix} \equiv W^\dagger \Sigma W. \tag{6.68}$$

Thus the transformation and its inverse can also be written as

$$\begin{pmatrix} \boldsymbol{\beta} \\ \mathcal{Q} \\ \boldsymbol{\beta}^\dagger \\ \mathcal{P} \end{pmatrix} = \tilde{\Sigma} W^\dagger \Sigma \begin{pmatrix} \tilde{\boldsymbol{\sigma}} \\ \tilde{\boldsymbol{\sigma}}^\dagger \end{pmatrix} \quad \text{and} \quad \begin{pmatrix} \tilde{\boldsymbol{\sigma}} \\ \tilde{\boldsymbol{\sigma}}^\dagger \end{pmatrix} = W \begin{pmatrix} \boldsymbol{\beta} \\ \mathcal{Q} \\ \boldsymbol{\beta}^\dagger \\ \mathcal{P} \end{pmatrix}. \tag{6.69}$$

For completeness, we write down the explicit form of this transformation for the individual fluctuation operators, which is given by

$$\tilde{\sigma}^{(i)}_{\mathbf{k},s} = \sum_\alpha \left(u^{(\alpha)}_{i,s,\mathbf{k}}\beta_\alpha - v^{(\alpha)^*}_{i,s,\mathbf{k}}\beta^\dagger_\alpha\right) + iu^{(0)}_{i,s,\mathbf{k}}\mathcal{Q} + v^{(0)}_{i,s,\mathbf{k}}\mathcal{P}, \tag{6.70}$$

$$\tilde{\sigma}^{(i)^\dagger}_{\mathbf{k},s} = \sum_\alpha \left(u^{(\alpha)^*}_{i,s,\mathbf{k}}\beta^\dagger_\alpha - v^{(\alpha)}_{i,s,\mathbf{k}}\beta_\alpha\right) - iu^{(0)^*}_{i,s,\mathbf{k}}\mathcal{Q} + v^{(0)^*}_{i,s,\mathbf{k}}\mathcal{P}. \tag{6.71}$$

**Insulator**

As there always exists a complete basis of eigenvectors in the insulator, the transformation structure is significantly simpler in that case. Thus we only need to introduce the quasiparticle mode creation and annihilation operators $\beta^\dagger_\alpha$ and $\beta_\alpha$ as given

in (6.61) and (6.62), which also include the $(\mathbf{k} = 0, \gamma = 1)$ mode in this case. Accordingly the quasiparticle mode index may now take on any of the $\mathcal{D}$ possible values and the transformation matrix $W$ has the simplified structure

$$W = \left[\mathbf{x}^{(1)}, \ldots, \mathbf{x}^{(\mathcal{D})}, \mathbf{y}^{(1)}, \ldots, \mathbf{y}^{(\mathcal{D})}\right]. \tag{6.72}$$

So it is given via the – now complete – set of eigenvectors used as column vectors. The transformation and its inverse in matrix notation now simplify to

$$\begin{pmatrix} \boldsymbol{\beta} \\ \boldsymbol{\beta}^\dagger \end{pmatrix} = \Sigma W^\dagger \Sigma \begin{pmatrix} \tilde{\boldsymbol{\sigma}} \\ \tilde{\boldsymbol{\sigma}}^\dagger \end{pmatrix} \quad \text{and} \quad \begin{pmatrix} \tilde{\boldsymbol{\sigma}} \\ \tilde{\boldsymbol{\sigma}}^\dagger \end{pmatrix} = W \begin{pmatrix} \boldsymbol{\beta} \\ \boldsymbol{\beta}^\dagger \end{pmatrix}. \tag{6.73}$$

In explicit form the transformation back to the Gutzwiller fluctuation basis simplifies significantly in structure:

$$\tilde{\sigma}^{(i)}_{\mathbf{k},s} = \sum_\alpha \left( u^{(\alpha)}_{i,s,\mathbf{k}} \beta_\alpha - v^{(\alpha)^*}_{i,s,\mathbf{k}} \beta^\dagger_\alpha \right), \tag{6.74}$$

$$\tilde{\sigma}^{(i)^\dagger}_{\mathbf{k},s} = \sum_\alpha \left( u^{(\alpha)^*}_{i,s,\mathbf{k}} \beta^\dagger_\alpha - v^{(\alpha)}_{i,s,\mathbf{k}} \beta_\alpha \right). \tag{6.75}$$

**Eigenmodes in the full space of modes**

As we consider a translational invariant case in terms of a superlattice order, the collective mode index $\alpha$ splits into a pair of independent quantum numbers $\alpha \to (\mathbf{k}, \gamma)$ where $\gamma$ takes the role of a band index. Here we have to be careful as $\mathbf{k}$ may also refer to an element of a given vector when used in terms of the index set $(i, s, \mathbf{k})$, as for example used in the expression $u^{(\alpha)}_{i,s,\mathbf{k}}$. These two meanings should not be confused and a minus may appear due to the generalized unitary transformation whenever particle and hole fluctuation operators are coupled.

We now consider the case $\alpha = (\mathbf{k}, \gamma)$ resulting from a diagonalization of $\Sigma \tilde{\mathcal{H}}_{QP}(\mathbf{k})$, where we use the convention from earlier of having the $\mathbf{k}$ sector in the upper half and the $-\mathbf{k}$ sector in the lower half. The eigenvectors in this lower dimensional sub-space were introduced as $\mathbf{x}^{(\mathbf{k},\gamma)} = \begin{pmatrix} \mathbf{u}^{(\mathbf{k},\gamma)} \\ -\mathbf{v}^{(\mathbf{k},\gamma)} \end{pmatrix}$ and $\mathbf{y}^{(\mathbf{k},\gamma)} = \begin{pmatrix} -\mathbf{v}^{(\mathbf{k},\gamma)^*} \\ \mathbf{u}^{(\mathbf{k},\gamma)^*} \end{pmatrix}$, which in index notation have the index pair $(i, s)$ where $i$ refers to the local Gutzwiller modes[5] and $s$ to the unit cell sites. Thus when we consider the vectors $\mathbf{x}^{(\alpha)}$ and $\mathbf{y}^{(\alpha)}$ for the full space we have to keep in mind that their upper half vectors $\mathbf{u}^{(\mathbf{k},\gamma)}$ and $-\mathbf{v}^{(\mathbf{k},\gamma)^*}$ lie within the $\mathbf{k}$ sector, while the lower halves $-\mathbf{v}^{(\mathbf{k},\gamma)}$ and $\mathbf{u}^{(\mathbf{k},\gamma)^*}$ lie within the $-\mathbf{k}$ sector resepctively. This consideration implies the relations

$$u^{(\mathbf{k},\gamma)}_{i,s,\mathbf{k}'} = \delta_{\mathbf{k},\mathbf{k}'} u^{(\mathbf{k},\gamma)}_{i,s} \quad \text{and} \quad v^{(\mathbf{k},\gamma)}_{i,s,\mathbf{k}'} = \delta_{\mathbf{k},-\mathbf{k}'} v^{(\mathbf{k},\gamma)}_{i,s} \tag{6.76}$$

between the total and reduced sub-spaces.

Furthermore the conjugate pair of vectors $\mathbf{x}^{(\alpha)}$ and $\mathbf{y}^{(\alpha)}$ actually correspond to eigenvectors obtained from the diagonalization of two different blocks. Let $\mathbf{x}^{(\alpha)}$ be the full vector obtained from a positive eigenvector of $\Sigma \tilde{\mathcal{H}}_{QP}(\mathbf{k})$, then $\mathbf{y}^{(\alpha)}$ is its conjugated vector obtained from a negative eigenvector of $\Sigma \tilde{\mathcal{H}}_{QP}(-\mathbf{k})$. Therefore

[5] Various particle components are implicitly contained in the Gutzwiller modes.

the sub-vectors $\mathbf{u}^{(\pm\mathbf{k},\gamma)}$ and $\mathbf{v}^{(\pm\mathbf{k},\gamma)}$, obtained from the diagonalization of opposing $\mathbf{k}$ blocks, have to be chosen so the following relations hold:

$$\mathbf{u}^{(\mathbf{k},\gamma)} = \mathbf{u}^{(-\mathbf{k},\gamma)}, \tag{6.77}$$

$$\mathbf{v}^{(\mathbf{k},\gamma)} = \mathbf{v}^{(-\mathbf{k},\gamma)}. \tag{6.78}$$

No we can finally write down the explicit transformation relations (6.70) and (6.71), as obtained in the condensate for a system with periodic superlattice order:

$$\tilde{\sigma}^{(i)}_{\mathbf{k},s} = \sum_{\gamma}\left(u^{(\mathbf{k},\gamma)}_{i,s}\beta_{\mathbf{k},\gamma} - v^{(\mathbf{k},\gamma)^*}_{i,s}\beta^\dagger_{-\mathbf{k},\gamma}\right) + \delta_{\mathbf{k},\mathbf{G}_r}\left(v^{(0)}_{i,s}\mathcal{P} + iu^{(0)}_{i,s}\mathcal{Q}\right), \tag{6.79}$$

$$\tilde{\sigma}^{(i)^\dagger}_{\mathbf{k},s} = \sum_{\gamma}\left(u^{(\mathbf{k},\gamma)^*}_{i,s}\beta^\dagger_{\mathbf{k},\gamma} - v^{(\mathbf{k},\gamma)}_{i,s}\beta_{-\mathbf{k},\gamma}\right) + \delta_{\mathbf{k},\mathbf{G}_r}\left(v^{(0)^*}_{i,s}\mathcal{P} - iu^{(0)^*}_{i,s}\mathcal{Q}\right). \tag{6.80}$$

In this expression $u^{(\mathbf{k},\gamma)}_{i,s}$ is the $i$-th element on the $s$-th unit cell site of the sub-vector $u^{(\mathbf{k},\gamma)}$, which is the $\gamma$-th eigenvector resulting from a diagonalization of the $\mathcal{D}\times\mathcal{D}$-dimensional block labeled by the quasimomentum $\mathbf{k}$. Note that for $\mathbf{k} = \mathbf{G}_r$ the sum over $\gamma$ starts with the second mode in a condensate. In an insulating state, in contrast, the sum is always complete and the last two terms do not appear.

### 6.3.3 Jordan normal form of the quasiparticle Hamiltonian $\mathcal{H}^{(2)}$

Once more we have to consider two cases separately as the qualitative form of the non-interacting quasiparticle Hamiltonian depends on the existence of a complete basis of eigenvectors. While such a basis exists in the insulator it is incomplete in the condensate[6]. In the latter case we therefore get an additional term reminiscent of the kinetic energy of a free particle. To find the expression of $\mathcal{H}^{(2)}$ (6.29) in terms of quasiparticle mode operators and the momentum-like operator $\mathcal{P}$, we multiply $\tilde{\mathcal{H}}_{QP}$ by $\mathbb{1} = \Sigma\Sigma$ from the left and by the completeness relation, as given by (6.59) and (6.60), from the right. Applying the orthogonality and eigenvector relations (6.61)–(6.64) then yields the Jordan normal form of the quasiparticle Hamiltonian.

#### Condensate

In the condensate we have to use the extended completeness relation including the conjugate vectors $\mathbf{p}$ and $\mathbf{q}$ to obtain

$$\tilde{\mathcal{H}}_{QP} = \Sigma\left(\Sigma\tilde{\mathcal{H}}_{QP}\right)\mathbb{1} \tag{6.81}$$

$$= \tilde{\sum}_{\mathbf{k},\gamma}\left(\Sigma\mathbf{x}^{(\mathbf{k},\gamma)}\omega_{\mathbf{k},\gamma}\mathbf{x}^{(\mathbf{k},\gamma)^\dagger}\Sigma + \Sigma\mathbf{y}^{(\mathbf{k},\gamma)}\omega_{\mathbf{k},\gamma}\mathbf{y}^{(\mathbf{k},\gamma)^\dagger}\Sigma\right) + \frac{1}{\tilde{m}}\Sigma\mathbf{p}\mathbf{p}^\dagger\Sigma \tag{6.82}$$

Here the summation $\tilde{\sum}_{\mathbf{k},\gamma}$ denotes the reduced sum including all quasimomenta $\mathbf{k}$ and band indices $\gamma$, except for the combination $(\mathbf{k} = 0, \gamma = 1)$[7] which is replaced by a momentum-like term given by $\mathbf{p}$. When we now use the quasiparticle operator

[6] The corresponding collapse of eigenvectors also happens in the limit of infinitely strong interactions due to the localization of modes.

[7] This is related to the fact that there is no bosonic sound mode at $\mathbf{k} = 0$ in the condensate.

definitions (6.61) and (6.62) in combination with (6.63) we end up with the following representation of the second order quasiparticle Hamiltonian (6.29), within the assumption of exact bosonic commutations relations for the fluctuation operators:

$$\mathcal{H}^{(2)} = \frac{1}{2}\tilde{\sum}_{\mathbf{k},\gamma}\omega_{\mathbf{k},\gamma}\left(\beta^{\dagger}_{\mathbf{k},\gamma}\beta_{\mathbf{k},\gamma} + \beta_{\mathbf{k},\gamma}\beta^{\dagger}_{\mathbf{k},\gamma}\right) + \frac{\mathcal{P}^2}{2\tilde{m}} - \frac{1}{2}\mathrm{Tr}(h) \tag{6.83}$$

$$= \tilde{\sum}_{\mathbf{k},\gamma}\omega_{\mathbf{k},\gamma}\beta^{\dagger}_{\mathbf{k},\gamma}\beta_{\mathbf{k},\gamma} + \frac{\mathcal{P}^2}{2\tilde{m}} + \frac{1}{2}\left(\tilde{\sum}_{\mathbf{k},\gamma}\omega_{\mathbf{k},\gamma} - \mathrm{Tr}(h)\right). \tag{6.84}$$

This representation is given in terms of the generalized Bogoliubov creation (annihilation) operators $\beta^{\dagger}_{\mathbf{k},\gamma}$ ($\beta_{\mathbf{k},\gamma}$) and includes the momentum-like operator $\mathcal{P}$ which can be considered the generator of translations in the global phase of the condensate mode [LY96]. By expressing the Hamiltonian with $\beta^{\dagger}_{\mathbf{k},\gamma}$ and $\beta_{\mathbf{k},\gamma}$ in normal form we find an additional scalar contribution proportional to $\tilde{\sum}_{\mathbf{k},\gamma}\omega_{\mathbf{k},\gamma}$. Note that the two scalar terms generate a shift of the total energy. While both contributions $\tilde{\sum}_{\mathbf{k},\gamma}\omega_{\mathbf{k},\gamma}$ and $\mathrm{Tr}(h)$ would diverge individually in the limit of no truncation ($N \to \infty$), even in a finite system, in combination they yield a finite correction of the quasiparticle ground-state energy, effectively lowering its value in relation to the Gutzwiller state energy.

#### Insulator

In contrast to the condensate, the insulator always has a complete basis of eigenvectors within which the quasiparticle matrix can be represented. As the same derivation applies, the Hamiltonian (6.29) can be expressed fully in terms of the generalized Bogoliubov operators:

$$\mathcal{H}^{(2)} = \sum_{\mathbf{k},\gamma}\omega_{\mathbf{k},\gamma}\beta^{\dagger}_{\mathbf{k},\gamma}\beta_{\mathbf{k},\gamma} + \frac{1}{2}\left(\sum_{\mathbf{k},\gamma}\omega_{\mathbf{k},\gamma} - \mathrm{Tr}(h)\right). \tag{6.85}$$

Thus we see that the summation includes every mode, including the ($\mathbf{k} = 0, \gamma = 1$) mode. The lowest two bands $\gamma \in \{1, 2\}$ in the regular homogeneous Mott insulator represent hole and particle excitations respectively. They are fully delocalized quasiparticles, each with a well defined quasimomentum. In the limit $t \to 0$ the bands become flat, implying a localization of the states.

It should also be noted that the diagonal form we find here seems to be indistinguishable from the homogeneous case. But we have to keep in mind, that we actually consider more general states with periodic superlattice order. In that case the quasimomentum summation is limited to a reduced Brillouin zone, which has $1/N_c$ independent quasimomenta in comparison to the full Brillouin zone[8]. Accordingly the number of possible values for the mode index $\gamma$ is increased by the factor $N_c$. Thus we can see that the total number of independent modes always remains the same.

### 6.3.4 Quasiparticle ground-state

Now we have finally shown that the initial Hamiltonian (6.1) expanded up to second order in the quasi-bosonic Gutzwiller fluctuations can approximately be rewritten in

[8] Quasimomenta outside the reduced Brillouin zone correspond to quasimomenta inside the reduced Brillouin zone, which are obtained by adding a proper reciprocal lattice vector $\mathbf{G}_r$.

terms of a simple non-interacting quasiparticle Hamiltonian. The main approximations made along the way were the assumption of an exact bosonic commutation relation for the fluctuation operators and the omission of quasiparticle interactions given by $\mathcal{H}^{(3)}$ and $\mathcal{H}^{(4)}$. The former property can be checked a posteriori, as we will see in Sec. 6.4. Depending on the existence of a condensate fraction one either obtains (6.84), or (6.85) when there is no condensate. Both expressions represent approximately bosonic quasiparticles which can be described by the two quantum numbers $\mathbf{k}$ (quasimomentum) and $\gamma$ (internal mode index or simply band index). We also note the appearance of an additional scalar term denoting an energy correction proportional to the system size, which lowers the energy in relation to the Gutzwiller state. Considering the set of quasiparticle operators, we are furthermore able to define the quasiparticle ground-state $|\psi_0\rangle$ implicitly as the state with none of the quasiparticle modes occupied. Therefore it is annihilated by the application of any of the operators $\beta_{\mathbf{k},\gamma}$:

$$\beta_{\mathbf{k},\gamma}\,|\psi_0\rangle = 0. \tag{6.86}$$

Considering the momentum-like Hermitian operator $\mathcal{P}$, which appears in the quasiparticle Hamiltonian of a condensate Gutzwiller state in the term $\mathcal{P}^2/\tilde{m}$ and has a continuous spectrum, one can further characterize the ground-state as minimizing this energy, implying

$$\mathcal{P}\,|\psi_0\rangle = 0. \tag{6.87}$$

We note that the operator $\mathcal{Q}$ is not part of $\mathcal{H}^{(2)}$ while it can be shown that its time-dependent expectation value $\langle\mathcal{Q}\rangle$ changes linearly in time with a rate proportional to $\langle\mathcal{P}\rangle$ [Bis12]. As that value vanishes in the ground-state, one can choose the ground-state such that $\langle\mathcal{Q}\rangle = 0$ as well.

As a final remark, any finite lowering $\left(\sum_{\mathbf{k},\gamma}\omega_{\mathbf{k},\gamma} - \mathrm{Tr}(h)\right)$ of the energy of the quasiparticle state implies that the ground-state $|\psi_0\rangle$ of the quasiparticle Hamiltonian actually differs from the Gutzwiller state $|\psi_G\rangle$. This difference stems from correlated Gutzwiller excitations lowering the energy for any finite and non-zero ratio $t_\sigma/U_\sigma$ in any species $\sigma$. These fluctuations are commonly called **quantum fluctuations**, which appear in the transformed quasiparticle Hamiltonian as a shift in energy even for zero occupation of any quasiparticle state. This is reminiscent of the zero-point energy known from the harmonic oscillator.

## 6.4 Operator representation in the quasiparticle basis

In order to calculate any non-trivial and thus often non-local expectation values, we have to express a given operator in terms of the quasiparticle operators $\beta^\dagger_{\mathbf{k},\gamma}$ and $\beta_{\mathbf{k},\gamma}$. This then allows for the evaluation of expectation values, which may even represent the effect of an external perturbation, as well as the time evolution of such a perturbation. Usually any operator in the many-body systems we consider is given in secod quantization. Independent of whether they are given in terms of Wannier state, momentum or quasimomentum creation and annihilation operators, one can always express individual operators in terms of the Gutzwiller basis states, as previously shown for the operators $\hat{b}_{\sigma,\ell}$ and $\hat{n}^\sigma_\ell$ in (6.25).

The representation is obtained by expressing any local product of operators in terms of $|i\rangle_{\ell\,\ell}\langle j|$ and the corresponding matrix elements of the considered operator. From these one can easily obtain any non-local operator by simple linear combination. The maximum number of $\beta^\dagger_{\mathbf{k},\gamma}$ and $\beta_{\mathbf{k},\gamma}$, which can appear in any term, is twice as large as the number of combined on-site operators used for each term. This immediately follows from the relation between $|i\rangle_{\ell\,\ell}\langle j|$ and the Gutzwiller state transition operators $\hat{\sigma}^{(i)^\dagger}_\ell$ and $\hat{\sigma}^{(i)}_\ell$.

A common class of operators – relevant in numerous applications – are ones which can be expressed as a sum of local operators $\hat{O}_\ell$, where each term is weighted by an exponential phase factor which depends on a quasimomentum index $\mathbf{k}$:

$$\mathcal{A}_\mathbf{k} \equiv \frac{1}{\sqrt{L}} \sum_\ell e^{i\mathbf{k}\cdot\mathbf{r}_\ell} \hat{A}_\ell. \tag{6.88}$$

The matrix elements of the local terms are resolved in the Gutzwiller eigenbasis and given by $A^{(\ell)}_{i,j} = {}_\ell\langle i|\hat{A}_\ell|j\rangle_\ell$. In an inhomogeneous superlattice system each conceivable local operator is represented by a set of $N_c$ independent matrices. Using (6.13)–(6.16) we are able to represent any local operator as a linear combination of fluctuation operators up to at most second order. In general we obtain the form

$$\begin{aligned}\mathcal{A}_\mathbf{k} =& \frac{1}{\sqrt{L}} \sum_\ell e^{i\mathbf{k}\cdot\mathbf{r}_\ell} \left[ A^{(\ell)}_{0,0} |0\rangle_{\ell\,\ell}\langle 0| + \sum_{i>0} \left( A^{(\ell)}_{i,0} |i\rangle_{\ell\,\ell}\langle 0| + A^{(\ell)}_{0,i} |0\rangle_{\ell\,\ell}\langle i| \right) + \sum_{i,j>0} A^{(\ell)}_{i,j} |i\rangle_{\ell\,\ell}\langle j| \right] \\ =& \frac{1}{\sqrt{N_c}} \sum_s \left[ \sqrt{L_c}\delta_{\mathbf{k},\mathbf{G}_r} A^{(s)}_{0,0} e^{i\mathbf{k}\cdot\mathbf{r}_s} \mathbb{1} + \sum_{i>0} \left( A^{(s)}_{i,0} \tilde{\sigma}^{(i)^\dagger}_{\mathbf{k},s} + A^{(s)}_{0,i} \tilde{\sigma}^{(i)}_{-\mathbf{k},s} \right) \right. \\ & \left. + \frac{1}{\sqrt{L_c}} \sum_{i,j>0} \left( A^{(s)}_{i,j} - \delta_{i,j} A^{(s)}_{0,0} \right) \sum_{\mathbf{k}'\in 1.\mathrm{BZ}'} \tilde{\sigma}^{(i)^\dagger}_{\lfloor \mathbf{k}'+\mathbf{k} \rfloor,s} \tilde{\sigma}^{(j)}_{\mathbf{k}',s} \right] \equiv \frac{1}{\sqrt{N_c}} \sum_s \mathcal{A}_{\mathbf{k},s}. \end{aligned} \tag{6.89}$$

In the last line we have used (6.37) and (6.40). Also note that while the sum for the quasimomentum $\mathbf{k}'$ only spans the reduced Brillouin zone $1.\mathrm{BZ}'$, the $\lfloor\cdot\rfloor$-brackets still describe a mapping back into the full Brillouin zone $1.\mathrm{BZ}$ as $\lfloor \mathbf{k}' \rfloor = \mathbf{G} + \mathbf{k}' = \tilde{\mathbf{k}}$. This is achived by adding a properly selected $\mathbf{G}$ among the set of $\{\mathbf{G}\} = \{\mathbf{G}|\mathbf{G}\cdot\mathbf{r}_\ell = 2\pi n\}$ with $n \in \mathbb{Z}$, so $\tilde{\mathbf{k}} \in 1.\mathrm{BZ}$. The two relevant sets of reciprocal lattice vectors we have introduced up to this point are related as $\{\mathbf{G}\} \subset \{\mathbf{G}_r\}$. Therefore one finds the following simplifying relation:

$$\frac{1}{\sqrt{L_c}} \sum_l e^{i\mathbf{k}\cdot(\mathbf{r}_l+\mathbf{r}_s)} \hat{\sigma}^{(i)^\dagger}_{l,s} \hat{\sigma}^{(j)}_{l,s} = \frac{1}{\sqrt{L_c}} \sum_{\mathbf{k}_2\in 1.\mathrm{BZ}'} \tilde{\sigma}^{(i)^\dagger}_{\mathbf{k}+\mathbf{k}_2,s} \tilde{\sigma}^{(i)}_{\mathbf{k}_2,s} = \frac{1}{\sqrt{L_c}} \sum_{\mathbf{k}_2\in 1.\mathrm{BZ}'} \tilde{\sigma}^{(i)^\dagger}_{\lfloor \mathbf{k}+\mathbf{k}_2 \rfloor,s} \tilde{\sigma}^{(i)}_{\mathbf{k}_2,s} \tag{6.90}$$

In order to obtain the back folded expression, which becomes relevant for any $\mathbf{k}$ close to the edge of the $1.\mathrm{BZ}$, we note that we can always write $\mathbf{k} + \mathbf{k}_2 = \mathbf{G} + \mathbf{k}'$ with $\mathbf{G}$ as a reciprocal lattice vector of the underlying optical lattice. Thus we have $\mathbf{k}' = \lfloor \mathbf{k} + \mathbf{k}_2 \rfloor$. To conclude the last step we just have to consider that $\tilde{\sigma}^{(i)^\dagger}_{\mathbf{G}+\mathbf{k}',s} = \tilde{\sigma}^{(i)^\dagger}_{\mathbf{k}',s} e^{i\mathbf{G}\cdot\mathbf{r}_s} = \tilde{\sigma}^{(i)^\dagger}_{\mathbf{k}',s} e^{i2\pi n}$.

We can see that any operator of the type (6.88) can exactly be represented in

the fluctuaction basis (6.89). Then it consists of three contributions of increasing order in the fluctuation operators. Its lowest order term is purely scalar and stems from the Gutzwiller ground-state. The terms in first and second order of the fluctuation operators account for the **depletion** of the Gutzwiller state. Due to the presence of Gutzwiller excitations in the quasiparticle ground-state the amplitude of the Gutzwiller ground-state gets reduced. The second order depletion term is suppressed by the system size. Inserting (6.79) and (6.80) into (6.89) we find the representation of the operator in terms of the quasiparticle operators:

$$\mathcal{A}_{\mathbf{k}} = \sum_s \left( \frac{\sqrt{L}}{N_c} A^{(s)}_{0,0} \delta_{\mathbf{k},\mathbf{G}_r} e^{i\mathbf{G}_r\cdot\mathbf{r}_s} + \sum_\gamma \left[ D^{(s)}_{\mathbf{k},\gamma}[\hat{A}^{(s)}]\beta^\dagger_{\mathbf{k},\gamma} + \tilde{D}^{(s)}_{-\mathbf{k},\gamma}[\hat{A}^{(s)}]\beta_{-\mathbf{k},\gamma} \right] \right.$$
$$\left. + D^{(s)}_P[\hat{A}^{(s)}]\mathcal{P} + D^{(s)}_Q[\hat{A}^{(s)}]\mathcal{Q} \right) + \mathcal{O}(\beta^2) = \frac{1}{\sqrt{N_c}} \sum_s \mathcal{A}_{\mathbf{k},s}. \tag{6.91}$$

Here we introduce the following set of coefficients for all first order quasiparticle terms.

$$D^{(s)}_{\mathbf{k},\gamma}[\hat{A}^{(s)}] = \sum_{i>0} \left( A^{(s)}_{i,0} u^{(\mathbf{k},\gamma)^*}_{i,s} - A^{(s)}_{0,i} v^{(-\mathbf{k},\gamma)^*}_{i,s} \right) \tag{6.92}$$

$$\tilde{D}^{(s)}_{\mathbf{k},\gamma}[\hat{A}^{(s)}] = \sum_{i>0} \left( A^{(s)}_{0,i} u^{(\mathbf{k},\gamma)}_{i,s} - A^{(s)}_{i,0} v^{(-\mathbf{k},\gamma)}_{i,s} \right) \tag{6.93}$$

$$D^{(s)}_P[\hat{A}^{(s)}] = \delta_{\mathbf{k},0} \sum_{i>0} \left( A^{(s)}_{0,i} v^{(0)}_{i,s} + A^{(s)}_{i,0} v^{(0)^*}_{i,s} \right) \tag{6.94}$$

$$D^{(s)}_Q[\hat{A}^{(s)}] = i\delta_{\mathbf{k},0} \sum_{i>0} \left( A^{(s)}_{0,i} u^{(0)}_{i,s} - A^{(s)}_{i,0} u^{(0)^*}_{i,s} \right) \tag{6.95}$$

In (6.91) we also use the notation $\mathcal{O}(\beta^2)$ for any term that is of second order in any of the products of $\beta, \beta^\dagger, \mathcal{P}, \mathcal{Q}$. Those terms can typically be neglected for low concentrations of excited quasiparticle modes, which is the case for the type of linear response calculations we are interested in.

### 6.4.1 Mode characterization via order parameter response

In order to get an insight into the structure and character of individual collective modes, we want to analyze the properties of a given quasiparticle ground-state $|\psi_0\rangle$. Considering a state excited with a single quasiparticle $|\psi\rangle = \beta^\dagger_{\mathbf{k},\gamma}|\psi_0\rangle$ one can verify that such a state does not break the discrete translational symmetry. Thus it describes neither a density wave nor an order parameter wave. To describe any of those, a state corresponding to the classical limit is required, which in analogy to the harmonic oscillator is a feature that is most pronounced in a coherent state. Therefore we investigate the properties of states of the form

$$|z,\mathbf{k},\gamma\rangle = e^{-|z|^2/2} e^{z\beta^\dagger_{\mathbf{k},\gamma}} |\psi_0\rangle. \tag{6.96}$$

These states on average contain $|z|^2 = \langle z,\mathbf{k},\gamma|\beta^\dagger_{\mathbf{k},\gamma}\beta_{\mathbf{k},\gamma}|z,\mathbf{k},\gamma\rangle$ quasiparticles, in analogy to any other coherent state. The specific structure and thus spatial symmetry breaking on the other hand is given by the combined complex phase contained in both the coherent state parameter $z = |z|e^{i\phi}$ and in the definition of $\beta^\dagger_{\mathbf{k},\gamma}$.

Now we want to analyze the signatures of individual quasiparticle modes by looking at – for now – unspecified expectation values. Having derived the quasiparticle theory in the limit of weak quasiparticle excitations, we may thus focus on the regime $|z| \ll 1$. Thus we may predict the lowest order response of any (local) operator $\hat{O}$. Considering the expectation value of $O_0 = \langle\psi_0|\hat{O}|\psi_0\rangle$ in the quasiparticle ground-state, we find a deviation from this ground-state value which in lowest order generally scales linearly in $z$:

$$\langle z, \mathbf{k}, \gamma|\hat{O}|z, \mathbf{k}, \gamma\rangle = O_0 + O_1 z + \mathcal{O}(z^2). \tag{6.97}$$

Thus by determining the real and imaginary linear response encoded in $O_1$ we are able to find the response of different relevant observables for the various quasiparticle modes, allowing us to give a characterization of the excitations.

### Density response

Using the density operator as a first example for which to derive its response, let us give a brief derivation of the first order term. Considering a coherent state that only contains a very small number of excitations on average we may use the approximation $e^{z\beta^\dagger_{\mathbf{k},\gamma}} = 1 + z\beta^\dagger_{\mathbf{k},\gamma} + \mathcal{O}(z^2)$. Thus we obtain the following expectation value for the local density $\hat{n}^\sigma_\ell = \hat{n}^\sigma_{l,s}$ in a weakly excited quasiparticle mode up to first order in $z = |z|e^{i\theta}$:

$$\begin{aligned}
&\langle z, \mathbf{k}, \gamma|\hat{n}^\sigma_\ell|z, \mathbf{k}, \gamma\rangle \\
\approx&\langle\psi_0|(1 + z^*\beta_{\mathbf{k},\gamma})\hat{n}^\sigma_\ell(1 + z\beta^\dagger_{\mathbf{k},\gamma})|\psi_0\rangle \\
=&n^\sigma_{\ell,0} + \frac{|z|}{\sqrt{L_c}}\left(e^{i\lfloor\mathbf{k}\rfloor'\cdot(\mathbf{r}_l+\mathbf{r}_s)-i\theta}D^{(s)}_{\lfloor\mathbf{k}\rfloor',\gamma}[\hat{n}^\sigma_\ell] + e^{-i\lfloor\mathbf{k}\rfloor'\cdot(\mathbf{r}_l+\mathbf{r}_s)+i\theta}\tilde{D}^{(s)}_{\lfloor\mathbf{k}\rfloor',\gamma}[\hat{n}^\sigma_\ell]\right)
\end{aligned}$$

In this derivation we have used the following commutation relation, which also determines the $\Sigma$-normalization condition as used for the eigenvectors of the quasiparticle matrix:

$$\begin{aligned}
\left[\beta_{\mathbf{k}+\mathbf{G}_r,\alpha}, \beta^\dagger_{\mathbf{k}',\gamma}\right] =&\delta_{\mathbf{k},\mathbf{k}'}\sum_{i,s}\left(u^{(\mathbf{k},\alpha)^*}_{i,s}e^{i\mathbf{G}_r\cdot\mathbf{r}_s}u^{(\mathbf{k},\gamma)}_{i,s} - v^{(\mathbf{k},\alpha)^*}_{i,s}e^{i\mathbf{G}_r\cdot\mathbf{r}_s}v^{(\mathbf{k},\gamma)}_{i,s}\right)e^{-i\mathbf{G}_r\cdot\mathbf{r}_s} \\
=&\left[\beta_{\mathbf{k},\alpha}, \beta^\dagger_{\mathbf{k}',\gamma}\right] = \delta_{\mathbf{k},\mathbf{k}'}\delta_{\alpha,\gamma}
\end{aligned} \tag{6.98}$$

This expression is valid for any reciprocal lattice vector $\mathbf{G}_r$ of the extended unit cells, while both quasimomenta $\mathbf{k}$ and $\mathbf{k}'$ have to lie within the reduced 1.BZ′. It also uses the approximation of a vanishing control parameter $R$ (6.20).

Thus we can see that a weak coherent excitation of any quasiparticle mode amounts to a plane wave spatial fluctuation of the density with an amplitude that depends on the specific mode. The phase of $z$ determines the phase shift of this oscillation. A proper choice of $\theta$ will thus yield the amplitude of the fluctuations on each site $s$ of the unit cell. With that in mind we may also rewrite the expression using $\vartheta_\ell = \lfloor\mathbf{k}\rfloor'\cdot\mathbf{r}_\ell - \theta$, so

$$\langle z,\mathbf{k},\gamma|\hat{n}^{\sigma}_{\ell}|z,\mathbf{k},\gamma\rangle = n^{\sigma}_{\ell} + \frac{|z|}{\sqrt{L_c}}\left(e^{i\vartheta_\ell} D^{(s)}_{\lfloor\mathbf{k}\rfloor',\gamma}[\hat{n}^{\sigma}_{\ell}] + e^{-i\vartheta_\ell}\tilde{D}^{(s)}_{\lfloor\mathbf{k}\rfloor',\gamma}[\hat{n}^{\sigma}_{\ell}]\right) + \mathcal{O}(z^2). \tag{6.99}$$

In the derivation of this expression we have introduced $\lfloor\mathbf{k}\rfloor' = \mathbf{k} - \mathbf{G}_r$, which maps any quasimomentum outside of the reduced Brillouin zone 1.BZ′ back to one inside of it, using a proper reciprocal lattice vector $\mathbf{G}_r$.

In the general case one expects both $D^{(s)}_{\lfloor\mathbf{k}\rfloor',\alpha}[\hat{n}^{\sigma}_{\ell}]$ and $\tilde{D}^{(s)}_{\lfloor\mathbf{k}\rfloor',\alpha}[\hat{n}^{\sigma}_{\ell}]$ to be complex. As we use the occupation operator in the present case, one has to consider the special property that both terms are related by complex conjugation. This results from the symmetry of $N^{\sigma,\ell}_{i,j} = N^{\sigma,\ell}_{j,i}$, which, when inserted in (6.92) and (6.93), always yields a real-valued response of the density fluctuations.

### Order parameter response

In order to derive the order parameter response we use $\hat{b}_{\sigma,\ell}$ as the considered local operator. Therefore the response is given as

$$\begin{aligned}\langle z,\mathbf{k},\gamma|\hat{b}_{\sigma,\ell}|z,\mathbf{k},\gamma\rangle =& \phi_{\sigma,\ell} + \frac{|z|}{\sqrt{L_c}}\left(e^{i\vartheta_\ell} D^{(s)}_{\lfloor\mathbf{k}\rfloor',\gamma}[\hat{b}_{\sigma,\ell}] + e^{-i\vartheta_\ell}\tilde{D}^{(s)}_{\lfloor\mathbf{k}\rfloor',\gamma}[\hat{b}_{\sigma,\ell}]\right) + \mathcal{O}(z^2)\\ \equiv& \phi_{\sigma,\ell} + |z|\delta\phi_{\sigma,\ell} + \mathcal{O}(z^2)\end{aligned} \tag{6.100}$$

Due to the non-hermitian nature of $\hat{b}_{\sigma,\ell}$, $D^{(s)}_{\lfloor\mathbf{k}\rfloor',\gamma}[\hat{b}_{\sigma,\ell}]$ and $\tilde{D}^{(s)}_{\lfloor\mathbf{k}\rfloor',\gamma}[\hat{b}_{\sigma,\ell}]$ are not related by a complex conjugation. Thus the condensate response will be a complex number in the general case. Without loss of generality we may consider a real-valued condensate order parameter $\phi_{\sigma,\ell}$ to begin with. In that case the imaginary response corresponds to a phase fluctuation of the condensate, while a real response corresponds to an amplitude fluctuation. These two responses are defining features for the Goldstone mode of a superfluid and the Higgs amplitude mode respectively.

Let us now determine the amplitudes of the two possible responses of a condensate, considering a given quasiparticle mode. We use the abbreviated notation $b_r + ib_i = D^{(s)}_{\lfloor\mathbf{k}\rfloor',\gamma}[\hat{b}_{\sigma,\ell}]$ and $\tilde{b}_r + i\tilde{b}_i = \tilde{D}^{(s)}_{\lfloor\mathbf{k}\rfloor',\gamma}[\hat{b}_{\sigma,\ell}]$ for the real and imaginary parts.

$$\begin{aligned}\mathrm{Re}(\delta\phi_{\sigma,\ell}) &= \cos(\vartheta_\ell)(b_r + \tilde{b}_r) + \sin(\vartheta_\ell)(\tilde{b}_i - b_i)\\ \mathrm{Im}(\delta\phi_{\sigma,\ell}) &= \cos(\vartheta_\ell)(b_i + \tilde{b}_i) + \sin(\vartheta_\ell)(b_r - \tilde{b}_r)\end{aligned}$$

Thus the amplitudes of the amplitude $(r)$ and phase $(i)$ response are maximal for the following values of the phase $\vartheta_\ell$.

$$\tan(\vartheta^{(r)}_{\ell}) = \frac{\tilde{b}_i - b_i}{\tilde{b}_r + b_r} = \frac{\mathrm{Im}(\tilde{D}^{(s)}_{\lfloor\mathbf{k}\rfloor',\gamma}[\hat{b}_{\sigma,\ell}] - D^{(s)}_{\lfloor\mathbf{k}\rfloor',\gamma}[\hat{b}_{\sigma,\ell}])}{\mathrm{Re}(\tilde{D}^{(s)}_{\lfloor\mathbf{k}\rfloor',\gamma}[\hat{b}_{\sigma,\ell}] + D^{(s)}_{\lfloor\mathbf{k}\rfloor',\gamma}[\hat{b}_{\sigma,\ell}])} \tag{6.101}$$

$$\tan(\vartheta^{(i)}_{\ell}) = \frac{b_r - \tilde{b}_r}{\tilde{b}_i + b_i} = \frac{\mathrm{Re}(D^{(s)}_{\lfloor\mathbf{k}\rfloor',\gamma}[\hat{b}_{\sigma,\ell}] - \tilde{D}^{(s)}_{\lfloor\mathbf{k}\rfloor',\gamma}[\hat{b}_{\sigma,\ell}])}{\mathrm{Im}(D^{(s)}_{\lfloor\mathbf{k}\rfloor',\gamma}[\hat{b}_{\sigma,\ell}] + \tilde{D}^{(s)}_{\lfloor\mathbf{k}\rfloor',\gamma}[\hat{b}_{\sigma,\ell}])} \tag{6.102}$$

Judging from the response of individual quasiparticle modes we can determine the composition of the bands, for example in order to ascertain the number of amplitude and Goldstone modes respectively, as well as the purity of such an assignment.

### 6.4.2 Spectral functions

Using the commutation relations of the quasiparticle mode operators we now calculate explicit expressions for various spectral functions, as obtained for the quasiparticle ground-state $|\psi_0\rangle$. In analogy to (4.59), the spectral representation of the ground-state spectral function $\mathcal{A}_{\mathbf{k}',\mathbf{k}}(\omega) = -\pi^{-1}\mathrm{Im}G_{\mathbf{k},\mathbf{k}'}(\omega)$ (see e.g. [AS10; Bis12]) can in general be written as

$$\begin{aligned}\mathcal{A}_{\mathbf{k}',\mathbf{k}}(\omega) &= \theta(\omega)\mathcal{A}^{>}_{\mathbf{k},\mathbf{k}'}(\omega) - \theta(-\omega)\mathcal{A}^{<}_{\mathbf{k},\mathbf{k}'}(\omega) \\ &= \langle\psi_0\left|\Theta(\omega)\hat{b}_{\mathbf{k}'}\delta(\hat{H}-E_0-\omega)\hat{b}^\dagger_{\mathbf{k}} - \Theta(-\omega)\hat{b}^\dagger_{\mathbf{k}}\delta(\hat{H}-E_0+\omega)\hat{b}_{\mathbf{k}'}\right|\psi_0\rangle.\end{aligned} \tag{6.103}$$

The $\delta$-function as an expression depending on an operator has to be understood as a notation which actually is given in terms of the eigenvalues and eigenstates of that operator:

$$\delta(\hat{H}-E_0-\omega) = \sum_\nu \delta(E_\nu - E_0 - \omega)|\psi_\nu\rangle\langle\psi_\nu|. \tag{6.104}$$

Remember that we only consider the expansion of the original Hamiltonian up to second order in the Gutzwiller fluctuations, namely $H^{(2)} = H_{GW} + \mathcal{H}^{(2)}$. Thus the quasiparticle modes are assumed to be non-interacting. In that case we are primarily interested in the most relevant entries, which are given by the diagonal. We therefore define the spectral function $\mathcal{A}^{(2)}(\mathbf{k},\omega)$, as

$$\begin{aligned}\mathcal{A}^{(2)}(\mathbf{k},\omega) \equiv& \mathcal{A}^{(2)}_{\mathbf{k},\mathbf{k}}(\omega) = \theta(\omega)\mathcal{A}^{(2)}_{>}(\mathbf{k},\omega) - \theta(-\omega)\mathcal{A}^{(2)}_{<}(\mathbf{k},\omega) \\ =& \langle\psi_0|\Theta(\omega)b_{\mathbf{k}}\delta(\hat{H}^{(2)}-E_0-\omega)b^\dagger_{\mathbf{k}} - \Theta(-\omega)b^\dagger_{\mathbf{k}}\delta(\hat{H}^{(2)}-E_0+\omega)b_{\mathbf{k}}|\psi_0\rangle.\end{aligned} \tag{6.105}$$

As we have shown before the Bloch state creation (annihilation) operators can be expressed in terms of the fluctuation operators and thus via the quasiparticle mode operators. In an inhomogeneous, but still spatially periodic system with extended unit cells, the fluctuation representation takes the following form (with the component index suppressed):

$$\begin{aligned}\hat{b}^\dagger_{\mathbf{k}} =& \frac{1}{\sqrt{N_c}}\sum_s\Bigg[\sqrt{L_c}\delta_{\mathbf{k},\mathbf{G}_r}B^{(s)^*}_{0,0}e^{i\mathbf{k}\cdot\mathbf{r}_s}\mathbb{1} + \sum_{i>0}\left(B^{(s)^*}_{0,i}\tilde{\sigma}^{(i)^\dagger}_{\mathbf{k},s} + B^{(s)^*}_{i,0}\tilde{\sigma}^{(i)}_{-\mathbf{k},s}\right) \\ &+ \frac{1}{\sqrt{L_c}}\sum_{i,j>0}\left(B^{(s)^*}_{i,j} - \delta_{i,j}B^{(s)^*}_{0,0}\right)\sum_{\mathbf{k}'\in 1.\mathrm{BZ}'}\tilde{\sigma}^{(j)^\dagger}_{\lfloor\mathbf{k}'+\mathbf{k}\rfloor,s}\tilde{\sigma}^{(i)}_{\mathbf{k}',s}\Bigg].\end{aligned} \tag{6.106}$$

Next we use the quasiparticle mode representations (6.80) and (6.79) which yield a representation of $b^\dagger_{\mathbf{k}}$ in terms of the generalized Bogoliubov amplitudes $v^{(\mathbf{k}\gamma)}_{is}$ and $u^{(\mathbf{k}\gamma)}_{is}$. As we are specifically interested in the ground-state we find

$$\begin{aligned}\hat{b}^\dagger_{\mathbf{k}}|\psi_0\rangle =& \delta_{\mathbf{k},\mathbf{G}_r}\frac{\sqrt{L}}{N_c}\sum_s B^{(s)^*}_{0,0}e^{i\mathbf{k}\cdot\mathbf{r}_s}|\psi_0\rangle \\ &+\frac{1}{\sqrt{N_c}}\sum_s\sum_{i>0,\gamma}\left(B^{(s)^*}_{0,i}u^{(\mathbf{k},\gamma)^*}_{i,s}-B^{(s)^*}_{i,0}v^{(\mathbf{k},\gamma)^*}_{i,s}\right)\beta^\dagger_{\mathbf{k},\gamma}|\psi_0\rangle \\ &+\frac{i\delta_{\mathbf{k},\mathbf{G}_r}}{\sqrt{N_c}}\sum_s\sum_{i>0}\left(B^{(s)^*}_{i,0}u^{(0)}_{i,s}-B^{(s)^*}_{0,i}u^{(0)^*}_{i,s}\right)\mathcal{Q}|\psi_0\rangle \\ &+\frac{1}{\sqrt{L}}\sum_s\sum_{i,j>0}\tilde{B}^{(s)^*}_{i,j}\sum_{\mathbf{k}'\in 1.\mathrm{BZ}'}\tilde{\sigma}^{(j)^\dagger}_{\lfloor\mathbf{k}'+\mathbf{k}\rfloor,s}\tilde{\sigma}^{(i)}_{\mathbf{k}',s}|\psi_0\rangle.\end{aligned} \tag{6.107}$$

We evaluate the last term involving products of two fluctuation operators separately, keeping in mind that $\mathbf{k}' \in 1.\mathrm{BZ}'$:

$$\begin{aligned}\tilde{\sigma}^{(j)^\dagger}_{\lfloor\mathbf{k}'+\mathbf{k}\rfloor,s}\tilde{\sigma}^{(i)}_{\mathbf{k}',s}|\psi_0\rangle =& -\sum_{\gamma_1,\gamma_2}v^{(\mathbf{k}',\gamma_1)^*}_{i,s}u^{(\lfloor\mathbf{k}'+\mathbf{k}\rfloor,\gamma_2)^*}_{j,s}\beta^\dagger_{\lfloor\mathbf{k}'+\mathbf{k}\rfloor,\gamma_2}\beta^\dagger_{-\mathbf{k}',\gamma_1}|\psi_0\rangle \\ &+\delta_{-\lfloor\mathbf{k}'+\mathbf{k}\rfloor,-\mathbf{k}'}\sum_\gamma v^{(\mathbf{k}',\gamma)^*}_{i,s}v^{(\lfloor\mathbf{k}'+\mathbf{k}\rfloor,\gamma)}_{j,s}|\psi_0\rangle \\ &+i\delta_{\mathbf{k}',0}u^{(0)^*}_{i,s}\sum_\gamma u^{(\lfloor\mathbf{k}'+\mathbf{k}\rfloor,\gamma)^*}_{j,s}\beta^\dagger_{\lfloor\mathbf{k}'+\mathbf{k}\rfloor,\gamma}\mathcal{Q}|\psi_0\rangle \\ &+i\delta_{\lfloor\mathbf{k}'+\mathbf{k}\rfloor,0}u^{(0)^*}_{j,s}\sum_\gamma v^{(\mathbf{k}',\gamma)^*}_{i,s}\beta^\dagger_{-\mathbf{k}',\gamma}\mathcal{Q}|\psi_0\rangle \\ &-\delta_{\mathbf{k}',\mathbf{0}}\delta_{\lfloor\mathbf{k}'+\mathbf{k}\rfloor,0}u^{(0)}_{i,s}v^{(0)^*}_{j,s}|\psi_0\rangle \\ &+\delta_{\mathbf{k}',0}\delta_{\lfloor\mathbf{k}'+\mathbf{k}\rfloor,0}u^{(0)}_{i,s}u^{(0)^*}_{j,s}\mathcal{Q}\mathcal{Q}|\psi_0\rangle.\end{aligned} \tag{6.108}$$

Summation of these terms over $\mathbf{k}'$ within the *reduced* $1.\mathrm{BZ}'$ yields the expression

$$\begin{aligned}\sum_{\mathbf{k}'}\tilde{\sigma}^{(j)^\dagger}_{\lfloor\mathbf{k}'+\mathbf{k}\rfloor,s}\tilde{\sigma}^{(i)}_{\mathbf{k}',s}|\psi_0\rangle =& -\sum_{\mathbf{k}'}\sum_{\gamma_1,\gamma_2}v^{(\mathbf{k}',\gamma_1)^*}_{i,s}u^{(\lfloor\mathbf{k}'+\mathbf{k}\rfloor,\gamma_2)^*}_{j,s}\beta^\dagger_{\lfloor\mathbf{k}'+\mathbf{k}\rfloor,\gamma_2}\beta^\dagger_{-\mathbf{k}',\gamma_1}|\psi_0\rangle \\ &+\delta_{\mathbf{k},\mathbf{G}_r}\left(-u^{(0)}_{i,s}v^{(0)^*}_{j,s}+\sum_{\gamma,\mathbf{k}'}v^{(\mathbf{k}',\gamma)^*}_{i,s}v^{(\mathbf{k}',\gamma)}_{j,s}\right)|\psi_0\rangle \\ &+i\sum_\gamma\left(u^{(0)^*}_{j,s}v^{(-\lfloor\mathbf{k}\rfloor,\gamma)^*}_{i,s}+u^{(0)}_{i,s}u^{(\lfloor\mathbf{k}\rfloor,\gamma)^*}_{j,s}\right)\beta^\dagger_{\lfloor\mathbf{k}\rfloor,\gamma}\mathcal{Q}|\psi_0\rangle \\ &+\delta_{\mathbf{k},\mathbf{G}_r}u^{(0)}_{i,s}u^{(0)^*}_{j,s}\mathcal{Q}\mathcal{Q}|\psi_0\rangle.\end{aligned} \tag{6.109}$$

From now on we focus on the insulating (non-condensed) case, for which a complete basis of eigenmodes always exists, so neither $\mathcal{Q}$ nor $\mathcal{P}$ appear. Then we obtain the state

$$\hat{b}^\dagger_{\mathbf{k}}|\psi_0\rangle = \left(\delta_{\mathbf{k},\mathbf{G}_r}\sqrt{L}C^0_{\mathbf{k}}+\sum_\gamma S_{\mathbf{k},\gamma}\beta^\dagger_{\mathbf{k},\gamma}+\frac{1}{\sqrt{L}}\sum_{\gamma_1,\gamma_2}\sum_{\mathbf{k}'\in 1.\mathrm{BZ}'}S_{\mathbf{k}'\lfloor\mathbf{k}-\mathbf{k}'\rfloor,\gamma_1\gamma_2}\beta^\dagger_{\lfloor\mathbf{k}-\mathbf{k}'\rfloor,\gamma_2}\beta^\dagger_{\mathbf{k}',\gamma_1}\right)|\psi_0\rangle\,. \tag{6.110}$$

The individual contributions depend on the coefficients, which are given as follows:

$$C^0_{\mathbf{k}} = \sum_s \frac{B^{(s)*}_{0,0}}{N_c} e^{i\mathbf{k}\cdot\mathbf{r}_s} + \sum_s \sum_{i,j>0} \frac{\tilde{B}^{(s)*}_{i,j}}{L} \left( \sum_{\gamma,\mathbf{k}\in 1.\mathrm{BZ}'} v^{(\mathbf{k}\gamma)*}_{i,s} v^{(\mathbf{k}\gamma)}_{j,s} - u^{(0)}_{i,s} v^{(0)*}_{j,s} \right), \tag{6.111}$$

$$S_{\mathbf{k},\gamma} = \frac{1}{\sqrt{N_c}} \sum_{s,i>0} \left( B^{(s)*}_{0,i} u^{(\mathbf{k},\gamma)*}_{i,s} - B^{(s)*}_{i,0} v^{(\mathbf{k},\gamma)*}_{i,s} \right), \tag{6.112}$$

$$S_{\mathbf{k}_1\mathbf{k}_2,\gamma_1\gamma_2} = -\sum_s \sum_{i,j>0} \tilde{B}^{(s)*}_{i,j} v^{(-\mathbf{k}_1,\gamma_1)*}_{i,s} u^{(\mathbf{k}_2,\gamma_2)*}_{j,s}. \tag{6.113}$$

Using this expression the spectral function can straightforwardly be calculated. The greater spectral function then simply becomes

$$\mathcal{A}^{(2)}_{>}(\mathbf{k},\omega) = \delta_{\mathbf{k},\mathbf{G}_r}\delta(\omega) L |C^0_{\mathbf{k}}|^2 + \sum_\gamma |S_{\mathbf{k},\gamma}|^2 \delta(\omega_{\mathbf{k},\gamma} - E_0 - \omega) + \mathcal{O}(L^{-1}). \tag{6.114}$$

All terms in second order of the quasiparticle amplitudes $u$ and $v$ are suppressed by the factor $1/L$. So we may neglect them for large system sizes assuming a small occupation of the quasiparticle modes, while they become relevant for small system sizes and especially for a large occupation of quasiparticle modes. They describe contributions from states, where adding or removing a particle generates two quasiparticles. We also do not consider the additional terms proportional to the $\mathcal{P}$ and $\mathcal{Q}$ operators, which only appear in the condensate regime. We justify this by arguing that those expressions only yield a constant correction in the $1/L$ expansion to the $(\mathbf{k} = 0, \omega = 0)$ spectral weight of $\mathcal{A}^{(2)}_{>}(\mathbf{k},\omega)$, which itself diverges linearly in system size whenever a condensate is present. Furthermore, as equal (divergent) terms also appear in the lesser spectral function $\mathcal{A}^{(2)}_{<}(\mathbf{k} = 0, \omega = 0)$, both terms cancel in the full spectral function due to their opposite signs.

What remains to complete a derivation of the full spectral function is the calculation of the lesser spectral function $\mathcal{A}^{(2)}_{<}(\mathbf{k},\omega)$, which is analogous to the presented derivation. The main differences stem from interchanging $\hat{b}^\dagger_{\mathbf{k}}$ and $\hat{b}_{\mathbf{k}}$ in combination with an additional minus sign in the frequency, in turn leading to a complex conjugation of the terms, while $u$ and $v$ switch roles.

### Green's functions

As is well known, knowledge of the spectral functions can be used to calculate Green's functions using the spectral representation (see e.g. [AS10; Bis12]). Thus one obtains the time-ordered Green's function via

$$G_{\mathbf{k},\mathbf{k}'}(\omega) = \int_{-\infty}^{\infty} d\omega' \frac{\mathcal{A}^{(2)}_{\mathbf{k},\mathbf{k}'}(\omega')}{\omega - \omega' + i\mathrm{sgn}(\omega')0^+}, \tag{6.115}$$

while the retarded ($r$) and advanced ($a$) Green's functions are obtained via

$$G^{r}_{a\,\mathbf{k},\mathbf{k}'}(\omega) = \int_{-\infty}^{\infty} d\omega' \frac{\mathcal{A}^{(2)}_{\mathbf{k},\mathbf{k}'}(\omega')}{\omega - \omega' \pm i0^+}, \tag{6.116}$$

where the sign $(\pm)$ depends on the chosen Greens function $\binom{r}{a}$.

### 6.4.3 Single-particle density of states

The density of states DOS($\omega$) for a given many-particle state $|\psi(N)\rangle$ containing $N$ particles is a measure for the number of many-particle eigenstates in the energy interval $[\omega, \omega + d\omega[$. It contains available states both in the $(N+1)$ particle subspace (particle excitations) for positive quasiparticle energies with frequencies above the chemical potential and in the $(N-1)$ particle subspace (hole excitations) for negative quasiparticle energies with frequencies below the chemical potential. It is defined as the trace of the spectral function:

$$\mathrm{DOS}(\omega) = \sum_{\ell} \mathcal{A}_{\ell,\ell}(\omega) = \sum_{\mathbf{k}\epsilon 1.\mathrm{BZ}} \mathcal{A}_{\mathbf{k},\mathbf{k}}(\omega). \tag{6.117}$$

As such it is independent of the choice of the single particle basis and therefore a universal, frequency dependent function. Its shape and the existence of singular points strongly depends on dimensionality, on lattice geometry and expressly on interactions as well as the occurrence of spontaneous symmetry breaking (see Sec. 7.4.2 and Sec. 8.3.2). In Fig. 4.2 an exemplary comparison of the quasiparticle density of states with ones obtained using RB-DMFT is shown.

### 6.4.4 Corrections to local observables

Due to the depletion of the Gutzwiller ground-state $|\psi_G\rangle$ in favor of the quasiparticle ground-state $|\psi_0\rangle$, we expect to observe corrections for the local observables in $|\psi_0\rangle$ compared to the mean-field state. These corrections can directly be derived using the fluctuation representation (6.13)–(6.16) of the local operators. Thus once more omitting the component index $\sigma$ we find

$$\begin{aligned}\langle \hat{b}_{ls}^\dagger \rangle =& B_{0,0}^{(s)*} + \sum_{i,j>0} \tilde{B}_{i,j}^{(s)*} \langle \hat{\sigma}_{ls}^{(j)\dagger} \hat{\sigma}_{ls}^{(i)} \rangle \\ =& B_{0,0}^{(s)*} + \sum_{i,j>0} \frac{\tilde{B}_{i,j}^{(s)*}}{L_c} \sum_{\mathbf{k},\mathbf{k}'\epsilon 1.\mathrm{BZ}'} \langle \tilde{\sigma}_{\mathbf{k}s}^{(j)\dagger} \tilde{\sigma}_{\mathbf{k}'s}^{(i)} \rangle e^{-i(\mathbf{k}-\mathbf{k}')\cdot(\mathbf{r}_l+\mathbf{r}_s)},\end{aligned} \tag{6.118}$$

$$\begin{aligned}\langle \hat{n}_{ls} \rangle =& N_{0,0}^{(s)} + \sum_{i,j>0} \tilde{N}_{i,j}^{(s)} \langle \hat{\sigma}_{ls}^{(j)\dagger} \hat{\sigma}_{ls}^{(i)} \rangle \\ =& N_{0,0}^{(s)} + \sum_{i,j>0} \frac{\tilde{N}_{i,j}^{(s)}}{L_c} \sum_{\mathbf{k},\mathbf{k}'\epsilon 1.\mathrm{BZ}'} \langle \tilde{\sigma}_{\mathbf{k}s}^{(j)\dagger} \tilde{\sigma}_{\mathbf{k}'s}^{(i)} \rangle e^{-i(\mathbf{k}-\mathbf{k}')\cdot(\mathbf{r}_l+\mathbf{r}_s)}.\end{aligned} \tag{6.119}$$

The remaining expectation values in the quasiparticle ground-state can be simplified using (6.79) and (6.80) in combination with the commutation relation of the quasiparticle mode operators (6.66).

$$\begin{aligned}\langle \hat{\sigma}_{ls}^{(j)\dagger} \hat{\sigma}_{ls}^{(i)} \rangle =& \frac{1}{L_c} \sum_{\mathbf{k},\mathbf{k}'\epsilon 1.\mathrm{BZ}'} \langle \tilde{\sigma}_{\mathbf{k}s}^{(j)\dagger} \tilde{\sigma}_{\mathbf{k}'s}^{(i)} \rangle e^{-i(\mathbf{k}-\mathbf{k}')\cdot(\mathbf{r}_l+\mathbf{r}_s)} \\ =& \frac{1}{L_c} \sum_{\mathbf{k}\epsilon 1.\mathrm{BZ}'} \left( \sum_{\gamma} v_{j,s}^{(\mathbf{k},\gamma)} v_{i,s}^{(\mathbf{k},\gamma)*} + u_{j,s}^{(0)*} u_{i,s}^{(0)} \delta_{\mathbf{k},0} \langle \mathcal{Q}\mathcal{Q} \rangle \right)\end{aligned} \tag{6.120}$$

Thus we find that the correction terms in the condensate always depend on $\langle \mathcal{Q}\mathcal{Q} \rangle$ taking the place of the $(\mathbf{k} = 0, \gamma = 1)$ term. Unfortunately, this term does not allow

for an exact direct calculation. Once more a possible approximation is to neglect this term entirely. As $\mathcal{Q}$ and $\mathcal{P}$ are canonical conjugate operators corresponding to the $U(1)$ degree of freedom in the phase of the condensate, $\mathcal{Q}$ is limited to a finite range, contrary to its behavior in the corresponding *linearized* equation of motion (discussed in [Bis12]). Therefore any of its higher order expectation values actually has to be finite, so its contribution will vanish in the limit of infinite system size $L_c \to \infty$.

### 6.4.5 Single-particle density matrix

The single-particle density matrix is given by the equal time Green's function, but can also be calculated directly in the quasiparticle basis. Let us briefly derive it in the Wannier basis, where it depends on the two positional singleparticle indices $\ell = (l, s)$ and $\ell' = (l', s')$ as well as the considered component, the index of which we once more omit for improved readability.

$$\rho_{\ell,\ell'} = \langle \hat{b}_\ell^\dagger \hat{b}_{\ell'} \rangle \tag{6.121}$$

While the diagonal elements of the single-particle density matrix just give the on-site density of particles for a given particle component of the lattice gas, it is the off-diagonal elements which contain information on the off-diagonal long range order (ODLRO) corresponding to the existence of a condensate fraction. As we have already shown the calculation of the diagonal elements the previous section, we now focus on the off-diagonal elements.

Once more we use the relations (6.13)–(6.16) in order to represent the local annihilation and creation operators in the Wannier basis in terms of the Gutzwiller fluctuations:

$$\hat{b}_{l,s} = B_{0,0}^{(s)} \mathbb{1} + \sum_{i>0} \left( B_{i,0}^{(s)} \hat{\sigma}_{l,s}^{(i)^\dagger} + B_{0,i}^{(s)} \hat{\sigma}_{l,s}^{(i)} \right) + \sum_{i,j>0} \tilde{B}_{i,j}^{(s)} \hat{\sigma}_{l,s}^{(i)^\dagger} \hat{\sigma}_{l,s}^{(j)} . \tag{6.122}$$

Thus the off-diagonal elements equate to the expression

$$\begin{aligned} \langle \hat{b}_{l,s}^\dagger \hat{b}_{l',s'} \rangle = \Bigg\langle & \left[ B_{0,0}^{(s)^*} \mathbb{1} + \sum_{i>0} \left( B_{i,0}^{(s)^*} \hat{\sigma}_{l,s}^{(i)} + B_{0,i}^{(s)^*} \hat{\sigma}_{l,s}^{(i)^\dagger} \right) + \sum_{i,j>0} \tilde{B}_{i,j}^{(s)^*} \hat{\sigma}_{l,s}^{(j)^\dagger} \hat{\sigma}_{l,s}^{(i)} \right] \\ & \times \left[ B_{0,0}^{(s')} \mathbb{1} + \sum_{i>0} \left( B_{i,0}^{(s')} \hat{\sigma}_{l',s'}^{(i)^\dagger} + B_{0,i}^{(s')} \hat{\sigma}_{l',s'}^{(i)} \right) + \sum_{i,j>0} \tilde{B}_{i,j}^{(s')} \hat{\sigma}_{l',s'}^{(i)^\dagger} \hat{\sigma}_{l',s'}^{(j)} \right] \Bigg\rangle . \end{aligned} \tag{6.123}$$

The advantage of evaluating the elements of the density matrix in the local Wannier basis lies in the fact that all fluctuation operators on *different* sites commute exactly, due to their original definition (6.11). In the next step we bring all terms in normal order, while only considering terms up to second order in the fluctuation operators. As the transformation relating the fluctuation operators $\hat{\sigma}^\dagger$ and $\hat{\sigma}$ to the quasiparticle mode operators $\hat{\beta}^\dagger$ and $\hat{\beta}$ is linear, the same order of approximation is guaranteed in the quasiparticle basis. This furthermore implies that when evaluating the matrix elements in the quasiparticle ground-state $|\psi_0\rangle$, we know that all terms of first order in $\hat{\sigma}^\dagger$ and $\hat{\sigma}$ vanish exactly, due to (6.86), (6.87) as well as the relation $\langle \psi_0 | \mathcal{Q} | \psi_0 \rangle = 0$, which has been discussed in Sec. 6.3.4. Thus expanded up to second order, we find

$$\begin{aligned}\langle \hat{b}^\dagger_{l,s}\hat{b}_{l',s'}\rangle =& B^{(s)^*}_{0,0}B^{(s')}_{0,0} + B^{(s)^*}_{0,0}\sum_{i',j'>0}\tilde{B}^{(s')}_{i',j'}\langle \hat{\sigma}^{(i')^\dagger}_{l',s'}\hat{\sigma}^{(j')}_{l',s'}\rangle + B^{(s')}_{0,0}\sum_{i,j>0}\tilde{B}^{(s)^*}_{i,j}\langle \hat{\sigma}^{(j)^\dagger}_{l,s}\hat{\sigma}^{(i)}_{l,s}\rangle \\ &+ \sum_{i,j>0}\Big[B^{(s)^*}_{i,0}B^{(s')}_{j,0}\langle \hat{\sigma}^{(j)^\dagger}_{l',s'}\hat{\sigma}^{(i)}_{l,s}\rangle + B^{(s)^*}_{i,0}B^{(s')}_{0,j}\langle \hat{\sigma}^{(j)}_{l',s'}\hat{\sigma}^{(i)}_{l,s}\rangle \\ &\quad + B^{(s)^*}_{0,i}B^{(s')}_{j,0}\langle \hat{\sigma}^{(j)^\dagger}_{l',s'}\hat{\sigma}^{(i)^\dagger}_{l,s}\rangle + B^{(s)^*}_{0,i}B^{(s')}_{0,j}\langle \hat{\sigma}^{(i)^\dagger}_{l,s}\hat{\sigma}^{(j)}_{l',s'}\rangle\Big] + \mathcal{O}(\hat{\sigma}^3).\end{aligned} \tag{6.124}$$

In a last step we need to evaluate the individual expectation values by expressing them in terms of the quasiparticle mode operators as well as $\mathcal{P}$ and $\mathcal{Q}$. Using the notation $\mathbf{r}_\ell = \mathbf{r}_l + \mathbf{r}_s$ we find the following expressions:

$$\langle \hat{\sigma}^{(j)^\dagger}_{l',s'}\hat{\sigma}^{(i)}_{l,s}\rangle = \frac{1}{L_c}\sum_{\mathbf{k}\in 1.\mathrm{BZ}'} e^{-i\mathbf{k}\cdot(\mathbf{r}_{\ell'}-\mathbf{r}_\ell)}\left(\sum_\gamma v^{(\mathbf{k},\gamma)}_{j,s'}v^{(\mathbf{k},\gamma)^*}_{i,s} + u^{(0)^*}_{j,s'}u^{(0)}_{i,s}\delta_{\mathbf{k},0}\langle\mathcal{Q}\mathcal{Q}\rangle\right), \tag{6.125}$$

$$\langle \hat{\sigma}^{(j)}_{l',s'}\hat{\sigma}^{(i)}_{l,s}\rangle = -\frac{1}{L_c}\sum_{\mathbf{k}\in 1.\mathrm{BZ}'} e^{i\mathbf{k}\cdot(\mathbf{r}_{\ell'}-\mathbf{r}_\ell)}\left(\sum_\gamma u^{(\mathbf{k},\gamma)}_{j,s'}v^{(\mathbf{k},\gamma)^*}_{i,s} + u^{(0)}_{j,s'}u^{(0)}_{i,s}\delta_{\mathbf{k},0}\langle\mathcal{Q}\mathcal{Q}\rangle\right), \tag{6.126}$$

$$\langle \hat{\sigma}^{(j)^\dagger}_{l',s'}\hat{\sigma}^{(i)^\dagger}_{l,s}\rangle = -\frac{1}{L_c}\sum_{\mathbf{k}\in 1.\mathrm{BZ}'} e^{i\mathbf{k}\cdot(\mathbf{r}_{\ell'}-\mathbf{r}_\ell)}\left(\sum_\gamma v^{(\mathbf{k},\gamma)}_{j,s'}u^{(\mathbf{k},\gamma)^*}_{i,s} + u^{(0)^*}_{j,s'}u^{(0)^*}_{i,s}\delta_{\mathbf{k},0}\langle\mathcal{Q}\mathcal{Q}\rangle\right). \tag{6.127}$$

With these we can obtain the spatial density matrix, provided a proper treatment of $\langle\mathcal{Q}\mathcal{Q}\rangle$ (appearing in place of the $(\mathbf{k}=0,\gamma=1)$ term in a condensate), which may be done as previously discussed by neglecting it for a large system size.

Let us now briefly discuss the form of (6.124). Its first three terms all only contribute in the presence of a finite (local) condensate order parameter due to the $B^{(s)}_{0,0}$ terms. Their independence of the indices $l$ and $l'$ shows that they yield a finite background term describing the ODLRO. The remaining terms in the square brackets, which stem from non-local quasiparticle correlations, are always present in any condensate or insulating phase. We furthermore note that the diagonal of the single-particle density matrix equates to the local occupation number $\langle\hat{n}_{ls}\rangle$, which can also be derived directly as shown in the previous section. But as $N^{(s)}_{0,0}$ and $B^{(s)^*}_{0,0}B^{(s)}_{0,0}$ are only identical for $t/U\to\infty$ the identity of (6.119) and (6.124) for any site can possibly be used in order to obtain $\langle\mathcal{Q}\mathcal{Q}\rangle$.

### 6.4.6 Quasimomentum distribution

The quasimomentum distribution is given by the diagonal elements of the single-particle density matrix in quasimomentum space and can be obtained via a Fourier transform of its Wannier space counterpart (6.124):

$$\tilde{\rho}_{\mathbf{k},\mathbf{k}'} = \langle \hat{b}^\dagger_{\mathbf{k}}\hat{b}_{\mathbf{k}'}\rangle = \frac{1}{L}\sum_{\ell,\ell'} e^{i(\mathbf{k}\cdot\mathbf{r}_\ell - \mathbf{k}'\cdot\mathbf{r}_{\ell'})}\rho_{\ell,\ell'}. \tag{6.128}$$

Alternatively one can also consider the relation to the spectral function in order to obtain the quasimomentum distribution from previous results, namely from $\mathcal{A}^{(2)}_<(\mathbf{k},\omega)$:

$$n(\mathbf{k}) = \tilde{\rho}_{\mathbf{k},\mathbf{k}} = \langle \hat{b}^\dagger_{\mathbf{k}} \hat{b}_{\mathbf{k}} \rangle = -\int_{-\infty}^{0} \mathcal{A}^{(2)}_{<}(\mathbf{k},\omega) d\omega. \tag{6.129}$$

We should note at this point regarding the general case of an inhomogeneous system that also off-diagonal terms of the single-particle density matrix can be non-zero. So the momentum distribution does not contain the full information regarding an arbitrary single-particle measurement. In the case considered in this work, where a reduced translational symmetry survives in terms of a superlattice of extended unit cells, the relevant non-vanishing matrix elements are related by the set of reciprocal lattice vectors $\{\mathbf{G}_r\}$.

### 6.4.7 Dynamic structure factor

By definition, the dynamic structure factor is obtained as the discrete spatial and continuous time Fourier transform of the expectation value of the on-site density operator $\hat{n}_\ell = \hat{b}^\dagger_\ell \hat{b}_\ell$ (see e.g. [Stu93; Bis12]), which for the quasiparticle ground-state $\psi_0$ yields the following expression:

$$\begin{aligned} S(\mathbf{k},\omega) =& \frac{1}{2\pi L} \sum_{\ell,\ell'} \int_{-\infty}^{\infty} \left\langle \psi_0 \left| \hat{n}_\ell(t) \hat{n}^\dagger_{\ell'}(0) \right| \psi_0 \right\rangle e^{i\mathbf{k}\cdot(\mathbf{r}_{\ell'} - \mathbf{r}_\ell)} e^{i\omega t} dt \\ =& \left\langle \psi_0 \left| \hat{n}_{\mathbf{k}} \delta(\hat{H} - E_0 - \omega) \hat{n}_{-\mathbf{k}} \right| \psi_0 \right\rangle \\ =& \left\langle \psi_0 \left| \hat{n}_{\mathbf{k}} \delta(\hat{H} - E_0 - \omega) \hat{n}_{\mathbf{k}} \right| \psi_0 \right\rangle \end{aligned} \tag{6.130}$$

Owing to the inversion symmetry, which is also retained in case of a broken lattice symmetry with periodic unit cells, we find that $\hat{n}_{\mathbf{k}} = \hat{n}_{-\mathbf{k}}$. Thus follows the last line of (6.130). For a quick overview of the general behavior of the dynamical structure factor we also consider the momentum integrated dynamical structure factor

$$S(\omega) = \frac{1}{L} \sum_{\mathbf{k}} S(\mathbf{k},\omega). \tag{6.131}$$

We do not show the explicit form of the dynamic structure factor in terms of the quasiparticle amplitudes $v$ and $u$, as the derivation is fully analogous to the spectral function (6.114). One simply has to replace the $B^{(s)}$ and $\tilde{B}^{(s)}$ matrices by the matrices $N^{(s)}$ and $\tilde{N}^{(s)}$ corresponding to the density operator represented in the local Gutzwiller basis, either with or without its mean-field expectation value on the diagonal.

#### Static structure factor

The static structure factor is obtained from the dynamic structure factor via a simple frequency integration, so

$$S(\mathbf{k}) = \int_0^\infty S(\mathbf{k},\omega) d\omega \tag{6.132}$$

It describes the scattering patterns obtained in diffraction experiments as for example achieved via Bragg scattering in cold atom experiments but also in noise correlations (see Sec. 1.4.3) or for electron or neutron scattering as commonly used in

condensed matter experiments. With an additional sensitivity and control over the energy of the scattered particles, one also can access the dynamical properties of the structure factor and thus resolve the quasiparticle band structure (see Sec. 1.4.4).

# Chapter 7

# Ground-state phases for off-resonant Rydberg excitation

In this chapter, which is based on the research published in [Li+18], we will address the many-body equilibrium ground-state phases for off-resonant and coherent excitation of the Rydberg state, commonly referred to as dressing, while the phrase **weak dressing** will be used throughout this thesis, in order to distinguish it from near-resonant driving of the transition, which we will refer to as **strong dressing** (see Chap. 8). In addition we will be considering the mobility of the atoms, allowing for a fluid component in the many-body ground-state. Interest in this regime is stimulated by recent experimental advances, illustrating the realization of long-range two-body interactions as induced via laser coupling of the atomic ground state to Rydberg states [Zei+16; Jau+16]. We will thus discuss supersolidity (SS) of Rydberg dressed lattice Bosons in an already experimentally relevant setup. We will consider two-component atoms on a two-dimensional (2D) square lattice, with one component ($d$) weakly dressed by a Rydberg state ($r$), which generates a tunable, soft-core shape long-range two-body interaction, in addition to the common local inter- and intraspecies interactions. The second species on the other hand will remain bare ($b$), e.g. corresponding to a hyperfine electronic state that is not Rabi-coupled to a Rydberg state, as would be the case for the dressed component (see Fig. 7.1(a)).

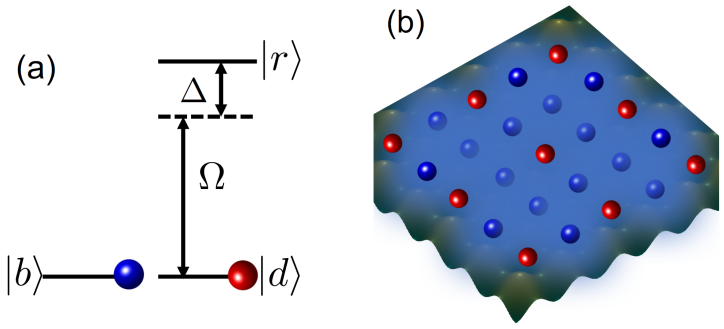


FIGURE 7.1: (a) Two electronic ground states $|b\rangle$ (blue) and $|d\rangle$ (red) in combination with a Rydberg state $|r\rangle$ are considered. The states $|d\rangle$ and $|r\rangle$ are off-resonantly coupled by a laser with Rabi frequency $\Omega$ and a detuning $\Delta$. (b) Artistic depiction of a supersolid of the bare state (corresponding to type SS1, as discussed in the text), while dressed atoms are in a crystalline order.

After a brief introduction of the considered Hamiltonian, we will first discuss the many-body phase diagram, as obtained using real-space bosonic dynamical mean-field theory (RB-DMFT). In addition to Mott insulator (MI), superfluid (SF) and ordered density wave phases (DW), especially a pronounced region of SS phases can be found, which is stabilized by the on-site interspecies interactions. More

specifically we will observe two types of supersolids, where the undressed (bare) species forms supersolid phases, which are immersed in either a crystalline solid (see Fig. 7.1(*b*)) or a SS of the dressed atoms. Regarding the former case we will discuss the corresponding mechanism behind supersolidity formation, based on a simple Bogoliubov treatment, revealing how a roton-like instability emerges due to inter-species interactions. The operator based generalization of this method introduced in Chap. 6 will then further allow us to study specific spectral properties of the system in detail. We will finish by discussing the possible experimental realization of the model using weak dressing of rubidium in an optical lattice in a two-dimensional system.

## 7.1 Many-body Hamiltonian

We study a two-component bosonic mixture of atoms on a 2D optical lattice, which is sufficiently deep, such that our system is described by a single-band, two-component extended Bose-Hubbard model,

$$\hat{H} = \sum_{i,\sigma\sigma'} \frac{U_{\sigma\sigma'}}{2} \hat{n}_{i\sigma} \left( \hat{n}_{i\sigma'} - \delta_{\sigma,\sigma'} \right) - \sum_{\langle i,j \rangle,\sigma} t_\sigma \left( \hat{b}^\dagger_{i\sigma} \hat{b}_{j\sigma} + \text{h.c.} \right) - \sum_{i,\sigma} \mu_\sigma \hat{n}_{i\sigma} + \sum_{i<j} V_{ij} \hat{n}_{id} \hat{n}_{jd}. \tag{7.1}$$

The indices $\sigma, \sigma' \in \{b, d\}$ denote the internal degree of freedom, which can either be a bare or a dressed state, while $\hat{b}^\dagger_{i\sigma}(\hat{b}_{i\sigma})$ are the bosonic creation (annihilation) operators for the two species $\sigma$ at site $i$ and $\hat{n}_{i\sigma} = \hat{b}^\dagger_{i\sigma}\hat{b}_{i\sigma}$. $U_{\sigma\sigma'}$ specifies the local inter- and intraspecies Hubbard interaction with $\delta_{\sigma,\sigma'}$ guaranteeing corret counting, while $t_\sigma$ and $\mu_\sigma$ specify the hopping rate and chemical potential of each bosonic species. And finally, $\langle i, j \rangle$ represents all nearest neighbor sites $i, j$.

We assume identical hopping rates $t = t_b = t_d$ for both species, as they essentially only differ in the hyperfine state, while the inter- and intraspecies local (on-site) interactions can be tuned, either via state-dependent optical lattices [Gad+10], Feshbach resonances [Wid+04] or a combination of both. As we now are considering the weak dressing regime, the long-range interaction betweens sites $i$ and $j$ takes the form of a soft-core potential

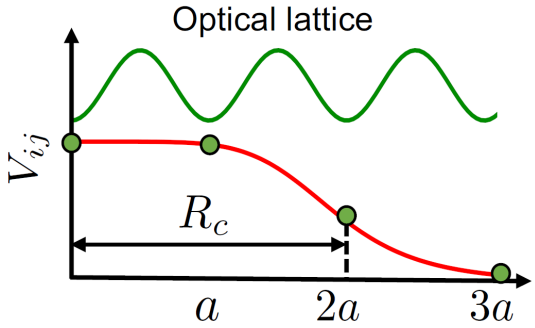


FIGURE 7.2: Shape of the soft-core interaction potential $V_{ij}$ (red) in relation to a typical optical lattice (green). The interaction couples atoms in the Rydberg dressed state $|d\rangle$ at a finite distance up to the soft-core radius $R_c$, which is typically larger than the lattice spacing $a$. Here $R_c = 2a$ is shown. Beyond this distance, the tail of the interaction decreases as $1/r^6$, corresponding to the van der Waals interaction between pure Rydberg atoms.

$$V_{ij} \equiv \frac{V}{\left(\frac{a}{R_c}\right)^6 (\mathbf{r}_i - \mathbf{r}_j)^6 + 1}, \tag{7.2}$$

as shown in Fig. 7.2. The maximum of the soft-core interaction potential is characterized by $V = \tilde{C}_6/R_c^6$. $\tilde{C}_6$, $R_c$ and $a$ are the effective van der Waals constant, the soft-core radius, and lattice constant, respectively. For the following simulations we fix the local intra-species interactions $U_{bb} = U_{dd} = U$, thus setting the unit of energy. In Sec. 7.5 we will discuss these parameters in further detail, focusing on the experimental realization.

RB-DMFT provides a nonperturbative method to describe many-body systems in two and three spatial dimensions. As it is able to capture both higher order quantum fluctuations and strong correlations in combination with arbitrary long-range order in a unified framework (see Chap. 4 and e.g. [Li+11; LHH16]), it is our tool of choice to determine the many-body ground-state phases. The details of this method are provided in Chap. 4. We typically consider lattice sizes as large as $N_{lat} = 48 \times 48$ sites with periodic boundary conditions and an experimentally relevant soft-core radius $R_c = 3a$ [Zei+16]. A supersolid is characterized by a non-vanishing condensate order parameter $\phi_{i\sigma} \equiv \langle \hat{b}_{i\sigma} \rangle$ in combination with crystalline order, manifest in the real-space density distribution $n_{i\sigma} \equiv \langle \hat{n}_{i\sigma} \rangle$ of either species or in the total density $n_i \equiv n_{ib} + n_{id}$. Note that a similar model based on dipolar gases has previously been investigated numerically within the static mean-field Gutzwiller ansatz, while also only considering the nearest-neighbor part of the dipolar interactions [WSN16]. Here we take into account the full range of the interaction potential within a self-consistent Hartree ansatz (see Sec. 2.2.3), while we also give a comparison of the two systems in Sec. 7.6.

## 7.2 Many-body ground-state phase diagram

The phase diagram shown in Fig. 7.3 summarizes the main results. Depending on the parameters $t/U$, $V/U$ as well as the chemical potentials $\mu_b$ and $\mu_d$, we find five different phases realized in the two-component system. Besides MI and SF, the long-range interaction also stabilizes two kinds of supersolid (SS1 and SS2) as well as ordered density wave phases, which are discussed later in this section. For now we will focus on the features of the phases in the vicinity of unit filling $n_{ib} + n_{id} \approx 1$.

Starting in the strong coupling limit, where $U_{\sigma\sigma'} \gg t$, the 2D system expectedly favors MI phases with uniform total densities. On the level of the pseudo-spin states $|b\rangle$ and $|d\rangle$, these insulating phases show a rich variety in pseudo spin order, which can be changed by varying the two-body interactions (as given by $V/U$). One example is given in Fig. 7.3$(a)$, showing an inhomogeneous structure in the relative densities. Furthermore, when one increases $V/U$ continuously, the filling fractions $f_d \equiv \sum_i n_{id}/N_{lat}$ of the dressed component can form a devil's staircase structure, as depicted in Fig. 7.4$(a)$. As only finite system sizes with periodic boundary conditions are considered, the completeness of the staircase in this 2D system remains an open question. In 1D lattice systems on the other hand, the devil's staircase has been studied extensively [Bur+09; WB10; BP12], as well as its completeness for a convex long-range repulsive interaction [BB82]. In addition to these phases there are also very small regions, which are occupied by DW phases at non-uniform total density, as shown in Fig. 7.5.

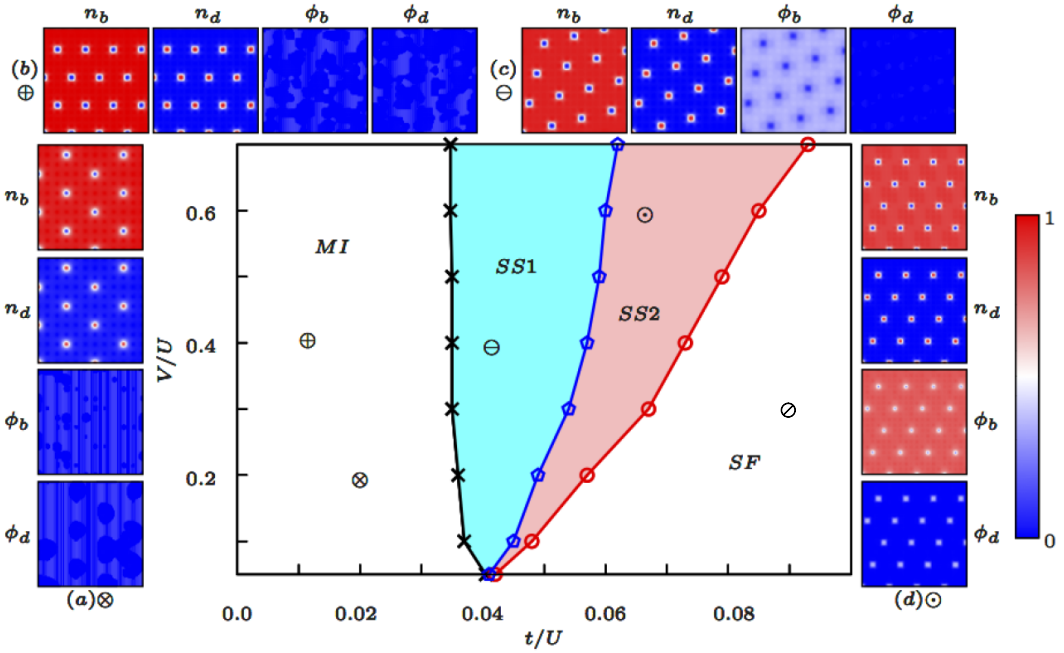


FIGURE 7.3: Phase diagram of a two-component mixture of a ground-state species $b$ and a Rydberg dressed species $d$, on a square lattice in terms of hopping amplitude $t$ and Rydberg dressed interaction strength $V$. One can distinguish four stable phases in the diagram: Mott insulator (MI) with spatially uniform total local density and crystalline density order for each species, homogeneous superfluid (SF), and two types of supersolids (SS1 with Rydberg dressed species being in the crystalline phase, and SS2 with both species being in the supersolid). The remaining parameters of the model (7.1) are $U_{bd} = U_{db} = U$, $\mu_b = 0.2U$ and $\mu_d = 0.7U$. $(a)$-$(d)$: Real-space density $n_{b,d}$ and condensate order parameter $\phi_{b,d}$ distributions of different phases, with lattice sizes being the square of the area of the unit cell of the Rydberg dressed species [MI, $N_{lat} = 12 \times 12(\otimes)$; MI, $N_{lat} = 16 \times 16(\oplus)$; SS1, $N_{lat} = 15 \times 15(\odot)$; SS2, $N_{lat} = 20 \times 20(\ominus)$], as shown by the markers in the main figure. For $\oslash$ the spectral properties of the superfluid phase are discussed in Sec. 7.4.

Increasing the hopping rate, we observe a phase transition to a pronounced region of supersolids, starting with the SS1 phase, where the bare state is the first to encounter a non-vanishing condensate order parameter, which is accompanied by a finite superfluid fraction. Apart from that the dressed state remains in an insulating phase with a crystalline order (one example is depicted in Fig. 7.3$(c)$). For even larger hopping rates $t$, both species are in supersolid phases (SS2, with an example shown in Fig. 7.3$(d)$), for which both condensate order parameters show a spatial inhomogeneity, as does the density distribution, corresponding to a non-trivial on- and off-diagonal long-range order. The existence of a large supersolid region indicates a higher chance for directly observing these phases in realistic experiments, as compared to the single-component case [Hen+12; Cin+14; Mat+13; Dal+15] at weak dressing.

Considering the bare species all by itself one would only expect either a SF or MI phase, due to the local interactions [Fis+89; Jak+98; Gre+02a]. But when immersed in a background of the dressed species, the flow of the bare component is suppressed by the crystalline distribution of the dressed part. As this suppression is mediated by the local interspecies interaction, the widths of the supersolid phases SS1 and SS2 will strongly depend on the interspecies interaction $U_{bd}$. This relation is depicted in Fig. 7.4$(b)$, showing that both phases shrink as $U_{bd}$ decreases, with the SS1 eventually

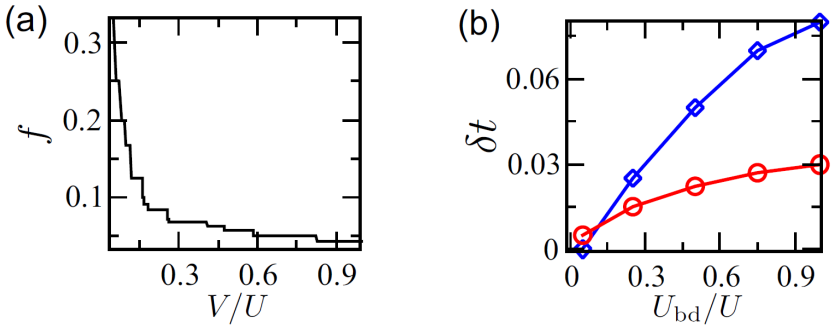


FIGURE 7.4: (a) Devil's staircase pattern of the filling fraction $f_d = \sum_i n_{id}/N_{lat}$ for the Rydberg dressed species in the (frozen) zero-hopping limit. (b) Width $\delta t \equiv t_c^{\max} - t_c^{\min}$ of the supersolid phases SS1 (blue) and SS2 (red), as a function of the interspecies interaction $U_{bd}/U$ for fixed Rydberg dressed interaction $V/U = 0.1$, where $t_c^{\max/\min}$ corresponds to the upper/lower phase boundary of the individual SS phase.

disappearing for sufficiently small values of $U_{bd}$. For vanishing $U_{bd}$ both components can be considered as independent sub-systems, where the long-range interacting dressed species forms a SS all on its own, corresponding to the SS2 phase at $U_{bd} = 0$. With that in mind, it is especially noteworthy that also the SS2 phase widens as a function of $U_{bd}$, which implies a stabilization of non-trivial crystalline order, originally induced by a long-range interaction, by a simple local interaction.

A further increase in the hopping rate finally leads to a melting of any crystalline order, resulting in a SF phase, characterized by nonzero SF order parameters for both components, while either spatial density becomes homogeneous.

As all results so far are at approximately unit filling, we now study the stability of the observed quantum phases for varying filling, realized by switching from fixed chemical potentials, to fixed long-range interaction, while still varying the hopping rate $t$. Considering the limit $U_{\sigma\sigma'} \gg t$, the system is found to favor either a MI or DW phase, both with various types of crystalline order in either of the atomic components. The DW can be observed as a phase with non-uniform total density, breaking the lattice translational symmetry. Observed densities are $n_{ib} = 1$ and $n_{id} = 2$, appearing in the green region depicted in Fig. 7.5(e). These DW further exhibit nonzero local density fluctuations in both components, while they are limited to the $n_d = 2$ site in the dressed component, as is shown in Fig. 7.6($b$). Quantum fluctuations as a result of higher-order tunneling processes otherwise are weak, owing to the strong collective long-range interactions. The DW phases of the dressed species have furthermore been previously predicted in the single-species case [Pup+10].

In the intermediate hopping regime, away from the deep MI regime, two types of quantum phase transitions can be observed. The first transition is from MI to supersolid, realized by the undressed species, exhibiting a non-zero condensate order parameter avoiding sites occupied by the Rydberg dressed species. This is followed by the dressed species itself undergoing a transition to a supersolid. These regions appear already for relatively small long-range interactions, as shown in Fig. 7.5. Once more we specifically observe, that the additional local interaction to a bare component ($U_{bd}$) tends to stabilize the supersolid phase, as it widens for increasing $U_{bd}$ (see Fig. 7.5(f)), while the SS1 phase clearly disappears for decreasing $U_{bd}$. Additionally we find that the long-range interaction shifts the phase transition between MI and SS1, even though the bare species does not exhibit long-range interactions itself. As seen in both Fig. 7.3 and Fig. 7.5, the phase boundary tends to move towards lower hopping rates with increasing long-range interaction $V$.

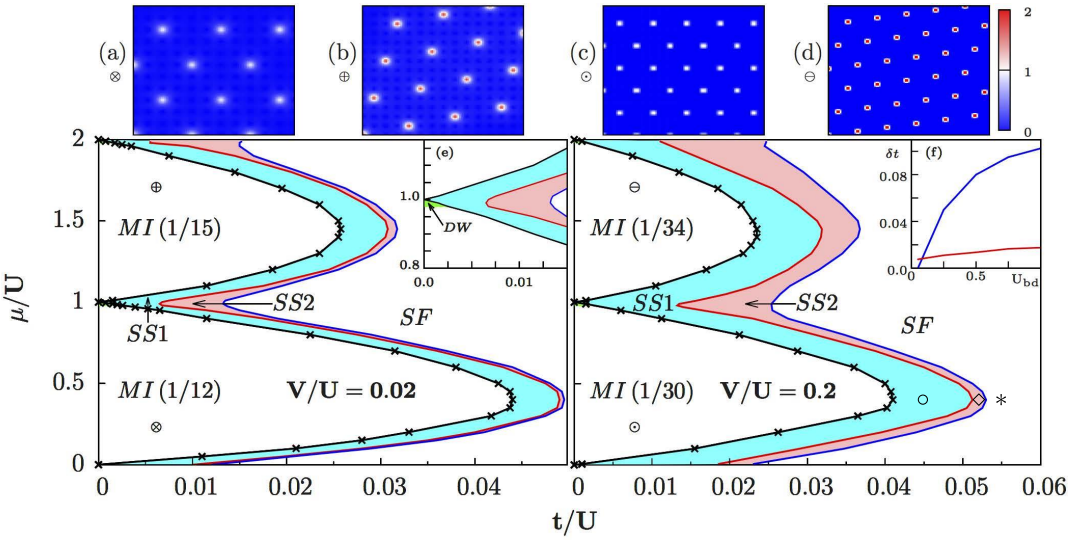


FIGURE 7.5: Phase diagram of the Rydberg dressed system (7.1) on a square lattice, with dressed interaction $V/U = 0.02$ and $0.2$ respectively. Regions of stable supersolid phases are denoted by the cyan (SS1) and pink color (SS2). The Mott insulating phase (MI) exhibits spatially uniform total density, while an inhomogeneous superlattice order appears in the dressed component, as is shown in (a)-(d) for the corresponding real-space density distribution of $n_d$. Lattice sizes of these are given by the square of the area of the unit cell of the crystalline order in the dressed species [$N_{\text{lat}} = 12 \times 12(\otimes)$; $N_{\text{lat}} = 15 \times 15(\oplus)$; $N_{\text{lat}} = 30 \times 30(\odot)$; and $N_{\text{lat}} = 34 \times 34(\ominus)$]. Inset: (e) Density wave phase (DW) with $n_b = 1$ and $n_d = 2$ for the respective sites filled by either of the two species, following the crystalline order of the dressed component. The width $\delta t \equiv t_c^{\max} - t_c^{\min}$ of the SS phases [SS1 (blue) and SS2 (red)] is shown in (f), as a function of the interspecies interaction $U_{bd}/U$ with $U = 1$ for the Rydberg dressed interaction $V/U = 0.2$ and the chemical potential $\mu/U = 0.4$. Other parameters are $\mu/U = \mu_b/U = \mu_d/U - 0.05$ and $U_{bd} = U$ is used for the phase diagrams. The spectral properties of the various phases (for $\circ$, $\diamond$ and $*$) are discussed in Sec. 7.4.

A final quantum phase transition at even higher hopping rates in the weakly interacting regime ends in a superfluid phase, where a uniform distribution of the total density is found in the simulations. In this phase both components exhibit homogeneous density distributions for the first time, meaning any superlattice order has melted, owing to the increasingly large density fluctuations. Thus the system only supports a superfluid of uniform density.

## 7.3 Supersolidity mechanism of the bare species

In this section we will develop an approximate cluster-type Bogoliubov mean-field theory, in order to shed light on the supersolidity formation in the SS1 phase, where the dressed species by itself has an oblique superlattice order. In that case we can assume that the total ground-state wave function can approximately be decoupled as $|\psi_0\rangle \approx |\text{DW}_d\rangle \otimes |\psi_b\rangle$, where $|\psi_b\rangle$ is the wave function of the bare species and $|\text{DW}_d\rangle$ is the wave function of the dressed species corresponding to the observed crystalline structure in this component. Within this ansatz we neglect quantum fluctuations of the density wave. Tracing out the dressed part, we can thus derive an effective Hamiltonian $\hat{H}_{eff}$ as $\hat{H}_{eff} = \langle \text{DW}_d|\hat{H}|\text{DW}_d\rangle$. Omitting the component index of the remaining bare species, we obtain the following form:

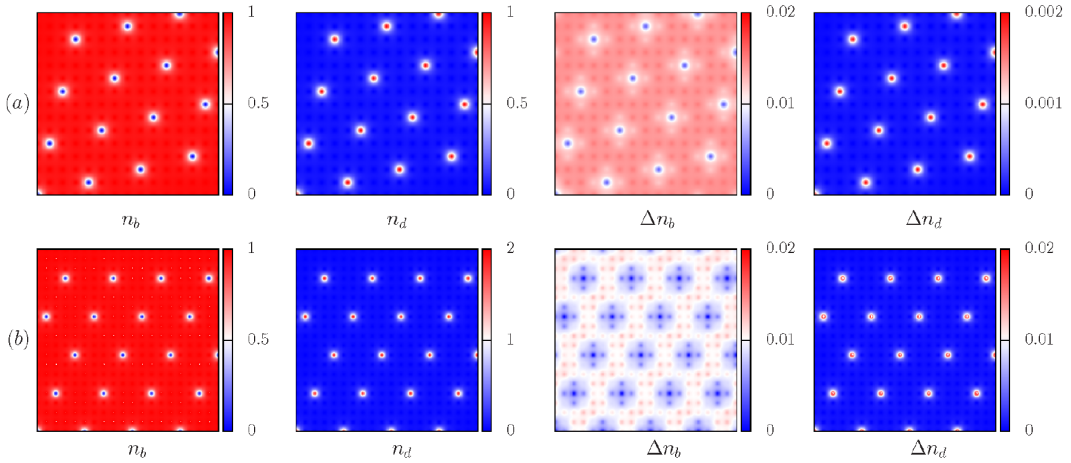


FIGURE 7.6: Real-space density $n_{b,d}$ and density fluctuations $\Delta_{b,d} \equiv \left\langle (\hat{n}_{b,d} - \langle \hat{n}_{b,d} \rangle)^2 \right\rangle$ in MI ($a$) and DW ($b$) phases. Lattice sizes of the considered system are the square of the area of the unit cell of the crystalline distribution of the dressed atoms [$N_{\text{lat}} = 15 \times 15$(a); $N_{\text{lat}} = 20 \times 20$(b)]. Other parameters are $t/U = 0.03$, $V/U = 0.3$, $U_{bd} = U$, $\mu_b/U = 0.2$ and $\mu_d/U = 0.7$ ($a$), and $t/U = 0.0023$, $V/U = 0.02$, $U_{bd} = U$, $\mu_b/U = 0.98$ and $\mu_d/U = 1.03$ ($b$) respectively.

$$\hat{H}_{eff} = -\sum_{\langle i,j \rangle} t \left( \hat{b}_i^\dagger \hat{b}_j + \text{h.c.} \right) + \frac{U}{2} \sum_i \hat{n}_i \left( \hat{n}_i - 1 \right) - \sum_i \mu \hat{n}_i + U_1 \sum_{\{i\}} \hat{n}_i. \tag{7.3}$$

Here we introduce the notation $\{i\}$, denoting every lattice site occupied by dressed atoms and $U_1 = \bar{n}_d U_{bd}$ with $\bar{n}_d$ the lattice average of $n_d$. The last term stems from the interspecies interaction, where the mean particle number of the dressed atoms has been used explicitly for each occupied site as $n_d = 1$, in accordance to the numerical results in the considered regime. Furthermore, $C \equiv \langle \text{DW}_d | \sum_{i<j} V_{ij} \hat{n}_{id} \hat{n}_{jd} | \text{DW}_d \rangle$, a constant term, denoting the long-range interaction energy, can be neglected in the effective Hamiltonian.

Interspecies interactions imprint the spatially periodic superlattice structure of the dressed atoms onto the undressed atoms, thus also breaking the discrete lattice symmetry of the optical lattice in the undressed component. We will now show that this mechanism is manifest in the emergence of a roton-like instability in the effective Hamiltonian. As an example, we consider parameters corresponding to Fig. 7.3($c$). In that case the dressed component forms an oblique lattice, depicted in Fig. 7.7(a). As can be seen, the unit cell of this lattice is larger compared to the optical lattice. The example has $a_1 = (1, 4)$ and $a_2 = (4, 1)$ as its primitive lattice vectors. From these we obtain an area of $A = |a_1 \times a_2| = 15$ sites of the underlying lattice.

Via Fourier transformation we find the effective Hamiltonian in its momentum space representation. Due to the truncated summation, one has to be especially careful about the last term,

$$\sum_{\{i\}} \hat{n}_i = \frac{1}{N} \sum_{\mathbf{k},\mathbf{k}'} \sum_{\{i\}} e^{i(\mathbf{k}-\mathbf{k}')\cdot \mathbf{r}_i} \hat{b}_{\mathbf{k}}^\dagger \hat{b}_{\mathbf{k}'} = \frac{N_d}{N} \sum_{\mathbf{k},\mathbf{k}'} \delta_{\mathbf{G}_r, \mathbf{k}-\mathbf{k}'} \hat{b}_{\mathbf{k}}^\dagger \hat{b}_{\mathbf{k}'}. \tag{7.4}$$

In this expression $N$ is the total number of sites, $N_d$ is the number of unit cells and $\mathbf{G}_r$ is a reciprocal lattice vector, implicitly defined via $\mathbf{G}_r \cdot \mathbf{r}_i = 2\pi n$, with $n \in \mathbb{Z}$ and

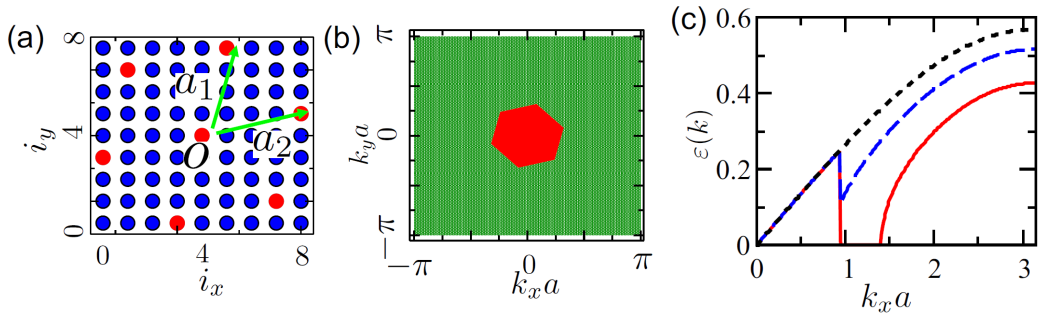


FIGURE 7.7: (a) Density distribution of the dressed (red) and bare species (blue). The distribution of the dressed atoms follows an oblique lattice with lattice vectors $a_1$ and $a_2$. This structure corresponds to the configuration shown in Fig. 7.3$(c)$. (b) The first Brillouin zone of both, the optical lattice (green) and the oblique lattice (red) of the dressed atoms, also referred to in the text as the reduced Brillouin zone. As the length of the lattice vectors exceeds the lattice parameter ($|a_j| > a$ for $j = 1, 2$), both shape and size of the reduced Brillouin zone significantly differ from the square reciprocal lattice of the underlying optical lattice structure. (c) Roton instability of the bare species in the approximate Bogoliubov model (7.10). Interspecies interactions $U_{bd}$ significantly modify the dispersion relation (shown along the $k_x$-axis) of phonons in the SS1 phase. When $U_{bd}$ is increased, a roton-like instability emerges, which induces an instability in the SF ground-state phase, leading to SS order. The shown graphs correspond to $U_{bd}/U = 0$ (dotted,black), $U_{bd}/U = 0.45$ (dashed,blue) and $U_{bd}/U = 1$ (solid,red). Further parameters are $k_y = 0$, $V/U = 0.4$ and $t/U = 0.04$.

$i \in \{i\}$. The size of the unit cell is thus given by $L_d = N/N_d$, so the lattice average density of dressed atoms in our case is $\bar{n}_d = n_d/L_d$. Following the generalized ansatz of the Fourier transformation introduced in Sec. 6.3, we now consider the operators $\hat{b}^\dagger_{\mathbf{k},s} = N_d^{-1/2} \sum_{\{i\}} \exp(i\mathbf{k}\cdot(\mathbf{r}_i + \mathbf{r}_s))\hat{b}^\dagger_{i,s}$, where $s$ denotes the relative site index inside a given unit cell specified by $i$. For these operators we find the relations

$$\hat{b}^\dagger_{\mathbf{k}} = \frac{1}{\sqrt{L_d}} \sum_s \hat{b}^\dagger_{\mathbf{k},s}, \tag{7.5}$$

$$\hat{b}^\dagger_{\mathbf{k}+\mathbf{G}_r,s} = \hat{b}^\dagger_{\mathbf{k},s} e^{i\mathbf{G}_r\cdot\mathbf{r}_s}. \tag{7.6}$$

Using these relations we can rewrite (7.4), by splitting the momenta $\mathbf{k} = \lfloor\mathbf{k}\rfloor + \mathbf{G}_r$ into a linear combination of a reciprocal lattice vector $\mathbf{G}_r$ and a remainder, such that $\lfloor\mathbf{k}\rfloor$ lies within the first Brillouin zone generated by the $\mathbf{G}_r$ vectors, thus defining the reduced Brillouin zone marked red in Fig. 7.7(b). The reduced size of this BZ is a reflection of the increased area $A$ of the unit cell compared to the optical lattice, with the corresponding BZ shown in green in Fig. 7.7(b). Obviously they only overlap in a region of small absolute momentum. We represent the set of all momenta inside this reduced BZ by $\{\mathbf{k}\}$. Thus

$$\frac{N_d}{N} \sum_{\mathbf{k},\mathbf{k}'} \delta_{\mathbf{G}_r,\mathbf{k}-\mathbf{k}'} \hat{b}^\dagger_{\mathbf{k}} \hat{b}_{\mathbf{k}'} = \frac{1}{L_d} \sum_{\{\mathbf{k},\mathbf{k}'\}} \sum_{\mathbf{G}_r,\mathbf{G}'_r} \delta_{\tilde{\mathbf{G}}_r=0,\mathbf{k}-\mathbf{k}'} \hat{b}^\dagger_{\mathbf{k}+\mathbf{G}_r} \hat{b}_{\mathbf{k}'+\mathbf{G}'_r} \tag{7.7}$$

$$= \frac{1}{L_d} \sum_{\{\mathbf{k}\}} \sum_{\mathbf{G}_r,\mathbf{G}'_r} \hat{b}^\dagger_{\mathbf{k}+\mathbf{G}_r} \hat{b}_{\mathbf{k}+\mathbf{G}'_r}. \tag{7.8}$$

As momenta inside the reduced Brillouin zone cannot differ by a non-zero $\tilde{\mathbf{G}}_r$ by definition, we only need to consider $\tilde{\mathbf{G}}_r = 0$ for the delta symbol. Inserting both (7.5)

and (7.6) into the last expression yields further simplifications, so

$$\frac{1}{L_d}\sum_{\{\mathbf{k}\}}\sum_{\mathbf{G}_r,\mathbf{G}'_r}\hat{b}^\dagger_{\mathbf{k}+\mathbf{G}_r}\hat{b}_{\mathbf{k}+\mathbf{G}'_r}=\frac{1}{L_d^2}\sum_{\{\mathbf{k}\}}\sum_{\substack{\mathbf{G}_r,\mathbf{G}'_r\\ s,s'}}\hat{b}^\dagger_{\mathbf{k},s}\hat{b}_{\mathbf{k},s'}e^{i(\mathbf{G}_r\cdot\mathbf{r}_s+\mathbf{G}'_r\cdot\mathbf{r}_{s'})}=\sum_{\{\mathbf{k}\}}\hat{b}^\dagger_{\mathbf{k},0}\hat{b}_{\mathbf{k},0}=\sum_{\{i\}}\hat{n}_i. \tag{7.9}$$

The truncated spatial sum $\sum_{\{i\}}$ thus leads to the introduction of cluster momentum states, annihilated by the $\hat{b}_{\mathbf{k},s}$ operators. We approximate these operators by the full lattice momentum operators, keeping the crucial truncated momentum sum, to find a simple approximate form of the Hamiltonian in momentum space:

$$\tilde{H}_{\text{app.}}\equiv-\sum_{\mathbf{k}}\left[\mu+2t(\cos k_x a+\cos k_y a)\right]\hat{b}^\dagger_{\mathbf{k}}\hat{b}_{\mathbf{k}}+\frac{U}{2N}\sum_{\mathbf{q},\mathbf{k},\mathbf{k}'}\hat{b}^\dagger_{\mathbf{k}}\hat{b}^\dagger_{\mathbf{k}'}\hat{b}_{\mathbf{k}'+\mathbf{q}}\hat{b}_{\mathbf{k}-\mathbf{q}}+U_1\sum_{\{\mathbf{k}\}}\hat{b}^\dagger_{\mathbf{k}}\hat{b}_{\mathbf{k}}. \tag{7.10}$$

In a next step we consider the expansion of this Hamiltonian in the vicinity of $|\mathbf{k}|=0$, which in the presence of a condensate is occupied macroscopically, so we may replace $\hat{b}^\dagger_{\mathbf{k}=0},\hat{b}_{\mathbf{k}=0}\to\sqrt{N_0}$, and only keep terms up to quadratic order in the operators:

$$\begin{aligned}\tilde{H}_{\text{app.}}\approx E_0&-\sum_{\mathbf{k}\neq\mathbf{0}}\left[\mu+2t(\cos k_x a+\cos k_y a)-2U\bar{n}_b\right]\hat{b}^\dagger_{\mathbf{k}}\hat{b}_{\mathbf{k}}\\&+\frac{U\bar{n}_b}{2}\sum_{\mathbf{k}\neq\mathbf{0}}\left(\hat{b}_{\mathbf{k}}\hat{b}_{-\mathbf{k}}+\hat{b}^\dagger_{-\mathbf{k}}\hat{b}^\dagger_{\mathbf{k}}\right)+U_1\sum_{\{\mathbf{k}\neq0\}}\hat{b}^\dagger_{\mathbf{k}}\hat{b}_{\mathbf{k}}.\end{aligned} \tag{7.11}$$

Here we introduce $E_0=-UN_0^2/2N$, which is the energy of the condensed atoms, where $N_0$ is their total number. Furthermore the chemical potential is now fixed to $\mu=-4t+U\bar{n}_b+U_1$, while the mean occupation number of the condensed atoms is $\bar{n}_b=N_0/N$. Most notably, the interspecies interaction only contributes in the low momentum regions, corresponding to the reduced BZ, which only partially overlaps with the full BZ, see Fig. 7.7(b). Therefore we have two different forms of the approximate Hamiltonian, for momenta inside and outside of the reduced BZ. Explicitly substituting $\mu$, the approximate Hamiltonian can be separated into sub-blocks, which in the reduced BZ take the form

$$\tilde{H}_{\text{app.}}(\mathbf{k}\in\{\mathbf{k}\})\approx\sum_{s=\pm1}\left[(\epsilon_{s\mathbf{k}}+U\bar{n}_b)\hat{b}^\dagger_{s\mathbf{k}}\hat{b}_{s\mathbf{k}}+\frac{U\bar{n}_b}{2}(\hat{b}_{s\mathbf{k}}\hat{b}_{-s\mathbf{k}}+\hat{b}^\dagger_{-s\mathbf{k}}\hat{b}^\dagger_{s\mathbf{k}})\right]. \tag{7.12}$$

With $U_1=\bar{n}_d U_{bd}$, the corresponding Bogoliubov spectrum is given by

$$\varepsilon(\mathbf{k})=\sqrt{\epsilon_{\mathbf{k}}(\epsilon_{\mathbf{k}}+2U\bar{n}_b)}, \tag{7.13}$$

where $\epsilon_{\mathbf{k}}=-2t(\cos k_x a+\cos k_y a-2)$. This part of the spectrum is similar to that of a weakly interacting Bose gas in a square lattice. Momenta outside the reduced BZ yield a different form of the Hamiltonian sub-blocks,

$$\tilde{H}_{\text{app.}}(\mathbf{k} \notin \{\mathbf{k}\}) \approx \sum_{s=\pm 1} \left[ (\epsilon_{s\mathbf{k}} + U\bar{n}_b - U_1)\hat{b}^\dagger_{s\mathbf{k}}\hat{b}_{s\mathbf{k}} + \frac{U\bar{n}_b}{2}(\hat{b}_{s\mathbf{k}}\hat{b}_{-s\mathbf{k}} + \hat{b}^\dagger_{-s\mathbf{k}}\hat{b}^\dagger_{s\mathbf{k}}) \right]. \tag{7.14}$$

The corresponding Bogoliubov spectrum is given by

$$\varepsilon(\mathbf{k}) = \sqrt{(\epsilon_{\mathbf{k}} - \bar{n}_d U_{bd})(\epsilon_{\mathbf{k}} - \bar{n}_d U_{bd} + 2U\bar{n}_b)}, \tag{7.15}$$

which only is non-zero for large momenta outside the reduced BZ. Given the system parameters and the mean populations $\bar{n}_b$ ($\bar{n}_d$) of the bare (dressed) species, we thus find a dispersion that is only continuous when either the interspecies interaction $U_{bd}$ or the dressed population $\bar{n}_d$ vanishes. Otherwise a discontinuity emerges at the boundary of the reduced BZ. We plot the corresponding dispersion relations in Fig. 7.7(c) along the $k_x$-axis for various values of $U_{bd}$. An extended region of momenta can be observed, where the mode frequency becomes complex at $U_{bd} = U$, which is a roton-like instability. It indicates that the formation of the supersolid in this regime is induced by the strong interspecies interaction.

The roton-like instability occurs precisely for momenta just outside of the reduced BZ. In that region the spectrum (7.15) becomes complex when $\varepsilon_{\mathbf{k}} < \bar{n}_d U_{bd}$. From this we can determine a critical value for the tunneling rate,

$$t_c = \frac{\bar{n}_d U_{bd}}{2\left(2 - \cos k_x^{(b)} a - \cos k_y^{(b)} a\right)}. \tag{7.16}$$

Here the superscript $(b)$ indicates that values of the momentum at the boundary of the reduced BZ have to be considered.

As the explicit structure of the oblique lattice is strongly affected by the soft-core interaction, we expect $t_c$ to change as the interaction $V$ changes. Furthermore, due to the mostly irregular shape of the reduced BZ (compare Fig. 7.7(b)), a range of $k_x^{(b)}$ and $k_y^{(b)}$ has to be considered, leading to a range of critical values for $t_c$. As an example we evaluate critical values of $t_c$ for a few test cases. We use the crystalline structure of dressed atoms at the SS1-SS2 phase boundary, as obtained in the numerical DMFT calculations. For $V = 0.3U$ we then find that $t_c$ lies in the range $[0.087U, 0.094U]$. Increasing the long-range interaction, we find an increase in the range of $t_c$, so for $V = 0.4U$ we find $t_c \in [0.085U, 0.11U]$ while for $V = 0.5U$ we find $t_c \in [0.073U, 0.13U]$. Although these values roughly follow the tendency of the numerical calculations, they are obviously unfit to determine the phase boundaries accurately within the presented approximate Bogoliubov calculation. This also should not come as too much of a suprise, considering that the presented type of instability (crystalline structure of dressed atoms and bare atoms in a homogeneous superfluid), does not correspond to any situation in the vicinity of the actually observed phase boundaries (MI-SS1-SS2-SF).

A further limitation of this calculation stems from the observation, that the unit cell size of the crystalline structure tends to shrink for weak $V$. In that case long-range correlations become important in determining the ground-state phase diagram, preventing us from decoupling the total wave function in two parts. Therefore the presented Bogoliubov calculation is expected to fail in capturing the many-body physics in that limit.

## 7.4 Spectral properties in quasiparticle picture

In order to further our understanding of the instabilities driving the various phase transitions, leading to supersolid order, we now analyse various spectral properties of the dressed limit. Obviously the long-range interaction is the primary cause behind the appearance of phases with broken lattice symmetry. Therefore we start our discussion by considering the properties of this interaction.

Due to its soft-core shape (7.2), the long-range interaction possesses a length scale, given by $R_c$, which is in contrast to the pure van der Waals potential $\propto 1/r^6$, it is based on. As it corresponds to the only long-range term in the Hamiltonian, we expect that this length scale plays a crucial role in emergent crystalline phases. This conjecture is reinforced, when we consider the Fourier transform $\tilde{V}_{\mathbf{k}}$ of the long-range interaction. As is shown in Fig. 7.8, the long-range potential possesses an attractive minimum in momentum-space. The momentum of this minimum is approximately at $k_0 = |\mathbf{k}| \gtrapprox \pi/R_c$. We therefore expect a finite momentum instability to appear at this momentum for a finite interaction strength $V/U$, while the system resides in a homogeneous phase.

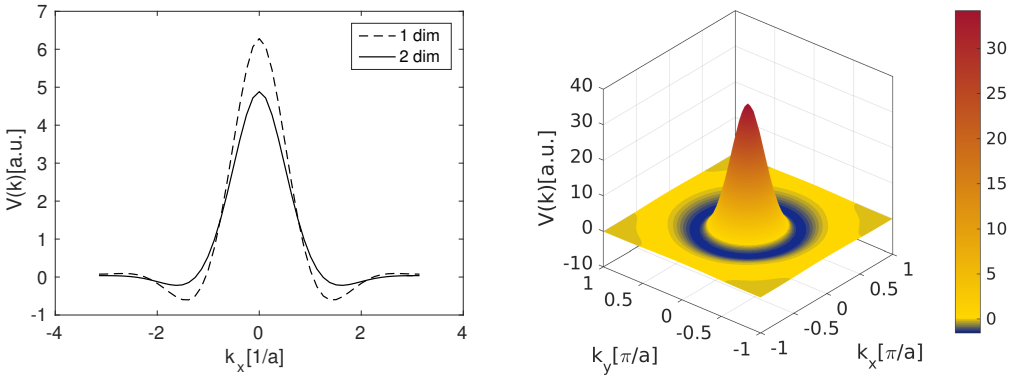


FIGURE 7.8: Fourier transform of the long-range soft-core interaction (7.2), with $R_c = 3a$. We consider both a 1-dimensional (dashed line on the *left*) and a 2-dimensional system (solid line on the *left* and *right*). Although the soft-core potential is always repulsive in real-space, its Fourier transform has attractive regions for $|\mathbf{k}| > k_c$. In 1 dimension, the sign change happens at about $\pi/R_c \approx k_c$, while the actual minimum of either potential is at a slightly larger momentum $|\mathbf{k}|$.

Indeed, if we consider a system close to the SF-SS2 transition, approaching it from the homogeneous superfluid, this instability shows up in the momentum distribution of the dressed component (see Fig. 7.9), as well as its static structure factor (shown in Fig. 7.10). While the momentum distribution of the undressed atoms corresponds to that of a homogeneous superfluid, where the $\mathbf{k} = 0$ momentum state is populated macroscopically, this central peak is surrounded by a second local maximum in the shape of a ring at $k_0 \neq 0$, corresponding to the minimum of $\tilde{V}_{\mathbf{k}}$. The same ring structure can equally be observed in the static structure factor shown in Fig. 7.10. Another measure of instability is the overlap of the Gutzwiller mean-field state $|\psi_G\rangle$ (6.6) and the quasiparticle ground-state $|\psi\rangle$ (6.86), both defined in Chap. 6. $|\langle\psi_G|\psi\rangle|^2$ quantifies the quality of the Gutzwiller result and is related to the deviation of the quasiparticle commutator from exact bosonic behavior. Close to the transition this deviation grows to 20% on the superfluid side, hinting at an increased instability of the static mean-field solution. We further note, that this quantity also serves

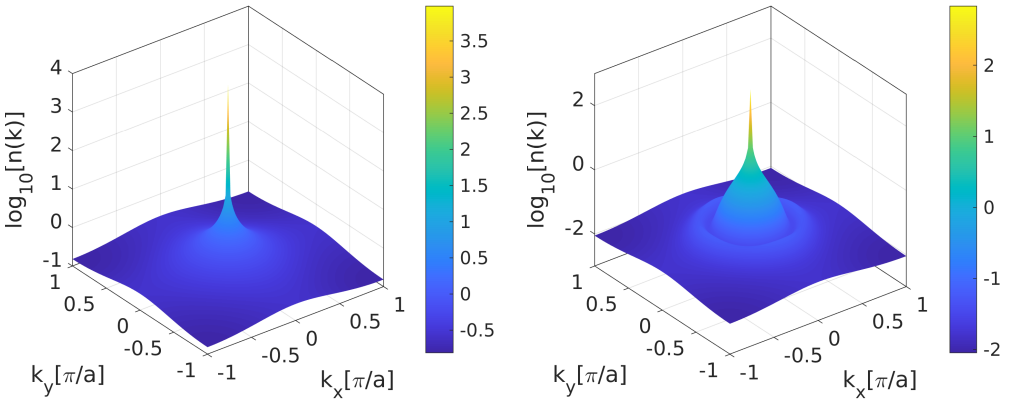


FIGURE 7.9: Momentum distribution $n(\mathbf{k})$ of the bare (*left*) and dressed states (*right*) in the homogeneous superfluid ground-state of (7.1), in a system of $2^7 \times 2^7$ sites with periodic boundary conditions. The long-range interaction of the dressed component induces the occupation of finite momentum states in the dressed component, while the peaks at zero momentum signifiy the macroscopic occupation of the (ungapped) zero momentum state, as expected in a superfluid state. Parameters are the same as in Fig. 7.3(⊘), with $V/U = 0.3$ and $t/U = 0.09$.

as an upper bound for the control parameter of the quasiparticle method, denoting the deviation from bosonic commutation relations for the Gutzwiller fluctuation operators (6.13)-(6.16).

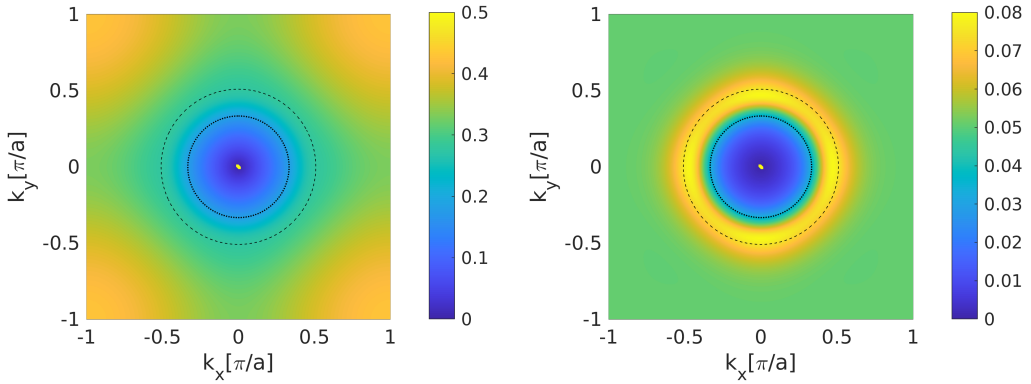


FIGURE 7.10: Static structure factor of the bare (*left*) and dressed states (*right*) in the homogeneous superfluid ground-state of (7.1), in a system of $2^7 \times 2^7$ sites with periodic boundary conditions. Dotted lines correspond to $|\mathbf{k}| = \pi/R_c$, while the dashed lines are given by $|\mathbf{k}| = k_0$, where $k_0$ is the momentum, for which the Fourier transformation of the dressed soft-core potential has its minimum value (see Fig. 7.8). In addition to the central (forward-scattering) peak, a second ring shaped maximum appears in the dressed component for momenta $\mathbf{k}$ close to $k_0 \approx |\mathbf{k}|$. Parameters are the same as in Fig. 7.3(⊘), with $V/U = 0.3$ and $t/U = 0.09$.

### 7.4.1 Band composition

The nature of the instability is better understood by considering the band composition in terms of order parameter responses within the various contributing quasiparticle bands, as introduced in (6.97), describing fluctuations $\delta O$ in local observables $\hat{O}$ induced by the quasiparticle states. In this section we will consider amplitude

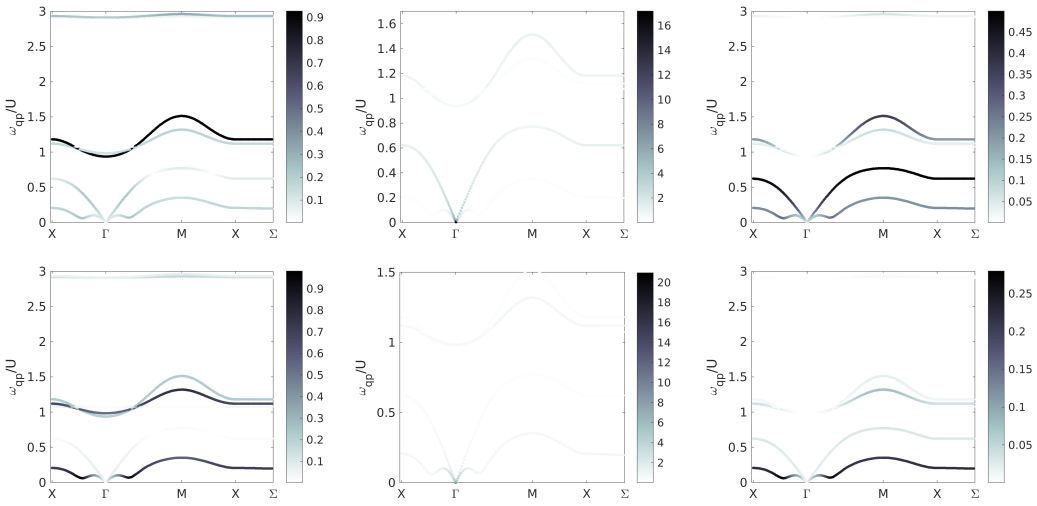


FIGURE 7.11: Order parameter responses in a two-component superfluid close to the SF-SS2 transition at a high dressed fraction $n_e = 0.05$. Shown are the amplitude Re($\delta\phi$) (*left*), phase Im($\delta\phi$) (*center*) and occupation number response $\delta n$ (*right*) of the bare (*top row*) and dressed (*bottom row*) components. Parameters are the same as in Fig. 7.3(⊘), with $V/U = 0.3$ and $t/U = 0.09$.

Re$\delta\phi$ and phase response Im$\delta\phi$, as well as the particle number fluctuation $\delta n$ in first order ($O_1$ in (6.97)) of the fluctuation operators, under a weak coherent excitation of individual quasiparticle states (6.96).

As a first example we consider the two-component superfluid with strong long-range interactions and a large fraction of dressed atoms corresponding to the parameters $V/U = 0.3$ and $t/U = 0.09$, with the remaining parameters the same as in Fig. 7.3. The corresponding many-body ground-state is close to unit filling, as $n = n_b + n_d = 0.9$.

In the vicinity of the quasiparticle ground-state we find six relevant bands in the limit of non-interacting quasiparticles, shown in Fig. 7.11. As the two bosonic components of the considered system only exhibit local density interactions but cannot exchange roles, two gapless Nambu-Goldstone modes are found, corresponding to the two separate condensate fractions of either component. Both have a vanishing amplitude response accompanied by a maximum in the phase response. While one of the gapless bands, which primarily constitutes phase fluctuations of the bare species condensate order parameter, strongly resembles that of a weakly interacting lattice gas in a Bogoliubov description, the other is strongly deformed at small momenta, exhibiting a roton-minimum due to the soft-core potential. For all momenta at the roton minimum and beyond, we furthermore observe a pronounced amplitude response, in contrast to the behavior in the (dominantly) bare gapless band. Both gapless bands also constitute the largest fluctuations in the total density $\delta n$ in each component, when compared to the other bands.

In the second set of bands, both with a gap of $\mathcal{O}(U)$, each primarily corresponds to the generation of amplitude fluctuations with very uniform amplitudes, which conforms to the behavior of a Higgs amplitude mode, albeit not at unit filling in this case. While none of the bands yields a pure response in a single component only, which is due to the local interspecies interaction, differences between the bands still allow for an assignment of a dominant role for each band. Thus we find that the

dominantly dressed state band of Higgs-type has a band-width that is slightly reduced in comparison to the bare species, which only differs in the absence of a long-range interaction. This bandwidth suppression is thus a signature of the localizing effect the long-range interaction imprints on the dressed species.

The remaining two bands almost fall on top of each other and have a gap of $\mathcal{O}(3U)$. This gap points at the primary involvement of local $n = 3$ Fock-states, which is in accordance to considerations about higher bands discussed in [SEW15]. Again the dominantly dressed species has a reduced bandwidth compared to the undressed component, while both bands are very flat as a result of the dominating interactions.

As a comparison let us now consider the case of a reduced fraction of dressed atoms, which is of more relevance to experimental realizations, due to the limited lifetime of Rydberg states. Thus we now consider the case corresponding to Fig. 7.5, where $V/U = 0.2$, $\mu/U = 0.4$ and $t/U = 0.055$, which corresponds to a state at almost unit filling, as $n = n_b + n_d = 1.005$, where $n_d = 7.5 \times 10^{-3}$.

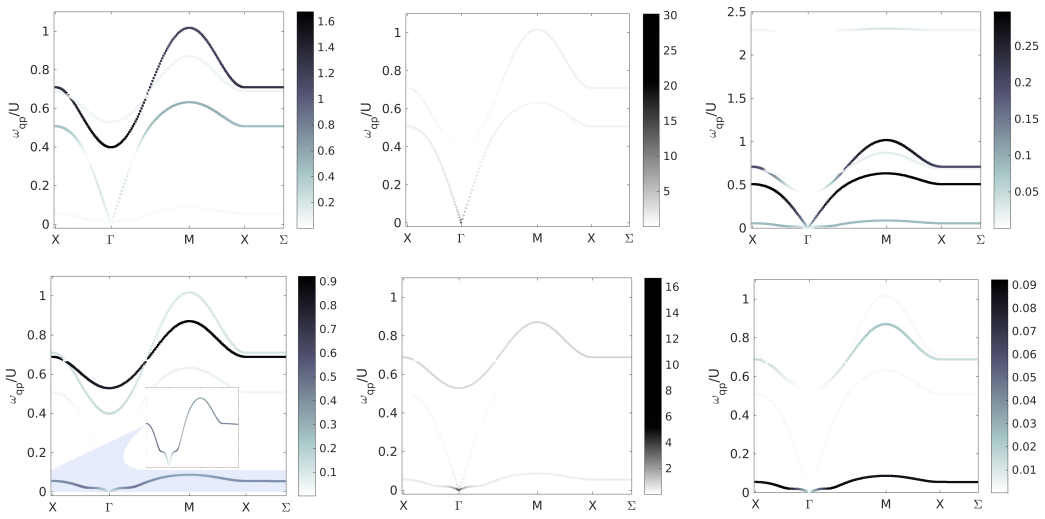


FIGURE 7.12: Order parameter responses in a two-component superfluid close to the SF-SS2 transition at a low dressed fraction $n_d = 7.5 \times 10^{-3}$. Shown are the amplitude $\mathrm{Re}(\delta\phi)$ (*left*), phase $\mathrm{Im}(\delta\phi)$ (*center*) and occupation number response $\delta n$ (*right*) of the bare (*top row*) and dressed (*bottom row*) components. Parameters are the same as in Fig. 7.5(∘), with $V/U = 0.2$, $\mu/U = 0.4$ and $t/U = 0.055$.

Considering the various responses in the amplitude and phase of the dressed and undressed condensate order parameter as well as the occupation number fluctuations, all shown in Fig. 7.12, we can conclude that the band composition remains the same for a reduced dressed state fraction, while the primary difference lies in the significantly reduced bandwidth of the gapless modes of the dressed species and only a weak signature of a roton-minimum (see inset for the amplitude response of the dressed component, *top left* in Fig. 7.12).

### 7.4.2 Spectral functions

Keeping the typical band composition in mind, we now discuss the spectral properties of the different quantum phases with non-vanishing condensate fractions. Starting from the homogeneous superfluid, as given for $V/U = 0.2$, $\mu/U = 0.4$ and $t/U = 0.055$, with the remaining parameters the same as in Fig. 7.5, we subsequently

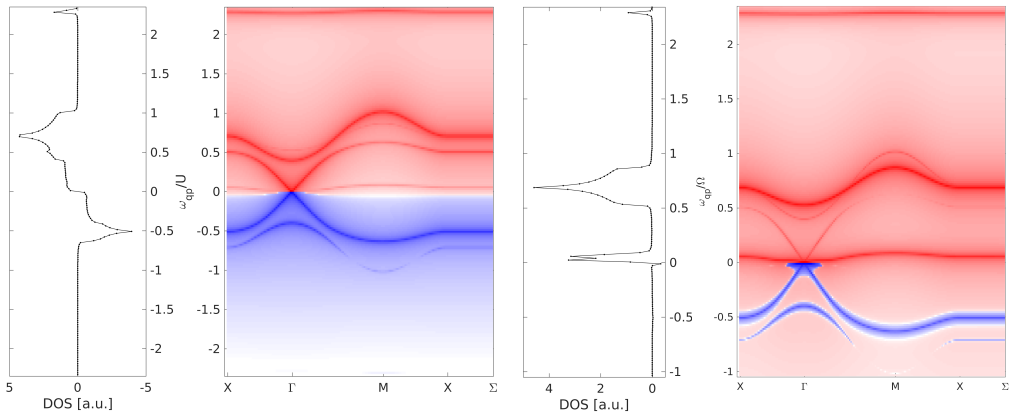


FIGURE 7.13: Density of states and spectral function along high symmetry points of the bare (*left*) and dressed component (*right*), in the two component homogeneous superfluid ground-state. The spectral functions are plotted with a logarithmic colorscale $\propto |\log_{10}[A(\mathbf{k},\omega)]|$ normalized to a lower cutoff, while a blue hue corresponds to negative spectral weights and red corresponds to positive weights. Parameters are $V/U = 0.2$, $\mu/U = 0.4$ and $t/U = 0.055$ with the remaining parameters the same as in Fig. 7.5.

progress to the supersolid phases SS2 and SS1, by reducing the hopping rate to $t/U = 0.052$ and $t/U = 0.045$ respectively. As we will see, the spontaneously broken lattice symmetry induces a back folding of modes to a reduced Brillouin zone and avoided crossings of the quasiparticle bands.

All spectral functions $A(\mathbf{k},\omega)$ and the derived density of states $\mathrm{DOS}(\omega)$ are obtained in the quasiparticle description leading to (6.114). In the presentation of numerical data, delta-functions in the energy are usually broadened as Gaussian functions with the same peak area, unless specified otherwise. The peak width $\sigma$ is usually set such that the density of states becomes smooth at the considered energy resolution and is typically on the order of $\sigma \lesssim 0.01U$.

### Homogeneous two-component superfluid

In the numerical simulations a finite system of $2^7 \times 2^7$ sites with periodic boundary conditions was assumed. Therefore we represent the finite sum of delta-peaks in the spectral function via a Lorentzian broadening with a linewidth $\sigma$, such that the density of states becomes smooth at the chosen resolution. Here we have $\sigma \lesssim 0.01U$.

As can be seen in Fig. 7.13, the bare state spectral function barely deviates from the behavior of a regular interacting lattice-superfluid. Dominantly there are two quasiparticle and -hole branches. On the particle site we also observe contributions from the strongly localized third band. The local interspecies interaction leads to very weak contributions from the particle branches of the dressed species to the bare component modes. This behavior is mirrored by the particle branches of the dressed component, while corresponding hole excitations only follow the bare species dispersion, which is a result of the small dressed state density, and thus also of a very small dressed species condensate fraction. The difference between filling fractions also leads to different energy scales, such that the roton-like feature is barely visible in the spectral function.

**Supersolid of type SS2**

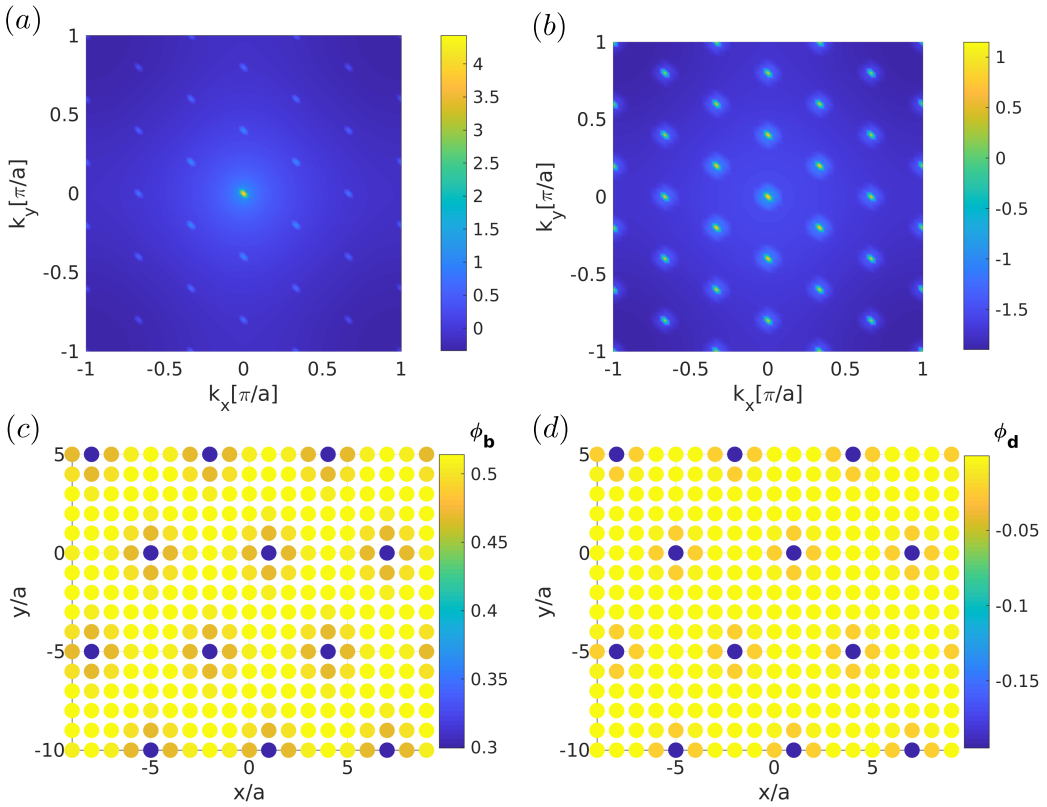


FIGURE 7.14: Momentum $(a, b)$ and real-space condensate order parameter distribution [$(c, d)$, showing a few unit cells] of bare $(a, c)$ and dressed species $(b, d)$ in the SS2 phase. A logarithmic color scale is used in the momentum distributions, due to the peaks, which signify condensation in a finite number of momentum states, leading to a macroscopic occupation of these states and thus to significantly different orders of magnitude.

Reducing the hopping rate (e.g. to $t/U = 0.052$ for the case considered here) leads to a spontaneous breaking of numerous discrete translational and rotational symmetries of the optical lattice, which is best illustrated in the momentum distributions of both components, as shown in Fig. 7.14 for a system of $60 \times 60$ sites with periodic boundary conditions. The peaks at non-zero momentum are a signature of supersolid order. Their positions are the reciprocal lattice, given by the spatial order of the dressed atoms, which is spanned by unit cells of 30 sites, as shown in Fig. 7.14$(c)$. The magnitude of the peaks scales with the system size, as can be seen in the mean-field contribution (6.111). The peak values at non-zero momentum on the other hand stem from the spatial fluctuation in the condensate order parameter. From this we can also see that the bare component condensate is extended, due to the dominant role of the zero momentum peak, while the peaks of the dressed state barely differ in magnitude, implying localized bubbles of dressed state condensate (in accordance to previous predictions in systems with a soft-core potential, see e.g. [Pup+10; Hen+12]). Indeed, the real-space distribution of either component, shown in Fig. 7.14 behaves exactly as described.

Let us now consider the spectral functions, as shown in Fig. 7.15. For the bare component we can observe that the principal structure of excitations is retained in the SS2 phase, while there are significant changes in the dressed component. The

broken lattice symmetry manifests itself in numerous momenta, where the band gap closes in addition to $\mathbf{k} = 0$. Furthermore, the increased unit cell leads to a back folding and avoided crossings of the original bands, which can be observed in both components. We note that the dressed species is almost entirely gapped, with most of the hole excitations shifted to lower energies, while the low lying particle excitations are split into two (nearly flat) bands at increased energies. In contrast we observe a slight increase in low energy excitations of the bare component, induced by the local interspecies interaction, which couples to the additional phonon cones at non-zero momenta.

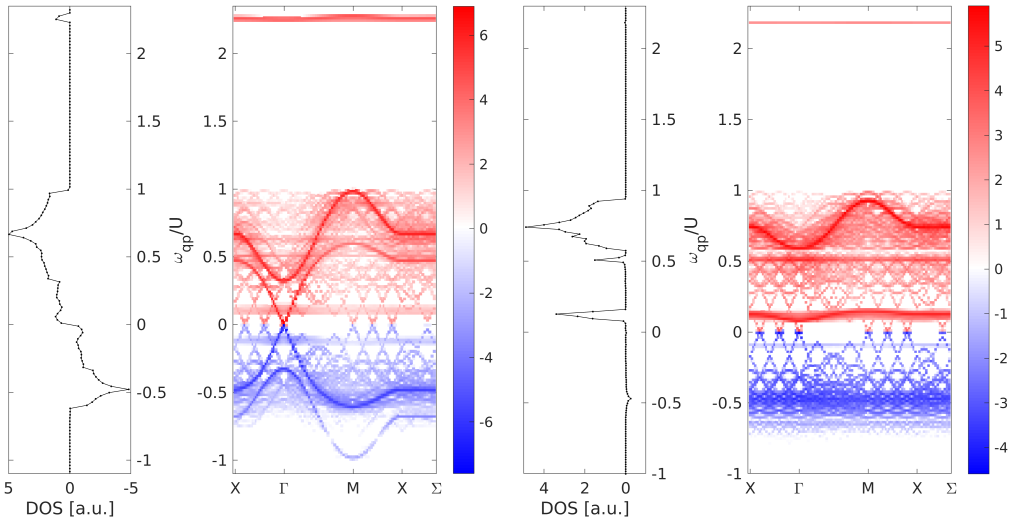


FIGURE 7.15: Density of states and spectral function along high symmetry points of the bare (*left*) and dressed component (*right*), in the two-component supersolid SS2 phase. The spectral functions are plotted with a logarithmic colorscale $\propto |\log_{10}[A(\mathbf{k},\omega)]|$ normalized to a lower cutoff, while a blue hue corresponds to negative spectral weights and red corresponds to positive weights. Parameters are $V/U = 0.2$, $\mu/U = 0.4$ and $t/U = 0.052$, with the remaining parameters the same as in Fig. 7.5.

### Supersolid of type SS1

A further reduction in the hopping rate (e.g. to $t/U = 0.045$ for the case considered here) leads to a further localization of the dressed component, which suppresses the condensate fraction of the dressed atoms, which marks the transition to the supersolid of type SS1. Thus the condensate peaks of the dressed species disappear in the corresponding momentum distribution shown in Fig. 7.16.

As a result of the vanishing dressed state condensation, the corresponding spectrum becomes fully gapped, with most of the excitations almost fully localized and therefore flat, as shown in Fig. 7.17. The bare component excitations on the other hand undergo only minor changes. Most significantly the gap of the amplitude mode excitations starts to close at zero momentum, as the bare atoms approach the tip of the Mott-lobe, while the back-folded excitations further deform the density of states at low energies.

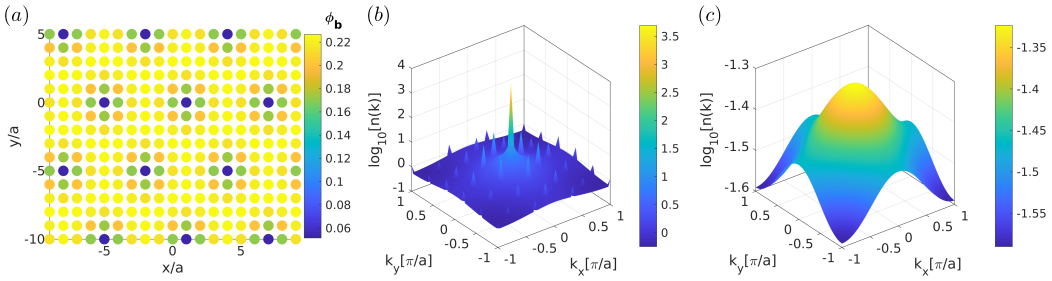


FIGURE 7.16: Real-space condensate order parameter of the bare species [$(a)$, showing a few unit cells], and momentum distributions of bare $(b)$ and dressed species $(c)$ in the SS1 phase.

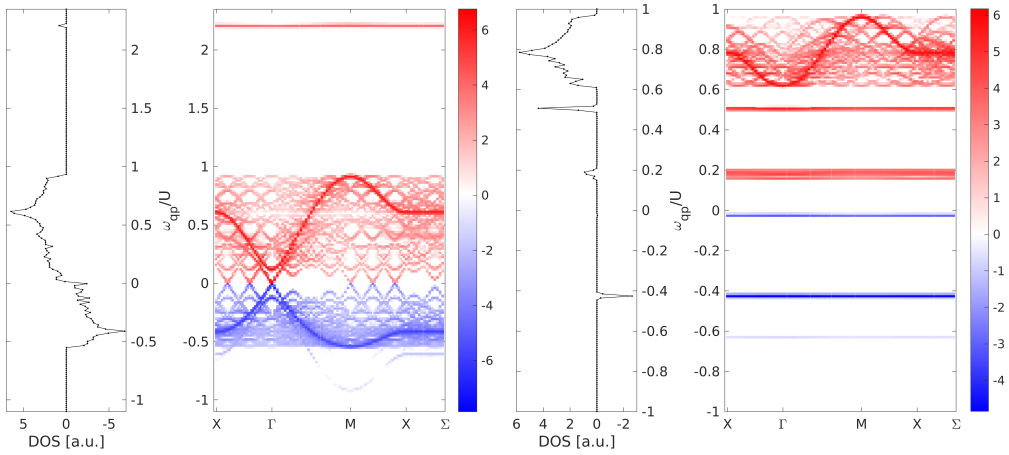


FIGURE 7.17: Density of states and spectral function along high symmetry points of the bare (*left*) and dressed component (*right*), in the spin-wave-supersolid SS1 phase. The spectral functions are plotted with a logarithmic colorscale $\propto |\log_{10}[A(\mathbf{k},\omega)]|$ normalized to a lower cutoff, while a blue hue corresponds to negative spectral weights and red corresponds to positive weights. Parameters are $V/U = 0.2$, $\mu/U = 0.4$ and $t/U = 0.045$, with the remaining parameters the same as in Fig. 7.5.

### 7.4.3 Structure factors

We end our discussion of spectral properties with an analysis of the dynamic and static structure factors, which are observables relevant for Bragg spectroscopy.

#### Homogeneous two-component superfluid

Due to the presence of the condensate in the two-component superfluid, the structure factor is dominated by the condensate peak at $\mathbf{k} = 0$. In the vicinity of the SS2 phase, we can see that the bare state dynamic structure factor has contributions from all four lowest gapped and gapless bands, while one of the gapped bands (i.e. the one which is dominated by the dressed component) contributes the least. For the dressed component we almost only observe contributions from the corresponding bands in addition to the zero momentum peak. We also recover an extended circular local maximum in the static structure factor of the dressed component at $|\mathbf{k}| = k_0$.

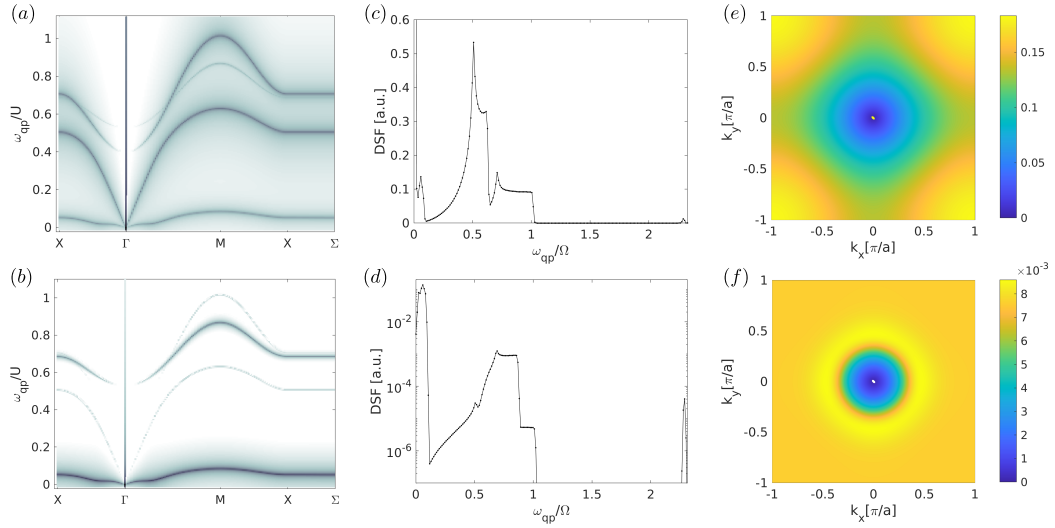


FIGURE 7.18: Dynamic $(a, b, c, d)$ and static structure factor $(e, f)$ for the bare $(a, c, e)$ and dressed component $(b, d, f)$, in the two component homogeneous superfluid ground-state. The dynamic structure factors are plotted with a logarithmic colorscale $\propto |\log_{10}[S(\mathbf{k}, \omega)]|$, normalized to a lower cutoff. Furthermore a Lorentzian broadening is used, which leads to the pronounced feature at the $\Gamma$-point due to the macroscopic weight of the condensate at $\mathbf{k} = 0$ and $\omega = 0$. Parameters are $V/U = 0.2$, $\mu/U = 0.4$ and $t/U = 0.055$, with the remaining parameters the same as in Fig. 7.5.

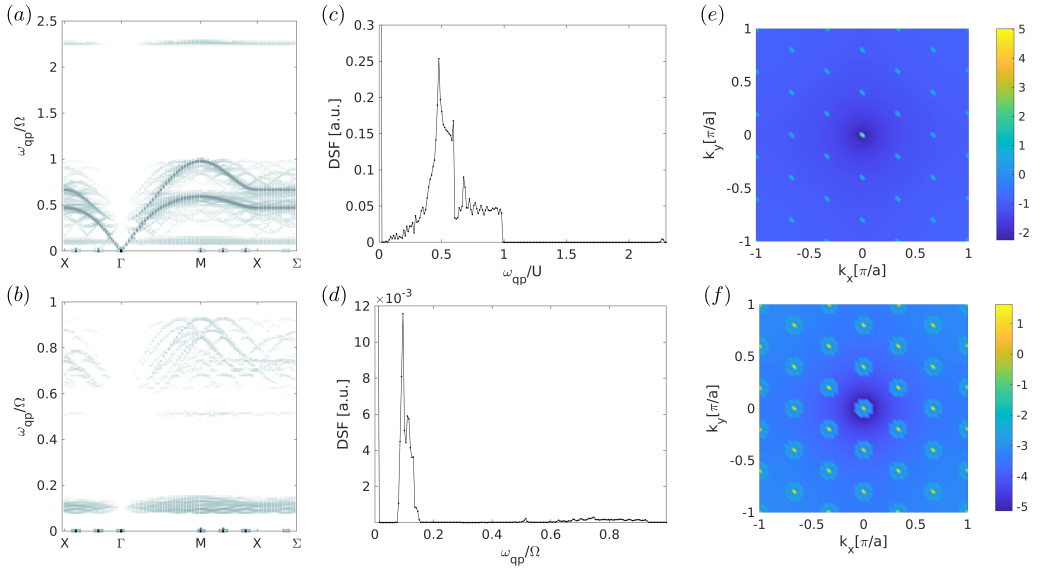


FIGURE 7.19: Dynamic $(a, b, c, d)$ and static structure factor $(e, f)$ for the bare $(a, c, e)$ and dressed component $(b, d, f)$, in the two component SS2 phase. The dynamic structure factors are plotted with a logarithmic color scale $\propto |\log_{10}[S(\mathbf{k}, \omega)]|$ normalized to a lower cutoff. Parameters are $V/U = 0.2$, $\mu/U = 0.4$ and $t/U = 0.052$, with the remaining parameters the same as in Fig. 7.5.

### Supersolid of type SS2

While the dynamic structure factor of the bare species resolves most of the phase and amplitude excitations in the lattice symmetry breaking SS2 phase, almost only the lowest (nearly localized) gapped band is visible in the dynamic structure factor of the dressed species. In addition to the recovered multitude of back folded bands,

the most remarkable features in the static structure factor are the additional peaks for momenta corresponding to the reduced reciprocal lattice of the oblique unit cell. These are associated to gapless modes. Their existence, in addition to the $\mathbf{k} = 0$ peak in the momentum distribution, is a signature of supersolid order.

**Supersolid of type SS1**

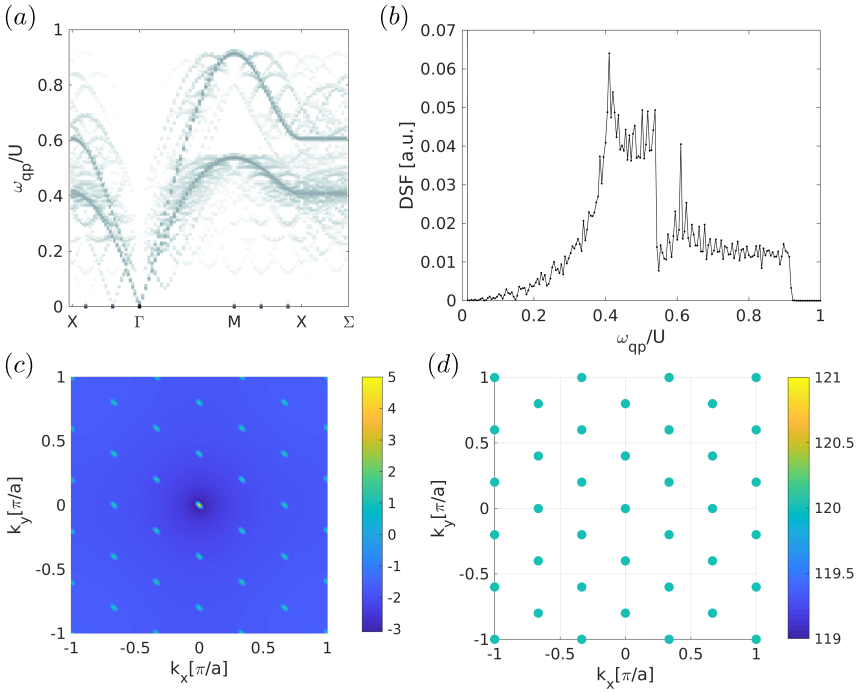


FIGURE 7.20: Dynamic [$(a, b)$, for bare species] and static structure factor $(c, d)$ for the bare $(c)$ and dressed component $(d)$, in the two component spin-wave SS1 phase. The dynamic structure factors are plotted with a logarithmic color scale $\propto |\log_{10}[S(\mathbf{k}, \omega)]|$ normalized to a lower cutoff. Parameters are $V/U = 0.2$, $\mu/U = 0.4$ and $t/U = 0.045$, with the remaining parameters the same as in Fig. 7.5.

In the SS1 phase the dynamic structure factor of the dressed species vanishes for all $\omega > 0$ in the first order fluctuation expansion, which we consider in the quasiparticle method. While the bands of the bare component are resolved in the corresponding dynamic structure factor, only the peaks corresponding to the reduced reciprocal lattice can be observed in the dressed atoms. The peak values in the static structure factor of the dressed component is easily explained, as the lattice we consider consists of $60 \times 60$ sites, while the unit cells consist of 30 sites containing only one dressed atom each, localized at one lattice site. Thus we expect a value of $60 \cdot 60/30 = 120$ at every momentum corresponding to the reciprocal lattice.

## 7.5 Interaction potentials of Rydberg dressed potentials

In this section we will discuss the parameters of the long-range interaction potential, in order to relate our results to current experimental conditions. Considering the level structure shown in Fig. 7.1(a), our main ingredient is the inclusion of a species $|d\rangle$, which is coupled to a Rydberg state $|r\rangle$ by an off-resonant laser with Rabi-frequency $\Omega$ and detuning $\Delta$. Interactions between Rydberg atoms are of van der Waals type $V_{vdW} = C_6/r^6$, with the respective dispersion coefficient $C_6$, which

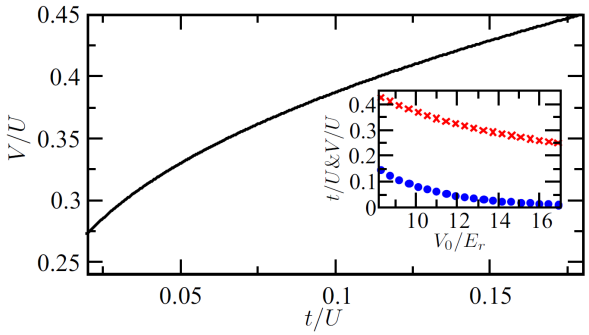


FIGURE 7.21: The value of the lattice depth $V_0/E_r$ determines the value of both hopping rate $t$ and on-site interaction $U$ simultaneously, resulting in parameter pairs along the black curve. Changing $V_0/E_r$, one can thus advance through the phases discussed in Sec. 7.2. The individual changes of $t/U$ (•) and $V/U$ (×) as a function of $V_0/E_r$ are shown in the inset. All relevant parameters are given by $\lambda = 1064$nm, $a_s = 5.2$nm, $\Delta = 7$MHz and $\Omega = 0.44$MHz

has a strong dependence on the principal quantum number of the Rydberg level $C_6 \propto n^{11}$. Due to $|\Delta| \gg \Omega$, we are in the regime of (weak) Rydberg dressing, resulting in a soft-core interaction potential $V_{ij}$ for the dressed component, with an effective dispersion coefficient $\tilde{C}_6 = (\Omega/\Delta)^4 C_6$ and soft-core radius $R_c = (C_6/2\Delta)^{1/6}$. $R_c$ therefore varies with the Rydberg state and detuning, while the core potential $V$ is a function of only the laser parameters $\Omega$ and $\Delta$ (not of $C_6$). For example let us consider $n = 30 - 36$ Rydberg $nS$ states of $^{87}$Rb atoms (e.g. with $C_6 = 241.6\text{MHz}\,\mu m^6$ for $36S$) in an optical lattice with $a = 532$nm. For $\Delta = 7$MHz, this leads to a range of $R_c \approx 2 - 3a$. For furthermore fixed detuning $\Delta$, the strength of the long-range interaction solely depends on the (two-photon) Rabi frequency $\Omega$.

In order to probe the different phases shown in Fig. 7.3 and Fig. 7.5, one needs to change the parameters $V$, $U$ and $t$ – preferable individually – over certain ranges. A natural control parameter in optical lattices is the lattice potential depth $V_0$, which usually is considered in relation to the recoil energy $E_r = h^2/2m\lambda^2$, where $\lambda = 2a$ is the wavelength of the lattice potential and $m$ is the mass of the atoms. The on-site interaction $U$ and the hopping rate $t$ both depend on the lattice depth via the relations [Zwe03]

$$U = \sqrt{\frac{8}{\pi}} k a_s E_r \left(\frac{V_0}{E_r}\right)^{\frac{2}{4}} \left(\frac{V_0^{\perp}}{E_r}\right)^{\frac{1}{4}}, \tag{7.17}$$

$$t = \frac{4}{\sqrt{\pi}} E_r \left(\frac{V_0}{E_r}\right)^{\frac{3}{4}} e^{-2\sqrt{\frac{V_0}{E_r}}}, \tag{7.18}$$

which hold for sufficiently deep lattices $(V_0, V_0^{\perp}) \gg E_r$, while more shallow lattices demand a more rigorous treatment, as discussed in Sec. 3.1.4 (see [Bis12]). For $V_0^{\perp} \gg V_0$ the geometry is effectively two dimensional as the perpendicular tunneling is suppressed exponentially. In these expressions $k = 2\pi/\lambda$ is the wave vector of the lattice potential and $a_s$ is the s-wave scattering length. Varying $V_0/E_r$ and keeping the remaining parameters fixed lead to a continuous and simultaneous change in the ratios $t/U$ and $V/U$. We give an example in Fig. 7.21, showing that one can cross the various phases presented in Sec. 7.2 in an experimentally relevant parameter regime.

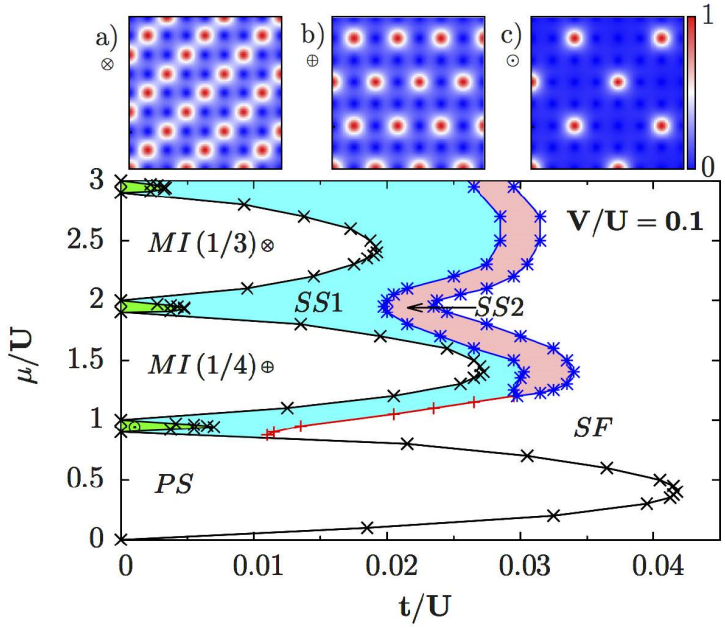


FIGURE 7.22: Phase diagram for a nondipolar-dipolar mixture, corresponding to $b$ and $d$ in (7.1), but with a dipolar interaction $V_{ij} = V/|\mathbf{r}_i - \mathbf{r}_j|^3$ for dipoles aligned perpendicular to the lattice plane. A square lattice is considered, while $V/U = 0.1$. This system exhibits pronounced regions of supersolid phases, which are marked by cyan (SS1) and light red (SS2) shaded areas. In contrast to the simplified nearest-neighbor case [WSN16], various types of crystalline orders of the real-space distribution of the dipolar species are observed, as shown in a)-c). In the strong interacting limit either a MI phase is found, where the total density distributes spatially uniform, or a DW develops (marked in green), where the total density distributes spatially nonuniform. Furthermore phase separation (PS) is observed in the MI region with total filling $n_b + n_d = 1$, while sufficiently large $t$ leads to melting of any crystalline order, resulting in a spatially uniform superfluid. Remaining parameters are given by $U_{bd} = 0.9U$ and $\mu_{b/d} = \mu$.

## 7.6 Dipolar system

So far we have studied emergent crystalline order in Rydberg dressed optical lattice systems. However for the sake of completeness it should be noted that the physics of the observed competing orders can also be exhibited in dipolar optical lattice systems, following the quick developments in cooling and trapping of magnetic atoms (see e.g. [Gri+05]) and diatomic molecules (see e.g. [Ni+08]). Based on these developments, a recent study presents a Gutzwiller mean-field phase diagram of a binary Bose mixture on a square lattice, where one species possesses a significant dipole moment [WSN16]. Despite their model being similar to (7.1), only the nearest-neighbor part of the dipolar interaction was studied by them. Thus to further the understanding of the Rydberg dressed system in relation to similar models, we briefly study a mixture of dipolar and nondipolar bosons on a square lattice, considering *actual* long-range interactions beyond NN approximations while assuming that the dipoles are aligned perpendicular to the lattice plane.

Using RB-DMFT, which can be considered a higher-order expansion of Gutzwiller mean-field theory taking into account quantum fluctuations in a non-perturbative way, we find the phase diagram shown in Fig. 7.22. In this model we also find five phases, which in addition to the well known SF, MI, and DW are two types of supersolid (SS1 and SS2). In comparison to the nearest-neighbor approximated static

mean-field treatment [WSN16], we observe two major differences. Firstly, rich spin patterns appear, as depicted in Fig. 7.22 a)-c), resulting in a filling factor of the dipolar component equal to $1/3$, $1/4$ and $1/8$ respectively. Secondly the observed region of supersolid phases is altered in relation to the static mean-field results, while we recover the mean-field phase diagram with NN interactions within Gutzwiller approximations, as obtained in [WSN16].

# Chapter 8

# Ground-state phases for near-resonant Rydberg excitation

In this chapter, which is based on the research for the publications [GVH17; BGH18; GBH18], we will address the many-body equilibrium ground-state phases in the regime of near-resonant and coherent excitation of the Rydberg state, while also considering itinerant behavior of the bosonic atoms on a square lattice. Previous theoretical work in this regime has only considered either the NN limit of the van der Waals interaction in a Gutzwiller mean-field calculation [SSS14], or the **frozen** limit of a one-dimensional system [WB10; PDL10; Sch+10a], predicting a series of lattice incommensurate ordered phases (**devil's staircase**), but also the effect of tunneling induced spin-exchange [SPG11] has been considered, so far. Furthermore, in frozen two-dimensional systems, the cluster formation [LG14] and crystallization of Rydberg excitations [Ver+15] has been predicted and already observed in experiments [Sch+15]. Below we will discuss the ground-state phase diagram as obtained in dynamical mean-field theory. The combination of a frozen-limit model and a real-space extension of bosonic dynamical mean-field theory (RB-DMFT), introduced in Chap. 4, allows for an efficient quantitative analysis of the phase diagram for an arbitrary range of the interaction. We will first introduce the extended two-species Bose-Hubbard model describing the system, which includes the long-range VdW interaction via the Rydberg state, as shown schematically in Fig. 8.1. We will further discuss the Hartree-approximation used for the long-range interaction, especially in the frozen limit, where it yields relevant spatial configurations for the dynamical mean-field simulations, presented in the following sections. Finally, we will discuss the obtained quantum phases and the different types of long-range order predicted in an itinerant lattice gas, with a focus on spectral properties obtained in RB-DMFT as well as the quasiparticle expansion of the static mean-field result, presented in Chap. 6. Although the RB-DMFT results can be expected to be of limited quality, due to the discrete spectrum of the impurity model used in the DMFT-loop and because of the incapability of DMFT to represent the long-wavelength Nambu-Goldstone-modes as of its limited consideration of non-local correlations, we will see that both results agree remarkably well.

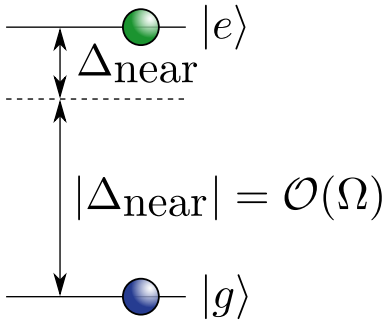


FIGURE 8.1: Reduced two-level scheme of the extended Bose-Hubbard model for near resonant excitation of the Rydberg state. The two components are given by the ground state $|g\rangle$ (blue) and the Rydberg state $|e\rangle$ (green), which is addressed by the Rabi process.

Let us briefly reiterate the model which we are going to investigate. We consider a two-component system of ground state $|g\rangle$ and Rydberg excited $|e\rangle$ atoms (see Chap. 2 and Fig. 8.1) in second quantization, so the full grand canonical Hamiltonian $\hat{H}$ can be written in terms of bosonic annihilation (creation) operators $\hat{b}_{\sigma,i}$ ($\hat{b}^\dagger_{\sigma,i}$), for the two species $\sigma = g, e$, acting on site $i$ of a square OL:

$$\hat{H} = \hat{H}_{2BH,kin} + \sum_i^N \left(\hat{H}_{2BH,loc,i} + \hat{H}_{R,i} + \hat{H}_{vdW,i}\right), \tag{8.1}$$

where $\hat{n}^\sigma_i$ is the usual occupation number operator. With the kinetic energy given by the hopping amplitudes $t$ and $\eta t$ between all pairs of NN sites, denoted by the expression $\langle i,j\rangle$, we have

$$\hat{H}_{2BH,kin} = -t \sum_{\langle i,j\rangle} \left(\hat{b}^\dagger_{g,i}\hat{b}_{g,j} + \eta \hat{b}^\dagger_{e,i}\hat{b}_{e,j} + h.c.\right). \tag{8.2}$$

Furthermore, the local Hubbard interaction terms for a two-component Bose-Hubbard are given by

$$\hat{H}_{2BH,loc,i} = U\left(\frac{\hat{n}^g_i}{2}(\hat{n}^g_i - 1) + \lambda \hat{n}^g_i \hat{n}^e_i + \tilde{\lambda}\frac{\hat{n}^e_i}{2}(\hat{n}^e_i - 1)\right) - \mu\left(\hat{n}^g_i + \hat{n}^e_i\right). \tag{8.3}$$

Here $U, \lambda U$ and $\tilde{\lambda}U$ are the amplitudes of the three possible intra- and inter-species Hubbard interaction terms and $\mu$ is the chemical potential determining the total particle number $\sum_{i,\sigma} \hat{n}^\sigma_i$.

The excited electronic (Rydberg) states of the atoms are populated via coherent driving, which leads to Rabi oscillations between ground and Rydberg states. Note that we will neglect the effect of the finite life time of Rydberg states in the discussed many-body ground-state simulations, which is valid for states that can be prepared on a sufficiently small time scales and with a small total Rydberg fraction, discussed in Sec. 2.2.2. As introduced in Sec. 2.2.1, for each lattice site this Rabi process takes the following form in the rotating wave approximation, where we, at least for now, consider a homogeneous laser driving and thus a homogeneous beam profile, so

$$\hat{H}_{R,i} = \frac{\Omega}{2}\left(\hat{b}^\dagger_{g,i}\hat{b}_{e,i} + \hat{b}^\dagger_{e,i}\hat{b}_{g,i}\right) - \Delta\hat{n}^e_i. \tag{8.4}$$

In addition we also consider the non-local van der Waals (vdW) interaction between Rydberg states. At distances relevant in OLs, it is dominated by its long-range tail. Thus for atoms at sites $\mathbf{i}$ and $\mathbf{j}$

$$\hat{H}_{vdW,i} = \frac{V_{vdW}}{2}\sum_{j\neq i}\frac{\hat{n}^e_i\hat{n}^e_j}{|\mathbf{i}-\mathbf{j}|^6}, \tag{8.5}$$

where $V_{vdW} = C_6/a^6$, with the vdW coefficient $C_6$ and the lattice parameter $a$. This model has previously been investigated in the limit of NN interactions only, by applying Gutzwiller mean-field theory [SSS14]. In our study we go beyond this approximation and show that the phase diagram is far richer as previously predicted.

## 8.1 Frozen-limit model

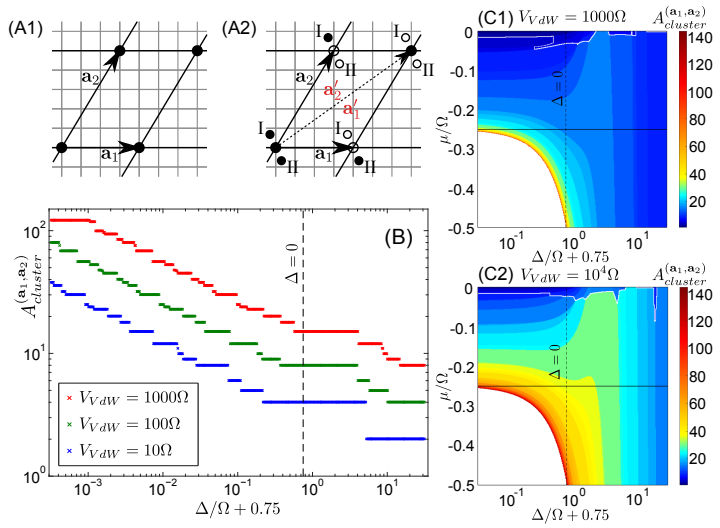


FIGURE 8.2: (A1) Spanning vectors $(\mathbf{a}_1, \mathbf{a}_2)$ define the Bravais cell of a superlattice for the underlying OL (gray). Black solid circles correspond to occupied sites, while remaining sites are empty. (A2) Possible checkerboard generalizations of (A1), where spanning vectors connect two different sublattices (solid and empty circles). Mapping to the striped versions (I and II) is explained in the text. In (B) and (C) different crystalline phases of the frozen-limit model can be distinguished by $A^{(\mathbf{a}_1,\mathbf{a}_2)}_{cluster}$ (explained in the text). (B) shows devil's staircases (for values of the long-range interaction, increasing from bottom to top, as given in the legend) for the logarithmic approach to $\Delta/\Omega = -3/4$ at $\mu_0/\Omega = -1/4$ [solid lines in (C1) and (C2)]. Phases above white lines in (C1) and (C2) correspond to two-sublattice order with canted state orientation.

Due to the many possible spatial crystalline orderings, an efficient method to distinguish them is needed. Therefore we first analyze the frozen limit, where all spatial hopping terms are set to zero ($t = 0$). This allows for a simple analytical investigation of the ground-state manifold with few approximations. Moreover, it makes for a useful exact starting point for considering finite hopping ($t \neq 0$), which we simulate within RB-DMFT. Assuming a mean lattice filling $\bar{n} < 1$, where $\bar{n} = \sum_{i,\sigma}\langle \hat{n}_i^\sigma \rangle / N$, only empty or singly occupied sites are to be expected. We may also assume that such a system always has a spatially periodic ground-state. For such crystalline order, we consequently only need to consider those sites $i$ of the full Hamiltonian which are nonempty in order to calculate the energy:

$$\begin{aligned} H_i =& \frac{\Omega}{2}\left(\hat{b}^\dagger_{g,i}\hat{b}_{e,i} + \hat{b}^\dagger_{e,i}\hat{b}_{g,i}\right) - \Delta\hat{n}^e_i \\ &- \mu\left(\hat{n}^g_i + \hat{n}^e_i\right) + \frac{V_{vdW}}{2}\sum_{j\neq i}\frac{\hat{n}^e_i\hat{n}^e_j}{|\mathbf{i}-\mathbf{j}|^6}. \end{aligned} \tag{8.6}$$

Any periodic superlattice structure can be constructed from a set of spanning vectors [one per spatial dimension, Fig. 8.2(A1)], which in our case are restricted to the discrete set of points given by the OL. Applying the Hartree approximation for a given set of spanning vectors $(\mathbf{a}_1, \mathbf{a}_2)$ (given in units of lattice spacings $a$), the Hamiltonian reduces to a set of self-consistent single-site problems with at most $A^{(\mathbf{a}_1,\mathbf{a}_2)}_{cluster}$ different self consistent values $n^e_j = \langle \hat{n}^e_j \rangle$, where $A^{(\mathbf{a}_1,\mathbf{a}_2)}_{cluster}$ is the area (in units of lattice sites) spanned by the given vectors. Due to low filling $\bar{n} < 1$ we consider only

two values $(n_A^e, n_B^e)$, where each corresponds to one of the two sublattices defined by their sets of sites $A$ and $B$ [indicated by open and solid circles in Fig. 8.2(A2)] of a checkerboard version of the spanned superlattice.

In Fig. 8.2(A2) two further versions are indicated by I and II for the given vectors $(\mathbf{a}_1, \mathbf{a}_2)$, where one of the two transformations $\mathbf{a}_{1/2} \to \mathbf{a}'_{1/2} = \mathbf{a}_{1/2} + \mathbf{a}_{2/1}$ was applied. This allows for energy optimization via canted state orientation, which is equivalent to canted Ising antiferromagnetic (CIAF) order and becomes important for increased lattice fillings. Generally, frozen states – within the Hartree approximation – can be written as

$$|\Psi\rangle = \prod_C \prod_{i \in C}^{L} \left( \cos\phi_i \, |\downarrow\rangle_i + e^{i\theta_i} \sin\phi_i \, |\uparrow\rangle_i \right), \tag{8.7}$$

where the state of the full system is given by a product over a lattice of unit cells $C$ containing $L$ sites each, with an internal structure given by the set of $\phi_i \in [0, \pi/2]$ and $\theta_i \in [0, 2\pi]$ for $i = 1, \ldots, L$. Setting at least one $\phi_i \notin \{0, \pi/2\}$ yields CIAF order. In case of the Mott-like frozen limit, the not yet specified quasispin states can, in principle, be any set of two bosonic Fock states, including the empty vacuum state $|n^g = 0, n^e = 0\rangle$. Note that the use of different particle numbers for the states at a site $i$, for example, the combination of an empty site with any allowed Fock state on this site, implies $\phi_i = 0, \pi/2$. Also note that $\theta_i = \pi$ combined with $(\downarrow, \uparrow) = (g, e)$ corresponds to a dark state, as is used for an $s$-state to $s$-state transition (required for isotropically interacting $^{87}$Rb Rydberg states) to suppress decay via the intermediary $p$-state. An example of CIAF order is schematically shown in Fig. 8.3, where the two sublattices correspond to the $A$ and $B$ sites.

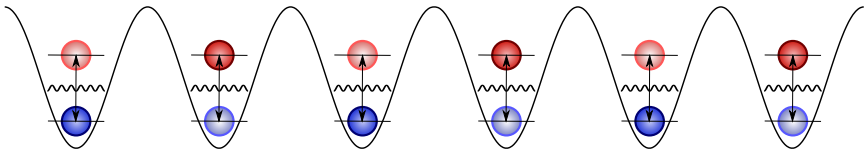

FIGURE 8.3: Schematic representation of a one dimensional CIAF state in an optical lattice. Colored circles correspond to the ground (blue, bottom row) and excited (red, top row) Fock-states, and the opacity is related to the amplitudes in the local linear combinations (8.7). A complete polarization of the state is suppressed by the Rabi process induced by the incident light field (small black waves and arrows).

For the interaction energy for each sublattice within Hartree approximation we obtain $(A \leftrightarrow B)$

$$H_{vdW,A}^{\text{Hartree}} = V_{vdW} \hat{n}_A^e \left( \sum_{\mathbf{j} \in A \setminus 0} \frac{\langle n_A^e \rangle}{\mathbf{j}^6} + \sum_{\mathbf{j} \in B} \frac{\langle n_B^e \rangle}{\mathbf{j}^6} \right), \tag{8.8}$$

where $\mathbf{j}$ points from a given site (0) of $A$ to any site of both $A$ and $B$. Thus the site-averaged grand canonical potential $f$ is simply given by $f = \sum_i \langle H_i \rangle / A_{cluster}^{(\mathbf{a}_1, \mathbf{a}_2)} = \sum_{l=A,B} \frac{\langle H_l \rangle}{2} \bar{n}$, with the vdW interaction evaluated by (8.8).

Minimizing $f$ with respect to a set $\mathcal{V}_s$ of spanning vectors then yields the many-body ground-state phase diagram in the frozen limit for $\bar{n} < 1$, as shown in Figs. 8.2(B) and 8.2(C). For this variational minimization it is useful to represent the remaining sums over the sublattices $A$ and $B$ as functions of the spanning vectors

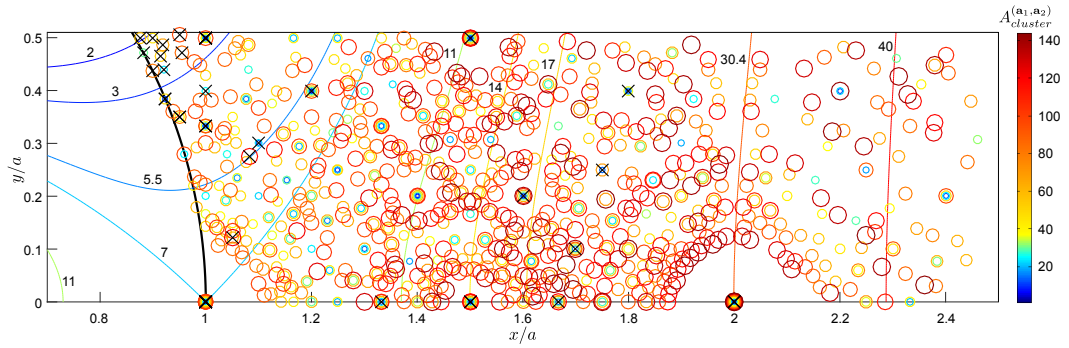


FIGURE 8.4: Each colored marker represents a pair of tested spanning vectors (each in units of lattice spacing $a$) from the set $\mathcal{V}_s$. Their coordinates are given by the larger vector, after a combined scaling and rotation of both vectors, so that the smaller vector is mapped onto $(0,1)$. They can thus only appear outside of the unit circle (thick black line). Their color and size corresponds to the area of each crystal unit cell. In addition, also some contour lines for $R^{(x,y)}_{(0,1)}$ are shown. Crossed markers correspond to crystal structures actually appearing as ground-states of the atomic limit model in the blue detuned regime for $V_{vdW} < 10^4\Omega$.

$$V^{\mathbf{a}_2}_{\mathbf{a}_1} = \sum_{\mathbf{j}\in A\setminus 0} \frac{1}{\mathbf{j}^6} \quad \text{and} \quad W^{\mathbf{a}_2}_{\mathbf{a}_1} = \sum_{\mathbf{j}\in B} \frac{1}{\mathbf{j}^6},$$

for which we define the convenient expression

$$R = R^{\mathbf{a}_2}_{\mathbf{a}_1} \equiv \max(V^{\mathbf{a}_2}_{\mathbf{a}_1}, W^{\mathbf{a}_2}_{\mathbf{a}_1})/\min(V^{\mathbf{a}_2}_{\mathbf{a}_1}, W^{\mathbf{a}_2}_{\mathbf{a}_1}), \tag{8.9}$$

as the crystal-structure-dependent ratio of the long-range interaction sums. The dependence of $R^{\mathbf{a}_2}_{\mathbf{a}_1}$ on the spanning vectors is shown by the contour lines in Fig. 8.4. It should be noted that there is no dependence on the actual form of the interaction, as we use a scale-free long-range interaction in the present case. In order to perform the minimization procedure, we generate a set $\mathcal{V}_s$ (as shown in Fig. 8.4), which needs to at least represent the whole range of superlattices, which can in principle be expected in the regime under consideration. In our frozen model (8.6) the on-site interaction $U$ is neglected for $\bar{n} < 1$. With $\Omega$ as the energy scale, only $V_{vdW}$, $\Delta$ and $\mu$ remain as tunable parameters, defining the region to be investigated.

Especially, $V_{vdW}$ is important for the choice of $\mathcal{V}_s$, as it defines the blockade radius $R_b = (C_6/\Omega)^{1/6}$ for Rydberg excitations, which corresponds to a radius of up to 5 OL sites for $V_{vdW} \leq 10^4\Omega$. On a square lattice this would correspond to a volume of up to 25 lattice sites. In order to allow for even lower fillings, enabled by the chemical potential or the detuning, we will consider volumes of up to $12 \times 12$ lattice sites. The complete set $\mathcal{V}_s$ of spanning vectors used here is shown in Fig. 8.4, modulo similarity transformations for each pair.

If we then also define $V \equiv V_{vdW}\min(V^{\mathbf{a}_2}_{\mathbf{a}_1}, W^{\mathbf{a}_2}_{\mathbf{a}_1})$ and use the Rabi frequency $\Omega$ as the energy scale, the self-consistency conditions for $n^e_{A/B} = \langle \hat{n}^e_{A/B} \rangle$ in the many-body ground-state are given by

$$n^e_{A/B} = 1 - n^e_{A/B} \left| V(n^e_{B/A} + R n^e_{A/B}) - \Delta \sqrt{1 + \left( V(n^e_{B/A} + R n^e_{A/B}) - \Delta \right)^2} \right|. \tag{8.10}$$

The solutions of this effective model, where $R$ is just the the ratio of any inter- and intra-sublattice interactions, are shown in Fig. 8.5 for some relevant values of $R$ (compare Fig. 8.4).

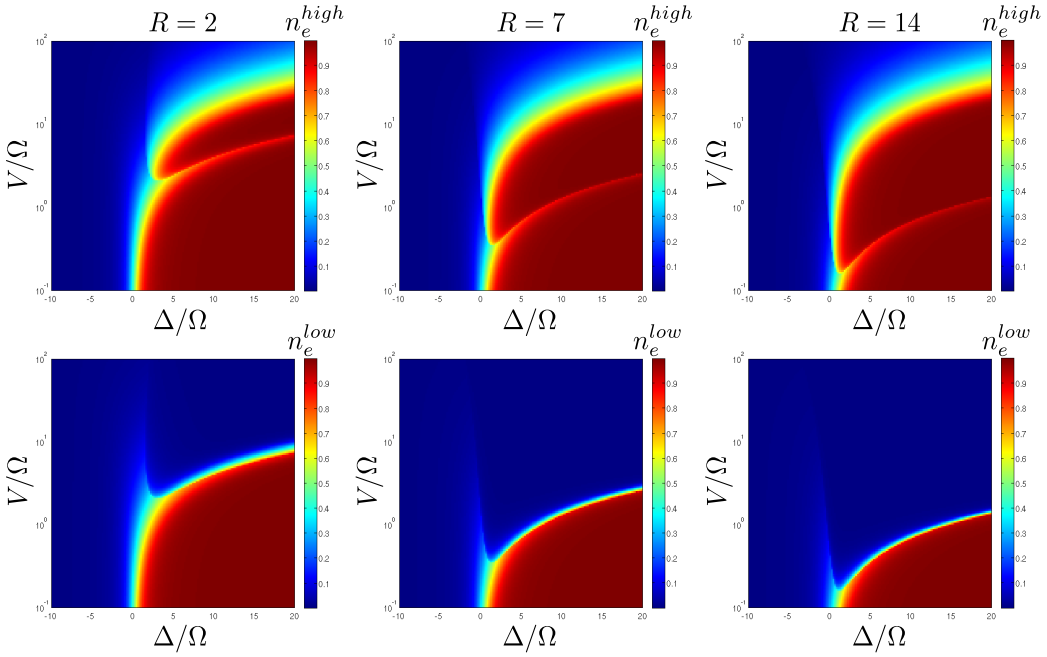


FIGURE 8.5: Various solutions of the effective frozen model (8.10) for $R = 2, 7, 14$. Shown are the Rydberg fractions $n_e$ for each of the two sublattices, which are respectively indexed by whether the sublattice with high or low Rydberg fraction is considered. Canting appears if $n_e^{low} \neq n_e^{high}$ and at least one of them is not equal to unity.

As $f = \sum_{l=A,B} \frac{\langle H_l \rangle}{2} \bar{n}$ within these limits and approximations, its minimization with respect to our set $\mathcal{V}_s$ yields the many-body ground-state phase diagram in the atomic limit and for $\bar{n} < 1$, as is shown in Figs. 8.2 (B) and 8.2(C). In the comparison of all lattice structures from the set $\mathcal{V}_s$, as shown in Fig. 8.4, the configurations of minimal energy anywhere in the analyzed parameter region [see Figs. 8.2 (B) and 8.2(C) for parameter ranges] are marked by crosses. Those points primarily accumulate where they correspond to either triangular order, $\mathbf{a}_2 = (\sqrt{3}/2, 1/2)$, or a square lattice, $\mathbf{a}_2 = (1, 0)$. Points with increased $R > 10$, on the other hand, are more susceptible to the formation of CIAF order, as can be seen in Fig. 8.5. If one then considers only one of the two sublattices, for example, the one with the increased Rydberg fraction, it again resembles triangular order more closely, as would be possible without canted order, while keeping the lattice filling constant. On the other hand, no spanning vectors with minimal energy are to be found beyond a radius of 2; in particular the point $(2, 0)$ is the most distant, as shown in Fig. 8.4), which rules out stripe-like order.

From (8.6) in the Hartree approximation it furthermore follows that the chemical potential $\mu_0$, determining the transition to the vacuum state, is given by

$$\mu_0 = -\frac{\Delta + \sqrt{\Omega^2 + \Delta^2}}{2}. \tag{8.11}$$

Approaching this limit by varying either $\mu$, $\Delta$ or $\Omega$ yields a devil's staircase of fractional lattice commensurate fillings [see Fig. 8.2(B)], stabilized by the long-range interactions. Note that our ansatz allows only for fillings of the form $\frac{1}{n}$ with $n \in \mathbb{N}$ (see

also [LMF12; Rad+13]).

## 8.2 Dynamical mean-field theory

We now use the frozen-limit results as an exact starting point for our RB-DMFT simulations since both models map to each other in Hartree approximation for vanishing $t$ and $\bar{n} < 1$. However, for nonzero $t$ we cannot expect the crystal symmetry to always be given by the frozen-limit results. Therefore other crystalline structures corresponding to similar mean inter-atom distances are also simulated. Furthermore, RB-DMFT requires a truncation of the local Fock-space. Since a hard cutoff, using only the first $N_c$ Fock states, strongly restricts the maximum observable local particle number in a condensate, we instead use a soft cutoff utilizing the coherent-tail state $\propto \sum_{n=N_c}^{\infty} \frac{\alpha^n}{\sqrt{n!}} |n\rangle$ [GH17], discussed in Chap. 5, where $N_c = 4$, leading to a negligible error in the calculated observables, which is maximal for values of $t/\Omega > 0.1$, where it is on the order of a few percent ($< 3\%$, see App.D). The ground-state is then found by comparing the resulting lattice-averaged grand canonical potentials $f = \langle \hat{H} \rangle / A_{cluster}$, for each of the considered crystal structures. In order to allow for checkerboard order on all cluster types, even those of odd-valued volume, we always simulate clusters generated by the spanning vectors $(2 \cdot \mathbf{a}_1, 2 \cdot \mathbf{a}_2)$.

Calculating $f$ is not straightforward within RB-DMFT, as the total kinetic energy $E_{kin} = \langle \hat{H}_{2BH,kin} \rangle$ is given in terms of *nonlocal* expectation values $\langle \hat{b}^\dagger_{\sigma,i} \hat{b}_{\sigma,j} \rangle$, which therefore cannot directly be calculated from the self-consistent local Anderson impurity models used by RB-DMFT. But as we have shown in Sec. 4.5, presuming RB-DMFT self-consistency conditions, $E_{kin}$ can also be written in terms of the connected local Green's functions $\mathbf{G}_i^{\sigma\sigma C}$ (4.68) and Anderson impurity hybridization functions $\mathbf{\Delta}_i^{\sigma\sigma}$:

$$\begin{aligned} E_{kin} =& \frac{2}{\beta} \lim_{\epsilon \to 0^+} \sum_{i\sigma, n \geq 0} \mathrm{Re}\left( \left[ \mathbf{\Delta}_i^{\sigma\sigma}(i\omega_n) \mathbf{G}_i^{\sigma\sigma C}(i\omega_n) \right]_{11} e^{i\omega_n \epsilon} \right) \\ & - \sum_{i\sigma} \frac{\mathrm{Tr}\left[ \mathbf{\Delta}_i^{\sigma\sigma}(0) \mathbf{G}_i^{\sigma\sigma C}(0) \right]}{2\beta} - \sum_{ij\sigma} t_{ij} \phi^*_{\sigma,i} \phi_{\sigma,j}. \end{aligned} \tag{8.12}$$

### 8.2.1 Periodic system

Minimizing $f$, as calculated in the described RB-DMFT scheme, with respect to the relevant crystal orders yields the ground-state phase diagram shown by the lines in Fig. 8.6(E). In Fig. 8.7 we additionally give a comparison to results obtained in a static Gutzwiller mean-field ansatz (6.6) [BGH18]. Overall, one can observe a remarkable good match between both results, while there are some pronounced differences in the crossover region between low and high Rydberg fractions near $\Delta/\Omega \gtrsim 0$, where fluctuations are more relevant. Also note the differences in the insulating density wave (DW) regime, which stem from the consideration of fluctuations of the non-condensed particles in DMFT, while these are absent in the static mean-field. For selected points in Fig. 8.6 also the spatial distributions of important local observables are shown, such as the occupation numbers $n_i^\sigma$, squared condensate order parameters $|\phi_i^\sigma|^2$, and $\langle \hat{b}^\dagger_{g,i} \hat{b}_{e,i} \rangle$, with the latter related to in-plane magnetization of the pseudospin. The phase boundaries are obtained from kinks (second-order)

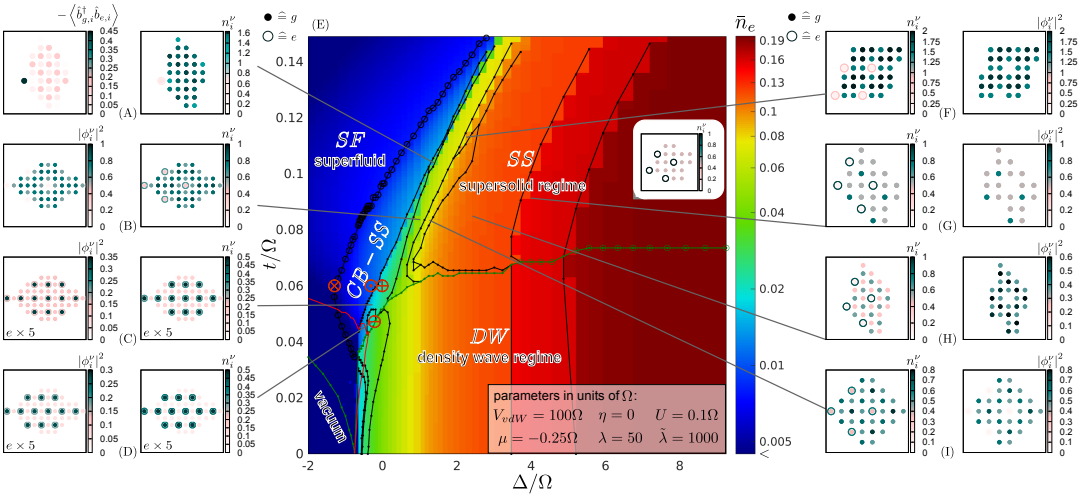


FIGURE 8.6: Lines in (E) show the phase diagram of the two-species extended Bose-Hubbard model with vdW-interacting excited Rydberg species (8.1). Shown is the dependence of the average GS Rydberg fraction $\bar{n}_e$ on detuning $\Delta$ and hopping $t$, while the fixed parameters of the model are given in the inset (see App. D for a motivation of $\eta = 0$). The occurrence of a finite condensate order parameter at finite $t$ is marked by the green line with dots. Transitions between different phases of supersolid (SS) order above this line, as well as between density wave (DW) ordered phases below, are separated by black lines (circles for second-order, points for first-order). As it has the simplest order beyond a homogeneous superfluid (SF), we specifically label the checkerboard supersolid (CB-SS) in the diagram. All DMFT results in the region between the red line without dots and vacuum have lattice-averaged grand-canonical potentials $f > 0$. (E) shows the lattice-averaged Rydberg fraction $\bar{n}_e$ (with the smallest values for $\Delta/\Omega < 0$), which is strongly related to the effective lifetime of Rydberg states [JR10]. (A)-(D), the inset in (E), and (F)-(I) show depictions of the spatial distribution of specified local observables. These plots correspond to different points indicated in the phase diagram in (E). If mentioned in a diagram, the values for excited states are rescaled by the indicated factor. The markers ($\otimes, \odot, \oplus, \ominus$) specify phases where spectral properties are analyzed in Sec. 8.3.

and jumps (first-order) in the spatially averaged observable $\bar{n}_e = \sum_i \langle \hat{n}_i^e \rangle / A_{cluster}^{(\mathbf{a}_1,\mathbf{a}_2)}$ [see Fig. 8.6(E)], which acts as an order parameter.

Thus we find various ground-state phases, starting with the well-known homogeneous superfluid (SF) and the devil's staircase in the DW regime at small hopping, separated by a peculiar series of supersolids (SS). We can distinguish two distinct regimes of supersolids, dominated by either weak or strong Rydberg dressing, arising due to two competing effects. One is the melting, induced by a large hopping amplitude $t$, while the other is the crystallizing effect of the detuning $\Delta$. Since blue detuning facilitates Rydberg crystallization at higher densities, as well as

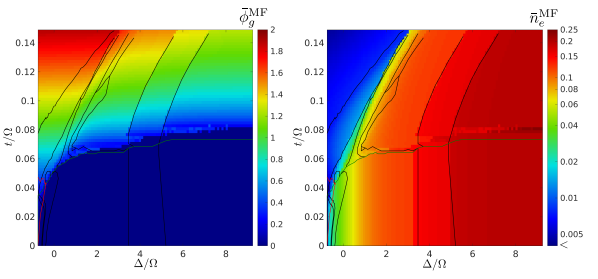


FIGURE 8.7: Comparison of the RB-DMFT result to the static mean-field results obtained in [BGH18]. Shown are the spatial averages $\bar{\phi}_g^{\mathrm{MF}}$ and $\bar{n}_e^{\mathrm{MF}}$, obtained for the ground-state of the Gutzwiller static mean-field ansatz (6.6), while the overlaid lines are given by the RB-DMFT results. Parameters of both simulations are identical to those given in Fig. 8.6.

a higher Rydberg fraction in general, the latter effect is easily understood.

Traversing the phase diagram in the supersolid regime, starting at high $\Delta$ [see Fig. 8.6(E), inset] and reducing its value continuously, one first finds a series of GS supersolids with growing wavelength, until there is a sudden drop in the wavelength, accompanied by a rising Rydberg condensate and a fast drop of the Rydberg fraction for the sites with the highest admixture of the Rydberg state [Figs. 8.6(A)-(D)]. Contrary to the devil's staircase in the DW regime, the staircase in the SS regime does not end in an empty or homogeneous system, but instead with short-wavelength supersolids, most notably the checkerboard supersolid (CB-SS) [see also Figs. 8.6(C) and 8.6(D)], which is the only previously predicted SS phase [SSS14]. The competition between crystallizing and melting effects becomes especially evident in the two cases where two supersolids meet, which both have the same number of sites in their unit cells, while their spanning vectors differ [compare Figs. 8.6(C) and (D), and Figs. 8.6(H) and (I)]. In this regime, the crystallizing effect dominates for small hopping, as the excitations minimize interaction energy by maximizing their NN distances. For increased hopping the system then prefers the configuration with slightly reduced NN distances while restoring a spatial order commensurate with the OL. Additionally, the eight-site unit cells are almost degenerate, while the unit cell less favored by $V_{vdW}$ has a transition into SF at lower $t$. Regarding the two distinct SS regimes with strong and weak dressing, the narrow phase dominated by a long-range order with a unit cell of 32 sites [Fig. 8.6(A)] implies crossover behavior. This phase marks the boundary between the two regimes, as it consists mostly of CB-SS with the CB order strongly visible in $\langle \hat{b}^\dagger_{g,i} \hat{b}_{e,i} \rangle$, interspersed by a low density of strongly dressed (impurity) atoms suppressing the short-range CB order.

Another noteworthy configuration appears in a band with a width $\Delta/\Omega \approx 0.2$, starting slightly above resonance [Fig. 8.6(B)]. There the ground-state condensate and the nearly Fock-state Rydberg excited atoms are spatially separated from one another, as is the case for most of the interaction-dominated part of the SS regime. But in addition, the excitations are aligned in a triangular lattice, while the condensate is arranged on its dual honeycomb lattice, at least as much as possible on a square lattice.

Finally, since the effective total decay rate of excitations is directly proportional to the fraction $n_e$ of their occupation [JR10], this quantity, shown in Fig. 8.6(E), implies that the region with low Rydberg occupation should be most suitable for experiment, especially in a setup where the avalanche effect can effectively be neglected or suppressed (see Sec. 2.2.2). Even at detunings $\Delta > 0$, Rydberg blockade causes a value of $\bar{n}_e$ which is nearly two orders of magnitude less than the full resonant excitation of single atoms, thus increasing the feasibility of realizing the corresponding supersolids. We further note that the Rydberg fraction also yields another limitation to the validity of the results, which is related to the single-band assumption for the Bose-Hubbard model (see Sec. 3.1.2). For the supersolid phases at large positive detuning the interaction energy among nearest neighbors at a distance of about two lattice spacings is on the order of about $100t$ for $t = 0.1\Omega$, which roughly marks the edge of validity for the single-band approximation.

In conclusion, while dressed models break down close to resonant Rydberg dressing, the combined effort of an analytically solvable frozen-limit model and RB-DMFT simulations at finite hopping allows for the analysis of the rich phase diagram of (8.1). In particular we find two distinct regimes of supersolid order dominated by either weak or strong dressing reminiscent of the bistable behavior in nonitinerant dissipative systems [LHC12; Car+13; Mar+14]. Due to our limitation to periodic systems with finite unit cells, the behavior at the crossover remains an open question. It

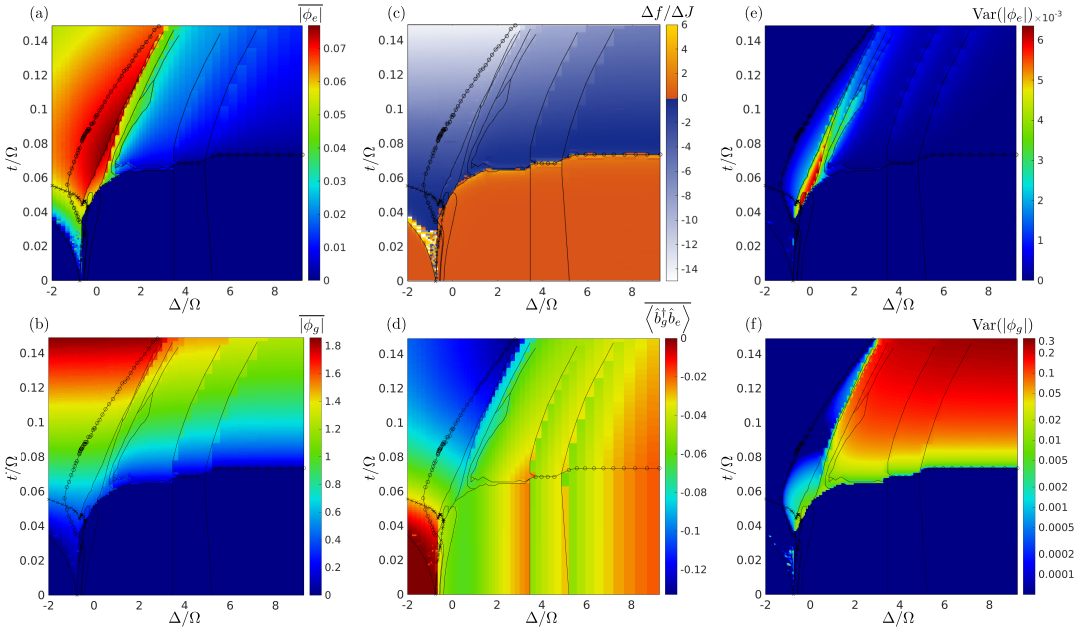


FIGURE 8.8: Here we show the different averaged order parameters one may use to distinguish the different supersolid phases as explained in the text. (a) and (b) are the spatially averaged condensate order parameters $\overline{|\phi_\sigma|} = \sum_i |\phi_i^\sigma| / A$. Averages are normalized by the size $A$ of the system simulated within RB-DMFT. Both species have opposite but spatially constant phases, as one might expect from a dark state. (c) Difference quotient $\Delta f/\Delta t$ of the mean grand canonical potential $f$ by the hopping amplitude $t$. (d) Spatial average of the local fluctuations $\left\langle \hat{b}_{g,i}^\dagger \hat{b}_{e,i} \right\rangle$ induced by the Rabi term (8.4) of the Hamiltonian (8.1). A non-zero value is related to in-plane magnetization of the pseudo-spins $\sigma = \{g, e\}$, while its magnitude grows near resonance and with total particle number. (e) and (f) show the spatial variance $\mathrm{Var}(|\phi_\sigma|) = \overline{|\phi_\sigma|^2} - \overline{|\phi_\sigma|}^2$ of the condensate order parameters. Note that for the excited state the maximum is close to $\Delta/\Omega \approx 0$, while in the ground-state $\Delta/\Omega > 1$ leads to the largest values. Lines correspond to those shown in Fig. 8.6(E), where circles represent second-order transitions, simple lines represent first-order transitions, and the line with crosses signifies the regime of $f > 0$, as explained in Fig. 8.6(E).

should also be noted that the Rabi frequency was taken to be in the range of a few megahertz, while so far realized values of hopping amplitudes reach only a fraction of this. But considering the phase diagram of the Bose-Hubbard-model, the transition to supersolid phases can be expected at strongly reduced hopping for values of $\mu$ close to zero where the assumption of low filling $\bar{n} < 1$ breaks down, leaving this regime open for further research.

### 8.2.2 Additional observables

The phase boundaries for finite hopping $t$, shown in Fig. 8.6(E), were obtained via the spatially averaged values of the local observables, which act as order parameters of the system. As can be seen in Fig. 8.8, they exhibit either jumps or kinks at certain points in the phase diagram, allowing us to determine the phase boundaries as well as the order of the phase transitions. As the Rydberg fraction $\bar{n}_e$ exhibits the most prominent changes [see Fig. 8.6(E)], it was used to obtain the phase boundaries between the various SS and DW phases.

Due to the complex nature of the model (8.1), additional observables allow for further characterization of its ground-state phases. While nonzero condensate order

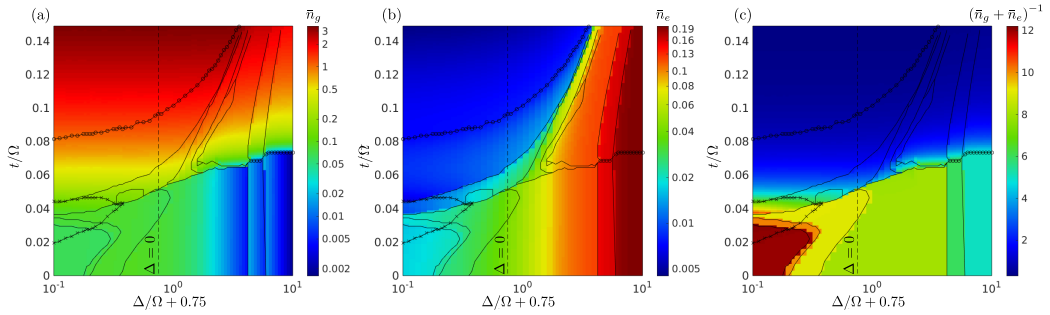


FIGURE 8.9: (a) and (b) depict averaged occupation numbers $\bar{n}_\sigma = \sum_i n_i^\sigma / A$, where $A$ is the normalization due to the considered number of sites. Note that $\Delta/\Omega > 0$ favors $\bar{n}_e$ over $\bar{n}_g$ in the DW phases. (c) The inverse of the average lattice filling becomes an integer in the DW regime. The values of these integers correspond to the area defined by the spanning vectors introduced earlier (e.g., equal to 12 in the lower left; compare also Fig. 8.2). Lines correspond to those shown in Fig. 8.6(E), where circles represent second-order transitions, simple lines represent first-order transitions and the line with crosses signifies the regime of $f > 0$, as explained in Fig. 8.6 (E). The dashed lines represent the case of resonant detuning $\Delta = 0$.

parameters $\phi_i^\sigma = \langle \hat{b}_{\sigma,i} \rangle$ determine the occurrence of a superfluid ($SF$) [see Figs. 8.8(a) and 8.8(b)], the suppression of the spatial average $\overline{|\phi_e|}$ at large $\Delta/\Omega$ is a result of the dominant interactions. The spatial variance $\mathrm{Var}(|\phi_\sigma|) = \overline{|\phi_\sigma|^2} - \overline{|\phi_\sigma|}^2$ of the condensate order parameters [see Figs. 8.8(e) and 8.8(f)] further extends and justifies the picture of two supersolid regimes due to the distinct behavior at small and large $\Delta/\Omega$. A vanishing value of these variances marks the loss of crystalline order and thus the transition from SS to a homogeneous SF. The large spatial variances in $\phi_i^\sigma$, on the other hand, are due to suppressed condensation on sites occupied by atoms strongly dressed with a Rydberg state. At the crossover between the two SS regimes, the observable related to the Rabi process (8.4), $\langle \hat{b}_{g,i}^\dagger \hat{b}_{e,i} \rangle$, also undergoes a significant change in behavior [see Fig. 8.8(d)]. Regarding the transitions between the various supersolid phases, we want to point out that divergences of $\Delta f / \Delta t$ (see (c) in Fig. 8.8) are almost absent in between SS phases and remarkably also at the SS-SF transition.

Note that in the region where the ground state contribution $\bar{n}_g$ vanishes [see Fig. 8.9(a)], the Rydberg states become almost pure number states [compare Figs. 8.9(b) and 8.9(c)]. As the corresponding property, namely, that $\bar{n}_e$ nearly equals $\frac{1}{q}$, where $q$ is the area of the unit cell corresponding to the inverse of the mean lattice filling at a vanishing condensate fraction, also extends into the region with a finite condensate, the Rydberg state can be understood to remain in a Fock state even for increased hopping amplitudes. Condensation then happens purely in the ground state species, which implies that the condensate part spatially separates from the long-range interacting part of the system.

### 8.2.3 Finite systems

The presence of blackbody radiation and spontaneous decay both can drive transitions to nearby Rydberg $p$-states for the considered $s$-state Rydberg excitations. Note that for these states exists an important dissipative channel, which generates a strong global loss of coherence and atoms due to incoherent $s$-$p$-dipole scattering, referred to as Förster processes discussed in Sec. 2.2.2 (see also [Gol+16; Ama+16; Zei+16]). The important figure of merit in this context is the time $\tau$ until creation of

the first contaminant $p$-state. As it is a global process, we have to consider the creation of such a state anywhere in the system, implying an integration of the Rydberg fraction over all sites, so

$$\frac{1}{\tau} = b\Gamma_0 \sum_i \langle \hat{n}_i^e \rangle. \tag{8.13}$$

The term $b$ denotes the branching ratio of the decay into detrimental states, with a typical value of $b \gtrsim 20\%$ at room temperature, and $\Gamma_0$ is the full natural decay rate, for example, $\Gamma_0^{-1} = \tau_0 \gtrsim 30\mu$s for the $36S$ state of $^{87}$Rb [Bou+17]. While this expression obviously diverges with the system size for any nonzero average Rydberg fraction, it is possible to limit its value in a finite system. We note that in the far detuned regime $\langle \hat{n}_i^e \rangle$ is given by the ratio $(\Omega/2\Delta)^2 = n^e$, as the detuning in this regime does not exhibit a mean-field shift due to many-body effects. As can be seen from the parameters considered in Chap. 7, there the local Rydberg fraction amounts to $\approx 0.1\%$ per dressed atom. Considering that in the SS1 phase we typically have one dressed atom per unit cell and for a proper (micro) crystal one might arguably require at least about $5 \times 5$ unit cells for the system size, this implies a collective Rydberg fraction of $\approx 2.5\%$ and thus a time-scale of up to $\tau \approx 6$ms.

Note that it is also possible at near-resonant excitation of Rydberg states to obtain a local Rydberg fraction of $< 0.1\%$ in the bulk of the system, as shown in Fig. 8.6(E). But as this value is achieved via many-body correlations induced by the strong long-range interactions, one has to be careful at the boundary, which is either given by the edge of the cloud and can be controlled by the shape of the external optical trap, or the intensity beam-profile of the Rabi laser. For a sufficiently sharp boundary, it significantly differs from the bulk via a reduced number of neighbors which get excited to the Rydberg states, most notably resulting in a reduced local mean-field shift of the detuning at site $i$,

$$\Delta^i_{\text{shift}} = V_{vdW} \sum_{j \neq i} \frac{n_j^e}{|\mathbf{i} - \mathbf{j}|^6}. \tag{8.14}$$

Thus the effective Rabi process becomes increasingly near-resonant at the edge of the system, leading to a strong increase in the Rydberg fraction. In that case one easily observes local Rydberg fractions on the order of $0.5$, expected for the on-resonant coherent driving of the Rydberg excitation. So the numerous excitations that form at the edge, as observed in [Sch+12], for example, quickly induce the avalanche on a time scale, which is well approximated by the bare lifetime of about $\tau_0 = 30\mu$s in the above mentioned example. Itinerant physics are therefore out of reach in this limit.

Let us now consider a system with parameters as given in Tab. 8.1, with one minor change regarding the geometry of the system. We consider a finite system of $21 \times 21$ sites with periodic boundary conditions, but no longer assume a spatially constant value for $\Omega$ and instead consider a Rabi laser which results in a beam-waist with the shape of a "4th-power" Gaussian,

$$\Omega(r) = \Omega \exp(-r^4/\kappa^4), \tag{8.15}$$

where $r$ is the distance from the center of the system and we set $\kappa = 8.5a$. This beam waist separates the system into three parts: the center with roughly constant Rabi

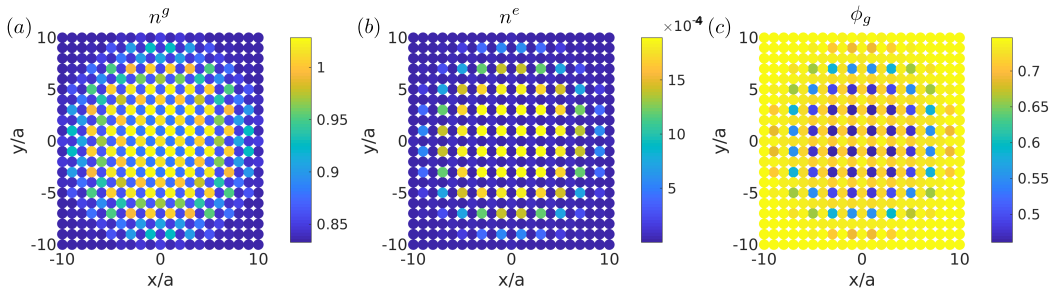


FIGURE 8.10: Supersolid formation in a finite system illuminated by a Rabi-laser with a beam-waist of about 15 lattice sites in diameter. Shown are the real-space distributions of $(a)$ the ground state density $n^g$, $(b)$ the excited state density (local Rydberg fraction) $(n^e)$, and the condensate order parameter of the ground state $\phi^g$ in a flat dimple trap, generated using a 4th-power Gaussian beam-waist for the Rabi laser. Density of the ground (a) and excited (b) state, condensate parameter of the ground state (c) are shown respectively.

frequency $\Omega(r) \approx \Omega$, the edge with roughly constant Rabi frequency $\Omega(r) = 0$, which can just as well be considered as the center of a system without Rydberg excitations, and the crossover region between those two regions, which can be considered as a soft edge. All other parameters are given in Tab. 8.1.

| $U$ | $U\lambda$ | $U\tilde{\lambda}$ | $t$ | $t\eta$ | $\mu$ | $\Delta$ | $\Omega$ | $V_{vdW}$ |
|---|---|---|---|---|---|---|---|---|
| $3 \times 10^{-3}$ | 5 | 100 | $3 \times 10^{-4}$ | $3 \times 10^{-4}$ | $3 \times 10^{-4}$ | $-0.2$ | 0.2 | $10^4$ |

TABLE 8.1: Model parameters of (8.1) used for the finite system discussed in this section. Using natural units, all values are given in units of MHz.

The idea behind this setup is to counteract the overshoot of the Rydberg fraction at a hard edge, such that we can obtain an overall more smooth distribution of the Rydberg fraction, which is much closer to the bulk value, as can be seen in Fig. 8.10. We therefore get a system with a 4-site-supersolid order at the center of the beam with a local Rydberg fraction $n_i^e < 2 \times 10^{-3}$. Note that we also have a very low total Rydberg fraction $\sum_i n_i^e = 0.1062$, which via (8.13) implies a timescale of $\tau \approx 1.4$ms. This is on the same order of magnitude as the tunneling time, so we can expect to observe this phase in experiments, especially with the additional aid of post-selecting for results without avalanches [Zei+16].

As this real-space simulation naturally describes the crossover between a homogeneous superfluid and the supersolid, we can use this opportunity to analyze the evolution between the two phases. In Fig. 8.11 we show the radial dependence of local density of states (DOS) from RB-DMFT, averaged over rings with a width of two lattice sites. One can nicely observe the transition from the supersolid bulk to the surrounding superfluid. The most remarkable features are a broadening of the particle modes, as well as the separation of a very narrow gapped hole mode for the ground state component. From a comparison with quasiparticle results we can further observe a very good match between the results, both in the supersolid phase and in the superfluid. The observed discrepancies either stem from the inherently discretized nature of the DMFT spectrum due to the discrete nature of the considered impurity models, or they are due to the incapability of DMFT to properly describe long-wavelength Goldstone modes, which are always gapped in DMFT. The reason for this is the limitation of DMFT to the lowest order non-local correlations.

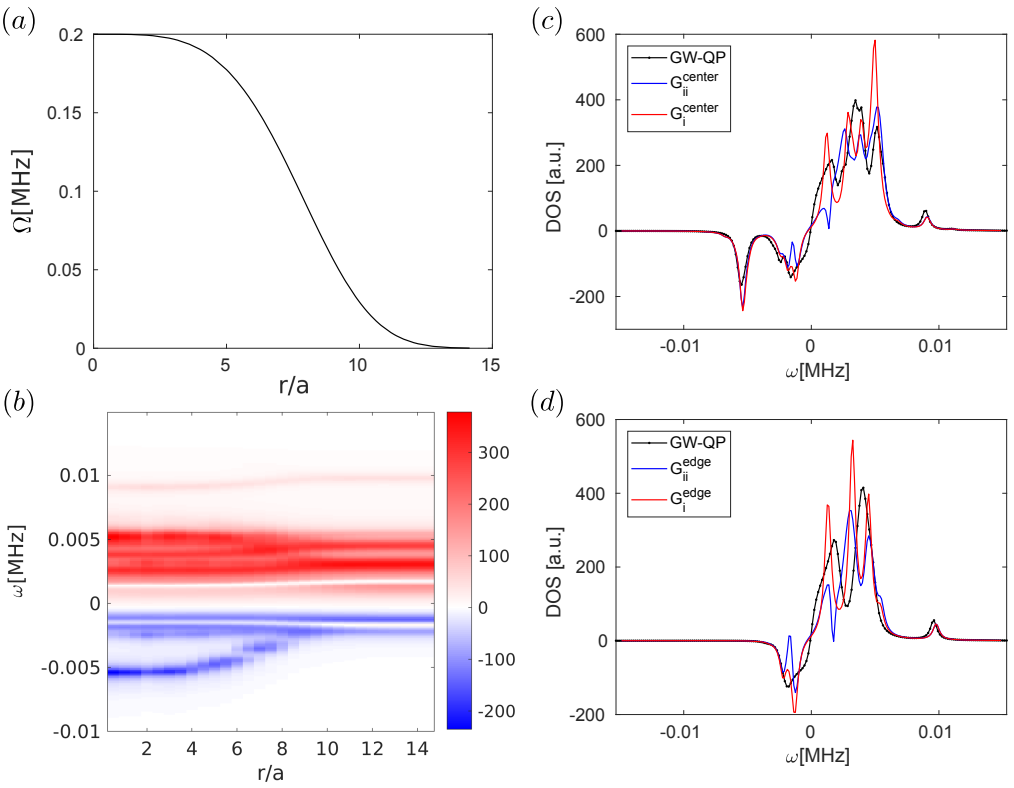


FIGURE 8.11: Spectral properties of the finite supersolid. $(a)$ Assumed radial shape of the Rabi-laser beam, with a FWHM of about 15 lattice spacings a. $(b)$ Average local DOS of the ground state component as a function of the distance from the beam center, obtained from the local terms of the self-consistent RB-DMFT result for the interacting lattice Green's function. $(c)$ and $(d)$ show comparisons of the local DOS of the ground state component calculated in RB-DMFT, either from the local terms of the lattice Green's function $G_{ii}(\omega)$ or from the local interacting Green's functions, obtained for the individual Anderson impurity models, with the result of the quasiparticle method applied to a system with periodic boundary conditions and $2^7 \times 2^7$ lattice sites. Here, either the center $(c)$ with $r/a = 0.5$ or the edge $(d)$ with $r/a = 12.5$ is considered. All shown DOS fulfill the sum rule, $\int A(\mathbf{k},\omega)d\omega = 1$, to within $3\%$, while the quasiparticle result is the closest and the result from the lattice Green's function deviates most. For all shown results a Lorentzian broadening of $0.3$kHz was considered.

## 8.3 Spectral properties in quasiparticle picture

In the preceding section we have seen that spectral data from the quasiparticle method matches well with results obtained in the supersolid regime via RB-DMFT. Thus we will now give a detailed discussion of the spectral properties , including the band composition, momentum distribution, and dynamic and static structure factor. For all discussed quasiparticle results in this section a systems size of $2^7 \times 2^7$ sites with periodic boundary conditions was used. We focus on four points of the phase diagram Fig. 8.6, respectively given by $\Delta/\Omega = \{-1.3, -0.25, -0.1, -0.2\}$ and $t/\Omega = \{0.06, 0.06, 0.06, 0.045\}$.

### 8.3.1 Band composition

In the case of near-resonant Rydberg excitation considered here, the two components of the system are strongly mixed by the Rabi driving. Therefore we do not expect

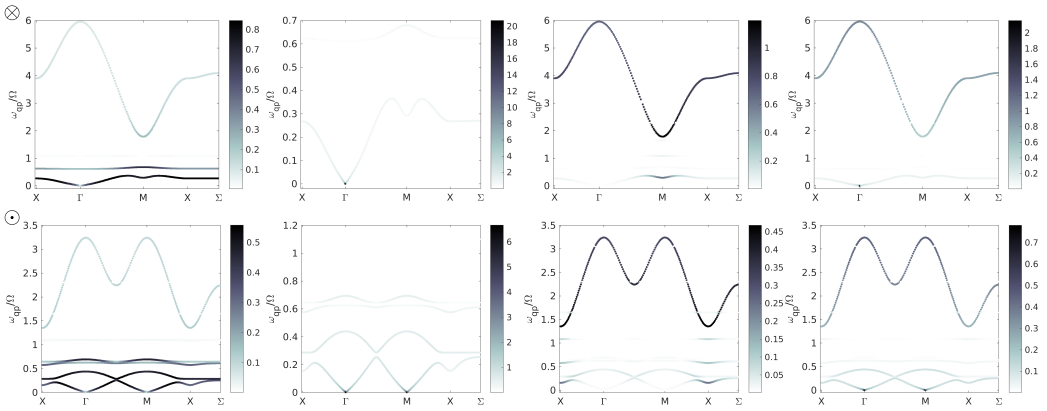

FIGURE 8.12: Band composition in the homogeneous superfluid [corresponding to ⊗ in Fig. 8.6(E)] and checkerboard supersolid phases [corresponding to ⊙ in Fig. 8.6(E)] in the vicinity of structural phase transitions. Each of the columns gives the first-order response of different observables upon a weak coherent excitation of a given quasiparticle mode. *Left to right*: Amplitude response of the ground state Re($\delta\phi_g$), phase response of the Rydberg state Im($\delta\phi_g$), amplitude response of the Rydberg state Re($\delta\phi_e$) and phase response of the Rydberg state Im($\delta\phi_g$).

to have a separate condensation in each component. Indeed, we only find a single gapless mode, corresponding to the Nambu-Goldstone-mode of a single condensate.

Altogether, there are three relevant bands in the homogeneous superfluid [see Fig. 8.12, with parameters corresponding to ⊗ and ⊙ in Fig. 8.6(E)]. In subsequent structural phase transitions, induced via an increase in $\Delta/\Omega$, the size of the unit cell increases, such that the bands exhibit back-folding and avoided crossings, as can be seen in Fig. 8.12. The lowest band always remains gapless, due to the presence of a condensate. Depending on the broken lattice symmetry, additional phonon cones appear at nonzero momenta, corresponding to the reciprocal lattice of the new superlattice. Modes in the vicinity of the gapless cones almost purely generate phase fluctuations in both condensates. The remainder of the lowest band, as well as the remaining two gapped bands predominantly yield amplitude fluctuations in either condensate order parameter.

In the ungapped band we can also observe the emergence of roton-minima. As the bare van der Waals interaction does not have a length scale of its own, we cannot explain the position of the roton minimum via the long-range interaction alone, but instead the optical lattice provides the length-scale, as the first roton minimum appears at the edge of the Brillouin zone at $\mathbf{k} = (\pi/a, \pi/a)$. In the CB-SS phase we observe a subsequent roton at the edge of the reduced Brillouin zone, corresponding to the $X$-point in the original Brillouin zone. In the vicinity of each roton we observe a pronounced amplitude response of the Rydberg condensate, as expected for an instability related to the formation of a supersolid.

The lower of the two gapped bands corresponds to the first gapped band which can be found in a single component Bose-Hubbard model. At unitary filling it contains the Higgs amplitude mode. In our case it predominantly yields amplitude fluctuations in the ground state. The remaining gapped band has very different energy scales and a bandwidth $> 4\Omega$, while it mainly contains phase and amplitude fluctuations in the Rydberg part of the condensate.

In the supersolid phases beyond the checkerboard case, high-lying bands become less relevant (see Fig. 8.13). Due to the back-folding induced by the increased unit cells, individual bands become collections of bands in the more complex phases.

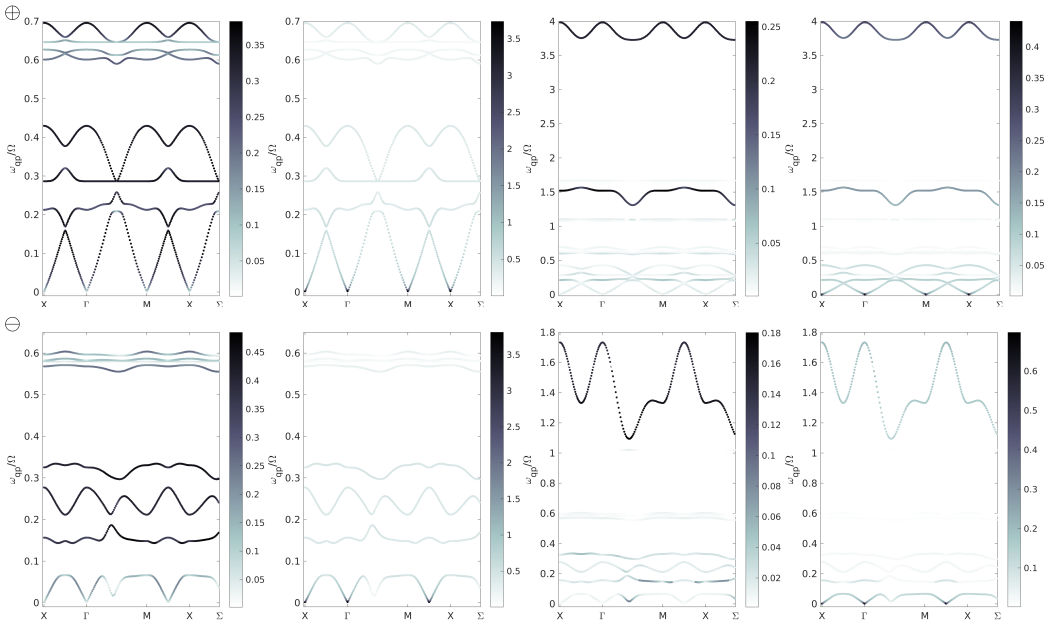

FIGURE 8.13: Band composition in two different supersolid phases [corresponding to $\oplus$ and $\ominus$ in Fig. 8.6(E)]. Shown is the first-order response of various observables upon a weak coherent excitation of a given quasiparticle mode. *Left to right*: Amplitude response of the ground state $\mathrm{Re}(\delta\phi_g)$, phase response of the Rydberg state $\mathrm{Im}(\delta\phi_g)$, amplitude response of the Rydberg state $\mathrm{Re}(\delta\phi_e)$ and phase response of the Rydberg state $\mathrm{Im}(\delta\phi_g)$.

But still there is only a single ungapped band, containing multiple gapless cones at momenta corresponding to the reciprocal lattice of the associated superlattice. Each cone yields Nambu-Goldstone-type phase excitations of the condensate. All remaining gapped bands primarily provide amplitude fluctuations to a varying degree. Note that a remnant of the roton-minimum still is visible in the first gapped band of the ($\oplus$)-supersolid in Fig. 8.13. Indeed the roton minima tend to close the gap at a phase transition and retract in the first gapped band afterwards. An exact gap closing has only been observed in the simulations at second-order phase transitions, where changes in the order parameters as well as the excitation spectrum happen continuously.

### 8.3.2 Spectral functions

When considering the spectral weights we observe that the gapless and the first gapped (set of) band(s) contribute almost solely to the spectral function of the ground state component. While the Rydberg component also gets contributions from the gapless band, it has its major contributions in the high-lying gapped band, which has a shape that strongly depends on the supersolid state. We note that all spectral functions discussed in this section satisfy the sum rule to within $1\%$, while the deviation systematically lies below the rule and is a result of the Fock-space truncation.

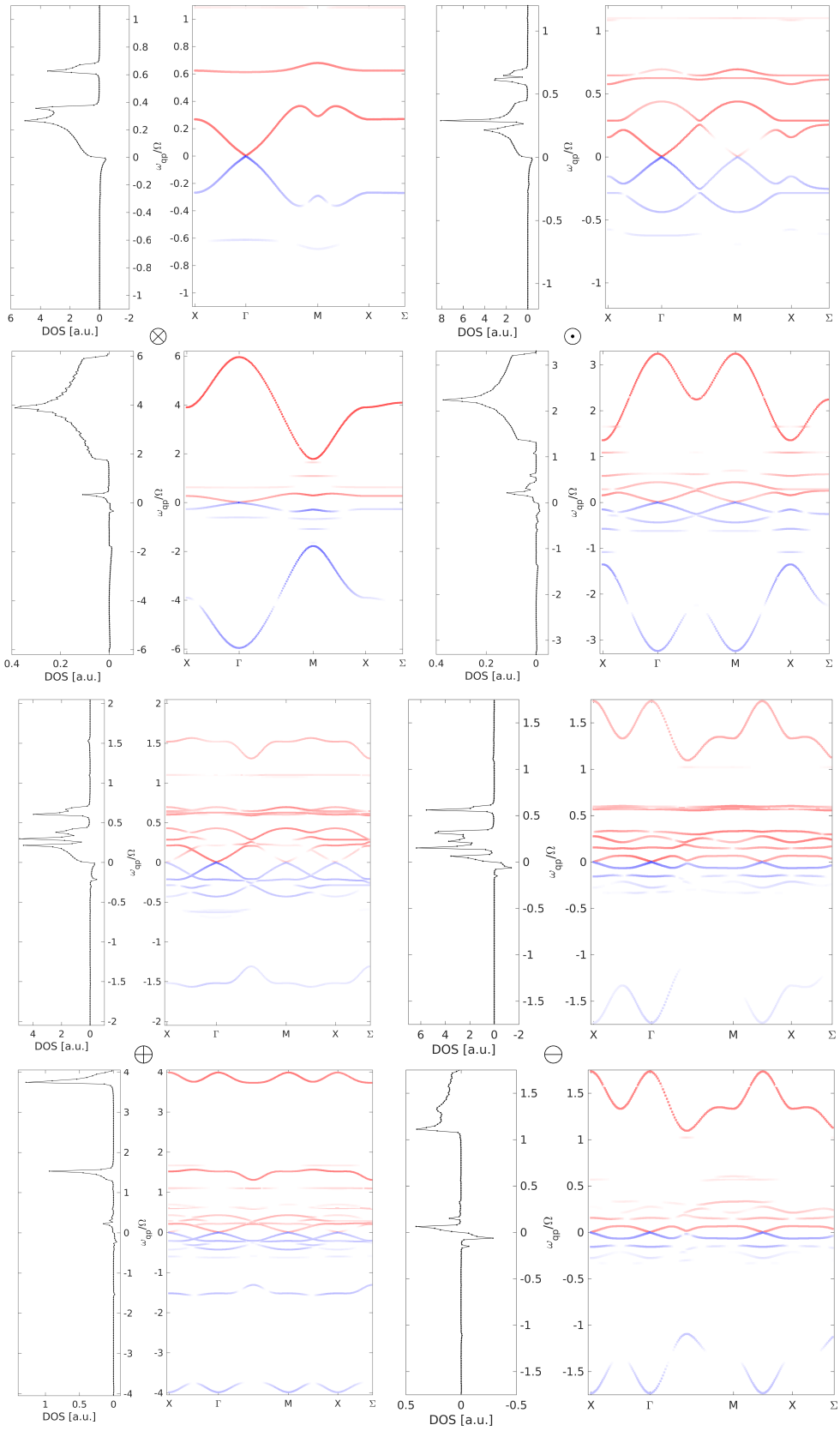


FIGURE 8.14: Density of states (DOS) and the spectral function $\mathcal{A}(\mathbf{k}, \omega_{qp})$ along high symmetry points for ground (*top row* of each group) and Rydberg state (*bottom row* of each group). The symbols $(\otimes, \odot, \oplus, \ominus)$ at the center of each group of four plots signify the phase it corresponds to, as shown in Fig. 8.6(E).

For the ground state component the energy range of excitations barely changes throughout the various supersolid phases. Instead the band structure changes tremendously, resulting in various gaps and Van-Hove-singularities in the density of states. The high lying bands, constituting most of the excited state spectral weights, change significantly between phases. This is best illustrated comparing the CB-SS case ($\odot$ in Fig. 8.14) to the 4-site SS ($\oplus$ in Fig. 8.14), which the former evolves into, when increasing the detuning $\Delta$. As a result of the strong long-range interaction, this band exhibits a strong avoided crossing after the back-folding of modes at the phase transition. Subsequently, most of the spectral weight migrates to the lower branch of the – now doubled – bands. As a result the energy scale of the relevant modes is significantly reduced.

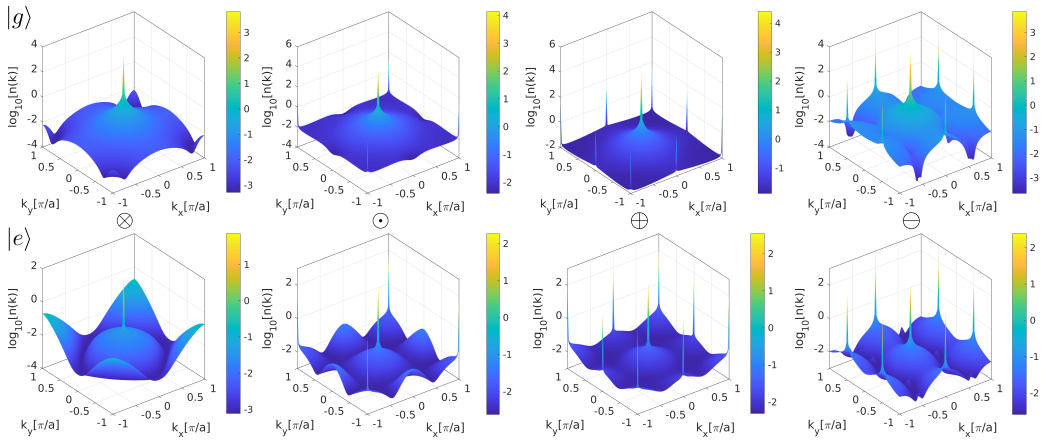


FIGURE 8.15: Momentum distributions of ground (*top row*) and Rydberg state (*bottom row*). The symbols ($\otimes, \odot, \oplus, \ominus$) signify the phase of each plot [compare Fig. 8.6(E)].

Throughout the various supersolid phases, one can observe the appearance of sharp peaks at quasimomenta corresponding to the reciprocal lattice of emergent superlattice structures (see Fig. 8.15). These macroscopic maxima show the condensation in certain momentum states, starting with a single peak at $\mathbf{k} = 0$, as expected in the homogeneous superfluid. Due to the Rydberg fraction of usually no more than $1\%$, the peaks in the Rydberg component are reduced proportionally. Also note that the $\mathbf{k} = 0$ peak always dominates.

Additional pronounced local maxima emerge in the Rydberg component when approaching a structural phase transition, which only have minor counterparts in the ground state component. These maxima peak at momenta where a roton mode exists in the lowest band. As these roton minima are a result of the long-range Rydberg-Rydberg interaction, the local maxima in the momentum distribution predominantely appear in the Rydberg species.

### 8.3.3 Structure factors

Bragg scattering experiments allow for the measurement of the dynamic as well as the static structure factor. Thus one can map the band structure, as well as observe signatures of crystallization in experiment. In this section, we give an overview of the signatures of supersolid order one might observe in experiments. Note that the ground state structure factors are more accessible in experiments, as suitable laser setups are already commonplace, while the level structure in the vicinity of a Rydberg state would necessitate additional considerations in order to realize a Bragg experiment.

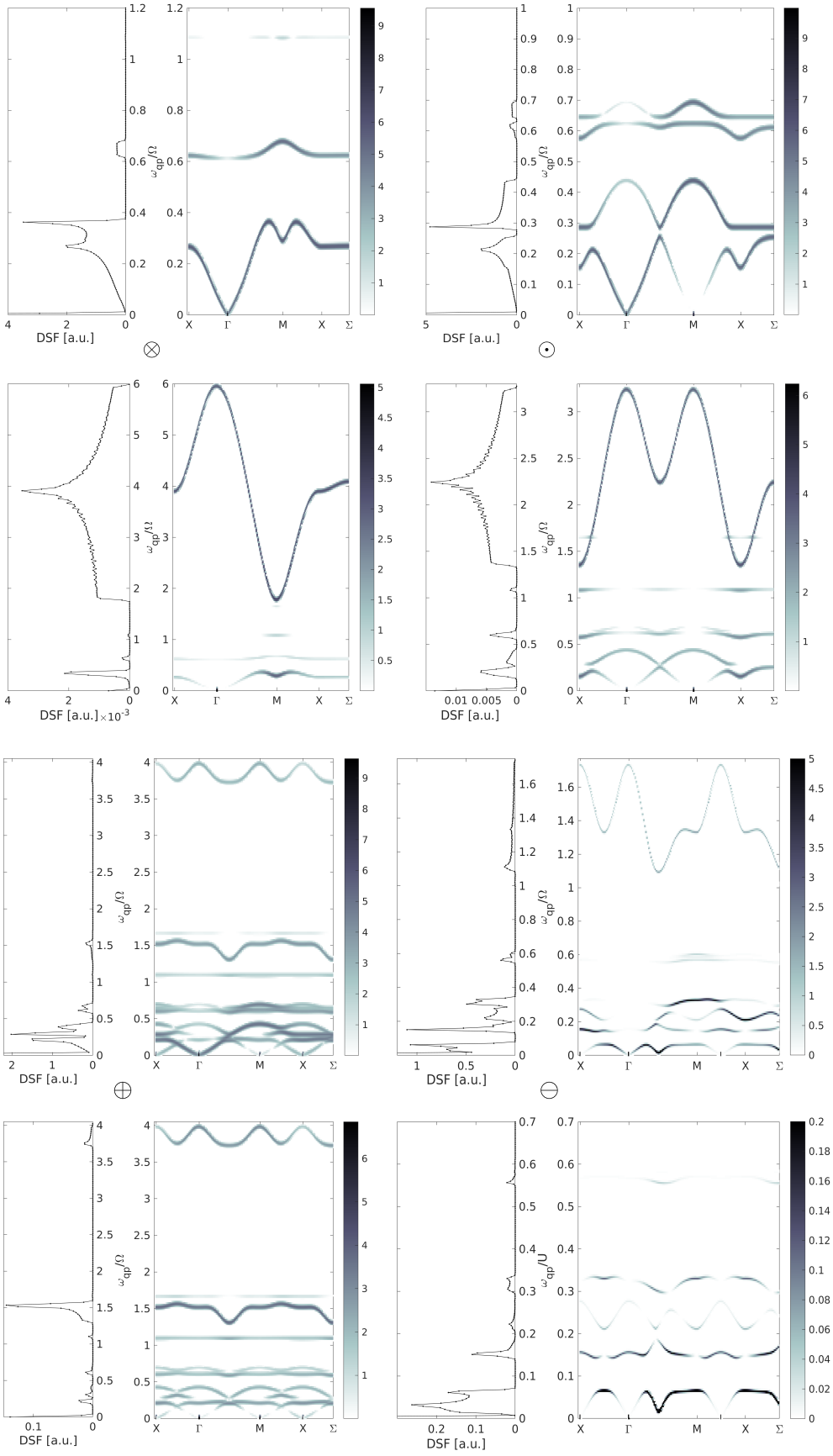


FIGURE 8.16: Dynamic structure factor integrated over the momenta DSF = $S(\omega)$ and along high symmetry points for ground (*top row* of each group) and Rydberg state (*bottom row* of each group). The symbols $(\otimes, \odot, \oplus, \ominus)$ at the center of each group of four plots signify the phase it corresponds to, as shown in Fig. 8.6(E).

### Dynamic structure factor

Contributions of the individual bands to the dynamic structure factor of either component are distributed very similar to the spectral function: the gapless and first gapped band(s) provide(s) most of the contributions for the ground state component. In the Rydberg component we observe contributions from the gapless band, mostly in the vicinity of roton minima, as well as major contributions from the high-lying gapped band(s). This picture changes close to the insulator transition, as for example in the quasi-triangular supersolid (⊖ in Fig. 8.16). There the high-lying gapped bands no longer contribute to the dynamic structure factor of the Rydberg species, while small contributions survive for the ground state component.

### Static structure factor

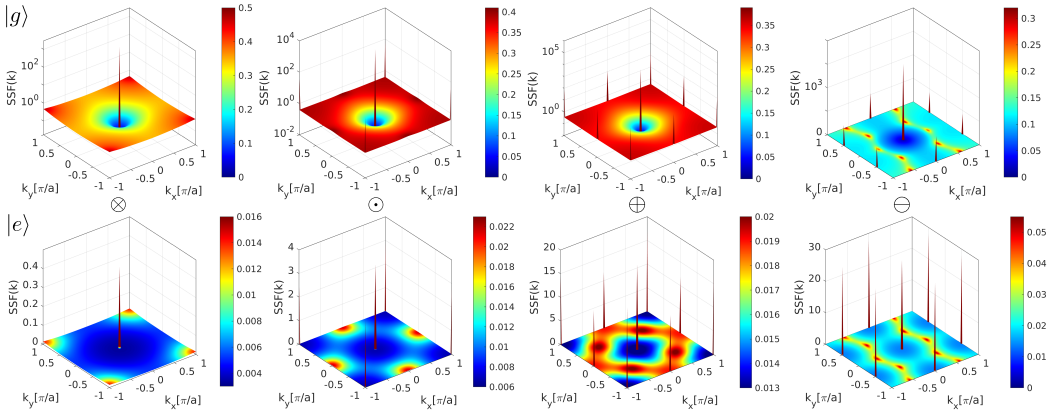


FIGURE 8.17: Static structure factor of ground (*top row*) and Rydberg state (*bottom row*). The symbols (⊗, ⊙, ⊕, ⊖) signify the phase of each plot [compare Fig. 8.6(E)].

We end our discussion of the near resonant Rydberg dressing with the static structure factor (see Fig. 8.17). In the homogeneous superfluid the condensation of a macroscopic part into the zero momentum state yields a strong peak in the static structure factor at $\mathbf{k} = 0$ in both species (⊗). As the considered superfluid is in the vicinity of the SF-SS transition, pronounced local maxima can be observed at the edge of the Brillouin zone, especially in the Rydberg component, as it carries the long-range interaction. The Brillouin zone gets reduced as the unit cell of a supersolid contains more than one site, and the maxima transform into peaks as a result of the condensation in the finite momentum states. Then new instabilities emerge at the edge of the reduced Brillouin zone, as $\Delta$ is increased further, giving rise to new local maxima of the static structure factor. This can be observed in each supersolid phase (for the Rydberg component ⊙, ⊕, ⊖ in Fig. 8.17). Only when the condensate fraction is vastly reduced, due to the vicinity to the insulating state, one can also observe the local maxima in the ground state component (see ⊖ in Fig. 8.17).

# Appendix A

# Hartree-Fock generalization of B-DMFT

In the main part we have derived the RB-DMFT equations for a system with long-range interactions, using the Hartee approximation only. The obtained effective cavity action was shown to depend on three and four-point correlations, which were subsequently treated using the Hartree approximation. In this section we briefly discuss a Hartree-Fock type treatment of the relevant terms, implying the need for a slightly more general form of the effective impurity Hamiltonian. Furthermore the generalized Hartree-Fock treatment is not limited to the impurity, but also extends to the used Dyson equation, which is required to close the self-consistent DMFT-loop.

## A.1 Effective impurity action

In the main part we have defined an expression for the effective action (4.11), which is of the following form.

$$S^0_{\text{eff}} = S_0 + y \tag{A.1}$$

Its first term is given by the local contributions of a given site, referred to by the index $0$.

$$S_0 = \int_0^\beta d\tau \sum_\sigma \left( b^*_{0\sigma} \frac{\partial b_{0\sigma}}{\partial \tau} - \mu_\sigma b^*_{0\sigma} b_{0\sigma} \right) + \sum_{\sigma,\gamma} \left( \Omega_{\sigma\gamma} (b^*_{0\sigma} b_{0\gamma} + b_{0\sigma} b^*_{0\gamma}) + \frac{U_{\sigma\gamma}}{2} |b_{0\sigma}|^2 |b_{0\gamma}|^2 \right) \tag{A.2}$$

The second term is given by an expansion in various orders of Green's functions, depending in leading order (in an expansion in the inverse number of neighbors) on the quantities $M(\tau,\eta)$ (4.15) and $F(\tau,\eta)$ (4.16), which are to be determined self-consistently.

$$y = \int_0^\beta d\tau \left( \sum_{\langle 0,i\rangle,\sigma} - \left( t^\sigma_{0i} b^*_{0\sigma} \langle b_{i\sigma} \rangle_{(0)} + c.c. \right) + \sum_{i\neq 0,\sigma} V_\sigma(i,0) \langle n_{i\sigma} \rangle_{(0)} n_{0\sigma} \right) \tag{A.3}$$

$$- \frac{1}{2} \int_0^\beta d\tau \int_0^\beta d\eta \Big( \left( \mathbf{b}^*_0(\tau)\, \mathbf{b}_0(\tau) \right) M(\tau,\eta) \left( \mathbf{b}_0(\eta)\, \mathbf{b}^*_0(\eta) \right)^T \tag{A.4}$$

$$+ \left( \mathbf{b}^*_0(\tau)\, \mathbf{n}_0(\tau) \right) F(\tau,\eta) \left( \mathbf{b}_0(\eta)\, \mathbf{n}_0(\eta) \right)^T \Big) \tag{A.5}$$

Regarding the implementation of a Hartree-Fock treatment, we only have to consider the last term (A.5).

$$\begin{aligned}
F_{11}^{\mu\nu}(\tau,\eta) &= 0 \\
F_{12}^{\mu\nu}(\tau,\eta) &= -2\sum_{i,j\neq 0} t_{0i}^{\mu} V_\nu(j,0)\left(\langle b_{i\mu}(\tau) n_{j\nu}(\eta)\rangle_{(0)} - \langle b_{i\mu}(\tau)\rangle_{(0)}\langle n_{j\nu}(\eta)\rangle_{(0)}\right) \\
F_{21}^{\mu\nu}(\tau,\eta) &= -2\sum_{i,j\neq 0} t_{0i}^{\mu *} V_\nu(j,0)\left(\langle b_{i\mu}^*(\tau) n_{j\nu}(\eta)\rangle_{(0)} - \langle b_{i\mu}^*(\tau)\rangle_{(0)}\langle n_{j\nu}(\eta)\rangle_{(0)}\right) \\
F_{22}^{\mu\nu}(\tau,\eta) &= \sum_{i\neq 0,j\neq 0} V_\mu(i,0) V_\nu(j,0)\left(\langle n_{i\mu}(\tau) n_{j\nu}(\eta)\rangle_{(0)} - \langle n_{i\mu}(\tau)\rangle_{(0)}\langle n_{j\nu}(\eta)\rangle_{(0)}\right)
\end{aligned} \tag{A.6}$$

Let us now formulate a Hartree-Fock type approximation of these terms. To do so, we extend the known Hartree approximation (as discussed in section 4.1 following equation (4.16)), by also including off-diagonal terms when forming contractions of the terms with three of four field variables[1]. Merging the various variables, position, component and imaginary time, using Latin letters ($(i,\mu,\tau)\hat{=}a,b,\ldots$), we may thus expand the correlation functions appearing in (A.5), by representing every field as a sum of its fluctuations $\delta_i$ and the expectation value $\phi_i = \langle b_i\rangle_{(0)}$, so $b_i = \phi_i + \delta_i$.

$$\begin{aligned}
\langle b_a b_b^* b_b\rangle_{(0)} &= \phi_a\langle b_b^* b_b\rangle_{(0)} + \phi_b^*\langle b_a b_b\rangle_{(0)} + \phi_b\langle b_a b_b^*\rangle_{(0)} - 2\phi_a\phi_b^*\phi_b + \langle\delta_a\delta_b^*\delta_b\rangle \\
&= \phi_a\langle b_b^* b_b\rangle_{(0)C} + \phi_b^*\langle b_a b_b\rangle_{(0)C} + \phi_b\langle b_a b_b^*\rangle_{(0)C} + \phi_a\phi_b^*\phi_b + \langle\delta_a\delta_b^*\delta_b\rangle_{(0)}
\end{aligned} \tag{A.7}$$

Here we have introduced the connected two-point correlation function, as the two-point function, from which the disconnected contributions are excluded, thereby it is the correlation function of the fluctuations of all fields.

$$\langle b_a b_b\rangle_C = \langle b_a b_b\rangle - \langle b_a\rangle\langle b_b\rangle = \langle\delta_a\delta_b\rangle \tag{A.8}$$

As a generalization thus follows from (A.7) the definition of the connected three-point correlation function. Also note that the definition of the connected correlations does not depend on the explicit type of the average.

$$\langle b_a b_b^* b_b\rangle_C = \langle\delta_a\delta_b^*\delta_b\rangle = \langle b_a b_b^* b_b\rangle - \left(\phi_a\langle b_b^* b_b\rangle_C + \phi_b^*\langle b_a b_b\rangle_C + \phi_b\langle b_a b_b^*\rangle_C + \phi_a\phi_b^*\phi_b\right) \tag{A.9}$$

The fourth order term can thus be represented as

$$\begin{aligned}
\langle b_a^* b_a b_b^* b_b\rangle_{(0)} &= \phi_b^*\phi_b\langle b_a^* b_a\rangle_{(0)C} + \phi_a^*\phi_a\langle b_b^* b_b\rangle_{(0)C} + \phi_b^*\phi_a\langle b_a^* b_b\rangle_{(0)C} \\
&+ \phi_a^*\phi_b\langle b_b^* b_a\rangle_{(0)C} + \phi_a\phi_b\langle b_a^* b_b^*\rangle_{(0)C} + \phi_a^*\phi_b^*\langle b_a b_b\rangle_{(0)C} \\
&+ \phi_a^*\langle b_a b_b^* b_b\rangle_{(0)C} + \phi_a\langle b_a^* b_b^* b_b\rangle_{(0)C} \\
&+ \phi_b^*\langle b_a^* b_a b_b\rangle_{(0)C} + \phi_b\langle b_a^* b_a b_b^*\rangle_{(0)C} \\
&+ \phi_a^*\phi_a\phi_b^*\phi_b + \langle b_a^* b_a b_b^* b_b\rangle_{(0)C}
\end{aligned} \tag{A.10}$$

Here we have used $\langle b_a^* b_a b_b^* b_b\rangle_C = \langle\delta_a^*\delta_a\delta_b^*\delta_b\rangle$. The last remaining step is an approximation for the third and fourth order terms which still appear in this expression, as they represent contributions from higher order (connected) Green's functions,

[1] Note that $n_{j\nu}(\eta) = b_{j\nu}^*(\eta) b_{j\nu}(\eta)$

which we aim to neglect within DMFT. In order to retain as much as possible from these terms, we therefore assume a factorization, as implied by the Wick-theorem, so $\langle b_a^* b_a b_b^* b_b\rangle_C \approx \langle b_a^* b_a\rangle_C\langle b_b^* b_b\rangle_C + \langle b_a^* b_b\rangle_C\langle b_b^* b_a\rangle_C + \langle b_a^* b_b^*\rangle_C\langle b_a b_b\rangle_C$. That way all third order terms vanish, while the contributions from the fourth order term remain, which are the only terms also relevant in a normal state (with vanishing condensate fraction). We thus obtain the following approximation of (A.5).

$$\begin{aligned} F_{12}^{\mu\nu}(\tau,\eta) &= -2\sum_{i,j\neq 0} t_{0i}^{\mu} V_\nu(j,0)\left(\langle b_{i\mu}(\tau) b_{j\nu}^*(\eta)\rangle_{(0)C}\phi_{j\nu}^{(0)}(\eta) + \langle b_{i\mu}(\tau) b_{j\nu}(\eta)\rangle_{(0)C}\phi_{j\nu}^{(0)*}(\eta)\right) \\ &= \left[F_{21}^{\mu\nu}(\tau,\eta)\right]^* \\ F_{22}^{\mu\nu}(\tau,\eta) &= \sum_{i\neq 0, j\neq 0} V_\mu(i,0)V_\nu(j,0)\left(-\phi_{i\mu}^{(0)*}(\tau)\phi_{i\mu}^{(0)}(\tau)\phi_{j\nu}^{(0)*}(\eta)\phi_{j\nu}^{(0)}(\eta)\right. \\ &\quad \left. + \langle b_{i\mu}^*(\tau) b_{j\nu}(\eta)\rangle_{(0)}\langle b_{j\nu}^*(\eta) b_{i\mu}(\eta)\rangle_{(0)} + \langle b_{i\mu}^*(\tau) b_{j\nu}^*(\eta)\rangle_{(0)}\langle b_{j\nu}(\eta) b_{i\mu}(\eta)\rangle_{(0)}\right) \end{aligned} \tag{A.11}$$

These terms imply that an extended impurity system is required, in comparison to (4.17), for a proper representation of the impurity action.

## A.2 Green's functions

Another part of the DMFT-loop, where a Hartree-Fock type treatment demands a generalization, is at the level of the connected interacting lattice Green's functions. For this derivation we follow Lü et al.[LPS14], where the derivation is presented for purely local interactions (and without anomalous terms). Let us start by considering the corresponding Dyson's equation.

$$\mathbf{G}_{i_1,i_2}(\tau_1-\tau_2) \equiv \mathbf{G}(x_1,x_2) = \mathbf{G}_0(x_1,x_2) + \oint\!\!\!\!\!\!\int \mathbf{G}_0(x_1,x_n)\mathbf{\Sigma}(x_n,x_m)\mathbf{G}(x_m,x_2)dx_n dx_m \tag{A.12}$$

Here we use a combined notation by defining $x_n = (l_n,\tau_n)$, where $l_n$ is the position in the lattice and $\tau_n$ is the imaginary time. The Green's matrices on the other hand are $2\times 2$ matrices corresponding to the Nambu notation as introduced in (4.14). Furthermore the interaction picture is used in this derivation, where for our purposes the non-interacting part of the original Hamiltonian (e.g. (4.1)) is considered to consist of all local terms (including the interacting ones) as well as all non-interacting non-local terms (i.e. the hopping terms).

$$H_{\mathrm{I}} = H_{\mathrm{vdW}} \longrightarrow H_0 = H - H_{\mathrm{I}} \tag{A.13}$$

Thus the operators in the interaction picture are given as follows.

$$\hat{b}(\tau) = \exp(\tau\hat{H}_0)\hat{b}\exp(-\tau\hat{H}_0) \quad \hat{b}^\dagger(\tau) = \exp(\tau\hat{H}_0)\hat{b}^\dagger\exp(-\tau\hat{H}_0) \quad \tau\in[-\beta,\beta] \tag{A.14}$$

In this representation, the normal connected interacting Green's function of the Rydberg (dressed) states in a periodic lattice system has the following form.

$$\mathbf{G}_{11}^{ij} = -\left\langle \mathcal{T}\left\{\hat{b}(x_i)\hat{b}^\dagger(x_j)\exp\left(-\int_0^\beta d\tau H_{\mathrm{I}}(\tau)\right)\right\}\right\rangle_C \tag{A.15}$$

This expression can be evaluated by expanding the exponential up to first order in the interaction term.

$$\mathbf{G}_{11}^{ij} = -\left\langle \mathcal{T}\left\{ \hat{b}(x_i)\hat{b}^\dagger(x_j)\left(1 - \sum_{n,m}\frac{V_{nm}}{2}\iint \hat{b}^\dagger(x_n)\hat{b}(x_n)\hat{b}^\dagger(x_m)\hat{b}(x_m)\delta(\tau_n-\tau_m)d\tau_n d\tau_m\right)\right\}\right\rangle_C \tag{A.16}$$

Note that $x_n = (n, \tau_n)$ and $x_m = (m, \tau_m)$ share the same time $\tau_n = \tau_m$ due to the instantaneous nature of the interaction (also because the original Hamiltonian is time independent). This expression is further simplified by evaluating the four possible contractions for each of the external fields with any of the fields which are integrated over. Contractions involving connected Green's function beyond two-point correlators are neglected as we want to implement this expansion in a DMFT-loop where only two-point Green's functions are considered.

$$\begin{aligned}
&\left\langle \mathcal{T}\left\{\hat{b}(x_i)\hat{b}^\dagger(x_j)\hat{b}^\dagger(x_n)\hat{b}(x_n)\hat{b}^\dagger(x_m)\hat{b}(x_m)\right\}\right\rangle_C \\
=&\langle \mathcal{T}\{\hat{b}(x_i)\hat{b}^\dagger(x_n)\}\rangle_C\left[\langle \mathcal{T}\{\hat{b}(x_n)\hat{b}^\dagger(x_j)\}\rangle_C\langle \mathcal{T}\{\hat{b}^\dagger(x_m)\hat{b}(x_m)\}\rangle_C\right. \\
&\left.+\langle \mathcal{T}\{\hat{b}(x_n)\hat{b}(x_m)\}\rangle_C\langle \mathcal{T}\{\hat{b}^\dagger(x_m)\hat{b}^\dagger(x_j)\}\rangle_C + \langle \mathcal{T}\{\hat{b}(x_n)\hat{b}^\dagger(x_m)\}\rangle_C\langle \mathcal{T}\{\hat{b}(x_m)\hat{b}^\dagger(x_j)\}\rangle_C\right] \\
&+\langle \mathcal{T}\{\hat{b}(x_i)\hat{b}(x_n)\}\rangle_C\left[\langle \mathcal{T}\{\hat{b}^\dagger(x_n)\hat{b}^\dagger(x_j)\}\rangle_C\langle \mathcal{T}\{\hat{b}^\dagger(x_m)\hat{b}(x_m)\}\rangle_C\right. \\
&\left.+\langle \mathcal{T}\{\hat{b}^\dagger(x_n)\hat{b}(x_m)\}\rangle_C\langle \mathcal{T}\{\hat{b}^\dagger(x_m)\hat{b}^\dagger(x_j)\}\rangle_C + \langle \mathcal{T}\{\hat{b}^\dagger(x_n)\hat{b}^\dagger(x_m)\}\rangle_C\langle \mathcal{T}\{\hat{b}(x_m)\hat{b}^\dagger(x_j)\}\rangle_C\right] \\
&+\langle \mathcal{T}\{\hat{b}(x_i)\hat{b}^\dagger(x_n)\}\rangle_C\left[n \longleftrightarrow m\right] + \langle \mathcal{T}\{\hat{b}(x_i)\hat{b}(x_m)\}\rangle_C\left[n \longleftrightarrow m\right]
\end{aligned} \tag{A.17}$$

By definition the connected bare lattice Green's functions (for the interacting component) are given as follows.

$$\mathbf{G}_0^{ij}(\tau) = \begin{pmatrix} -\left\langle \mathcal{T}\{\hat{b}(x_i)\hat{b}^\dagger(x_j)\}\right\rangle_C & -\left\langle \mathcal{T}\{\hat{b}(x_i)\hat{b}(x_j)\}\right\rangle_C \\ -\left\langle \mathcal{T}\{\hat{b}^\dagger(x_i)\hat{b}^\dagger(x_j)\}\right\rangle_C & -\left\langle \mathcal{T}\{\hat{b}^\dagger(x_i)\hat{b}(x_j)\}\right\rangle_C \end{pmatrix} \tag{A.18}$$

Inserting the definitions (A.18) into (A.17) yields a simplified form of the Hartree-Fock expansion terms.

$$\begin{aligned}
\mathbf{G}_{11}^{ij} = \mathbf{G}_{11,0}^{ij} - \sum_{n,m}\frac{V_{nm}}{2}\iint \Big(&\mathbf{G}_{11,0}^{in}\left[\mathbf{G}_{11,0}^{nj}\mathbf{G}_{22,0}^{mm} + \mathbf{G}_{12,0}^{nm}\mathbf{G}_{21,0}^{mj} + \mathbf{G}_{11,0}^{nm}\mathbf{G}_{11,0}^{mj}\right] \\
&+ \mathbf{G}_{12,0}^{in}\left[\mathbf{G}_{21,0}^{nj}\mathbf{G}_{22,0}^{mm} + \mathbf{G}_{22,0}^{nm}\mathbf{G}_{21,0}^{mj} + \mathbf{G}_{21,0}^{nm}\mathbf{G}_{11,0}^{mj}\right] \\
&+ \mathbf{G}_{11,0}^{im}\left[n \longleftrightarrow m\right] \\
&+ \mathbf{G}_{12,0}^{im}\left[n \longleftrightarrow m\right]\Big)\delta(\tau_n-\tau_m)d\tau_n d\tau_m
\end{aligned} \tag{A.19}$$

These terms can be reordered so one obtains two seperate expressions, where one can be identified as the Hartree term while the other is the Fock term.

$$\mathbf{G}^{ij}_{11} = \mathbf{G}^{ij}_{11,0} - \iint \sum_{n,m} V_{nm} \underbrace{\mathbf{G}^{mm}_{22,0}}_{=-n_0(m)} \left[\mathbf{G}^{in}_{11,0}\mathbf{G}^{nj}_{11,0} + \mathbf{G}^{in}_{12,0}\mathbf{G}^{nj}_{21,0}\right] \delta(\tau_n - \tau_m) d\tau_n d\tau_m$$
$$- \iint \sum_{n,m} V_{nm} \sum_{\alpha,\alpha'} \mathbf{G}^{in}_{1\alpha,0}\mathbf{G}^{nm}_{\alpha\alpha',0}\mathbf{G}^{mj}_{\alpha'1,0} \delta(\tau_n - \tau_m) d\tau_n d\tau_m \tag{A.20}$$

Here $n_0(m)$ is the non-interacting occupation number at site $m$. Similar derivations yield the remaining elements of the Nambu of Green's functions [2]. By comparison with the Dyson equation (A.12), we can fianlly extract the (one-loop) contribution to the self-energy.

$$\mathbf{\Sigma}^{nm}_{\mathrm{HF},0}(\tau_n - \tau_m) = \underbrace{\delta(\tau_n - \tau_m)\delta_{n,m}\mathbb{1}_2 \sum_j n_0(j) V_{nj}}_{\text{Hartree}} \underbrace{- \delta(\tau_n - \tau_m)\mathbf{G}^{nm}_0(\tau_n - \tau_m) V_{nm}}_{\text{Fock}} \tag{A.21}$$

The last term is readily included in RB-DMFT via the self-energy of the local Anderson impurity models, as it is included there in the form of a local shift in the chemical potential for the excited states. *But* in the RB-DMFT loop, the occupation number is calculated in the effective Anderson impurity model, which already includes interaction effects, thus the interacting occupation number $n$ has to be used in place of the non-interacting $n_0$. One should therefore also use the interacting Green's function when computing the second term (the Fock term), in order to compute the lattice Green's function on equal footing, when using the irreducible self-energy $\mathbf{\Sigma}$. This way the complete Hartree-Fock limit can be obtained. As both contributions are diagonal in $\tau$, the transformation to Matsubara frequencies is straightforward and the Hartree-Fock terms of the self-energy are as follows.

$$\mathbf{\Sigma}^{nm}_{\mathrm{HF}}(i\omega_n) = \int_0^\beta d\tau e^{i\omega_n\tau}\mathbf{\Sigma}^{nm}(\tau) = \underbrace{\delta_{n,m}\sum_j n(j)V_{nj}}_{\text{Hartree}} \underbrace{- \mathbf{G}^{nm}(\tau = 0)V_{nm}}_{\text{Fock}} \tag{A.22}$$

We further note that this form demands knowledge of the instantaneous and off-diagonal terms $\mathbf{G}^{nm}(0) = -\lim_{\epsilon\to 0^-}\mathbf{G}^{nm}(\epsilon) = -\frac{1}{\beta}\lim_{\epsilon\to 0^+}\sum_n \exp(i\omega_n\epsilon)\mathbf{G}^{nm}(i\omega_n)$. For methods realizing the DMFT self-consistency on the imaginary axis this implies the need for analytic continuation in order to obtain the Fock terms. That is especially noteworthy, as the kinetic energy trick (4.112) as used for (4.111) cannot be used here to circumvent the need to calculate $\mathbf{G}^{nm}(\tau = 0)$.

[2] $\mathbf{G}^{ij}_{12}$ is the only missing independent element, due to the well known symmetries for a time independent Hamiltonian. It can also be obtained from (A.20) by replacing each appearence $\mathbf{G}^{xj}_{y1,0} \to \mathbf{G}^{xj}_{y2,0}$

# Appendix B

# Coordination number scaling of the long-range interaction

In Sec. 4.1, when discussing the DMFT cavity action, we introduce a scaling of the long-range interaction using $z_{\text{eff}} \equiv \sum_{i\neq 0} V(i)/\max_{i\neq 0}(V(i))$ as an effective coordination number, on which we impose for any $|\mathbf{r}_i - \mathbf{r}_0| \gg R_c/a$ (where $R_c > 0$ is some finite length scale in units of the lattice spacing, e.g. the length scale of the dressed soft-core potential) such that $V(\mathbf{r}) \propto |\mathbf{r}|^{-(d+\epsilon)}$ with fixed $\epsilon > 0$ for a given dimension $d$ of the system, as this always guarantees a convergent and thus finite $z_{\text{eff}}$.

In order to investigate the dimensional scaling of $z_{\text{eff}}$, let us first consider the required summation for a given dimension $d$. To do so we define $\max_{i\neq 0}(V(i)) = V_{\max}$ and introduce a $d$-dimensional vector $\boldsymbol{\ell}$ for each of the sites of a hypercubic lattice, while the corresponding spatial vectors are given as $a\boldsymbol{\ell}$, where $a$ is the lattice spacing. As we are only counting the number of neighboring site weighted by relative interaction strength, we can simply disregard energy and length scale units:

$$z_{\text{eff}} = \sum_{i\neq 0} V_\sigma(i)/\max_{i\neq 0}(V_\sigma(i)) = \frac{1}{V_{\max}} \sum_{\boldsymbol{\ell}\neq 0} V\left(|\boldsymbol{\ell}|\right). \tag{B.1}$$

For high dimensional systems, this summation becomes increasingly hard to compute numerically. Therefore we try to focus on the dominant summation terms. Let us start by considering the general form of

$$\boldsymbol{\ell} = (\ell_1, \ldots, \ell_d). \tag{B.2}$$

Due to the isotropic nature of the interactions in the main part, we may restrict the summation without loss of generality to those $\boldsymbol{\ell}$, which have their entries sorted starting from the largest value, while we also only consider values $\ell_n \geq 0$ for $n > 1$ and $\ell_1 > 0$:

$$0 < \ell_1 \geq \ell_2 \geq \ldots \geq \ell_{d-1} \geq \ell_d \geq 0 \quad \rightarrow \quad \sum_i \ell_i > 0. \tag{B.3}$$

In that case we have to consider a multiplicative factor for each summation term considered. Due to the possible binary choice of the sign for any nonzero element there is a factor of $2^M$, where $M = \sum_i \theta(\ell_i - 0.5)$. Furthermore any nonzero element may appear multiple times. Therefore we define $\eta_\ell$ as the number of times a given integer $\ell$ appears in a vector $\boldsymbol{\ell}$, so each $\eta_\ell \geq 0$, while at least one is nonzero. Thus, noting that there is no sign choice for zero, we have another way to write the exponent

$$M = \sum_{\ell=1}^{\infty} \eta_\ell. \tag{B.4}$$

The number of ways one can distribute the various (multiple) integers within a given vector $\boldsymbol{\ell}$ is given as the multinomial

$$\frac{d!}{\prod_{\ell=1}^{\infty} \eta_\ell!(d-M)!}. \tag{B.5}$$

The norm of each of these vectors has the value

$$|\boldsymbol{\ell}| = \sqrt{\sum_{\ell=1}^{\infty} \eta_\ell \ell^2}. \tag{B.6}$$

Combining all these expressions we obtain an optimized summation for $z_{\text{eff}}$, as

$$z_{\text{eff}}(d) = \frac{1}{V_{\max}} \sum_{\{\eta_\ell\}\neq\{0\}}^{d} 2^{\sum_{\ell=1}^{\infty}\eta_\ell} \frac{d!}{\prod_{\ell=1}^{\infty} \eta_\ell!(d-M)!} V\left(\sqrt{\sum_{\ell=1}^{\infty} \eta_\ell \ell^2}\right). \tag{B.7}$$

Note that we exclude the case where all $\eta_\ell$ are zero, as this corresponds to a local interaction, which we do not consider in the scaling of the coordination number. In practice we can limit the set $\{\eta_\ell\}$ (especially when considering a numerical calculation), using only a finite set $\{\eta_1, \ldots, \eta_{\ell_m}\}$. The choice of $\ell_m$ depends on the convergence behavior of the sum, which depends on the tail of the interaction, thus $\ell_m$ can typically be taken to be small for large $\epsilon$. A similar consideration is also possible for the multiplicities $\eta_\ell$, particularly considering that each $\eta_\ell \leq d$ in any case. Thus convergence with regard to a given $\eta_\ell$ can easily be inferred. For any $\eta_\ell$ one simply increases its value step by step up to $\eta_\ell^m$, keeping all previous $\eta_{\ell'}^m$ with $\ell' < \ell$ fixed, until the additional summed contributions converge. This procedure is exemplified in Fig. B.1

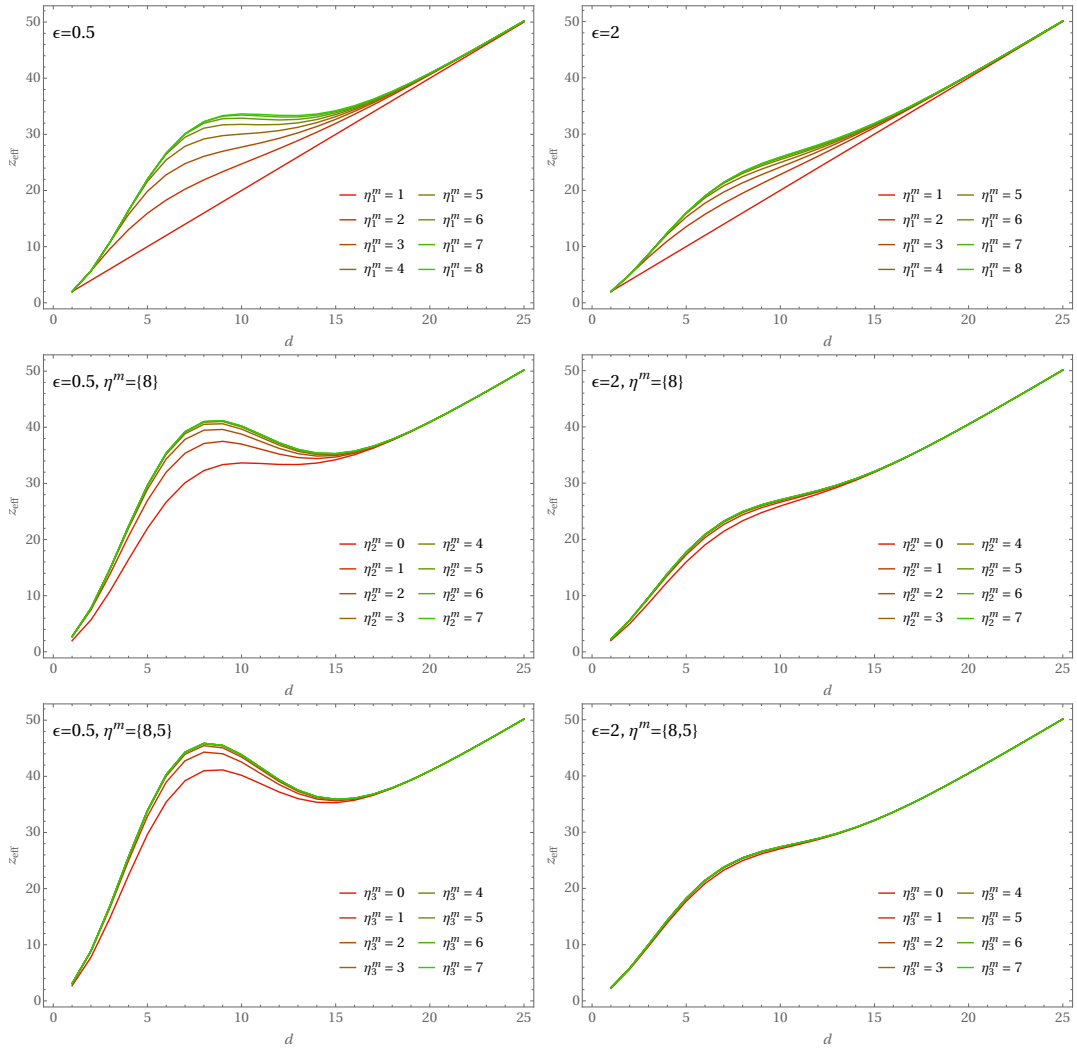


FIGURE B.1: Convergence behavior of the partial sums of $z_{\text{eff}}(d)$ for a bare power law interaction potential (B.8) for two distinct values of $\epsilon = (0.5, 2)$ up to a maximally considered $\ell_m$, which is increased from 1 to 3 (*top* to *bottom*), while in each case a comparison is made for increasing maximum multiplicities $\eta_\ell^m$, for the value of $\ell_m$ considered. The denoted arrays specify the values $\eta_\ell^m$ for $\ell < \ell_m$ used in each graph, corresponding to values where all lower orders are considered as converged.

## B.1 Power law potential

Let us now consider the case of a power law potential, for example the van der Waals potential as in the main part of this thesis, where we have simulated a two-dimensional square lattice system (so $d = 2$). In that case we would have $\epsilon = 4$. This case can be compared to others with reduced power laws, such as dipole-dipole interactions for example. For any of those cases let us consider the following simple interaction potential $V(r)$, where $r = |\boldsymbol{\ell}|$:

$$V(r) = \frac{1}{r^{d+\epsilon}}. \tag{B.8}$$

Here $d$ is the dimension of the considered system while $\epsilon$ is determined by the actual interaction, so $\epsilon = 1$, for example, corresponds to isotropic dipole-dipole interactions in a two-dimensional system.

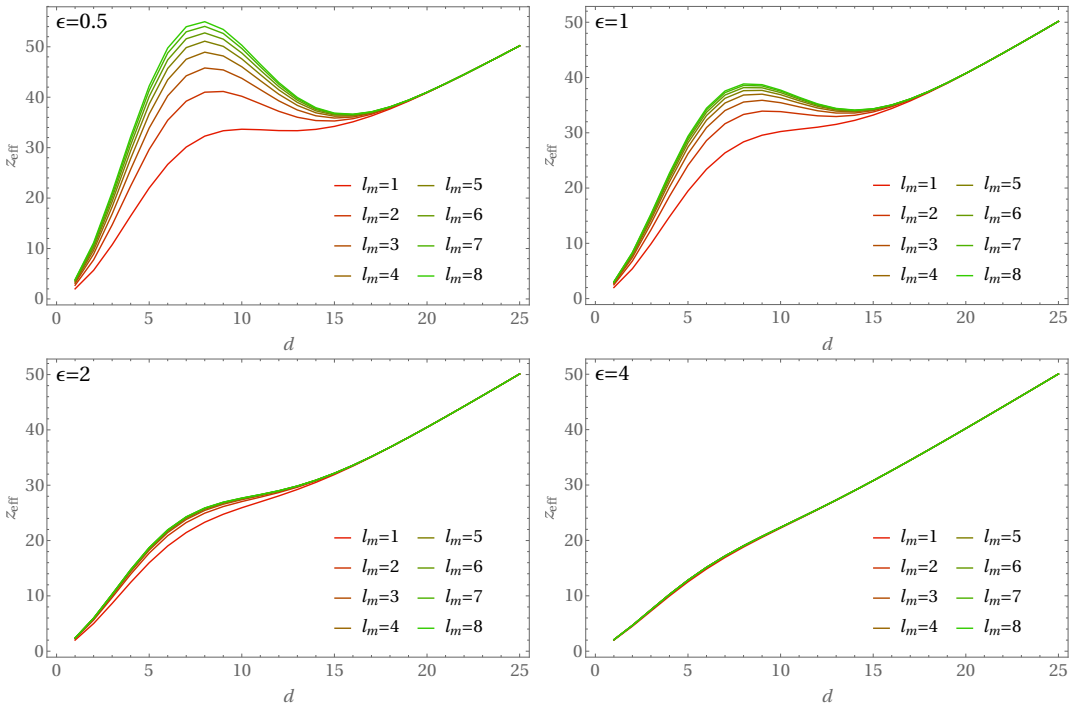


FIGURE B.2: Convergence behavior of $z_{\text{eff}}(d)$ for increasing values of $\ell_m$ up to 8 sites. Various cases for the power law scaling of the interaction are considered via the choice of $\epsilon$ as specified in each graph. The case $\epsilon = 1$ e.g. corresponds to dipolar interactions in a two-dimensional lattice, while the case $\epsilon = 4$ corresponds to van der Waals interactions in a two-dimensional system. In each graph the greatest multiplicities of each $\ell$ are set to the following values: $\eta^m = \{8, 5, 3, 3, 2, 2, 2, 1\}$

As can be seen in Fig. B.2, the long-range interaction unsuprisingly is dominated by nearest neighbours for power laws with $\epsilon > 1$, which follows from the almost linear dependence of $z_{\text{eff}}(d)$ on the dimension $d$ in that case. For the cases $\epsilon \approx 1$ and $\epsilon < 1$ on the other hand there is a strong increase of $z_{\text{eff}}(d)$ for $d < 8$ far beyond a simple linear increase. Note that the behavior of $z_{\text{eff}}(d)$ always becomes linear for large dimensions, even for $\epsilon < 1$. This behavior should remain for all $\epsilon > 0$ and clearly signifies that only nearest neighbors matter in the infinite dimensional limit, for which mean-field descriptions become exact.

## B.2 Rydberg dressed potential

For far red-detuned Rydberg dressed atoms with repulsive van der Waals interactions, one has to consider a dressed interaction potential (2.14) of the form

$$V(r) = \frac{R_c^{d+\epsilon} + 1}{R_c^{d+\epsilon} + r^{d+\epsilon}}, \tag{B.9}$$

which we already normalized to its largest value. As our focus is on two-dimensional systems in this thesis, we consider $d = 2$ and $\epsilon = 4$ here. Due to the plateau shape of the interaction, within its soft-core range $R_c$, we expect a strong increase in $z_{\text{eff}}(d)$

when compared to the bare interaction, which indeed we find for dimensions $d \lesssim 20$ for the considered values of $R_c$. Note that we still observe a return back to the linear (mean-field type) behavior for even higher dimensions.

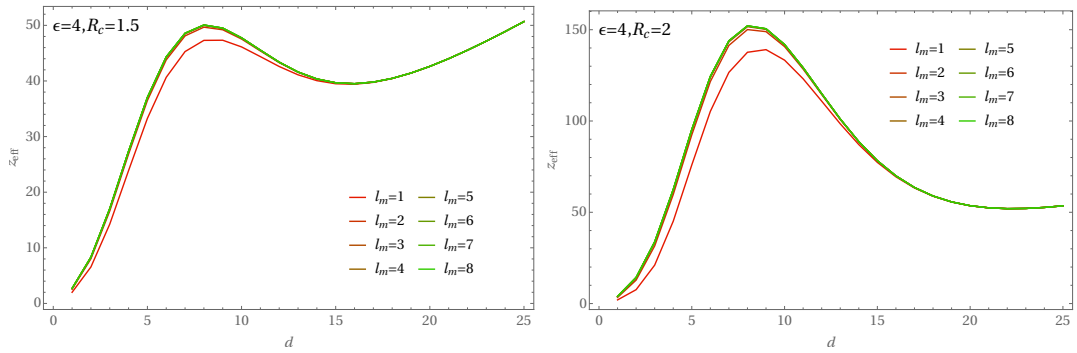


FIGURE B.3: Convergence behaviour of $z_{\text{eff}}(d)$ for increasing values of $\ell_m$ up to 8 sites. Two different cases of the soft-core radius are considered, with $R_c = 1.5$ and $R_c = 2$, while the long-range tail decays as a power law in $d+\epsilon$, $V(r) =\propto 1/r^{d+\epsilon}$. We consider the long-range soft-core interaction, as induced via weak Rydberg dressing of the ground state, which has a $1/r^6$ behavior, so $\epsilon = 4$ in a two-dimensional system. In each graph the greatest multiplicities of each $\ell$ are set to the following values: $\{\eta^m\} = \{8, 3, 2, 1, 1, 1, 1, 1\}$

## B.3 Conclusion

On the one hand, we can conclude that the use of an effective coordination number $z_{\text{eff}}$ for the long-range interaction terms in DMFT is well defined for any dimension and depends linearly on the dimension in the limit of large dimensions, just in the same way as the regular number of nearest neighbors. However on the other hand, $z_{\text{eff}}$ grows much faster then linearly in low dimensional systems, for certain types of interactions which we investigate in the main part of this thesis. This implies an increased accuracy for mean-field methods (both static and dynamic) and mean-field approximations, for example the Hartree decoupling used in both DMFT and the quasiparticle scheme.

We furthermore note that the obtained values for $z_{\text{eff}}$ can be considered as a lower bound in the context of the near-resonant Rydberg excitation discussed in Chap. 8. This is due to an interaction induced mean-field red-shift of the detuning of the Rabi process in the vicinity of Rydberg dressed atoms, which is a realization of the Rydberg blockade effect. As a result the interaction energy is vastly reduced for nearest neighbors, which can be interpreted as a reduced $V_{\text{max}}$ and thus an increased $z_{\text{eff}}$, implying a correspondingly increased validity of mean-field approximations for the long-range interaction.

# Appendix C

# Third and fourth order terms of the fluctuation expansion

In Sec. 6.1.3 the Gutzwiller fluctuation expansion of a multicomponent extended Bose-Hubbard model with long-range interactions is introduced. The so far neglected third order term is given by

$$\begin{aligned}
\mathcal{H}^{(3)} = &- \sum_{\sigma,\langle \ell,\ell'\rangle} t_\sigma \sum_{i_1,i_2,i_3>0} \Big[ \tilde{F}^{\sigma,(\ell,\ell')}_{0,i_1,i_2,i_3} {\sigma^{(i_1)}_{\ell'}}^\dagger \sigma^{(i_2)}_{\ell} \sigma^{(i_3)}_{\ell'} + \tilde{F}^{\sigma,(\ell,\ell')}_{i_1,0,i_2,i_3} {\sigma^{(i_1)}_{\ell}}^\dagger \sigma^{(i_2)}_{\ell} \sigma^{(i_3)}_{\ell'} \\
&+ \tilde{F}^{\sigma,(\ell,\ell')}_{i_1,i_2,0,i_3} {\sigma^{(i_1)}_{\ell}}^\dagger {\sigma^{(i_2)}_{\ell'}}^\dagger \sigma^{(i_3)}_{\ell'} + \tilde{F}^{\sigma,(\ell,\ell')}_{i_1,i_2,i_3,0} {\sigma^{(i_1)}_{\ell}}^\dagger {\sigma^{(i_2)}_{\ell'}}^\dagger \sigma^{(i_3)}_{\ell} \Big] \\
&+ \frac{1}{2} \sum_{\ell} \sum_{\delta\ell\neq 0} V(\mathbf{r}_\ell, \mathbf{r}_{\delta\ell}) \sum_{i_1,i_2,i_3>0} \Big[ \tilde{N}^{\sigma,(\ell)}_{0,i_1} \tilde{N}^{\sigma,(\ell'=\ell+\delta\ell)}_{i_2,i_3} {\sigma^{(i_2)}_{\ell'}}^\dagger \sigma^{(i_1)}_{\ell} \sigma^{(i_3)}_{\ell'} \\
&+ \tilde{N}^{\sigma,(\ell)}_{i_1,i_2} \tilde{N}^{\sigma,(\ell')}_{0,i_3} {\sigma^{(i_1)}_{\ell}}^\dagger \sigma^{(i_2)}_{\ell} \sigma^{(i_3)}_{\ell'} + \tilde{N}^{\sigma,(\ell)}_{i_1,0} \tilde{N}^{\sigma,(\ell')}_{i_2,i_3} {\sigma^{(i_1)}_{\ell}}^\dagger {\sigma^{(i_2)}_{\ell'}}^\dagger \sigma^{(i_3)}_{\ell'} \\
&+ \tilde{N}^{\sigma,(\ell)}_{i_1,i_2} \tilde{N}^{\sigma,(\ell')}_{i_3,0} {\sigma^{(i_1)}_{\ell}}^\dagger {\sigma^{(i_3)}_{\ell'}}^\dagger \sigma^{(i_2)}_{\ell} \Big],
\end{aligned} \tag{C.1}$$

while the fourth order term has the form

$$\begin{aligned}
\mathcal{H}^{(4)} = &- \sum_{\sigma,\langle \ell,\ell'\rangle} t_\sigma \sum_{\substack{i_1,i_2>0 \\ j_1,j_2>0}} \tilde{F}^{\sigma,(\ell,\ell')}_{i_1,i_2,j_1,j_2} |i_1\rangle_{\ell\,\ell}\langle j_1| \otimes |i_2\rangle_{\ell'\,\ell'}\langle j_2| \\
&+ \frac{1}{2} \sum_{\ell} \sum_{\delta\ell\neq 0} V(\mathbf{r}_\ell, \mathbf{r}_{\delta\ell}) \sum_{\substack{i_1,i_2>0 \\ j_1,j_2>0}} \tilde{N}^{\sigma,(\ell)}_{i_1,j_1} \tilde{N}^{\sigma,(\ell+\delta\ell)}_{i_2,j_2} |i_1\rangle_{\ell\,\ell}\langle j_1| \otimes |i_2\rangle_{\ell'\,\ell'}\langle j_2| \\
= &- \sum_{\sigma,\langle \ell,\ell'\rangle} t_\sigma \sum_{\substack{i_1,i_2>0 \\ j_1,j_2>0}} \tilde{F}^{\sigma,(\ell,\ell')}_{i_1,i_2,j_1,j_2} {\sigma^{(i_1)}_{\ell}}^\dagger {\sigma^{(i_2)}_{\ell'}}^\dagger \sigma^{(j_1)}_{\ell} \sigma^{(j_2)}_{\ell'} \\
&+ \frac{V}{2} \sum_{\ell} \sum_{\delta\ell\neq 0} V(\mathbf{r}_\ell, \mathbf{r}_{\delta\ell}) \sum_{\substack{i_1,i_2>0 \\ j_1,j_2>0}} \tilde{N}^{\sigma,(\ell)}_{i_1,j_1} \tilde{N}^{\sigma,(\ell+\delta\ell)}_{i_2,j_2} {\sigma^{(i_1)}_{\ell}}^\dagger {\sigma^{(i_2)}_{\ell'}}^\dagger \sigma^{(j_1)}_{\ell} \sigma^{(j_2)}_{\ell'}.
\end{aligned} \tag{C.2}$$

As mentioned in the the main text, they lead to a finite lifetime of quasiparticles as they introduce non-numberconserving and interacting terms.

# Appendix D

# Approximations in RB-DMFT

In Chap. 8 certain approximations are made with regard to the Rydberg state tunneling, which was set to zero, and the truncation used for the bosonic Fock-basis, which was set to $N_c = 4$ in the context of the coherent-tail state truncation procedure introduced in Chap. 5. Let us therefore briefly discuss the validity of these two approximations.

## D.1 Influence of Rydberg hopping

To probe our assumption, that we can limit itinerant behavior to the $|g\rangle$ component, namely, by setting $\eta = 0$, we compare the results discussed in Sec. 8.2.1 to selected simulations with $\eta = 1$. As can be seen in the comparison of the average Rydberg fraction $\bar{n}_e$, shown in Fig. D.1, hopping of Rydberg states has only a minor influence on the phases observed in Chap. 8. It primarily leads to changes in parameter regions, where given phases are almost degenerate. This can be seen as one of the four-site-unit-cells vanishes for the chosen parameters, leading to one less step in Figs. D.1(c) and D.1(d). Otherwise, there are only small deformations of the boundaries.

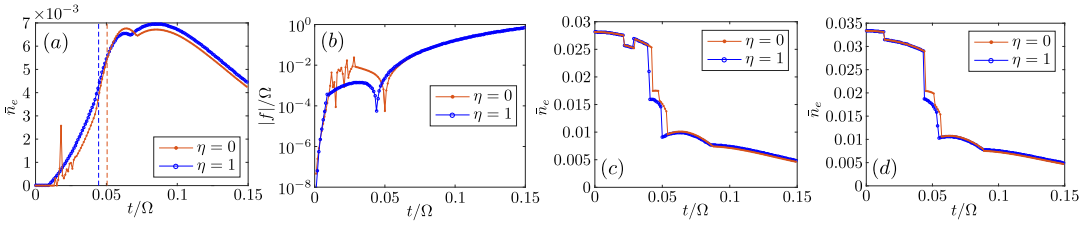


FIGURE D.1: $(a)$, $(c)$ and $(d)$ depict averaged Rydberg-state occupation numbers $n_e = \bar{n}_e$ of (mostly) converged RB-DMFT simulations for parameters as given in Fig. 8.6, except for $\eta$, which is given in the legend, with $(a)$ $\Delta/\Omega = -1$, $(c)$ $-0.415$, and $(d)$ $-0.303$. The dashed lines in $(a)$ mark $J_c/\Omega$ where $f$ changes sign, so results at low $J/\Omega$ have a higher energy as the vacuum state $|n^g = 0, n^e = 0\rangle$. $(b)$ The position of the sign change corresponds to a kink in the logarithmic plot $|f|$.

## D.2 Coherent-tail state truncation

In order to benchmark the choice of the Fock-space truncation, where we used a soft cutoff scheme, which replaces the highest Fock-state $N_c$ by the **coherent-tail** state $\propto \sum_{n=N_c}^{\infty} \frac{\alpha^n}{\sqrt{n}}$ introduced in Chap. 5, we probe the influence of a changed truncation, as given by a variation of $N_c$, on the observables and especially on the lattice-averaged grand-canonical potential $f$. We do this in a parameter region where the largest deviations are expected. As the lattice filling increases above 3 atoms per site, which is close to the used cutoff $N_c = 4$, for small $\Delta$ and large hopping [see Fig. 8.9(a)], we chose $\Delta/\Omega = -0.8$ and $J/\Omega > 0.05$ for the benchmark. Figs. D.2(a)-(c) depict the observables $\bar{\phi}_e, \bar{n}_e$ and $\overline{\langle \hat{b}_g^\dagger \hat{b}_e \rangle}$, which have the largest deviations. As can be seen, changing $N_c$ from 4 (used for all the main results) to 5 barely has any influence on these observables. The most pronounced changes appear for $J/\Omega > 0.1$, with only minor numerical changes in the values of the observables, while the transition SF $\leftrightarrow$ CB-SS is shifted only very slightly. This can be seen from the kink in $\bar{n}_e$, as shown in Fig. D.2(b) and its inset. $f$ also experiences only minor deviations, which have a maximum around $J/\Omega \approx 1.3$, as shown in the inset of Fig. D.2(d). We therefore conclude that our results can be considered as converged with respect to the Fock-space cutoff.

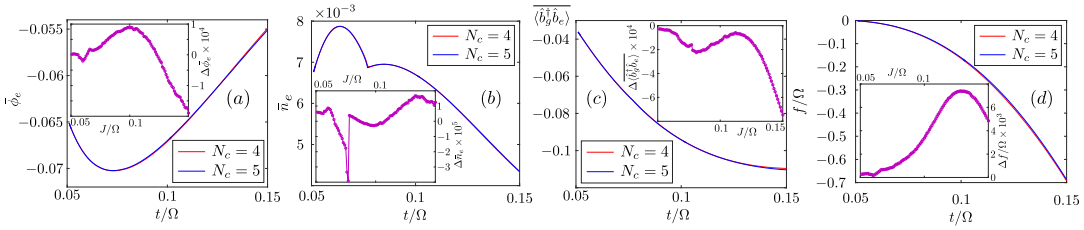


FIGURE D.2: The lattice averaged observables $(a)$ $\bar{\phi}_e$, $(b)$ $\bar{n}_e$, and $(c)$ $\overline{\langle \hat{b}_g^\dagger \hat{b}_e \rangle}$ as functions of $J/\Omega$ for $\Delta/\Omega = -0.8$, with the remaining parameters as in Fig. 8.6 and with a truncation scheme as given in the legends. $(d)$ The lattice-averaged grand-canonical potential $f$. All the insets depict each deviation for the two truncation schemes, $N_c = 5$ and $N_c = 4$ (the latter subtracted from the former).

# Bibliography


[ADL04] Ehud Altman, Eugene Demler, and Mikhail D. Lukin. "Probing many-body states of ultracold atoms via noise correlations". In: *Physical Review A* 70.1 (2004), p. 013603. ISSN: 1050-2947. DOI: 10.1103/PhysRevA.70.013603.

[AKL11] Enrico Arrigoni, Michael Knap, and Wolfgang von der Linden. "Extended self-energy functional approach for strongly correlated lattice bosons in the superfluid phase". In: *Physical Review B* 84.1 (2011), p. 014535. ISSN: 1098-0121. DOI: 10.1103/PhysRevB.84.014535.

[AL69] A.F. Andreev and I.M. Lifshitz. "Quantum Theory of Defects in Crystals". In: *Journal of Experimental and Theoretical Physics* 29.6 (1969), pp. 1107–1113.

[AM38] J. F. Allen and A. D. Misner. "Flow of Liquid Helium II". In: *Nature* 141.3558 (1938), pp. 75–75. ISSN: 0028-0836. DOI: 10.1038/141075a0.

[Ama+16] J. A. Aman et al. "Trap losses induced by near-resonant Rydberg dressing of cold atomic gases". In: *Physical Review A* 93.4 (2016), p. 043425. ISSN: 2469-9926. DOI: 10.1103/PhysRevA.93.043425.

[AMS04] Ian J. R. Aitchison, David A. MacManus, and Thomas M. Snyder. "Understanding Heisenberg's "magical paper" of July 1925: A new look at the calculational details". In: *American Journal of Physics* 72.11 (2004), pp. 1370–1379. ISSN: 0002-9505. DOI: 10.1119/1.1775243.

[And+10] Peter Anders et al. "Dynamical Mean Field Solution of the Bose-Hubbard Model". In: *Physical Review Letters* 105.9 (2010), p. 096402. ISSN: 0031-9007. DOI: 10.1103/PhysRevLett.105.096402.

[And+11] Peter Anders et al. "Dynamical mean-field theory for bosons". In: *New Journal of Physics* 13.7 (2011), p. 075013. ISSN: 1367-2630. DOI: 10.1088/1367-2630/13/7/075013.

[And+95] M H Anderson et al. "Observation of bose-einstein condensation in a dilute atomic vapor". In: *Science (New York, N.Y.)* 269.5221 (1995), pp. 198–201. ISSN: 0036-8075. DOI: 10.1126/science.269.5221.198.

[AS10] Alexander. Altland and Ben D. Simons. *Condensed Matter Field Theory*. Cambridge University Press, 2010, p. 786. ISBN: 0521769752.

[Bai+16] S Baier et al. "Extended Bose-Hubbard models with ultracold magnetic atoms." In: *Science (New York, N.Y.)* 352.6282 (2016), pp. 201–5. ISSN: 1095-9203. DOI: 10.1126/science.aac9812.

[Bak+09] Waseem S. Bakr et al. "A quantum gas microscope for detecting single atoms in a Hubbard-regime optical lattice". In: *Nature* 462.7269 (2009), pp. 74–77. ISSN: 0028-0836. DOI: 10.1038/nature08482.

[Bal+14] Jonathan B. Balewski et al. "Rydberg dressing: understanding of collective many-body effects and implications for experiments". In: *New Journal of Physics* 16.6 (2014), p. 063012. ISSN: 1367-2630. DOI: 10.1088/1367-2630/16/6/063012. arXiv: 1312.6346.

[Bal07] Sébastien Balibar. "The Discovery of Superfluidity". In: *Journal of Low Temperature Physics* 146.5-6 (2007), pp. 441–470. ISSN: 0022-2291. DOI: 10.1007/s10909-006-9276-7.

[Bar+12] M A Baranov et al. "Condensed matter theory of dipolar quantum gases." In: *Chemical reviews* 112.9 (2012), pp. 5012–61. ISSN: 1520-6890.

[BB11] Adam Bühler and Hans Peter Büchler. "Supersolid phase in atomic gases with magnetic dipole interaction". In: *Physical Review A* 84.2 (2011), p. 023607. ISSN: 1050-2947. DOI: 10.1103/PhysRevA.84.023607.

[BB82] Per Bak and R. Bruinsma. "One-Dimensional Ising Model and the Complete Devil's Staircase". In: *Physical Review Letters* 49.4 (1982), pp. 249–251. ISSN: 0031-9007. DOI: 10.1103/PhysRevLett.49.249.

[BBH14] Ulf Bissbort, Michael Buchhold, and Walter Hofstetter. "Quasi-Particle Theory for the Higgs Amplitude Mode". In: (2014). arXiv: 1401.4466.

[BCS57] J. Bardeen, L. N. Cooper, and J. R. Schrieffer. "Theory of Superconductivity". In: *Physical Review* 108.5 (1957), pp. 1175–1204. ISSN: 0031-899X. DOI: 10.1103/PhysRev.108.1175.

[Bec+10] C Becker et al. "Ultracold quantum gases in triangular optical lattices". In: *New Journal of Physics* 12.6 (2010), p. 065025. ISSN: 1367-2630. DOI: 10.1088/1367-2630/12/6/065025.

[Ben+09] Vera Bendkowsky et al. "Observation of ultralong-range Rydberg molecules". In: *Nature* 458.7241 (2009), pp. 1005–8. ISSN: 1476-4687.

[Ber+17] Hannes Bernien et al. "Probing many-body dynamics on a 51-atom quantum simulator". In: *Nature* 551.7682 (2017), pp. 579–584. ISSN: 0028-0836. DOI: 10.1038/nature24622.

[Ber71] V.L. Berezinskii. "Destruction of Long-range Order in One-dimensional and Two-dimensional Systems having a Continuous Symmetry Group I. Classical Systems". In: *Journal of Experimental and Theoretical Physics* 32.3 (1971), pp. 493–500.

[Ber72] V.L. Berezinskii. "Destruction of Long-range Order in One-dimensional and Two-dimensional Systems Possessing a Continuous Symmetry Group. II. Quantum Systems." In: *Journal of Experimental and Theoretical Physics* 34.3 (1972), pp. 610–616.

[Bet+09] I. I. Beterov et al. "Quasiclassical calculations of blackbody-radiation-induced depopulation rates and effective lifetimes of Rydberg $nS$, $nP$, and $nD$ alkali-metal atoms with $n \leq 80$". In: *Physical Review A* 79.5 (2009), p. 052504. ISSN: 1050-2947. DOI: 10.1103/PhysRevA.79.052504.

[BGH18] Mathieu Barbier, Andreas Geißler, and Walter Hofstetter. "Dissipation-induced steady states in bosonic Rydberg-dressed quantum gases in an optical lattice". In: *in preparation* (2018).

[BHJ26] M. Born, W. Heisenberg, and P. Jordan. "Zur Quantenmechanik. II." In: *Zeitschrift für Physik* 35.8-9 (1926), pp. 557–615. ISSN: 1434-6001. DOI: 10.1007/BF01379806.

[Bis12] Ulf Bissbort. "Dynamical effects and disorder in ultracold bosonic matter". PhD thesis. Johann Wolfgang Goethe-Universität, 2012.

[BJ25] M. Born and P. Jordan. "Zur Quantenmechanik". In: *Zeitschrift für Physik* 34.1 (1925), pp. 858–888. ISSN: 1434-6001. DOI: 10.1007/BF01328531.

[Bog47] N.N. Bogolyubov. "On the theory of superfluidity". In: *J.Phys.(USSR)* 11 (1947), pp. 23–32.

[Boh13a] N. Bohr. "I. On the constitution of atoms and molecules". In: *Philosophical Magazine Series 6* 26.151 (1913), pp. 1–25. ISSN: 1941-5982. DOI: 10.1080/14786441308634955.

[Boh13b] N. Bohr. "LXXIII. On the constitution of atoms and molecules". In: *Philosophical Magazine Series 6* 26.155 (1913), pp. 857–875. ISSN: 1941-5982. DOI: 10.1080/14786441308635031.

[Boh13c] N. Bohr. "XXXVII. On the constitution of atoms and molecules". In: *Philosophical Magazine Series 6* 26.153 (1913), pp. 476–502. ISSN: 1941-5982. DOI: 10.1080/14786441308634993.

[Boh54] Niels Bohr. *Rydberg's discovery of the spectral laws*. 1954.

[Boo+15] D Booth et al. "Molecular physics. Production of trilobite Rydberg molecule dimers with kilo-Debye permanent electric dipole moments." In: *Science (New York, N.Y.)* 348.6230 (2015), pp. 99–102. ISSN: 1095-9203. DOI: 10.1126/science.1260722.

[Bos24] Bose. "Plancks Gesetz und Lichtquantenhypothese". In: *Zeitschrift für Physik* 26.1 (1924), pp. 178–181. ISSN: 1434-6001. DOI: 10.1007/BF01327326.

[Bou+17] T. Boulier et al. "Spontaneous avalanche dephasing in large Rydberg ensembles". In: *Physical Review A* 96.5 (2017), p. 053409. ISSN: 2469-9926. DOI: 10.1103/PhysRevA.96.053409.

[BP12] Marianne Bauer and Meera M. Parish. "Dipolar Gases in Coupled One-Dimensional Lattices". In: *Physical Review Letters* 108.25 (2012), p. 255302. ISSN: 0031-9007. DOI: 10.1103/PhysRevLett.108.255302.

[Bra+10] Drew B. Branden et al. "Radiative lifetime measurements of rubidium Rydberg states". In: *Journal of Physics B: Atomic, Molecular and Optical Physics* 43.1 (2010), p. 015002. ISSN: 0953-4075. DOI: 10.1088/0953-4075/43/1/015002. arXiv: 0910.1073.

[Bra+95] C. C. Bradley et al. "Evidence of Bose-Einstein Condensation in an Atomic Gas with Attractive Interactions". In: *Physical Review Letters* 75.9 (1995), pp. 1687–1690. ISSN: 0031-9007. DOI: 10.1103/PhysRevLett.75.1687.

[BSH97] C. C. Bradley, C. A. Sackett, and R. G. Hulet. "Bose-Einstein Condensation of Lithium: Observation of Limited Condensate Number". In: *Physical Review Letters* 78.6 (1997), pp. 985–989. ISSN: 0031-9007. DOI: 10.1103/PhysRevLett.78.985.

[Buo+09] Pierfrancesco Buonsante et al. "Gutzwiller approach to the Bose-Hubbard model with random local impurities". In: *Physical Review A* 79.1 (2009), p. 013623. ISSN: 1050-2947. DOI: 10.1103/PhysRevA.79.013623.

[Bur+09] F. J. Burnell et al. "Devil's staircases and supersolids in a one-dimensional dipolar Bose gas". In: *Physical Review B* 80.17 (2009), p. 174519. ISSN: 1098-0121. DOI: 10.1103/PhysRevB.80.174519.

[BV08] Krzysztof Byczuk and Dieter Vollhardt. "Correlated bosons on a lattice: Dynamical mean-field theory for Bose-Einstein condensed and normal phases". In: *Physical Review B* 77.23 (2008), p. 235106. ISSN: 1098-0121. DOI: 10.1103/PhysRevB.77.235106.

[BZ08] Immanuel Bloch and Wilhelm Zwerger. "Many-body physics with ultracold gases". In: *Reviews of Modern Physics* 80.3 (2008), pp. 885–964. ISSN: 0034-6861. DOI: 10.1103/RevModPhys.80.885.

[Car+09] Lincoln D Carr et al. "Cold and ultracold molecules: science, technology and applications". In: *New Journal of Physics* 11.5 (2009), p. 055049. ISSN: 1367-2630. DOI: 10.1088/1367-2630/11/5/055049.

[Car+13] C. Carr et al. "Nonequilibrium Phase Transition in a Dilute Rydberg Ensemble". In: *Physical Review Letters* 111.11 (2013), p. 113901. ISSN: 0031-9007. DOI: 10.1103/PhysRevLett.111.113901.

[CB04] D. M. Ceperley and B. Bernu. "Ring Exchanges and the Supersolid Phase of He 4". In: *Physical Review Letters* 93.15 (2004), p. 155303. ISSN: 0031-9007. DOI: 10.1103/PhysRevLett.93.155303.

[CBP14] Fabio Cinti, Massimo Boninsegni, and Thomas Pohl. "Exchange-induced crystallization of soft-core bosons". In: *New Journal of Physics* 16.3 (2014), p. 033038. ISSN: 1367-2630. DOI: 10.1088/1367-2630/16/3/033038. arXiv: 1402.0840.

[Che+05] Qijin Chen et al. "BCS-BEC crossover: From high temperature superconductors to ultracold superfluids". In: *Physics Reports* 412.1 (2005), pp. 1–88. ISSN: 0370-1573. DOI: 10.1016/J.PHYSREP.2005.02.005.

[Che70] G. V. Chester. "Speculations on Bose-Einstein Condensation and Quantum Crystals". In: *Physical Review A* 2.1 (1970), pp. 256–258. ISSN: 0556-2791. DOI: 10.1103/PhysRevA.2.256.

[Cin+10] F. Cinti et al. "Supersolid Droplet Crystal in a Dipole-Blockaded Gas". In: *Physical Review Letters* 105.13 (2010), p. 135301. ISSN: 0031-9007.

[Cin+14] Fabio Cinti et al. "Defect-induced supersolidity with soft-core bosons". In: *Nature Communications* 5 (2014), p. 3235. ISSN: 2041-1723. DOI: 10.1038/ncomms4235. arXiv: 1302.4576.

[Cou+98] Ph. Courteille et al. "Observation of a Feshbach Resonance in Cold Atom Scattering". In: *Physical Review Letters* 81.1 (1998), pp. 69–72. ISSN: 0031-9007. DOI: 10.1103/PhysRevLett.81.69.

[CPC99] B. Chaudhuri, F. Pederiva, and G. V. Chester. "Monte Carlo study of vacancies in the bcc and hcp phases of 4 He". In: *Physical Review B* 60.5 (1999), pp. 3271–3278. ISSN: 0163-1829. DOI: 10.1103/PhysRevB.60.3271.

[CS+08] Barbara Capogrosso-Sansone et al. "Monte Carlo study of the two-dimensional Bose-Hubbard model". In: *Physical Review A* 77.1 (2008), p. 015602. ISSN: 1050-2947. DOI: 10.1103/PhysRevA.77.015602.

[CS+10] B Capogrosso-Sansone et al. "Critical entropies for magnetic ordering in bosonic mixtures on a lattice". In: *Physical Review A* 81.5 (2010), p. 053622. ISSN: 1050-2947. DOI: 10.1103/PhysRevA.81.053622. arXiv: arXiv:0912.1865v1.

[CT04] Claude Cohen-Tannoudji. *Atoms in electromagnetic fields*. World Scientific, 2004, p. 770. ISBN: 981256019X.

[Dal+15] M. Dalmonte et al. "Cluster Luttinger liquids and emergent supersymmetric conformal critical points in the one-dimensional soft-shoulder Hubbard model". In: *Physical Review B* 92.4 (2015), p. 045106. ISSN: 1098-0121. DOI: 10.1103/PhysRevB.92.045106.

[Dav+95] K. B. Davis et al. "Bose-Einstein Condensation in a Gas of Sodium Atoms". In: *Physical Review Letters* 75.22 (1995), pp. 3969–3973. ISSN: 0031-9007. DOI: 10.1103/PhysRevLett.75.3969.

[DB07] James Day and John Beamish. "Low-temperature shear modulus changes in solid 4He and connection to supersolidity". In: *Nature* 450.7171 (2007), pp. 853–856. ISSN: 0028-0836. DOI: 10.1038/nature06383.

[Des+12] Rémi Desbuquois et al. "Superfluid behaviour of a two-dimensional Bose gas". In: *Nature Physics* 8.9 (2012), pp. 645–648. ISSN: 1745-2473. DOI: 10.1038/nphys2378.

[Dir81] P. A. M. (Paul Adrien Maurice) Dirac. *The principles of quantum mechanics*. Clarendon Press, 1981, p. 314. ISBN: 0198520115.

[Dut+00] S. Dutta et al. "Ponderomotive Optical Lattice for Rydberg Atoms". In: *Physical Review Letters* 85.26 (2000), pp. 5551–5554. ISSN: 0031-9007.

[Dzy+07] O Dzyapko et al. "Direct observation of Bose-Einstein condensation in a parametrically driven gas of magnons". In: *New Journal of Physics* 9.3 (2007), pp. 64–64. ISSN: 1367-2630. DOI: 10.1088/1367-2630/9/3/064.

[Ehr11] Paul Ehrenfest. "Welche Züge der Lichtquantenhypothese spielen in der Theorie der Wärmestrahlung eine wesentliche Rolle?" In: *Annalen der Physik* 341.11 (1911), pp. 91–118. ISSN: 00033804. DOI: 10.1002/andp.19113411106.

[Ein05] A. Einstein. "Über einen die Erzeugung und Verwandlung des Lichtes betreffenden heuristischen Gesichtspunkt". In: *Annalen der Physik* 322.6 (1905), pp. 132–148. ISSN: 00033804. DOI: 10.1002/andp.19053220607.

[Ein24] Albert Einstein. "Quantentheorie des einatomigen idealen Gases". In: *Sitzungsberichte der preussischen Akademie der Wissenschaften* (1924), pp. 261–267.

[Ein25] Albert Einstein. "Quantentheorie des einatomigen idealen Gases (zweite Abhandlung)". In: *Sitzungsberichte der preussischen Akademie der Wissenschaften* (1925), pp. 3–10.

[End+12a] Martin Enderlein et al. "Single Ions Trapped in a One-Dimensional Optical Lattice". In: *Physical Review Letters* 109.23 (2012), p. 233004. ISSN: 0031-9007. DOI: 10.1103/PhysRevLett.109.233004.

[End+12b] Manuel Endres et al. "The 'Higgs' amplitude mode at the two-dimensional superfluid/Mott insulator transition". In: *Nature* 487.7408 (2012), pp. 454–458. ISSN: 0028-0836. DOI: 10.1038/nature11255.

[Ern+10] Philipp T. Ernst et al. "Probing superfluids in optical lattices by momentum-resolved Bragg spectroscopy". In: *Nature Physics* 6.1 (2010), pp. 56–61. ISSN: 1745-2473. DOI: 10.1038/nphys1476.

[Fes58] Herman Feshbach. "Unified theory of nuclear reactions". In: *Annals of Physics* 5.4 (1958), pp. 357–390. ISSN: 00034916. DOI: 10.1016/0003-4916(58)90007-1.

[Fes62] Herman Feshbach. "A unified theory of nuclear reactions. II". In: *Annals of Physics* 19.2 (1962), pp. 287–313. ISSN: 0003-4916. DOI: 10.1016/0003-4916(62)90221-X.

[Fey82] Richard P. Feynman. "Simulating physics with computers". In: *International Journal of Theoretical Physics* 21.6-7 (1982), pp. 467–488. ISSN: 0020-7748. DOI: 10.1007/BF02650179.

[FGS89] B. A. Fraass, P. R. Granfors, and R. O. Simmons. "X-ray measurements of thermal vacancies in hcp He 4". In: *Physical Review B* 39.1 (1989), pp. 124–131. ISSN: 0163-1829. DOI: 10.1103/PhysRevB.39.124.

[FH14] J. Franck and G. Hertz. "Über Zusammenstöße zwischen Elektronen und den Molekülen des Quecksilberdampfes und die Ionisierungsspannung desselben". In: *Verhandlungen der Deutschen Physikalischen Gesellschaft* 16.16 (1914), pp. 457–467. ISSN: 00319279. DOI: 10.1002/phbl.19670230702.

[FIM05] Michael Fleischhauer, Atac Imamoglu, and Jonathan P. Marangos. "Electromagnetically induced transparency: Optics in coherent media". In: *Reviews of Modern Physics* 77.2 (2005), pp. 633–673. ISSN: 0034-6861. DOI: 10.1103/RevModPhys.77.633.

[Fis+89] Matthew P. A. Fisher et al. "Boson localization and the superfluid-insulator transition". In: *Physical Review B* 40.1 (1989), pp. 546–570. ISSN: 0163-1829. DOI: 10.1103/PhysRevB.40.546.

[FL88] Richard P. (Richard Phillips) Feynman and Ralph. Leighton. *What do YOU care what other people think? : further adventures of a curious character*. Norton, 1988, p. 255. ISBN: 0393026590.

[Föl+05] Simon Fölling et al. "Spatial quantum noise interferometry in expanding ultracold atom clouds". In: *Nature* 434.7032 (2005), pp. 481–484. ISSN: 0028-0836. DOI: 10.1038/nature03500.

[Gad+10] Bryce Gadway et al. "Superfluidity of Interacting Bosonic Mixtures in Optical Lattices". In: *Physical Review Letters* 105.4 (2010), p. 045303. ISSN: 0031-9007. DOI: 10.1103/PhysRevLett.105.045303.

[Gar+11] Michael C. Garrett et al. "Growth dynamics of a Bose-Einstein condensate in a dimple trap without cooling". In: *Physical Review A* 83.1 (2011), p. 013630. ISSN: 1050-2947. DOI: 10.1103/PhysRevA.83.013630.

[Gau+16] C. Gaul et al. "Resonant Rydberg Dressing of Alkaline-Earth Atoms via Electromagnetically Induced Transparency". In: *Physical Review Letters* 116.24 (2016), p. 243001. ISSN: 0031-9007. DOI: 10.1103/PhysRevLett.116.243001.

[GBH18] Andreas Geißler, Ulf Bissbort, and Walter Hofstetter. "Quasiparticle spectra of bosonic lattice gases at near-resonant Rydberg-dressing". In: *in preparation* (2018).

[GDS00] Chris H. Greene, A. S. Dickinson, and H. R. Sadeghpour. "Creation of Polar and Nonpolar Ultra-Long-Range Rydberg Molecules". In: *Physical Review Letters* 85.12 (2000), pp. 2458–2461. ISSN: 0031-9007. DOI: 10.1103/PhysRevLett.85.2458.

[Geo+96] Antoine Georges et al. "Dynamical mean-field theory of strongly correlated fermion systems and the limit of infinite dimensions". In: *Reviews of Modern Physics* 68.1 (1996), pp. 13–125. ISSN: 0034-6861. DOI: 10.1103/RevModPhys.68.13.

[GH17] Andreas Geißler and Walter Hofstetter. "Infinite occupation number basis of bosons: Solving a numerical challenge". In: *Physical Review B* 95.22 (2017), p. 224516. ISSN: 2469-9950. DOI: 10.1103/PhysRevB.95.224516.

[GI07] Matthew T. Glossop and Kevin Ingersent. "Kondo physics and dissipation: A numerical renormalization-group approach to Bose-Fermi Kondo models". In: *Physical Review B* 75.10 (2007), p. 104410. ISSN: 1098-0121. DOI: 10.1103/PhysRevB.75.104410.

[GK63] H. A. Gersch and G. C. Knollman. "Quantum Cell Model for Bosons". In: *Physical Review* 129.2 (1963), pp. 959–967. ISSN: 0031-899X. DOI: 10.1103/PhysRev.129.959.

[GK92] Antoine Georges and Gabriel Kotliar. "Hubbard model in infinite dimensions". In: *Physical Review B* 45.12 (1992), pp. 6479–6483. ISSN: 0163-1829. DOI: 10.1103/PhysRevB.45.6479.

[Gla+14] A. W. Glaetzle et al. "Quantum Spin-Ice and Dimer Models with Rydberg Atoms". In: *Physical Review X* 4.4 (2014), p. 041037. ISSN: 2160-3308. DOI: 10.1103/PhysRevX.4.041037. arXiv: 1404.5326.

[Gol+16] E. A. Goldschmidt et al. "Anomalous Broadening in Driven Dissipative Rydberg Systems". In: *Physical Review Letters* 116.11 (2016), p. 113001. ISSN: 0031-9007.

[GR+09] J J García-Ripoll et al. "Dissipation-induced hard-core boson gas in an optical lattice". In: *New Journal of Physics* 11.1 (2009), p. 013053. ISSN: 1367-2630.

[Gre+00] Slava Grebenev et al. "Evidence for Superfluidity in Para-Hydrogen Clusters Inside Helium-4 Droplets at 0.15 Kelvin." In: *Science (New York, N.Y.)* 289.5484 (2000), pp. 1532–1535. ISSN: 1095-9203. DOI: 10.1126/SCIENCE.289.5484.1532.

[Gre+02a] Markus Greiner et al. "Collapse and revival of the matter wave field of a Bose-Einstein condensate". In: *Nature* 419.6902 (2002), pp. 51–54. ISSN: 0028-0836. DOI: 10.1038/nature00968.

[Gre+02b] Markus Greiner et al. "Quantum phase transition from a superfluid to a Mott insulator in a gas of ultracold atoms". In: *Nature* 415.6867 (2002), pp. 39–44. ISSN: 0028-0836. DOI: 10.1038/415039a.

[Gri+05] Axel Griesmaier et al. "Bose-Einstein Condensation of Chromium". In: *Physical Review Letters* 94.16 (2005), p. 160401. ISSN: 0031-9007. DOI: 10.1103/PhysRevLett.94.160401.

[GS22] Walther Gerlach and Otto Stern. "Der experimentelle Nachweis der Richtungsquantelung im Magnetfeld". In: *Zeitschrift für Physik* 9.1 (1922), pp. 349–352. ISSN: 1434-6001. DOI: 10.1007/BF01326983.

[GSL02] K. Góral, L. Santos, and M. Lewenstein. "Quantum Phases of Dipolar Bosons in Optical Lattices". In: *Physical Review Letters* 88.17 (2002), p. 170406. ISSN: 0031-9007. DOI: 10.1103/PhysRevLett.88.170406.

[GSS95] Allan. Griffin, D. W. Snoke, and S. Stringari. *Bose-Einstein condensation*. Cambridge University Press, 1995, p. 602. ISBN: 0521589908.

[Gul+11] Emanuel Gull et al. "Continuous-time Monte Carlo methods for quantum impurity models". In: *Reviews of Modern Physics* 83.2 (2011), pp. 349–404. ISSN: 0034-6861. DOI: 10.1103/RevModPhys.83.349.

[Gut63] Martin C. Gutzwiller. "Effect of Correlation on the Ferromagnetism of Transition Metals". In: *Physical Review Letters* 10.5 (1963), pp. 159–162. ISSN: 0031-9007. DOI: 10.1103/PhysRevLett.10.159.

[Gut64] Martin C. Gutzwiller. "Effect of Correlation on the Ferromagnetism of Transition Metals". In: *Physical Review* 134.4A (1964), A923–A941. ISSN: 0031-899X. DOI: 10.1103/PhysRev.134.A923.

[Gut65] Martin C. Gutzwiller. "Correlation of Electrons in a Narrow $s$ Band". In: *Physical Review* 137.6A (1965), A1726–A1735. ISSN: 0031-899X. DOI: 10.1103/PhysRev.137.A1726.

[GVH17] Andreas Geißler, Ivana Vasić, and Walter Hofstetter. "Condensation versus long-range interaction: Competing quantum phases in bosonic optical lattice systems at near-resonant Rydberg dressing". In: *Physical Review A* 95.6 (2017), p. 063608. ISSN: 2469-9926. DOI: 10.1103/PhysRevA.95.063608.

[Gün+13] G Günter et al. "Observing the dynamics of dipole-mediated energy transport by interaction-enhanced imaging". In: *Science (New York, N.Y.)* 342.6161 (2013), pp. 954–6. ISSN: 1095-9203. DOI: 10.1126/science.1244843.

[Had+06] Zoran Hadzibabic et al. "Berezinskii-Kosterlitz-Thouless crossover in a trapped atomic gas". In: *Nature* 441.7097 (2006), pp. 1118–1121. ISSN: 0028-0836. DOI: 10.1038/nature04851.

[Hal06] Karen A. Hallberg. "New trends in density matrix renormalization". In: *Advances in Physics* 55.5-6 (2006), pp. 477–526. ISSN: 0001-8732. DOI: 10.1080/00018730600766432.

[Hau+12] Philipp Hauke et al. "Non-Abelian Gauge Fields and Topological Insulators in Shaken Optical Lattices". In: *Physical Review Letters* 109.14 (2012), p. 145301. ISSN: 0031-9007. DOI: 10.1103/PhysRevLett.109.145301.

[HBT56] R. Hanbury Brown and R. Q. Twiss. "Correlation between Photons in two Coherent Beams of Light". In: *Nature* 177.4497 (1956), pp. 27–29. ISSN: 0028-0836. DOI: 10.1038/177027a0.

[Hei11] Werner 1901-1976 Heisenberg. *Physik und Philosophie*. Hirzel, 2011. ISBN: 9783777624327.

[Hei25] W. Heisenberg. "Über quantentheoretische Umdeutung kinematischer und mechanischer Beziehungen." In: *Zeitschrift für Physik* 33.1 (1925), pp. 879–893. ISSN: 1434-6001. DOI: 10.1007/BF01328377.

[Hen+12] N. Henkel et al. "Supersolid Vortex Crystals in Rydberg-Dressed Bose-Einstein Condensates". In: *Physical Review Letters* 108.26 (2012), p. 265301. ISSN: 0031-9007. DOI: 10.1103/PhysRevLett.108.265301.

[HNP10] N. Henkel, R. Nath, and T. Pohl. "Three-Dimensional Roton Excitations and Supersolid Formation in Rydberg-Excited Bose-Einstein Condensates". In: *Physical Review Letters* 104.19 (2010), p. 195302. ISSN: 0031-9007. DOI: 10.1103/PhysRevLett.104.195302. arXiv: 1001.3250.

[Hon+10] Jens Honer et al. "Collective Many-Body Interaction in Rydberg Dressed Atoms". In: *Physical Review Letters* 105.16 (2010), p. 160404. ISSN: 0031-9007. DOI: 10.1103/PhysRevLett.105.160404. arXiv: 1004.2499.

[HP15] Dario Hügel and Lode Pollet. "Thermodynamics of the Bose-Hubbard model in a Bogoliubov+U theory". In: *Physical Review B* 91.22 (2015), p. 224510. ISSN: 1098-0121. DOI: 10.1103/PhysRevB.91.224510.

[HSH09] A. Hubener, M. Snoek, and W. Hofstetter. "Magnetic phases of two-component ultracold bosons in an optical lattice". In: *Physical Review B* 80.24 (2009), p. 245109. ISSN: 1098-0121. DOI: 10.1103/PhysRevB.80.245109.

[Hsu+12] C.-H. Hsueh et al. "Quantum crystals in a trapped Rydberg-dressed Bose-Einstein condensate". In: *Physical Review A* 86.1 (2012), p. 013619. ISSN: 1050-2947. DOI: 10.1103/PhysRevA.86.013619.

[IF09] M. Iskin and J. K. Freericks. "Strong-coupling perturbation theory for the extended Bose-Hubbard model". In: *Physical Review A* 79.5 (2009), p. 053634. ISSN: 1050-2947. DOI: 10.1103/PhysRevA.79.053634.

[Ino+98] S. Inouye et al. "Observation of Feshbach resonances in a Bose-Einstein condensate". In: *Nature* 392.6672 (1998), pp. 151–154. ISSN: 0028-0836. DOI: 10.1038/32354.

[Jak+98] D. Jaksch et al. "Cold Bosonic Atoms in Optical Lattices". In: *Physical Review Letters* 81.15 (1998), pp. 3108–3111. ISSN: 0031-9007. DOI: 10.1103/PhysRevLett.81.3108.

[Jau+16] Y.-Y. Jau et al. "Entangling atomic spins with a Rydberg-dressed spin-flip blockade". In: *Nature Physics* 12.1 (2016), pp. 71–74. ISSN: 1745-2473. DOI: 10.1038/nphys3487.

[Jea05] J.H. Jeans. "XI. On the partition of energy between matter and Æther". In: *Philosophical Magazine Series 6* 10.55 (1905), pp. 91–98. ISSN: 1941-5982. DOI: 10.1080/14786440509463348.

[Jo+12] Gyu-Boong Jo et al. "Ultracold Atoms in a Tunable Optical Kagome Lattice". In: *Physical Review Letters* 108.4 (2012), p. 045305. ISSN: 0031-9007. DOI: 10.1103/PhysRevLett.108.045305.

[JR10] J. E. Johnson and S. L. Rolston. "Interactions between Rydberg-dressed atoms". In: *Physical Review A* 82.3 (2010), p. 033412. ISSN: 1050-2947. DOI: 10.1103/PhysRevA.82.033412. arXiv: 1006.3212.

[Kap38] P. Kapitza. "Viscosity of Liquid Helium below the $\lambda$-Point". In: *Nature* 141.3558 (1938), pp. 74–74. ISSN: 0028-0836. DOI: 10.1038/141074a0.

[KC04a] E Kim and M H W Chan. "Observation of superflow in solid helium". In: *Science (New York, N.Y.)* 305.5692 (2004), pp. 1941–4. ISSN: 1095-9203. DOI: 10.1126/science.1101501.

[KC04b] E. Kim and M. H. W. Chan. "Probable observation of a supersolid helium phase". In: *Nature* 427.6971 (2004), pp. 225–227. ISSN: 0028-0836. DOI: 10.1038/nature02220.

[KC12] Duk Y. Kim and Moses H. W. Chan. "Absence of Supersolidity in Solid Helium in Porous Vycor Glass". In: *Physical Review Letters* 109.15 (2012), p. 155301. ISSN: 0031-9007. DOI: 10.1103/PhysRevLett.109.155301.

[KCB92] Werner Krauth, Michel Caffarel, and Jean-Philippe Bouchaud. "Gutzwiller wave function for a model of strongly interacting bosons". In: *Physical Review B* 45.6 (1992), pp. 3137–3140. ISSN: 0163-1829. DOI: 10.1103/PhysRevB.45.3137.

[KHS15] Manas Kulkarni, David A. Huse, and Herbert Spohn. "Fluctuating hydrodynamics for a discrete Gross-Pitaevskii equation: Mapping onto the Kardar-Parisi-Zhang universality class". In: *Physical Review A* 92.4 (2015), p. 043612. ISSN: 1050-2947. DOI: 10.1103/PhysRevA.92.043612.

[Kiv82] S. Kivelson. "Wannier functions in one-dimensional disordered systems: Application to fractionally charged solitons". In: *Physical Review B* 26.8 (1982), pp. 4269–4277. ISSN: 0163-1829. DOI: 10.1103/PhysRevB.26.4269.

[KK09] Yasuyuki Kato and Naoki Kawashima. "Quantum Monte Carlo method for the Bose-Hubbard model with harmonic confining potential". In: *Physical Review E* 79.2 (2009), p. 021104. ISSN: 1539-3755. DOI: 10.1103/PhysRevE.79.021104.

[KN11] Konstantin V. Krutitsky and Patrick Navez. "Excitation dynamics in a lattice Bose gas within the time-dependent Gutzwiller mean-field approach". In: *Physical Review A* 84.3 (2011), p. 033602. ISSN: 1050-2947. DOI: 10.1103/PhysRevA.84.033602.

[Kol07] Andrey R. Kolovsky. "Semiclassical analysis of the Bogoliubov spectrum in the Bose-Hubbard model". In: *Physical Review E* 76.2 (2007), p. 026207. ISSN: 1539-3755. DOI: 10.1103/PhysRevE.76.026207.

[KT73] J M Kosterlitz and D J Thouless. "Ordering, metastability and phase transitions in two-dimensional systems". In: *Journal of Physics C: Solid State Physics* 6.7 (1973), pp. 1181–1203. ISSN: 0022-3719. DOI: 10.1088/0022-3719/6/7/010.

[KV04] Gabriel Kotliar and Dieter Vollhardt. "Strongly correlated materials: Insights from dynamical mean-field theory". In: *Physics Today* 57.3 (2004), pp. 53–59. ISSN: 0031-9228. DOI: 10.1063/1.1712502.

[Lah+07] Thierry Lahaye et al. "Strong dipolar effects in a quantum ferrofluid". In: *Nature* 448.7154 (2007), pp. 672–5. ISSN: 1476-4687. DOI: 10.1038/nature06036.

[Lan41] L. Landau. "Theory of the Superfluidity of Helium II". In: *Physical Review* 60.4 (1941), pp. 356–358. ISSN: 0031-899X. DOI: 10.1103/PhysRev.60.356.

[LBB10] Hyun-Jung Lee, Krzysztof Byczuk, and Ralf Bulla. "Numerical renormalization group for the bosonic single-impurity Anderson model: Dynamics". In: *Physical Review B* 82.5 (2010), p. 054516. ISSN: 1098-0121. DOI: 10.1103/PhysRevB.82.054516.

[Leg70] A. J. Leggett. "Can a Solid Be "Superfluid"?" In: *Physical Review Letters* 25.22 (1970), pp. 1543–1546. ISSN: 0031-9007. DOI: 10.1103/PhysRevLett.25.1543.

[Len00] P. Lenard. "Erzeugung von Kathodenstrahlen durch ultraviolettes Licht". In: *Annalen der Physik* 307.6 (1900), pp. 359–375. ISSN: 00033804. DOI: 10.1002/andp.19003070611.

[LG14] Igor Lesanovsky and Juan P. Garrahan. "Out-of-equilibrium structures in strongly interacting Rydberg gases with dissipation". In: *Physical Review A* 90.1 (2014), p. 011603. ISSN: 1050-2947. DOI: 10.1103/PhysRevA.90.011603. arXiv: 1402.2126.

[LHC12] Tony E. Lee, H. Häffner, and M. C. Cross. "Collective Quantum Jumps of Rydberg Atoms". In: *Physical Review Letters* 108.2 (2012), p. 023602. ISSN: 0031-9007.

[LHH16] Yongqiang Li, Liang He, and Walter Hofstetter. "Magnetic phase transitions of spin-1 ultracold bosons in a cubic optical lattice". In: *Physical Review A* 93.3 (2016), p. 033622. ISSN: 2469-9926. DOI: 10.1103/PhysRevA.93.033622.

[Li+11] Yongqiang Li et al. "Tunable anisotropic magnetism in trapped two-component Bose gases". In: *Physical Review B* 84.14 (2011), p. 144411. ISSN: 1098-0121. DOI: 10.1103/PhysRevB.84.144411. arXiv: 1105.4886.

[Li+12] Yongqiang Li et al. "Pomeranchuk effect and spin-gradient cooling of Bose-Bose mixtures in an optical lattice". In: *Physical Review A* 85.2 (2012), p. 023624. ISSN: 1050-2947. DOI: 10.1103/PhysRevA.85.023624.

[Li+17] Jun-Ru Li et al. "A stripe phase with supersolid properties in spin-orbit-coupled Bose-Einstein condensates". In: *Nature* 543.7643 (2017), pp. 91–94. ISSN: 0028-0836. DOI: 10.1038/nature21431.

[Li+18] Yongqiang Li et al. "Supersolidity of lattice bosons immersed in strongly correlated Rydberg dressed atoms". In: *Physical Review A* 97.2 (2018), p. 023619. ISSN: 2469-9926. DOI: 10.1103/PhysRevA.97.023619.

[Lin+12] Rasmus B. Linnet et al. "Pinning an Ion with an Intracavity Optical Lattice". In: *Physical Review Letters* 109.23 (2012), p. 233005. ISSN: 0031-9007. DOI: 10.1103/PhysRevLett.109.233005.

[LMF12] Achim Lauer, Dominik Muth, and Michael Fleischhauer. "Transport-induced melting of crystals of Rydberg dressed atoms in a one-dimensional lattice". In: *New Journal of Physics* 14.9 (2012), p. 095009. ISSN: 1367-2630. DOI: 10.1088/1367-2630/14/9/095009.

[Lon38] F. London. "The $\lambda$-Phenomenon of Liquid Helium and the Bose-Einstein Degeneracy". In: *Nature* 141.3571 (1938), pp. 643–644. ISSN: 0028-0836. DOI: 10.1038/141643a0.

[LPS14] Qin-Qin Lü, Kelly R. Patton, and Daniel E. Sheehy. "Self-consistent Hartree-Fock approach for interacting bosons in optical lattices". In: *Physical Review A* 90.6 (2014), p. 063625. ISSN: 1050-2947.

[LS91] Anthony J. Leggett and Fernando Sols. "On the concept of spontaneously broken gauge symmetry in condensed matter physics". In: *Foundations of Physics* 21.3 (1991), pp. 353–364. ISSN: 0015-9018. DOI: 10.1007/BF01883640.

[Lu+15] Zhen-Kai Lu et al. "Stable Dilute Supersolid of Two-Dimensional Dipolar Bosons". In: *Physical Review Letters* 115.7 (2015), p. 075303. ISSN: 0031-9007. DOI: 10.1103/PhysRevLett.115.075303. arXiv: 1409.7737.

[Luk+01] M. D. Lukin et al. "Dipole Blockade and Quantum Information Processing in Mesoscopic Atomic Ensembles". In: *Physical Review Letters* 87.3 (2001), p. 037901. ISSN: 0031-9007. DOI: 10.1103/PhysRevLett.87.037901.

[LY96] M. Lewenstein and L. You. "Quantum Phase Diffusion of a Bose-Einstein Condensate". In: *Physical Review Letters* 77.17 (1996), pp. 3489–3493. ISSN: 0031-9007. DOI: 10.1103/PhysRevLett.77.3489.

[LYL10] Mingwu Lu, Seo Ho Youn, and Benjamin L. Lev. "Trapping Ultracold Dysprosium: A Highly Magnetic Gas for Dipolar Physics". In: *Physical Review Letters* 104.6 (2010), p. 063001. ISSN: 0031-9007. DOI: 10.1103/PhysRevLett.104.063001.

[Löw+12] Robert Löw et al. "An experimental and theoretical guide to strongly interacting Rydberg gases". en. In: *Journal of Physics B: Atomic, Molecular and Optical Physics* 45.11 (2012), p. 113001. ISSN: 0953-4075.

[Lüh13] Dirk-Sören Lühmann. "Cluster Gutzwiller method for bosonic lattice systems". In: *Physical Review A* 87.4 (2013), p. 043619. ISSN: 1050-2947. DOI: 10.1103/PhysRevA.87.043619.

[Léo+17a] Julian Léonard et al. "Monitoring and manipulating Higgs and Goldstone modes in a supersolid quantum gas." In: *Science (New York, N.Y.)* 358.6369 (2017), pp. 1415–1418. ISSN: 1095-9203. DOI: 10.1126/science.aan2608.

[Léo+17b] Julian Léonard et al. "Supersolid formation in a quantum gas breaking a continuous translational symmetry". In: *Nature* 543.7643 (2017), pp. 87–90. ISSN: 0028-0836. DOI: 10.1038/nature21067.

[Mal+14] N Malossi et al. "Full Counting Statistics and Phase Diagram of a Dissipative Rydberg Gas". In: *Physical Review Letters* 113.2 (2014), p. 023006. ISSN: 0031-9007. DOI: 10.1103/PhysRevLett.113.023006. arXiv: 1308.1854.

[Mar+14] Matteo Marcuzzi et al. "Universal Nonequilibrium Properties of Dissipative Rydberg Gases". In: *Physical Review Letters* 113.21 (2014), p. 210401. ISSN: 0031-9007. DOI: 10.1103/PhysRevLett.113.210401. arXiv: 1406.1015.

[Mat+13] Marco Mattioli et al. "Cluster Luttinger Liquids of Rydberg-Dressed Atoms in Optical Lattices". In: *Physical Review Letters* 111.16 (2013), p. 165302. ISSN: 0031-9007. DOI: 10.1103/PhysRevLett.111.165302.

[Med+11] Patrick Medley et al. "Spin Gradient Demagnetization Cooling of Ultracold Atoms". In: *Physical Review Letters* 106.19 (2011), p. 195301. ISSN: 0031-9007. DOI: 10.1103/PhysRevLett.106.195301.

[MEK00] Giovanna Morigi, Jürgen Eschner, and Christoph H. Keitel. "Ground State Laser Cooling Using Electromagnetically Induced Transparency". In: *Physical Review Letters* 85.21 (2000), pp. 4458–4461. ISSN: 0031-9007. DOI: 10.1103/PhysRevLett.85.4458.

[MFC04] Zhao-Yuan Ma, Christopher J Foot, and Simon L Cornish. "Optimized evaporative cooling using a dimple potential: an efficient route to Bose–Einstein condensation". In: *Journal of Physics B: Atomic, Molecular and Optical Physics* 37.15 (2004), pp. 3187–3195. ISSN: 0953-4075. DOI: 10.1088/0953-4075/37/15/013.

[Mon92] A. (Arianna) Montorsi. *The Hubbard model : a reprint volume*. World Scientific, 1992, p. 282. ISBN: 9810205856.

[MS77] B. Misra and E. C. G. Sudarshan. "The Zeno's paradox in quantum theory". In: *Journal of Mathematical Physics* 18.4 (1977), p. 756. ISSN: 00222488.

[MSC14] Tommaso Macrì, Sebastiano Saccani, and Fabio Cinti. "Ground State and Excitation Properties of Soft-Core Bosons". In: *Journal of Low Temperature Physics* 177.1-2 (2014), pp. 59–71. ISSN: 0022-2291. DOI: 10.1007/s10909-014-1192-7. arXiv: 1402.3313.

[MT70] Hirotsugu Matsuda and Toshihiko Tsuneto. "Off-Diagonal Long-Range Order in Solids". In: *Progress of Theoretical Physics Supplement* 46 (1970), pp. 411–436. ISSN: 0375-9687. DOI: 10.1143/PTPS.46.411.

[MTL07] C. Menotti, C. Trefzger, and M. Lewenstein. "Metastable States of a Gas of Dipolar Bosons in a 2D Optical Lattice". In: *Physical Review Letters* 98.23 (2007), p. 235301. ISSN: 0031-9007. DOI: 10.1103/PhysRevLett.98.235301.

[Muk+11] R Mukherjee et al. "Many-body physics with alkaline-earth Rydberg lattices". en. In: *Journal of Physics B: Atomic, Molecular and Optical Physics* 44.18 (2011), p. 184010. ISSN: 0953-4075. DOI: 10.1088/0953-4075/44/18/184010.

[MV89] Walter Metzner and Dieter Vollhardt. "Correlated Lattice Fermions in $d = \infty$ Dimensions". In: *Physical Review Letters* 62.3 (1989), pp. 324–327. ISSN: 0031-9007. DOI: 10.1103/PhysRevLett.62.324.

[MVC07] V. Murg, F. Verstraete, and J. I. Cirac. "Variational study of hard-core bosons in a two-dimensional optical lattice using projected entangled pair states". In: *Physical Review A* 75.3 (2007), p. 033605. ISSN: 1050-2947. DOI: 10.1103/PhysRevA.75.033605.

[Mya+97] C. J. Myatt et al. "Production of Two Overlapping Bose-Einstein Condensates by Sympathetic Cooling". In: *Physical Review Letters* 78.4 (1997), pp. 586–589. ISSN: 0031-9007. DOI: 10.1103/PhysRevLett.78.586.

[Ni+08] K-K Ni et al. "A high phase-space-density gas of polar molecules." In: *Science (New York, N.Y.)* 322.5899 (2008), pp. 231–5. ISSN: 1095-9203. DOI: 10.1126/science.1163861.

[Nie+15] Thomas Niederprüm et al. "Giant Cross Section for Molecular Ion Formation in Ultracold Rydberg Gases". In: *Physical Review Letters* 115.1 (2015), p. 013003. ISSN: 0031-9007. DOI: 10.1103/PhysRevLett.115.013003. arXiv: 1503.01586.

[Nie+16] Thomas Niederprüm et al. "Observation of pendular butterfly Rydberg molecules". In: *Nature Communications* 7 (2016), p. 12820. ISSN: 2041-1723. DOI: 10.1038/ncomms12820.

[NT59] Isaac Newton and Herbert Westren Turnbull. *The correspondence of Isaac Newton. Vol. 1 1661-1675*. Cambridge Univ. Press, 1959. ISBN: 0521737834.

[Orú14] Román Orús. "A practical introduction to tensor networks: Matrix product states and projected entangled pair states". In: *Annals of Physics* 349 (2014), pp. 117–158. ISSN: 00034916. DOI: 10.1016/j.aop.2014.06.013.

[Ott+95] Anne van Otterlo et al. "Quantum phase transitions of interacting bosons and the supersolid phase". In: *Physical Review B* 52.22 (1995), pp. 16176–16186. ISSN: 0163-1829. DOI: 10.1103/PhysRevB.52.16176.

[PDL10] T. Pohl, E. Demler, and M. D. Lukin. "Dynamical Crystallization in the Dipole Blockade of Ultracold Atoms". In: *Physical Review Letters* 104.4 (2010), p. 043002. ISSN: 0031-9007.

[Pla01] Max Planck. "Ueber das Gesetz der Energieverteilung im Normalspectrum". In: *Annalen der Physik* 309.3 (1901), pp. 553–563. ISSN: 00033804. DOI: 10.1002/andp.19013090310.

[PO56] Oliver Penrose and Lars Onsager. "Bose-Einstein Condensation and Liquid Helium". In: *Physical Review* 104.3 (1956), pp. 576–584. ISSN: 0031-899X. DOI: 10.1103/PhysRev.104.576.

[Pol+10] L. Pollet et al. "Supersolid Phase with Cold Polar Molecules on a Triangular Lattice". In: *Physical Review Letters* 104.12 (2010), p. 125302. ISSN: 0031-9007. DOI: 10.1103/PhysRevLett.104.125302.

[Pol13] Lode Pollet. "A review of Monte Carlo simulations for the Bose-Hubbard model with diagonal disorder". In: *Comptes Rendus Physique* 14.8 (2013), pp. 712–724. ISSN: 16310705. DOI: 10.1016/j.crhy.2013.08.005.

[PS03] L. P. (Lev Petrovich) Pitaevskii and S. Stringari. *Bose-Einstein condensation*. Clarendon Press, 2003, p. 382. ISBN: 0198507194.

[PS05] Nikolay Prokof'ev and Boris Svistunov. "Supersolid State of Matter". In: *Physical Review Letters* 94.15 (2005), p. 155302. ISSN: 0031-9007. DOI: 10.1103/PhysRevLett.94.155302.

[PS08] Christopher. Pethick and Henrik. Smith. *Bose-Einstein condensation in dilute gases*. Cambridge University Press, 2008, p. 569. ISBN: 9780511802850.

[PSG02] Anatoli Polkovnikov, Subir Sachdev, and S. M. Girvin. "Nonequilibrium Gross-Pitaevskii dynamics of boson lattice models". In: *Physical Review A* 66.5 (2002), p. 053607. ISSN: 1050-2947. DOI: 10.1103/PhysRevA.66.053607.

[Pup+10] G. Pupillo et al. "Strongly Correlated Gases of Rydberg-Dressed Atoms: Quantum and Classical Dynamics". In: *Physical Review Letters* 104.22 (2010), p. 223002. ISSN: 0031-9007. DOI: 10.1103/PhysRevLett.104.223002.

[Rad+13] Louk Rademaker et al. "Influence of long-range interactions on charge ordering phenomena on a square lattice". In: *Physical Review E* 88.3 (2013), p. 032121. ISSN: 1539-3755. DOI: 10.1103/PhysRevE.88.032121. arXiv: 1306.4765.

[Ray00] Lord Rayleigh. "LIII. Remarks upon the law of complete radiation". In: *Philosophical Magazine Series 5* 49.301 (1900), pp. 539–540. ISSN: 1941-5982. DOI: 10.1080/14786440009463878.

[RBH01] J. M. Raimond, M. Brune, and S. Haroche. "Manipulating quantum entanglement with atoms and photons in a cavity". In: *Reviews of Modern Physics* 73.3 (2001), pp. 565–582. ISSN: 0034-6861. DOI: 10.1103/RevModPhys.73.565.

[Rei10] Eugenie Samuel Reich. "Condensed matter: The supersolid's nemesis". In: *Nature* 468.7325 (2010), pp. 748–750. ISSN: 0028-0836. DOI: 10.1038/468748a.

[RH05] F. Robicheaux and J. V. Hernández. "Many-body wave function in a dipole blockade configuration". In: *Physical Review A* 72.6 (2005), p. 063403. ISSN: 1050-2947. DOI: 10.1103/PhysRevA.72.063403.

[RK91] Daniel S. Rokhsar and B. G. Kotliar. "Gutzwiller projection for bosons". In: *Physical Review B* 44.18 (1991), pp. 10328–10332. ISSN: 0163-1829. DOI: 10.1103/PhysRevB.44.10328.

[RR06] Ann Sophie C. Rittner and John D. Reppy. "Observation of Classical Rotational Inertia and Nonclassical Supersolid Signals in Solid He 4 below 250 mK". In: *Physical Review Letters* 97.16 (2006), p. 165301. ISSN: 0031-9007. DOI: 10.1103/PhysRevLett.97.165301.

[Rut11] E. Rutherford. "LXXIX. The scattering of $\alpha$ and $\beta$ particles by matter and the structure of the atom". In: *Philosophical Magazine Series 6* 21.125 (1911), pp. 669–688. ISSN: 1941-5982. DOI: 10.1080/14786440508637080.

[Saf16] Mark Saffman. "Quantum computing with atomic qubits and Rydberg interactions: progress and challenges". In: *Journal of Physics B: Atomic, Molecular and Optical Physics* 49.20 (2016), p. 202001. ISSN: 0953-4075. DOI: 10.1088/0953-4075/49/20/202001. arXiv: 1605.05207.

[Sch+10a] J Schachenmayer et al. "Dynamical crystal creation with polar molecules or Rydberg atoms in optical lattices". en. In: *New Journal of Physics* 12.10 (2010), p. 103044. ISSN: 1367-2630.

[Sch+10b] Ch. Schneider et al. "Optical trapping of an ion". In: *Nature Photonics* 4.11 (2010), pp. 772–775. ISSN: 1749-4885. DOI: 10.1038/nphoton.2010.236.

[Sch+12] Peter Schauß et al. "Observation of mesoscopic crystalline structures in a two-dimensional Rydberg gas". In: *Nature* 491.7422 (2012), p. 10. ISSN: 1476-4687. DOI: 10.1038/nature11596. arXiv: 1209.0944.

[Sch+14] H Schempp et al. "Full Counting Statistics of Laser Excited Rydberg Aggregates in a One-Dimensional Geometry". In: *Physical Review Letters* 112.1 (2014), p. 013002. ISSN: 0031-9007. DOI: 10.1103/PhysRevLett.112.013002. arXiv: 1308.0264.

[Sch+15] P. Schauss et al. "Crystallization in Ising quantum magnets". In: *Science* 347.6229 (2015), pp. 1455–1458. ISSN: 0036-8075. DOI: 10.1126/science.1258351. arXiv: 1404.0980.

[Sch05] U. Schollwöck. "The density-matrix renormalization group". In: *Reviews of Modern Physics* 77.1 (2005), pp. 259–315. ISSN: 0034-6861. DOI: 10.1103/RevModPhys.77.259.

[Sch11] Ulrich Schollwöck. "The density-matrix renormalization group in the age of matrix product states". In: *Annals of Physics* 326.1 (2011), pp. 96–192. ISSN: 00034916. DOI: 10.1016/j.aop.2010.09.012.

[Sch26a] E. Schrödinger. "Quantisierung als Eigenwertproblem". In: *Annalen der Physik* 384.4 (1926), pp. 361–376. ISSN: 00033804. DOI: 10.1002/andp.19263840404.

[Sch26b] E. Schrödinger. "Quantisierung als Eigenwertproblem". In: *Annalen der Physik* 384.6 (1926), pp. 489–527. ISSN: 00033804. DOI: 10.1002/andp.19263840602.

[Sch26c] E. Schrödinger. "Quantisierung als Eigenwertproblem". In: *Annalen der Physik* 385.13 (1926), pp. 437–490. ISSN: 00033804. DOI: 10.1002/andp.19263851302.

[Sch26d] E. Schrödinger. "Quantisierung als Eigenwertproblem". In: *Annalen der Physik* 386.18 (1926), pp. 109–139. ISSN: 00033804. DOI: 10.1002/andp.19263861802.

[Sch26e] Erwin Schrödinger. "Über das Verhältnis der Heisenberg-Born-Jordanschen Quantenmechanik zu der meinem". In: *Annalen der Physik* 384.8 (1926), pp. 734–756. ISSN: 00033804. DOI: 10.1002/andp.19263840804.

[SEW15] Hugo U. R. Strand, Martin Eckstein, and Philipp Werner. "Beyond the Hubbard bands in strongly correlated lattice bosons". In: *Physical Review A* 92.6 (2015), p. 063602. ISSN: 1050-2947. DOI: 10.1103/PhysRevA.92.063602.

[SH13] Michiel Snoek and Walter Hofstetter. *Bosonic Dynamical Mean-Field Theory*, in *Quantum Gases: Finite Temperature and Non-Equilibrium Dynamics (Vol. 1 Cold Atoms Series)*. Ed. by N.P. Proukakis et al. World Scientific Publishing Company, 2013, p. 579. ISBN: 1848168101.

[She+93] K Sheshadri et al. "Superfluid and Insulating Phases in an Interacting-Boson Model: Mean-Field Theory and the RPA". In: *Europhysics Letters (EPL)* 22.4 (1993), pp. 257–263. ISSN: 0295-5075. DOI: 10.1209/0295-5075/22/4/004.

[Sin+05] Kilian Singer et al. "Long-range interactions between alkali Rydberg atom pairs correlated to the $ns-ns$, $np-np$ and $nd-nd$ asymptotes". en. In: *Journal of Physics B: Atomic, Molecular and Optical Physics* 38.2 (2005), S295–S307. ISSN: 0953-4075. DOI: 10.1088/0953-4075/38/2/021.

[Sla52] J. C. Slater. "A Soluble Problem in Energy Bands". In: *Physical Review* 87.5 (1952), pp. 807–835. ISSN: 0031-899X. DOI: 10.1103/PhysRev.87.807.

[SO15] Bodhaditya Santra and Herwig Ott. "Scanning electron microscopy of cold gases". In: *Journal of Physics B: Atomic, Molecular and Optical Physics* 48.12 (2015), p. 122001. ISSN: 0953-4075. DOI: 10.1088/0953-4075/48/12/122001.

[Som16] A. Sommerfeld. "Zur Quantentheorie der Spektrallinien". In: *Annalen der Physik* 356.17 (1916), pp. 1–94. ISSN: 00033804. DOI: 10.1002/andp.19163561702.

[SPG11] Eran Sela, Matthias Punk, and Markus Garst. "Dislocation-mediated melting of one-dimensional Rydberg crystals". In: *Physical Review B* 84.8 (2011), p. 085434. ISSN: 1098-0121.

[SS11] Philipp Strack and Subir Sachdev. "Dicke Quantum Spin Glass of Atoms and Photons". In: *Physical Review Letters* 107.27 (2011), p. 277202. ISSN: 0031-9007. DOI: 10.1103/PhysRevLett.107.277202.

[SSS14] K. Saha, S. Sinha, and K. Sengupta. "Phases and collective modes of Rydberg atoms in an optical lattice". In: *Physical Review A* 89.2 (2014), p. 023618. ISSN: 1050-2947.

[STH11] Michiel Snoek, Irakli Titvinidze, and Walter Hofstetter. "Canted antiferromagnetic order of imbalanced Fermi-Fermi mixtures in optical lattices by dynamical mean-field theory". In: *Physical Review B* 83.5 (2011), p. 054419. ISSN: 1098-0121. DOI: 10.1103/PhysRevB.83.054419. arXiv: 1007.5457.

[Stu93] K. Sturm. "Dynamic Structure Factor: An Introduction". In: *Zeitschrift für Naturforschung A* 48.1-2 (1993), pp. 233–242. ISSN: 1865-7109. DOI: 10.1515/zna-1993-1-244.

[Stö+04] Thilo Stöferle et al. "Transition from a Strongly Interacting 1D Superfluid to a Mott Insulator". In: *Physical Review Letters* 92.13 (2004), p. 130403. ISSN: 0031-9007. DOI: 10.1103/PhysRevLett.92.130403.

[SWM10] M. Saffman, T. G. Walker, and K. Mølmer. "Quantum information with Rydberg atoms". In: *Reviews of Modern Physics* 82.3 (2010), pp. 2313–2363. ISSN: 0034-6861.

[Tar+12] Leticia Tarruell et al. "Creating, moving and merging Dirac points with a Fermi gas in a tunable honeycomb lattice". In: *Nature* 483.7389 (2012), pp. 302–305. ISSN: 0028-0836. DOI: 10.1038/nature10871.

[TAV07] I. Tikhonenkov, J. R. Anglin, and A. Vardi. "Quantum dynamics of Bose-Hubbard Hamiltonians beyond the Hartree-Fock-Bogoliubov approximation: The Bogoliubov back-reaction approximation". In: *Physical Review A* 75.1 (2007), p. 013613. ISSN: 1050-2947. DOI: 10.1103/PhysRevA.75.013613.

[TIS38] L. TISZA. "Transport Phenomena in Helium II". In: *Nature* 141.3577 (1938), pp. 913–913. ISSN: 0028-0836. DOI: 10.1038/141913a0.

[Urv+15] A. Urvoy et al. "Strongly Correlated Growth of Rydberg Aggregates in a Vapor Cell". In: *Physical Review Letters* 114.20 (2015), p. 203002. ISSN: 0031-9007. DOI: 10.1103/PhysRevLett.114.203002. arXiv: 1408.0039.

[Vas+15] Ivana Vasić et al. "Chiral bosonic phases on the Haldane honeycomb lattice". In: *Physical Review B* 91.9 (2015), p. 094502. ISSN: 1098-0121. DOI: 10.1103/PhysRevB.91.094502.

[VCH14] Ivana Vidanović, Daniel Cocks, and Walter Hofstetter. "Dissipation through localized loss in bosonic systems with long-range interactions". In: *Physical Review A* 89.5 (2014), p. 053614. ISSN: 1050-2947. DOI: 10.1103/PhysRevA.89.053614. arXiv: 1402.0011.

[Ver+15] Benoît Vermersch et al. "Dynamical preparation of laser-excited anisotropic Rydberg crystals in 2D optical lattices". In: *New Journal of Physics* 17.1 (2015), p. 013008. ISSN: 1367-2630. DOI: 10.1088/1367-2630/17/1/013008. arXiv: 1408.0662.

[VGRC04] F. Verstraete, J. J. García-Ripoll, and J. I. Cirac. "Matrix Product Density Operators: Simulation of Finite-Temperature and Dissipative Systems". In: *Physical Review Letters* 93.20 (2004), p. 207204. ISSN: 0031-9007. DOI: 10.1103/PhysRevLett.93.207204.

[Vid03] Guifré Vidal. "Efficient Classical Simulation of Slightly Entangled Quantum Computations". In: *Physical Review Letters* 91.14 (2003), p. 147902. ISSN: 0031-9007. DOI: 10.1103/PhysRevLett.91.147902.

[Vid04] Guifré Vidal. "Efficient Simulation of One-Dimensional Quantum Many-Body Systems". In: *Physical Review Letters* 93.4 (2004), p. 040502. ISSN: 0031-9007. DOI: 10.1103/PhysRevLett.93.040502.

[VMC08] F. Verstraete, V. Murg, and J.I. Cirac. "Matrix product states, projected entangled pair states, and variational renormalization group methods for quantum spin systems". In: *Advances in Physics* 57.2 (2008), pp. 143–224. ISSN: 0001-8732. DOI: 10.1080/14789940801912366.

[WB10] Hendrik Weimer and Hans Peter Büchler. "Two-Stage Melting in Systems of Strongly Interacting Rydberg Atoms". In: *Physical Review Letters* 105.23 (2010), p. 230403. ISSN: 0031-9007.

[Web+15] T. M. Weber et al. "Mesoscopic Rydberg-blockaded ensembles in the superatom regime and beyond". In: *Nature Physics* 11.2 (2015), pp. 157–161. ISSN: 1745-2473. DOI: 10.1038/nphys3214. arXiv: 1407.3611.

[Wei+08] Hendrik Weimer et al. "Quantum Critical Behavior in Strongly Interacting Rydberg Gases". In: *Physical Review Letters* 101.25 (2008), p. 250601. ISSN: 0031-9007.

[Whi92] Steven R. White. "Density matrix formulation for quantum renormalization groups". In: *Physical Review Letters* 69.19 (1992), pp. 2863–2866. ISSN: 0031-9007. DOI: 10.1103/PhysRevLett.69.2863.

[Wid+04] Artur Widera et al. "Entanglement Interferometry for Precision Measurement of Atomic Scattering Properties". In: *Physical Review Letters* 92.16 (2004), p. 160406. ISSN: 0031-9007. DOI: 10.1103/PhysRevLett.92.160406.

[Wie96] Willy Wien. "Ueber die Energievertheilung im Emissionsspectrum eines schwarzen Körpers". In: *Annalen der Physik und Chemie* 294.8 (1896), pp. 662–669. ISSN: 00033804. DOI: 10.1002/andp.18962940803.

[Wil15] William Wilson. "LXXXIII. The quantum-theory of radiation and line spectra". In: *Philosophical Magazine Series 6* 29.174 (1915), pp. 795–802. ISSN: 1941-5982. DOI: 10.1080/14786440608635362.

[WS08] Thad G. Walker and M. Saffman. "Consequences of Zeeman degeneracy for the van der Waals blockade between Rydberg atoms". In: *Physical Review A* 77.3 (2008), p. 032723. ISSN: 1050-2947. DOI: 10.1103/PhysRevA.77.032723.

[WSN16] Ryan M. Wilson, Wilbur E. Shirley, and Stefan S. Natu. "Anomalous supersolidity in a weakly interacting dipolar Bose mixture on a square lattice". In: *Physical Review A* 93.1 (2016), p. 011605. ISSN: 2469-9926. DOI: 10.1103/PhysRevA.93.011605.

[Yan62] C. N. Yang. "Concept of Off-Diagonal Long-Range Order and the Quantum Phases of Liquid He and of Superconductors". In: *Reviews of Modern Physics* 34.4 (1962), pp. 694–704. ISSN: 0034-6861. DOI: 10.1103/RevModPhys.34.694.

[YAR10] Kelly Cooper Younge, Sarah Elizabeth Anderson, and Georg Raithel. "Adiabatic potentials for Rydberg atoms in a ponderomotive optical lattice". In: *New Journal of Physics* 12.2 (2010), p. 023031. ISSN: 1367-2630.

[You+10] K. C. Younge et al. "State-Dependent Energy Shifts of Rydberg Atoms in a Ponderomotive Optical Lattice". In: *Physical Review Letters* 104.17 (2010), p. 173001. ISSN: 0031-9007.

[Zei+15] Johannes Zeiher et al. "Microscopic Characterization of Scalable Coherent Rydberg Superatoms". In: *Physical Review X* 5.3 (2015), p. 031015. ISSN: 2160-3308. DOI: 10.1103/PhysRevX.5.031015. arXiv: 1503.02452.

[Zei+16] Johannes Zeiher et al. "Many-body interferometry of a Rydberg-dressed spin lattice". In: *Nature Physics* 12.12 (2016), pp. 1095–1099. ISSN: 1745-2473. DOI: 10.1038/nphys3835.

[Zei+17] Johannes Zeiher et al. "Coherent Many-Body Spin Dynamics in a Long-Range Interacting Ising Chain". In: *Physical Review X* 7.4 (2017), p. 041063. ISSN: 2160-3308. DOI: 10.1103/PhysRevX.7.041063.

[ZJW98] Chunli Zhang, Eric Jeckelmann, and Steven R. White. "Density Matrix Approach to Local Hilbert Space Reduction". In: *Physical Review Letters* 80.12 (1998), pp. 2661–2664. ISSN: 0031-9007. DOI: 10.1103/PhysRevLett.80.2661.

[ZRS11] S. Zhang, F. Robicheaux, and M. Saffman. "Magic-wavelength optical traps for Rydberg atoms". In: *Physical Review A* 84.4 (2011), p. 043408. ISSN: 1050-2947.

[ZV04] Michael Zwolak and Guifré Vidal. "Mixed-State Dynamics in One-Dimensional Quantum Lattice Systems: A Time-Dependent Superoperator Renormalization Algorithm". In: *Physical Review Letters* 93.20 (2004), p. 207205. ISSN: 0031-9007. DOI: 10.1103/PhysRevLett.93.207205.

[Zwe03] Wilhelm Zwerger. "Mott-Hubbard transition of cold atoms in optical lattices". In: *Journal of Optics B: Quantum and Semiclassical Optics* 5.2 (2003), S9–S16. ISSN: 1464-4266. DOI: 10.1088/1464-4266/5/2/352.

[De 25] Louis De Broglie. "Recherches sur la théorie des Quanta". In: *Annales de Physique* 10.3 (1925), pp. 22–128. ISSN: 0003-4169. DOI: 10.1051/anphys/192510030022.

[ÖR95] Stellan Östlund and Stefan Rommer. "Thermodynamic Limit of Density Matrix Renormalization". In: *Physical Review Letters* 75.19 (1995), pp. 3537–3540. ISSN: 0031-9007. DOI: 10.1103/PhysRevLett.75.3537.

# *Acknowledgements*

First of all I would like to thank my supervisor Prof. Walter Hofstetter for giving me the opportunity to do research in his group. His openness for discussion allowed me to gain knowledge on multiple uncounted occasions. I am further grateful for the mutual trust and respect we developed in our collaboration that encouraged me to also pursue my own personal scientific interests in this work.

Furthermore I want to thank Priv.-Doz. Axel Pelster, for his strong dedication in all our mentoring sessions, which helped me a lot to focus my work. I especially thank him for his willingness to be my second assessor.

I especially want to thank Ivana Vasić, who helped me tremendously to get started in the group and in understanding DMFT, while assisting me to avoid some of its possible pitfalls.

I am very thankful to Ulf Bissbort, whose work introduced me to the bosonic quasiparticle theory for a homogeneous Gutzwiller mean-field state. I especially want to thank him for all the insightful discussions we had.

I am sincerely grateful to all my colleagues, group members and friends whom I had the opportunity to get to know. I especially would like to thank Jan Lennart Bönsel, Arya Dhar, Mohsen Hafez-Torbati, Bernhard Irsigler, Jaromir Panas, Tao Qin and Junhui Zheng for careful proofreading. I would like to thank Karla Baumann, Ulrike Bornheimer, Agnieszka Cichy, Daniel Cocks, Jonathan Enders, Urs Gebert, Anna Golubeva, Pramod Kumar, Thomas Mertz, Rajbir Nirwan, Andrii Sotnikov, Dandan Su, Ivana Vasić, Tao Yin, and everyone else who regularly joined our lunch, for countless delightful conversations. I further thank Tao Yin and Jan Lennart Bönsel for having been such great office mates. I am deeply grateful to Christian Thurn and Onur Payir, who have long been great friends of mine. I also want to thank Mathieu Barbier, whose Bachelor and Master thesis I had the opportunity to supervise, for his many insightful question, from which also I could learn a lot.

I particularly want to thank Marie-Hélène Haußels and Michaela Groll, for their quick help in all organizational matters.

My gratitude goes to all the people I had the opportunity to discuss with and who helped me get new perspectives and insights on many occasions. They include Michael Fleischhauer, Christian Gross, Simon Hollerith, Thomas Niederprüm, Herwig Ott, Axel Pelster, Matthias Weidemüller, Hendrik Weimer, Shannon Whitlock, Johannes Zeiher and everyone else I might have forgotten.

I gratefully acknowledge the financial support from the Deutsche Forschungsgemeinschaft through SPP 1929 GiRyd, SFB/TR 49, FOR 801, the DAAD via PPP Serbia (project nr. 57215082) DAAD, as well as the high-performance computing center LOEWE-CSC.

Last but certainly not least, my deepest gratitude goes towards my wife Anna-Maria Geißler and our daughter Emilia Marie, whose immeasurable support always helped me to stay focused and never loose track.